NASA Contractor Report 167941

CALCULATION OF THE FLOW FIELD INCLUDING BOUNDARY LAYER EFFECTS FOR SUPERSONIC MIXED-COMPRESSION INLETS AT ANGLE OF ATTACK

Joseph Vadyak and Joe D. Hoffman

Purdue University
West Lafayette, Indiana

July 1982

Prepared for

NATIONAL AERONAUTICS AND SPACE ADMINISTRATION
Lewis Research Center
Under Grant NSG-3311

TABLE OF CONTENTS

APPENDICES Page

APPENDICES Page

APPENDICES Page

CALCULATION OF THE FLOW FIELD INCLUDING BOUNDARY LAYER EFFECTS FOR SUPERSONIC MIXED-COMPRESSION INLETS AT ANGLE OF ATTACK

Joseph Vadyak and Joe D. Hoffman
School of Mechanical Engineering
Purdue University, West Lafayette, Indiana 47907

SUMMARY

An analysis has been developed for calculating the flow field in supersonic mixed-compression aircraft inlets at angle of attack. A zonal modeling technique is employed to obtain the solution which divides the flow field into different computational regions. The computational regions consist of a supersonic core flow, boundary layer flows adjacent to both the forebody/centerbody and cowl contours, and flow in the shock wave-boundary layer interaction regions. This report describes the details of the zonal modeling analysis and presents some computational results.

The governing equations for the supersonic core flow form a hyperbolic system of partial differential equations. The equations for the characteristic surfaces and the compatibility equations applicable along these surfaces are derived. The characteristic surfaces are the stream surfaces, which are surfaces composed of streamlines, and the wave surfaces, which are surfaces tangent to a Mach conoid. The compatibility equations are expressed as directional derivatives along streamlines and bicharacteristics, which are the lines of tangency between a wave surface and a Mach conoid. The numerical integration procedure devised by D. S. Butler was employed to develop a numerical integration algorithm that is second-order accurate, explicit, and does not violate the domain of dependence of the differential equations.

The bow shock wave surrounding the forebody and the internal shock wave system inside of the inlet are determined by discrete shock wave fitting. The continuous flow field between shock waves is determined by the method of characteristics numerical integration procedure, and the flow properties across the shock waves are determined by the application of the Hugoniot jump conditions.

Characteristic unit processes were developed for interior field points, solid boundary points, field-shock wave points, and solid boundary-shock wave points. An inverse marching scheme is employed in which the solution is obtained on planes perpendicular to the axis of the centerbody and the cowl. The distance between successive solution planes is determined by the Courant-Friedrichs-Lewy stability criterion. Although the numerical integration

procedure developed herein is capable of analyzing three-dimensional flows in three-dimensional geometries, only axisymmetric geometries at angle of attack were considered in the present investigation.

The governing equations for the boundary layer flow adjacent to both the forebody/centerbody and the cowl form a parabolic system of partial differential equations. That system of equations is solved using a second-order implicit finite difference scheme which can compute both positive and negative cross flows. The finite difference algorithm is employed to compute all of the boundary layer flow except for that in the shock wave-boundary layer interaction regions.

The shock wave-boundary layer interaction region flow is characterized by an elliptic system of partial differential equations. The flow in an interaction region is computed using an efficient integral analysis which determines the property profiles in the boundary layer downstream of the interaction region. These profiles are then used as starting data for the analysis of the boundary layer flow downstream of the interaction region.

Selected computational results are presented for both external and internal flow cases to illustrate application of the analysis. Correlations with experiment are also given.

SECTION I

INTRODUCTION

1. INTRODUCTION

The purpose of this investigation was to develop a method for calculating the flow field, including boundary layer effects, for a supersonic mixed-compression aircraft inlet operating at angle of attack. A typical mixed-compression inlet is illustrated in Figure 1. Compression takes place both in the external flow about the forebody and in the internal flow inside the annulus. Since the free-stream velocity is supersonic, a bow shock wave is generated at the forebody tip. An internal shock wave emanates from the cowl lip and makes a number of reflections with the centerbody and cowl before terminating in the divergence downstream of the geometric throat of the annulus. The flow is subsonic downstream of that location.

A major objective in the design of any aircraft inlet is to achieve maximum flow compression with a minimum reduction in stagnation pressure. Moreover, since an adverse pressure gradient exists, suitable control of the boundary layer is a major design consideration. This is especially true for an inlet such as that illustrated in Figure 1, since a number of oblique shock wave-boundary layer interactions occur. In a mixed-compression inlet, it is not unusual to remove 10 percent or more of the cowl lip mass flow rate by boundary layer bleed to control separation of the boundary layer.

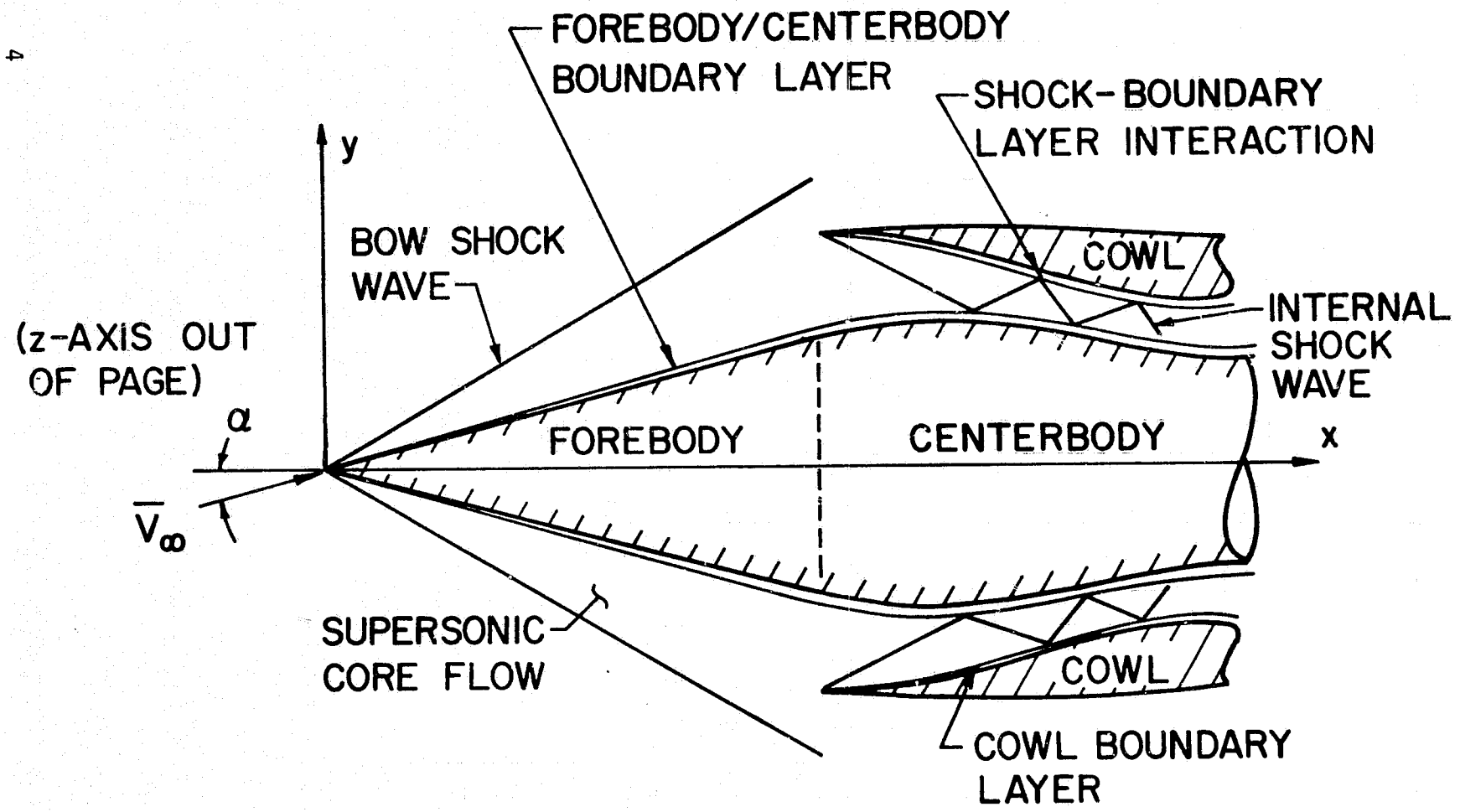

FIGURE 1. MIXED-COMPRESSION AIRCRAFT INLET.

The inlet illustrated in Figure 1 is axisymmetric. At zero incidence, the flow field is axisymmetric and can be computed using a two-dimensional method. However, at angle of attack, cross flow develops, and computation of the flow field requires a three-dimensional algorithm.

2. METHOD OF SOLUTION

A zonal modeling approach is employed in the present investigation. In this approach, the flow field is divided into different computational regimes, as illustrated in Figure 1. These regimes consist of the supersonic core flow, the centerbody and cowl boundary layers, and the shock wave-boundary layer interaction regions on both the centerbody and the cowl. An appropriate analysis is used for each of the different regimes.

The supersonic core flow is characterized by a hyperbolic system of governing partial differential equations. That system of equations is solved using a second-order pentahedral bicharacteristic scheme. The bow shock wave and the reflected internal shock wave system are computed using a discrete shock wave fitting procedure. The influence of viscous and thermal diffusion may be included in the supersonic core flow solution by treating the molecular transport terms as forcing functions in the bicharacteristic analysis.

The boundary layer flow is characterized by a parabolic system of governing partial differential equations. That system of equations is solved using a second-order implicit finite difference scheme which can compute both positive and negative cross flows. The finite

difference algorithm is used to compute all of the boundary flow except for the shock wave-boundary layer interaction regions.

The shock wave-boundary layer interaction region is characterized by an elliptic system of governing partial differential equations. The flow for this region is computed using an integral analysis which yields the property profiles in the boundary layer downstream of the interaction region. These profiles are then used as starting data for the analysis of the boundary layer flow downstream of the interaction region.

The present investigation is an extension of the study reported in References (1) and (2), which dealt with the development of the numerical algorithm used for the computation of the supersonic core flow. The present analysis deals with the development of the boundary layer and shock wave-boundary layer interaction computational procedures. A detailed description of the computer program developed to compute the entire flow field is given in NASA TM- , "A Computer Program for the Calculation of the Flow Field Including Boundary Layer Effects for Supersonic Mixed-Compression Inlets at Angle of Attack," by Joseph Vadyak, Joe D. Hoffman, and Allan R. Bishop.

SECTION II

GOVERNING EQUATIONS FOR THE SUPERSONIC CORE FLOW

1. INTRODUCTION

The fluid dynamic model for the supersonic core flow is based on the following major assumptions:

1. steady flow,
2. negligible body forces,
3. the working gas can be represented as a simple system in thermodynamic equilibrium,
4. no internal heat generation other than viscous dissipation, and
5. viscous and thermal diffusion effects of secondary importance.

The governing equations for the assumed flow model are written in the Cartesian coordinate system of Figure 1, and consist of the continuity equation, the component momentum equations, the energy equation, the thermal and caloric equations of state, and appropriate representations for the molecular transport properties. These equations are briefly presented in this section. A detailed development of these equations is given in Appendix A.

2. GOVERNING DIFFERENTIAL EQUATIONS

The continuity equation* [see Reference (3)] is given by

$$\frac{D\rho}{Dt} + \rho \frac{\partial u_i}{\partial x_i} = 0 \qquad (1)$$

*Repeated indices imply summation over the range of 1 to 3 unless otherwise noted.

where x_i (i = 1, 2, 3) denotes the three rectangular Cartesian coordinates x, y, and z, respectively, u_i denotes the corresponding velocity components u, v, and w, respectively, ρ denotes the density, and t denotes the time. The operator D( )/Dt in equation (1) is the material derivative given by

$$\frac{D(\ )}{Dt} = \frac{\partial(\ )}{\partial t} + u_j \frac{\partial(\ )}{\partial x_j} \tag{2}$$

For steady three-dimensional flow, equation (1) may be written in expanded form as

$$\rho u_x + \rho v_y + \rho w_z + u\rho_x + v\rho_y + w\rho_z = 0 \tag{3}$$

where the subscripts x, y, and z denote partial differentiation with respect to the corresponding direction.

The momentum equation is given by the Navier-Stokes equation (Ref. 3), which, in component form, is given by

$$\rho \frac{Du_i}{Dt} = B_i - \frac{\partial P}{\partial x_i} + \frac{\partial}{\partial x_j}\left[\mu\left(\frac{\partial u_i}{\partial x_j} + \frac{\partial u_j}{\partial x_i}\right)\right] - \frac{2}{3}\frac{\partial}{\partial x_i}\left(\mu \frac{\partial u_j}{\partial x_j}\right) + \frac{\partial}{\partial x_i}\left(\eta \frac{\partial u_j}{\partial x_j}\right) \quad (i = 1, 2, 3) \tag{4}$$

where B_i (i = 1, 2, 3) denotes the x, y, and z components of the body force, respectively, P denotes the pressure, μ denotes the dynamic viscosity, and η denotes the second coefficient of viscosity.

One of the assumptions of the present study is that the influence of molecular transport is considered to be of secondary importance as compared to the inertial effects in determining the supersonic core flow solution. As a consequence, the viscous and thermal diffusion terms appearing in the governing partial differential equations are treated as forcing functions or source terms in the method of characteristics scheme to be presented. In what follows, the molecular transport terms are placed on the right-hand sides of the respective governing equations, and the convective terms are placed on the left-hand sides of those equations. The convective terms then are considered as constituting the principal parts of these equations. Hence, by assuming steady flow, negligible body forces, $\eta = 0$ [Stokes's hypothesis (4)], inertial dominance, and variable transport properties, equation (4) may be written in expanded form for each of the three coordinate directions as

$$\rho u u_x + \rho v u_y + \rho w u_z + P_x = F_x \tag{5}$$

$$\rho u v_x + \rho v v_y + \rho w v_z + P_y = F_y \tag{6}$$

$$\rho u w_x + \rho v w_y + \rho w w_z + P_z = F_z \tag{7}$$

where

$$F_x = \mu_x\left[\frac{4}{3}u_x - \frac{2}{3}(v_y + w_z)\right] + \mu_y(u_y + v_x) + \mu_z(u_z + w_x)$$

$$+ \mu\left[\frac{4}{3}u_{xx} + u_{yy} + u_{zz} + \frac{1}{3}(v_{xy} + w_{xz})\right] \tag{8}$$

$$F_y = \mu_y\left[\frac{4}{3}v_y - \frac{2}{3}(u_x + w_z)\right] + \mu_x(v_x + u_y) + \mu_z(v_z + w_y)$$
$$+ \mu\left[\frac{4}{3}v_{yy} + v_{xx} + v_{zz} + \frac{1}{3}(u_{yx} + w_{yz})\right] \qquad (9)$$

$$F_z = \mu_z\left[\frac{4}{3}w_z - \frac{2}{3}(u_x + v_y)\right] + \mu_x(w_x + u_z) + \mu_y(w_y + v_z)$$
$$+ \mu\left[\frac{4}{3}w_{zz} + w_{xx} + w_{yy} + \frac{1}{3}(u_{zx} + v_{zy})\right] \qquad (10)$$

The appropriate form of the energy equation is now derived. In the following, the pressure P and density ρ are considered as being the primary thermodynamic variables. All secondary thermodynamic variables are then expressed in terms of the pressure and density.

It is assumed in the present investigation that the working gas may be represented as a simple system in thermodynamic equilibrium. For a simple system, specification of any two independent thermodynamic properties defines the thermodynamic state of the system (5). Hence, the following functional relationship may be written

$$P = P(\rho, s) \qquad (11)$$

where s is the entropy per unit mass. Employing the concept of the total derivative, and introducing the material derivative operator given by equation (2), the following equation is obtained.

$$\frac{DP}{Dt} = \left(\frac{\partial P}{\partial \rho}\right)_s \frac{D\rho}{Dt} + \left(\frac{\partial P}{\partial s}\right)_\rho \frac{Ds}{Dt} \qquad (12)$$

The sonic speed a is defined by

$$a^2 = \left(\frac{\partial P}{\partial \rho}\right)_s \qquad (13)$$

Introducing equation (13) into equation (12) yields

$$\frac{DP}{Dt} - a^2 \frac{D\rho}{Dt} = \left(\frac{\partial P}{\partial s}\right)_\rho \frac{Ds}{Dt} \tag{14}$$

The material derivative of entropy appearing in equation (14) may be expressed in terms of a thermal conduction function and a viscous dissipation function. The entropy may be expressed in terms of the internal energy by use of the thermodynamic relation (Ref. 5)

$$T\,ds = de + P\,d(1/\rho) \tag{15}$$

where T is the temperature, and e is the internal energy per unit mass. The internal energy may be expressed in terms of a thermal conduction function and a viscous dissipation function by use of the energy equation (Ref. 3)

$$\rho \frac{De}{Dt} = \frac{\partial}{\partial x_i}\left(\kappa \frac{\partial T}{\partial x_i}\right) + \frac{P}{\rho}\frac{D\rho}{Dt} + \Phi \tag{16}$$

where κ is the thermal conductivity, and Φ is the viscous dissipation function, which for $\eta = 0$ is given by

$$\Phi = \frac{1}{2}\mu\left[\left(\frac{\partial u_i}{\partial x_j} + \frac{\partial u_j}{\partial x_i}\right) - \frac{2}{3}\frac{\partial u_k}{\partial x_k}\delta_{ij}\right]^2 \tag{17}$$

where δ_{ij} is the Kronecker delta. Combining equations (14) to (17) and writing the resulting expression in expanded form for steady three-dimensional flow with variable transport properties yields

$$uP_x + vP_y + wP_z - a^2(u\rho_x + v\rho_y + w\rho_z) = F_e \tag{18}$$

where

$$F_e = \xi\Big\{ \kappa(T_{xx} + T_{yy} + T_{zz}) + \kappa_x T_x + \kappa_y T_y + \kappa_z T_z$$
$$+ \mu[2(u_x^2 + v_y^2 + w_z^2 + u_y v_x + u_z w_x + v_z w_y) + v_x^2$$
$$+ w_x^2 + u_y^2 + w_y^2 + u_z^2 + v_z^2 - \tfrac{2}{3}(u_x + v_y + w_z)^2]\Big\} \qquad (19)$$

and

$$\xi = \frac{1}{\rho T}\left(\frac{\partial P}{\partial s}\right)_\rho \qquad (20)$$

3. THERMODYNAMIC MODEL

Before a solution to the system of governing partial differential equations may be obtained, the temperature T, the sonic speed a, and the parameter ξ defined by equation (20) must be expressed in terms of the primary thermodynamic variables P and ρ. The general functional forms of the relations for T, a, and ξ are given by

$$T = T(P,\rho) \qquad (21)$$

$$a = a(P,\rho) \qquad (22)$$

$$\xi = \xi(P,\rho) \qquad (23)$$

The derivatives of the temperature appearing in equation (19) are expressed in terms of the derivatives of the pressure and the density by analytically differentiating equation (21).

For the special case of a thermally and calorically perfect gas, equations (21) to (23) take the following simple forms

$$T = P/\rho R \qquad (24)$$

$$a = (\gamma P/\rho)^{1/2} \qquad (25)$$

$$\xi = \gamma - 1 \tag{26}$$

where R is the gas constant, and γ is the specific heat ratio.

4. MOLECULAR TRANSPORT PROPERTIES

The dynamic viscosity μ and the thermal conductivity κ must be expressed in terms of the primary thermodynamic variables P and ρ. In general, both the viscosity and the thermal conductivity are assumed to be functions of temperature only. Hence,

$$\mu = \mu(T) \tag{27}$$

$$\kappa = \kappa(T) \tag{28}$$

The derivatives of the transport properties appearing in equations (8), (9), (10), and (19) are obtained in terms of the derivatives of the pressure and the density by analytically differentiating equations (27) and (28) with respect to the temperature, with the resulting temperature derivatives being obtained by analytically differentiating equation (21).

A widely accepted representation for equation (27) is the Sutherland formula (Ref. 4)

$$\mu = \mu_o \left(\frac{T}{T_o}\right)^{1.5} \left(\frac{T_o + S}{T + S}\right) \tag{29}$$

where μ_o is the viscosity at the reference temperature T_o, and S is a constant. The thermal conductivity may be represented as

$$\kappa = \frac{\mu c_p}{Pr} \tag{30}$$

where c_p is the constant pressure specific heat, and Pr is the laminar Prandtl number which is assumed constant in the analysis.

The contribution of turbulent transport may be considered in the computation by adding the appropriate eddy viscosity and eddy thermal conductivity functions to the molecular transport properties given by equations (27) and (28), respectively.

5. SUMMARY

In summary, the differential equations of motion for steady supersonic three-dimensional flow are given by equations (3), (5), (6), (7), and (18). For a thermally and calorically perfect gas, the thermodynamic model is represented by equations (24) to (26). The molecular transport properties are represented by equations (29) and (30).

SECTION III

SUPERSONIC CORE FLOW CHARACTERISTIC EQUATIONS

1. INTRODUCTION

Written in the form shown, with the left-hand sides constituting the principal parts, equations (3), (5), (6), (7), and (18) may be classified as a system of quasi-linear nonhomogenous partial differential equations of first order. The system is hyperbolic if the flow is supersonic. Systems of hyperbolic partial differential equations in three independent variables have the property that there exist surfaces in three-dimensional space on which linear combinations of the original partial differential equations can be formed that contain derivatives only in the surfaces themselves. These special surfaces are known as characteristic surfaces, and the linear combinations of the original partial differential equations are interior differential operators known as compatibility relations. In this section, the equations for the characteristic surfaces and the compatibility relations valid along these surfaces are listed and briefly discussed. A detailed development of these equations is given in Appendix B.

2. CHARACTERISTIC SURFACES

For steady three-dimensional supersonic flow, two families of characteristic surfaces exist, as illustrated in Figure 2. One family of characteristic surfaces consists of the stream surfaces given by

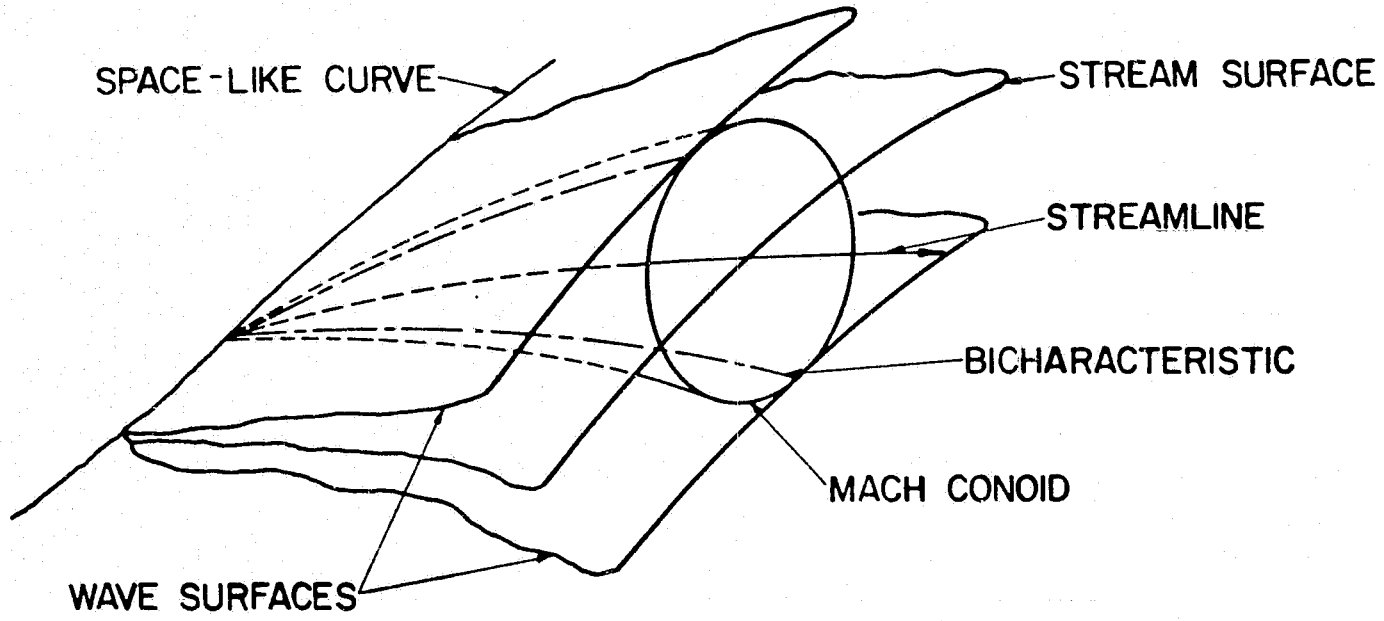

FIGURE 2. CHARACTERISTIC SURFACES

$$uN_x + vN_y + wN_z = 0 \tag{31}$$

where $\bar{N} = (N_x, N_y, N_z)$ denotes the normal to a stream surface. The envelope of all stream surfaces at a point forms a single pencil of planes whose axis is a streamline. A streamline may be represented by

$$dx/dt = u \qquad dy/dt = v \qquad dz/dt = w \tag{32}$$

where t is the time of travel of a fluid particle along the streamline.

The second family of characteristic surfaces consists of the wave surfaces given by

$$uN_x + vN_y + wN_z = a|\bar{N}| \tag{33}$$

where $\bar{N} = (N_x, N_y, N_z)$ denotes the normal to a wave surface. The envelope of all wave surfaces at a point forms a conoid known as the Mach conoid. The Mach conoid may be represented locally by a right circular cone known as the Mach cone. In differential form, the quadric surface of the Mach conoid is given by

$$\begin{aligned}[u^2 - (q^2 - a^2)](dx)^2 + [v^2 - (q^2 - a^2)](dy)^2 \\ + [w^2 - (q^2 - a^2)](dz)^2 + 2uv(dx)(dy) \\ + 2uw(dx)(dz) + 2vw(dy)(dz) = 0\end{aligned} \tag{34}$$

where q is the velocity magnitude ($q^2 = u^2 + v^2 + w^2$). The line of contact between a particular wave surface and the Mach conoid is known as a bicharacteristic. A bicharacteristic is a generator of the Mach conoid.

3. COMPATIBILITY RELATIONS

The compatibility relations which are applicable on the stream surfaces are given by

$$uP_x + vP_y + wP_z - a^2(u\rho_x + v\rho_y + w\rho_z) = F_e \tag{35}$$

$$\begin{aligned}&\rho u(uu_x + vu_y + wu_z) + \rho v(uv_x + vv_y + wv_z)\\ &+ \rho w(uw_x + vw_y + ww_z) + uP_x + vP_y + wP_z\\ &= uF_x + vF_y + wF_z\end{aligned} \tag{36}$$

$$\begin{aligned}&\rho S_x(uu_x + vu_y + wu_z) + \rho S_y(uv_x + vv_y + wv_z)\\ &+ \rho S_z(uw_x + vw_y + ww_z) + S_xP_x + S_yP_y + S_zP_z\\ &= S_xF_x + S_yF_y + S_zF_z\end{aligned} \tag{37}$$

In equation (37), $\overline{S} = (S_x, S_y, S_z)$ denotes a vector which lies in the stream surface and that is independent of the velocity vector. Equations (35) and (36) may be written in a form which contains differentiation in the streamline direction as follows.

$$\frac{dP}{dt} - a^2 \frac{d\rho}{dt} = F_e \tag{38}$$

$$\rho u \frac{du}{dt} + \rho v \frac{dv}{dt} + \rho w \frac{dw}{dt} + \frac{dP}{dt} = uF_x + vF_y + wF_z \tag{39}$$

In equations (38) and (39), the operator $d(\ )/dt$ represents the directional derivative along a streamline.

The compatibility relation which is applicable on the wave surfaces is given by

$$\rho a n_x(uu_x + vu_y + wu_z) + \rho a n_y(uv_x + vv_y + wv_z)$$
$$+ \rho a n_z(uw_x + vw_y + ww_z) + (an_x - u)P_x + (an_y - v)P_y$$
$$+ (an_z - w)P_z - \rho a^2(u_x + v_y + w_z) = \lambda \qquad (40)$$

where

$$\lambda = a(n_x F_x + n_y F_y + n_z F_z) - F_e \qquad (41)$$

In equations (40) and (41), $\hat{n} = (n_x, n_y, n_z)$ denotes the unit normal vector to the wave surface. Equation (40) may be written in a form which contains differentiation in the bicharacteristic direction as follows.

$$\rho a n_x \frac{du}{dt} + \rho a n_y \frac{dv}{dt} + \rho a n_z \frac{dw}{dt} - \frac{dP}{dt} = \lambda - \rho a^2[(n_x^2 - 1)u_x$$
$$+ (n_y^2 - 1)v_y + (n_z^2 - 1)w_z + n_x n_y(u_y + v_x)$$
$$+ n_x n_z(u_z + w_x) + n_y n_z(v_z + w_y)] \qquad (42)$$

In equation (42), the operator d( )/dt denotes the directional derivative along a bicharacteristic. The terms in brackets in equation (42) represent differentiation in the wave surface but in a direction normal to the bicharacteristic direction. Hereafter, these terms will be referred to as the cross derivatives.

At any point in the flow field there exists an infinite number of stream surfaces and wave surfaces. The number of independent

compatibility relations cannot exceed the number of independent equations of motion. As a consequence, it is necessary to determine which of the possible combinations of the compatibility relations form an independent set. Rusanov (6), using a proof in the space of characteristic normals, has shown for steady three-dimensional isentropic flow that two of the stream surface compability relations applied along a stream surface and the single wave surface compatibility relation applied along three different wave surfaces form an independent set of five characteristic relations. Rusanov's results may be extended to the present case since the principal parts of equations (3), (5), (6), (7), and (18) are the same as those for isentropic flow. Hence, the set of compatibility relations used in the present investigation consists of equations (38) and (39) applied along a streamline and equation (42) applied along three different bicharacteristics.

4. BUTLER'S PARAMETERIZATION OF THE CHARACTERISTIC EQUATIONS

D. S. Butler (7) developed a parameteric form for representing a bicharacteristic and the wave surface compatibility relation applicable along it. A detailed development of Butler's method is presented in Appendix B. A brief summary is given here.

Butler introduced the following parameteric form to represent a bicharacteristic.

$$dx_i = (u_i + c\alpha_i \cos\theta + c\beta_i \sin\theta)dt \qquad (i=1,2,3) \qquad (43)$$

In equation (43), t is the time of travel of a fluid particle along the streamline that is the axis of the Mach cone, θ is a parametric

angle denoting a particular element of the Mach cone and has the range $0 \leq \theta \leq 2\pi$, and c is given by

$$c^2 = q^2a^2/(q^2 - a^2) \tag{44}$$

where q is the velocity magnitude, and a is the sonic speed. The vectors α_i and β_i in equation (43) are parametric unit vectors with α_i, β_i, and u_i/q (i=1,2,3) forming an orthonormal set.

The corresponding parametric form of the wave surface compatibility relation, equation (40), is given by

$$\frac{dP}{dt} + \rho c(\alpha_i \cos\theta + \beta_i \sin\theta)\frac{du_i}{dt} = \Phi$$

$$- \rho c^2(\alpha_i \sin\theta - \beta_i \cos\theta)(\alpha_j \sin\theta - \beta_j \cos\theta)\frac{\partial u_i}{\partial x_j} \tag{45}$$

In equation (45), the operator d( )/dt represents differentiation in the bicharacteristic direction, and Φ is given by

$$\Phi = (c^2/a^2)[F_e - a(n_x F_x \quad n_y F_y + n_z F_z)] \tag{46}$$

where $\hat{n} = (n_x, n_y, n_z)$ denotes the unit normal to the wave surface, which may be written in parametric form as

$$n_i = (a/c)(cu_i/q^2 - \alpha_i \cos\theta - \beta_i \sin\theta) \quad (i=1,2,3) \tag{47}$$

In addition to the above relations, Butler also developed a non-characteristic relation which is applied along a streamline. This noncharacteristic relation is given by

$$\frac{dP}{dt} = \sigma - \rho c^2(\alpha_i \alpha_j + \beta_i \beta_j) \frac{\partial u_i}{\partial x_j} \tag{48}$$

where the operator $d(\ )/dt$ denotes differentiation along a streamline, and σ is given by

$$\sigma = (c^2/a^2)F_e - (c^2/q^2)(uF_x + vF_y + wF_z) \tag{49}$$

SECTION IV

NUMERICAL SOLUTION OF THE SUPERSONIC CORE FLOW EQUATIONS

1. INTRODUCTION

A variety of unit processes are employed in the computation of the supersonic core flow field. The unit processes may be classified into four major types: interior point, solid boundary point, field-shock wave point, and solid body-shock wave point. The basic unit processes are briefly discussed in this section. A detailed presentation of each unit process is given in Appendix E.

In the overall numerical algorithm, an inverse marching scheme is employed. The supersonic core flow solution is obtained on space-like planes of constant x, where the x-axis is the longitudinal axis of the centerbody and the cowl. For the internal flow, the solution is also obtained on the space curves which are defined by the intersections of the internal shock wave with the solid boundaries. Except in the vicinity of a shock wave-solid boundary intersection, the distance Δx between successive solution planes is determined by the application of the Courant-Friedrichs-Lewy (CFL) stability criterion (8). In the vicinity of a shock wave-solid boundary intersection, the axial step is controlled by special constraints, which are discussed later. The distance Δx is determined prior to the application of the unit processes.

2. INTERIOR POINT UNIT PROCESS

The computational network used in determining the solution for a typical interior point is illustrated in Figure 3. Points (1) to (4) represent the intersection points of four rearward-running bicharacteristics with the initial-value plane, point (5) is the streamline intersection point with the initial-value plane, and point (6) is the solution point on the solution plane. The axial (x) distance between the initial-value plane and the solution plane is determined prior to the application of the unit process by applying the CFL stability criterion. As in all the unit processes, the interior point unit process is divided into a predictor step and a corrector step. The corrector may be iterated to convergence if desired.

The interior point unit process is initiated by determining the location of the solution point, point (6). The coordinates of point (6) are determined by extending the streamline from point (5) to the solution plane using the following finite difference form of equation (32).

$$x_i(6) - x_i(5) = \frac{1}{2}[u_i(5) + u_i(6)][t(6) - t(5)] \quad (i=1,2,3) \qquad (50)$$

For the predictor, $u_i(6)$ is equated to $u_i(5)$. For the corrector, the previously determined value of $u_i(6)$ is employed. The axial step $[x(6) - x(5)]$ is computed before the unit process is applied. Hence, the time parameter $[t(6) - t(5)]$ may be obtained, after which the coordinates $y(6)$ and $z(6)$ are computed. Interpolated flow property values at point (5) are used in the integration, even though point (5) is a known field point. As shown by Ransom, Hoffman, and Thompson (9),

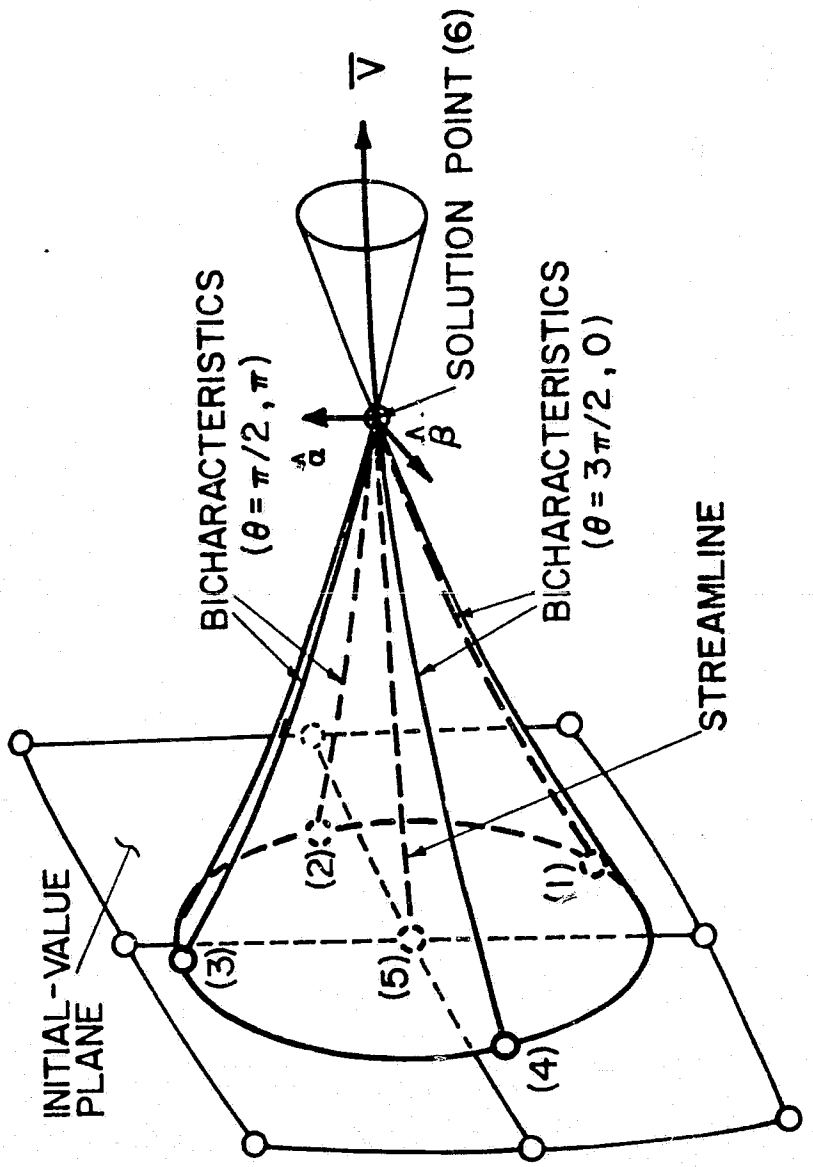

FIGURE 3. INTERIOR POINT COMPUTATIONAL NETWORK

this interpolation is required to produce a stable numerical scheme. The interpolated flow property values are obtained from the following quadratic bivariate interpolation polynomial

$$f(y,z) = a_1 + a_2 y + a_3 z + a_4 yz + a_5 y^2 + a_6 z^2 \qquad (51)$$

where $f(y,z)$ denotes a general function of the coordinates y and z, and the coefficients a_i (i=1 to 6) are obtained from a least squares fit of nine data points in the initial-value plane [point (5) and its eight immediate neighbors] as described in Appendix C.

With the location of the solution point determined, four bicharacteristics are extended from the solution point back to the initial-value plane to intersect this plane at points (1) to (4), as illustrated in Figure 3. The coordinates of each of these intersection points are determined using the following finite difference form of equation (43).

$$x_i(6) - x_i(k) = \frac{1}{2}\{u_i(k) + u_i(6) + [c(k) + c(6)][\alpha_i \cos\theta(k) + \beta_i \sin\theta(k)]\}[t(6) - t(k)] \qquad (i=1,2,3) \qquad (52)$$

The index k in equation (52) denotes the bicharacteristic-initial-value plane intersection points illustrated in Figure 3, and has a range of 1 to 4, corresponding to the $\theta(k)$ values of 0, $\pi/2$, π, and $3\pi/2$, respectively. Since the axial step $[x(6) - x(k)]$ is known, equation (52) is used to calculate $[t(6) - t(k)]$, $y(k)$, and $z(k)$. The flow property values at points (1) to (4) are obtained by interpolation using equation (51). On the initial application of equation (52), the flow property values at point (k) are equated to those at point (5).

For the external flow field integration, the parametric unit vectors α_i and β_i appearing in equation (52) are selected to straddle the projection of the pressure gradient on the initial-value plane. For the internal flow field integration, these vectors are selected to straddle the meridional plane through point (6).

Once the positions of and the flow properties at points (1) to (5) have been determined, the system of nonlinear compatibility equations, written in finite difference form, is solved to obtain the five dependent flow properties u(6), v(6), w(6), P(6) and $\rho(6)$. Two of the five required compatibility equations are given by equations (38) and (39). These equations are written in finite difference form by replacing the derivatives with simple differences, and by replacing the coefficients of the derivatives with the arithmetic average of the coefficients at the solution point and at the appropriate point in the initial-value plane. To obtain the remaining three required compatibility equations, appropriate linear combinations of the wave surface compatibility relation, equation (45), applied along each of the four bicharacteristics, and the noncharacteristic relation, equation (48), applied along the streamline are formed. Writing equation (45) for θ values of 0, $\pi/2$, π, and $3\pi/2$ yields

$$\frac{dP}{dt_1} + \rho c \alpha_i \frac{du_i}{dt_1} = \Phi_1 - \rho c^2 \beta_i \beta_j \frac{\partial u_i}{\partial x_j} \tag{53}$$

$$\frac{dP}{dt_2} + \rho c \beta_i \frac{du_i}{dt_2} = \Phi_2 - \rho c^2 \alpha_i \alpha_j \frac{\partial u_i}{\partial x_j} \tag{54}$$

$$\frac{dP}{dt_3} - \rho c \alpha_i \frac{du_i}{dt_3} = \Phi_3 - \rho c^2 \beta_i \beta_j \frac{\partial u_i}{\partial x_j} \tag{55}$$

$$\frac{dP}{dt_4} - \rho c \beta_i \frac{du_i}{dt_4} = \Phi_4 - \rho c^2 \alpha_i \alpha_j \frac{\partial u_i}{\partial x_j} \tag{56}$$

In equations (53) to (56), the operator $d(\ )/dt_k$ denotes differentiation along the kth bicharacteristic, and Φ_k denotes equation (46) evaluated for the specified value of $\theta(k)$. One independent linear combination of the compatibility equations is obtained by subtracting the finite difference form of equation (55) from the finite difference form of equation (53). Another independent linear combination is obtained by subtracting the finite difference form of equation (56) from the finite form of equation (54). The final independent linear combination is obtained by subtracting the finite difference form of the nonchar-acteristic relation, equation (48), from the sum of the finite differ-ence forms of equations (53) and (54). The resulting compatibility equations do not contain cross derivatives at the solution point [i.e., all terms containing $\partial u_i/\partial x_j(6)$ are eliminated]. These five finite difference equations are solved using Gaussian elimination. For the predictor, the flow property values at the solution point appearing in the coefficients of the derivatives in the set of difference equa-tions are equated to those at point (5). For the corrector, the flow property values at point (6) obtained on the previous iteration are used. The resulting scheme has second-order accuracy (9).

3. SOLID BOUNDARY POINT UNIT PROCESS

The computational network used for determining the solution at a typical point on a solid boundary is shown in Figure 4. The point notation used in this figure is identical to that employed in Figure 3. Here, however, both points (5) and (6) lie on the solid boundary, and point (4) is not used since it lies outside of the flow regime.

The unit process used to obtain the solution at a solid boundary point is almost identical to the interior point unit process. Here, however, point (4) corresponding to the bicharacteristic with $\theta = 3\pi/2$ is not located, and the corresponding compatibility relation valid along this bicharacteristic is not employed. That equation is replaced by the boundary condition

$$u_i(6)\, n_{bi}(6) = c \tag{57}$$

where $n_{bi}(6)$ $(i=1,2,3)$ is the unit normal to the solid boundary at point (6), and c is a specified constant which is identically zero for impermeable walls.

4. BOW SHOCK WAVE POINT UNIT PROCESS

The computational network used in determining the solution for a typical bow shock wave point is illustrated in Figure 5. A segment of the shock wave surface extending from the initial-value plane to the solution plane is shown in this figure. The intersection of the shock wave with the initial-value plane defines space curve (A), and the intersection of the shock wave with the solution plane defines space curve (B). The axial distance between the initial-value plane and the solution plane has been previously determined by the application of the CFL stability criterion. The bow shock wave solution point

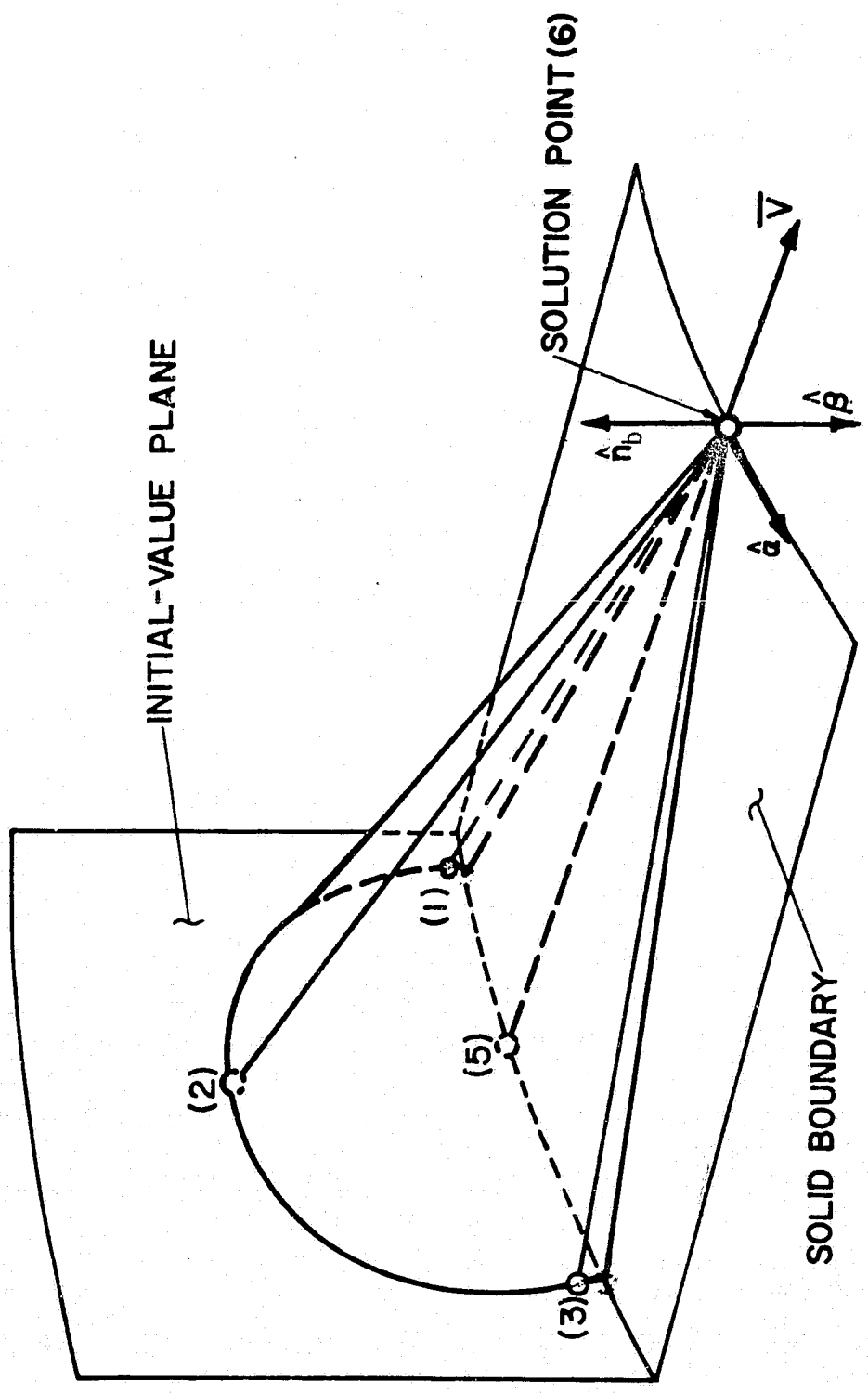

FIGURE 4. SOLID BOUNDARY POINT COMPUTATIONAL NETWORK

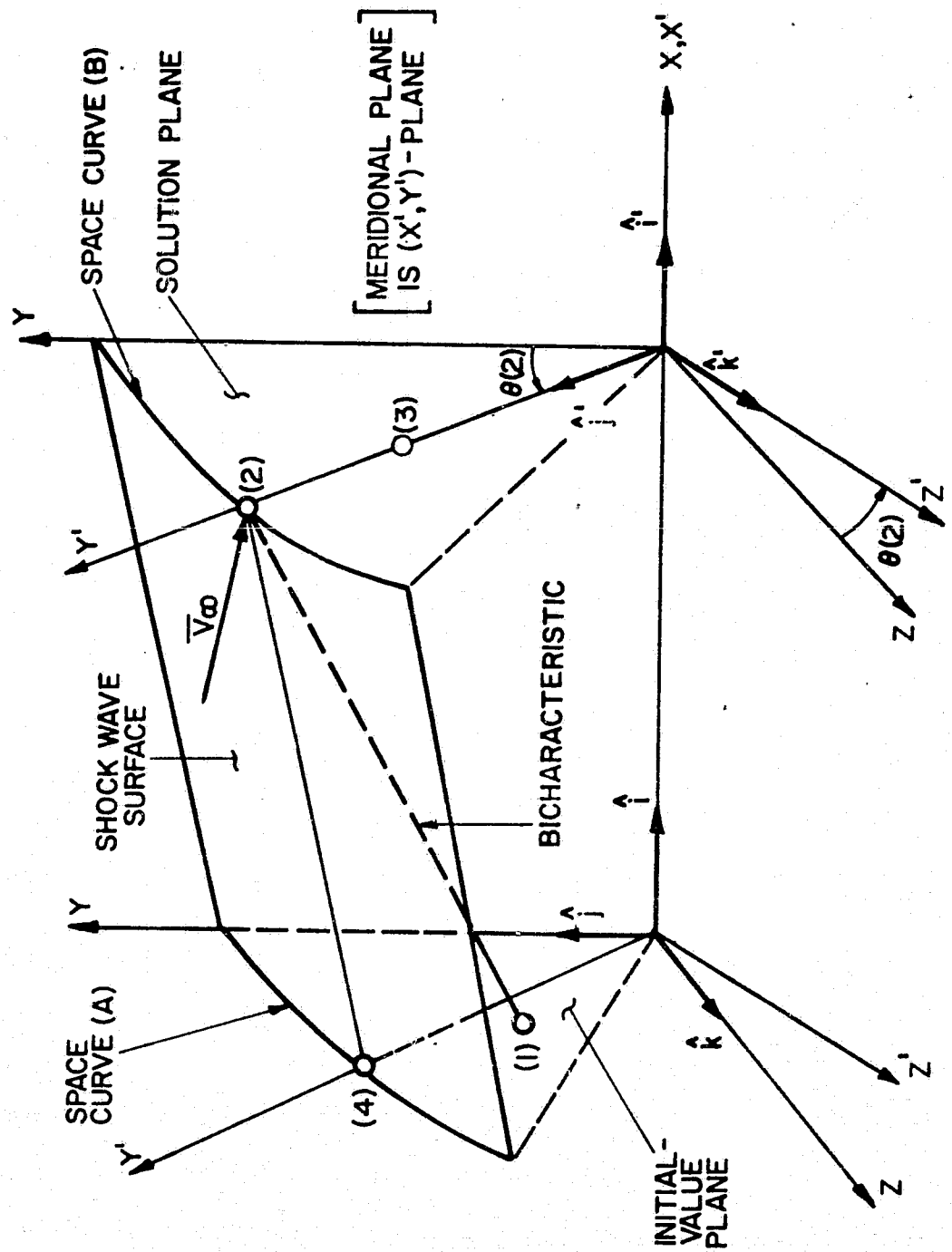

FIGURE 5. BOW SHOCK WAVE POINT COMPUTATIONAL NETWORK

is denoted by point (2). The flow properties at point (2) on the upstream side of the shock wave are known from the free-stream conditions. Hence, in the following discussion, the flow properties u(2), v(2), w(2), P(2), and $\rho(2)$ refer to the flow properties at point (2) on the downstream side of the shock wave. Point (1) is the intersection point of a rearward-running bicharacteristic with the initial-value plane. This bicharacteristic is extended backward from the solution point, point (2). Point (3) is a predetermined interior solution point which is adjacent to the shock wave and is used to define the meridional plane in which the bow shock wave solution point lies. Point (4) is the intersection point of space curve (A) with the meridional plane which passes through points (2) and (3).

In this unit process, a local cartesian coordinate system is employed for the description of the local shock wave surface. This local coordinate system has coordinates x', y', and z', where x' is coincident with the x-axis, y' is the radial direction in the meridional plane containing points (2) and (3), and z' is normal to the (x',y')-plane. The unit vectors in the x', y', and z' directions are denoted by $\hat{i}'$, $\hat{j}'$, and $\hat{k}'$, respectively. The orientation of the local shock wave surface at a point (P) is specified by a set of three unit vectors referenced to the (x',y',z')-coordinate system, as illustrated in Figure 6. This set of unit vectors consists of the unit vector $\hat{n}_s$ which is normal to the shock wave surface at point (P), and two unit vectors $\hat{\ell}$ and $\hat{t}$ which are tangent to this surface at point (P). The tangential unit vector $\hat{t}$ lies in the meridional plane [(x',y')-plane], subtends an angle ϕ with the x'-axis, and is defined by the intersection

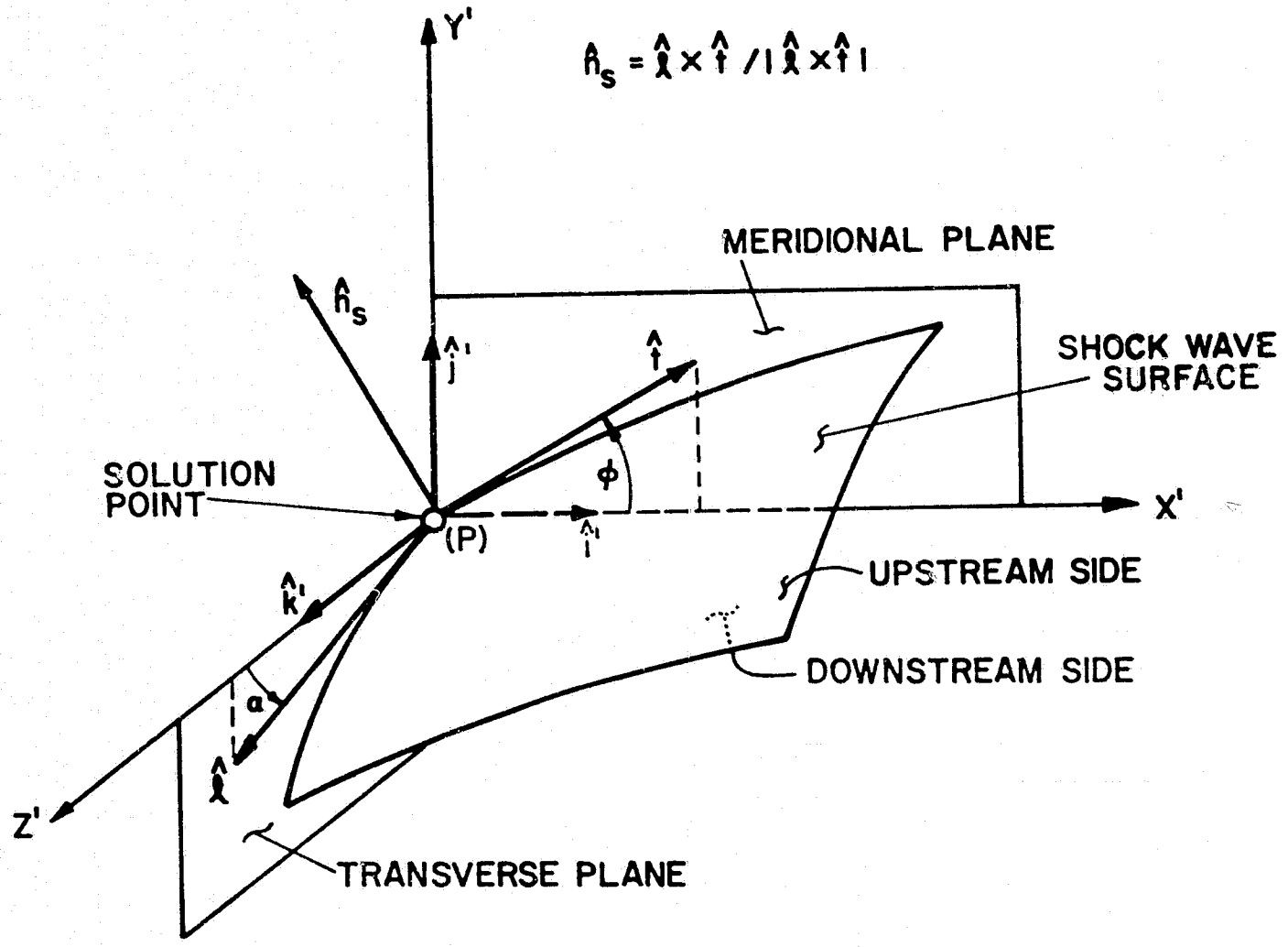

FIGURE 6. UNIT VECTORS FOR SPECIFICATION OF SHOCK WAVE SURFACE ORIENTATION

of the shock wave with the meridional plane at point (P). The tangential unit vector $\hat{\ell}$ lies in the transverse plane [(y',z')-plane], subtends an angle α with the z'-axis, and is defined by the intersection of the shock wave with the transverse plane at point (P). The tangential unit vectors $\hat{t}$ and $\hat{\ell}$ are given by

$$\hat{t} = \cos\phi\ \hat{i}' + \sin\phi\ \hat{j}' \tag{58}$$

$$\hat{\ell} = \sin\alpha\ \hat{j}' + \cos\alpha\ \hat{k}' \tag{59}$$

The shock wave normal unit vector $\hat{n}_s$ is given by

$$\hat{n}_s = \hat{\ell} \times \hat{t}/|\hat{\ell} \times \hat{t}| \tag{60}$$

To achieve second-order accuracy in the shock wave point unit process, global iteration must be performed. In global iteration, the corrector employs flow properties not only at the solution point itself, but also at neighboring points in the solution plane. As a consequence, before the corrector can be applied in global iteration, the entire solution plane (or at least an appropriate section of it) must be determined by a prior calculation. The interior point and solid boundary point unit processes do not require global iteration to achieve second-order accuracy. Consequently, those solution points are determined first. Then, the predictor is applied for each shock wave solution point, thereby giving a tentative solution for all of the shock wave points. At this stage, global correction is performed for the shock wave solution points using the previously determined field points in the solution plane. In the following discussion, the term "predictor" refers to the first application of the shock wave

point unit process used to obtain an initial estimate of the solution without using field point data in the solution plane. The term "global corrector" refers to the application of the shock wave point unit process which uses field point data in the solution plane. The shock wave point unit process is now outlined.

The shock wave point unit process is initiated by locating the solution point, point (2) in Figure 5. Denote the angle subtended by a meridional plane and the (x,y)-plane by θ. The solution point meridional plane is arbitrarily selected to contain the interior solution point, point (3), whose location is determined prior to the application of the shock wave point unit process. Hence, $\theta(2) = \theta(3)$. Denote the radial position of a point by r. Then the radial position of point (2) is obtained from

$$r(2) = r(4) + [x(2) - x(4)] \tan \left\{\frac{1}{2} [\phi(2) + \phi(4)]\right\} \qquad (61)$$

where $[x(2) - x(4)]$ is the axial distance between the initial-value plane and the solution plane. On the initial application of equation (61), the shock wave angle $\phi(2)$ is equated to $\phi(4)$, whereas, on ensuing applications, the value of $\phi(2)$ obtained on the previous iteration is used. At point (4), the radial position r(4) and the shock wave angle $\phi(4)$ are determined by interpolation using the quadratic univariate formulae

$$r(\theta) = a_1 + a_2\theta + a_3\theta^2 \qquad (62)$$

$$\phi(\theta) = b_1 + b_2\theta + b_3\theta^2 \qquad (63)$$

where the coefficients a_i and b_i (i=1,2,3) are determined by fitting these expressions to three local shock wave solution points on space curve (A).

After the solution point has been located, the shock wave normal unit vector $\hat{n}_s$ at the solution point is found by forming the normalized cross product of the tangential unit vectors $\hat{\ell}$ and $\hat{t}$ [see equation (60)]. The tangential unit vectors $\hat{t}$ and $\hat{\ell}$ are obtained by use of the current values of $\phi(2)$ and $\alpha(2)$ in equations (58) and (59), respectively. For a predictor application, $\alpha(2)$ is approximated by equating it to the α value at point (4). For a global corrector application, the value of $\alpha(2)$ that is employed is that evaluated at point (2). In either case, the value of $\alpha(2)$ may be determined by

$$\alpha(2) = \tan^{-1}\left[\frac{1}{r}\frac{dr}{d\theta}\right]\Bigg|_{\theta(2)} \tag{64}$$

where, for the predictor, the analytical form of $r(\theta)$ used in equation (64) is given by equation (62) applied along space curve (A), and for the global corrector, $r(\theta)$ is obtained by applying equation (62) along space curve (B).

At this stage, the local Hugoniot relations are applied at point (2) to obtain the downstream flow properties u(2), v(2), w(2), P(2), and $\rho(2)$. Next, a rearward-running bicharacteristic is extended from the solution point, point (2), back to the initial-value plane, intersecting this plane at point (1), as illustrated in Figure 5. The coordinates of point (1) are obtained using the following finite difference form of equation (43) evaluated for the parametric angle of $\theta = \pi/2$.

$$x_i(2) - x_i(1) = \frac{1}{2}\{u_i(1) + u_i(2) + [c(1) + c(2)]\beta_i\}\,[t(2) - t(1)] \qquad (i=1,2,3) \qquad (65)$$

For the first application of equation (65), the flow properties at point (1) are equated to those at point (2), whereas, for ensuing applications, the flow properties previously obtained at point (1) are employed. The flow properties at point (1) are obtained by interpolation using the quadratic bivariate polynomial given by equation (51). Since the axial step $[x(2) - x(1)]$ is determined by the CFL stability criterion, equation (65) is used to compute $[t(2) - t(1)]$, $y(1)$, and $z(1)$. The orientation of the parametric vector β_i in equation (65) is selected so that this vector lies in the meridional plane that contains the solution point. The unit vector α_i is obtained using the orthonormal relationship between α_i, β_i, and u_i/q $(i=1,2,3)$.

At this stage, the wave surface compatibility equation corresponding to the parametric angle $\theta = \pi/2$ is applied between points (1) and (2). The appropriate equation is obtained by writing equation (54) in finite difference form and solving for the pressure at point (2). Denote this pressure by $P^*(2)$. The resulting equation contains cross derivatives (terms containing $\partial u_i/\partial x_j$) at both points (1) and (2). For the predictor, the cross derivatives at point (2) are equated to those at point (1), whereas, for the global corrector, the cross derivatives at point (2) are evaluated at that point by fitting interpolation polynomials in the solution plane.

The pressure $P(2)$ is calculated from the local Hugoniot equations. The pressure $P^*(2)$ is calculated from the wave surface compatibility

relation. The difference between P(2) and $P^*(2)$ is driven to within a specififed tolerance of zero using the secant method with iteration being performed on the shock wave angle $\phi(2)$. Two initial estimates of $\phi(2)$ are required to start the iterative process.

The shock wave point unit process is first applied as a predictor for each shock wave solution point. In this application, the value of α used in equation (59) is obtained by curve fitting points along space curve (A), and the cross derivatives at the solution point are equated to those at the bicharacteristic base point in the initial-value plane. After a tentative solution has been obtained at each shock wave point, a number of ensuing global corrections are performed. Here, the value of α used in equation (59) is based on data along space curve (B), and the cross derivative terms at the solution point are evaluated at that point. The resulting overall algorithm has second-order accuracy when the global correction is performed. The global iteration is terminated when successive values of α have converged at each of the shock wave solution points.

5. SOLID BODY-SHOCK WAVE POINT UNIT PROCESS

The solid body-shock wave point unit process is used to determine the flow properties downstream of the shock wave at a point where the shock wave intersects a solid boundary. This unit process is used to determine the solution for the points on the cowl on the downstream side of the cowl lip shock wave, and for the points on the centerbody or cowl on the downstream side of an internal reflected shock wave. The method of computation is essentially the same for either application. For the internal shock wave reflection, the flow properties

downstream of the incident shock wave, which constitute the upstream flow properties for the reflected shock wave, are computed by the modified field-shock wave point unit process discussed in Appendix E.

A depiction of the computational network used in the solid body-shock wave point unit process is presented in Figure 7. A typical solid body-shock wave solution point is denoted by point (P), with the outward unit normal vector to the solid boundary at this point denoted by $\hat{n}_b$. The locus of solid body-shock wave solution points represents the intersection of the shock wave with the solid boundary and defines space curve (A) in Figure 7. The intersection of the shock wave with the meridional plane passing through point (P) defines space curve (B). The unit vectors tangent to space curves (A) and (B) at point (P) are denoted by $\hat{\ell}$ and $\hat{t}$, respectively. The unit vector normal to the shock wave at point (P) is denoted by $\hat{n}_s$.

As for the bow shock wave point unit process, the unit vectors $\hat{\ell}$, $\hat{t}$, and $\hat{n}_s$ are referenced to the local coordinate system (x',y',z'), where x', y', and z' have the same definitions as noted before. Moreover, the tangential unit vector $\hat{t}$ again lies in the meridional plane and is defined by equation (58). In this scheme, however, the tangential unit vector $\hat{\ell}$ does not lie in the (y',z')-plane in most cases, but rather can have a nonzero x'-component. This tangential unit vector along space curve (A) may be represented by

$$\hat{\ell} = \frac{dx'}{ds}\,\hat{i}' + \frac{dy'}{ds}\,\hat{j}' + \frac{dz'}{ds}\,\hat{k}' \tag{66}$$

where ds is the differential arc length given by

$$(ds)^2 = (dx')^2 + (dy')^2 + (dz')^2 \tag{67}$$

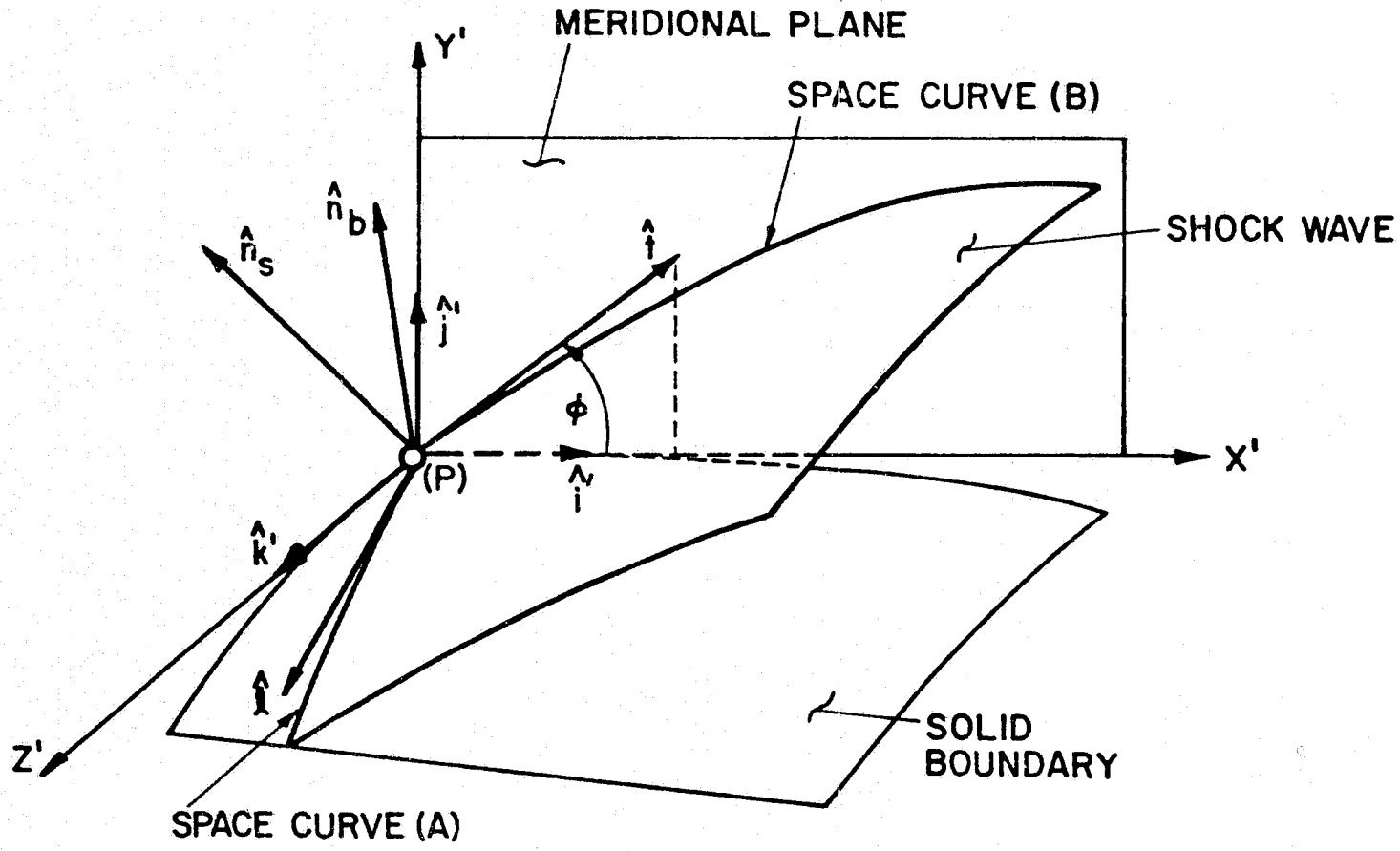

FIGURE 7. SOLID BODY-SHOCK WAVE POINT COMPUTATIONAL NETWORK

The derivatives in equation (66) are obtained by analytically differentiating the expressions

$$x'(\theta) = a_1 + a_2\theta + a_3\theta^2 \tag{68}$$

$$y'(\theta) = b_1 + b_2\theta + b_3\theta^2 \tag{69}$$

$$z'(\theta) = c_1 + c_2\theta + c_3\theta^2 \tag{70}$$

where coefficients a_i, b_i, and c_i (i=1,2,3) are obtained by curve fitting the respective expressions to three points on space curve (A). For the cowl lip shock wave points, space curve (A) is defined by the cowl lip itself, since the shock wave is assumed to be attached to the cowl lip. Alternatively, for computing the downstream flow properties at a reflected internal shock wave, space curve (A) is defined by the intersection of the incident shock wave with the solid boundary. The shock wave normal unit vector is found from equation (60).

The solid body-shock wave point unit process is initiated by determining the body normal unit vector $\hat{n}_b$ and the tangential unit vector $\hat{\ell}$. An assumption is then made for the shock wave angle ϕ in equation (58), and, by use of equation (60), the shock wave normal unit vector is determined. The local Hugoniot equations are then applied to obtain the downstream flow properties at point (P). The velocity normal to the wall is then obtained by forming the dot product of the body normal vector and the downstream velocity vector. The normal velocity is reduced to within a tolerance of a specified constant c by varying the shock angle ϕ using the secant iteration method. For impermeable walls, the constant c is identically zero.

6. INTERNAL FLOW SHOCK WAVE POINT UNIT PROCESSES

The unit process employed to compute the solution at a shock wave point in the internal flow field is similar to the bow shock wave point unit process. In the internal flow shock wave point unit process, however, the flow properties upstream of the shock wave at the solution point must be determined by the application of a modified interior point unit process. Moreover, modifications to the internal flow shock wave point unit process must be made when an internal flow shock wave solution point lies on or close to a solid boundary. The various versions of the internal flow shock wave point unit process are presented in Appendix E.

7. INTERNAL SHOCK MODIFIED-INTERIOR POINT AND -SOLID BODY POINT UNIT PROCESSES

In some situations during the computation of the internal flow field, the interior point and solid boundary point unit processes must be applied in a modified form. One such instance in which a modified form of the interior point unit process must be applied is shown in Figure 8. Here, the Mach cone, with apex at the interior solution point, intersects not only the initial-value plane but also the internal shock wave and a solid boundary. The unit process used in this case requires determining the bicharacteristic intersection points with the shock wave and the solid boundary in addition to the intersection points with the initial-value plane. Moreover, flow property values must be determined at all of these points. The bicharacteristic-shock wave and bicharacteristic-body intersection coordinates are calculated using the procedures discussed in Appendix D. The flow

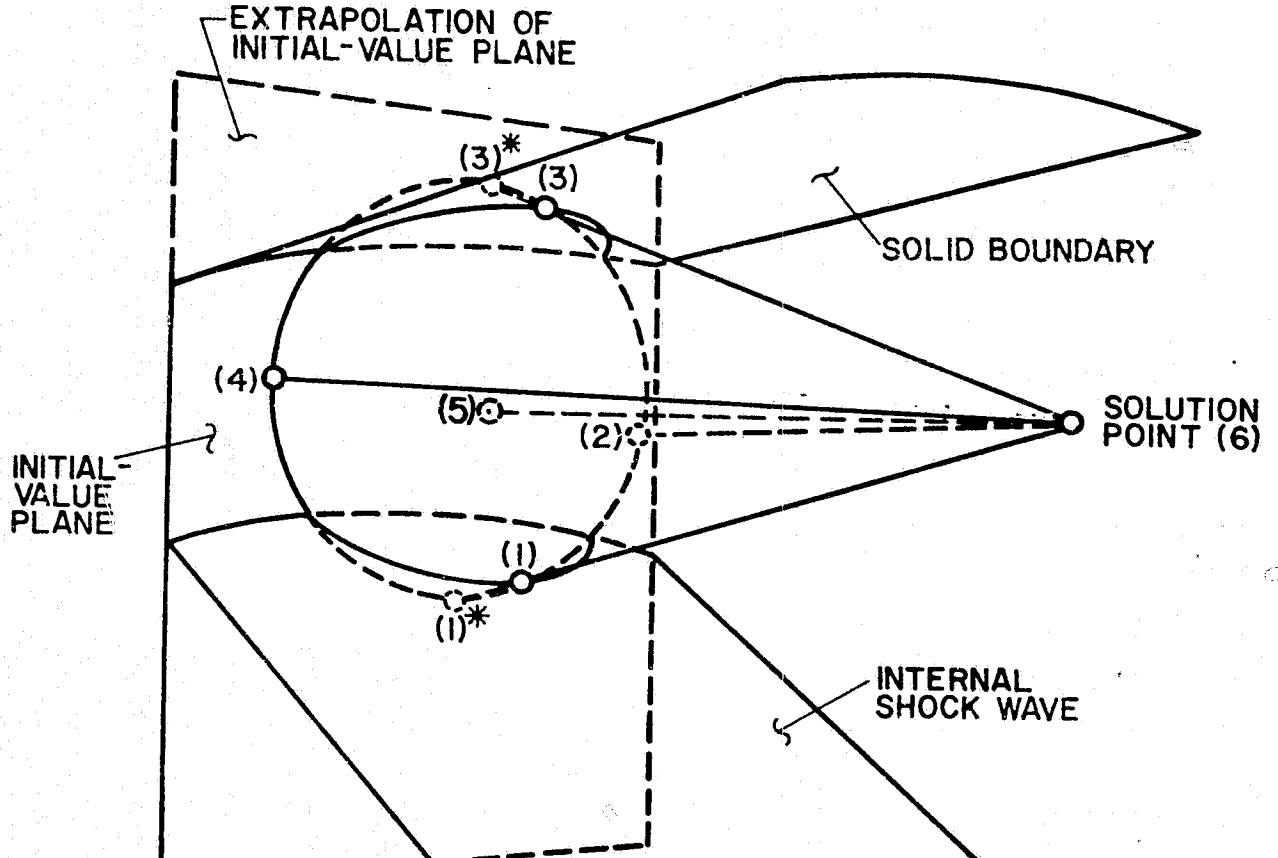

FIGURE 8. SHOCK-MODIFIED INTERIOR POINT COMPUTATIONAL NETWORK (STREAMLINE BASE POINT ON INITIAL-VALUE PLANE)

property values at these points are obtained by interpolation, either using a quadratic bivariate polynomial [equation (51)] for points on the initial-value plane, or using a quadratic trivariate polynomial for points on the shock wave surface or solid boundary surface. The various interpolation schemes are discussed in Appendix C. All of the unit processes, including the schemes incorporating the necessary modifications to handle the internal shock wave, are presented in Appendix E.

SECTION V

GOVERNING EQUATIONS FOR THE BOUNDARY LAYER FLOW

1. INTRODUCTION

The fluid dynamic model for the boundary layer flow is based on the following major assumptions:

1. steady flow,
2. negligible body forces,
3. the working gas can be represented as a simple system in thermodynamic equilibrium,
4. no internal heat generation other than viscous dissipation, and
5. negligible pressure variation in the boundary layer normal direction.

The governing equations for the assumed flow model are written in the orthogonal curvilinear coordinate system of Figure 9, and consist of the continuity equation, the component momentum equations, the energy equation, the thermal and caloric equations of state, and representations for the molecular transport properties and the turbulent eddy diffusities. These equations are briefly presented in this section. A detailed development of these equations is given in Appendix G.

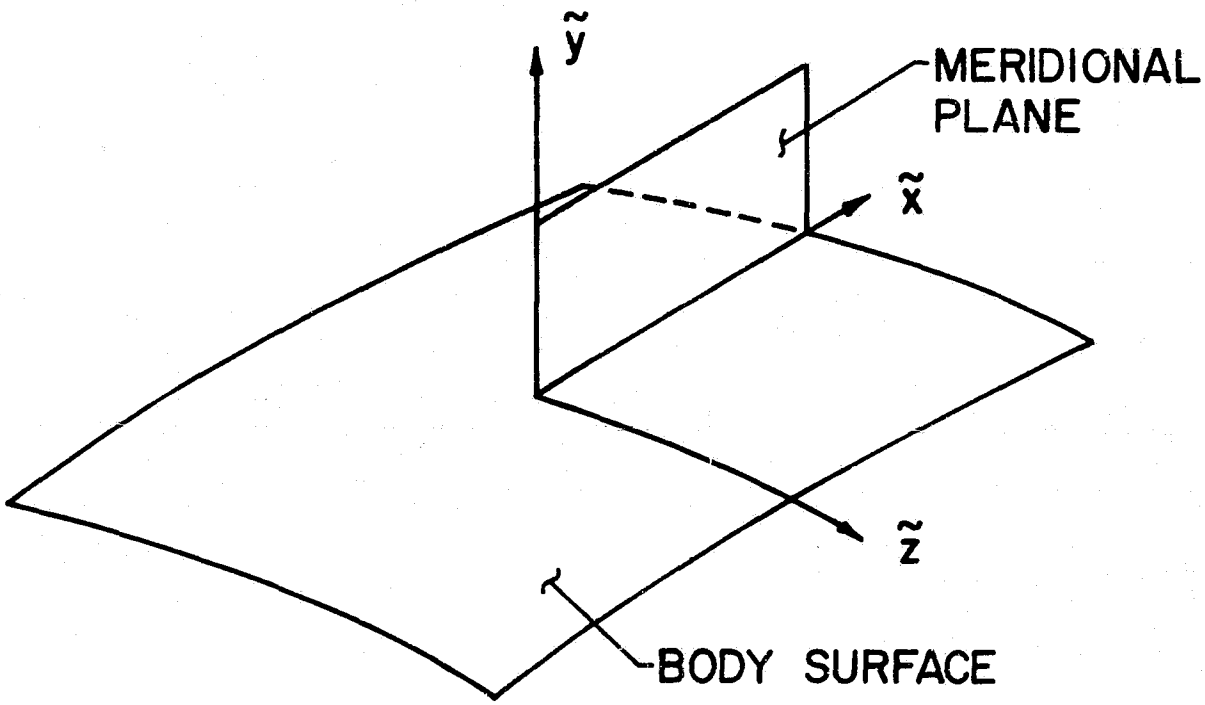

($\tilde{x}$ AND $\tilde{z}$ COINCIDENT WITH BODY SURFACE)

FIGURE 9. ORTHOGONAL CURVILINEAR COORDINATE SYSTEM FOR BOUNDARY LAYER COMPUTATION.

2. GOVERNING DIFFERENTIAL EQUATIONS

The equations of motion for the boundary layer flow have been derived in orthogonal curvilinear coordinates by Vaglio-Laurin (10). The coordinate system selected for the present application is the orthogonal curvilinear body-fitted coordinate system illustrated in Figure 9. The curvilinear coordinate $\tilde{x}$ is coincident with the body surface and lies in a given meridional plane, the coordinate $\tilde{y}$ is orthogonal to the body surface, and the curvilinear coordinate $\tilde{z}$ is orthogonal to both $\tilde{x}$ and $\tilde{y}$.

The continuity equation, when written in the $(\tilde{x}, \tilde{y}, \tilde{z})$-coordinate system, takes the form

$$\frac{\partial}{\partial \tilde{x}} (\rho h_2 \tilde{u}) + \frac{\partial}{\partial \tilde{z}} (\rho h_1 \tilde{w}) + \frac{\partial}{\partial \tilde{y}} (h_1 h_2 \overline{\rho \tilde{v}}) = 0 \tag{71}$$

where $\tilde{u}$, $\tilde{v}$, and $\tilde{w}$ denote the mean velocity components in the $\tilde{x}$-, $\tilde{y}$-, and $\tilde{z}$-directions, respectively, and ρ denotes the mean density. The overbar ($\overline{\ }$) denotes a time averaged product with

$$\overline{\rho \tilde{v}} = \rho \tilde{v} + \overline{\rho' \tilde{v}'} \tag{72}$$

where the primed quantities denote the respective time fluctuation components. The parameters h_1 and h_2 are metric coefficients which are functions of $\tilde{x}$ and $\tilde{z}$ only. For axisymmetric geometries, the metric coefficients h_1 and h_2 can be represented by simple algebraic expressions.

The component momentum equations in the $\tilde{x}$- and $\tilde{z}$-directions are termed the streamwise and cross flow momentum equations, respectively.

The $\tilde{x}$- and $\tilde{z}$- momentum equations, respectively, are given by

$$\rho \frac{\tilde{u}}{h_1} \frac{\partial \tilde{u}}{\partial \tilde{x}} + \rho \frac{\tilde{w}}{h_2} \frac{\partial \tilde{u}}{\partial \tilde{z}} + \overline{\rho \tilde{v}} \frac{\partial \tilde{u}}{\partial \tilde{y}} - \rho \tilde{u} \tilde{w} K_2 + \rho \tilde{w}^2 K_1$$

$$= -\frac{1}{h_1} \frac{\partial P}{\partial \tilde{x}} + \frac{\partial}{\partial \tilde{y}} \left(\mu \frac{\partial \tilde{u}}{\partial \tilde{y}} - \overline{\rho \tilde{u}' \tilde{v}'} \right) \tag{73}$$

$$\rho \frac{\tilde{u}}{h_1} \frac{\partial \tilde{w}}{\partial \tilde{x}} + \rho \frac{\tilde{w}}{h_2} \frac{\partial \tilde{w}}{\partial \tilde{z}} + \overline{\rho \tilde{v}} \frac{\partial \tilde{w}}{\partial \tilde{y}} - \rho \tilde{u} \tilde{w} K_1 + \rho \tilde{u}^2 K_2$$

$$= -\frac{1}{h_2} \frac{\partial P}{\partial \tilde{z}} + \frac{\partial}{\partial \tilde{y}} \left(\mu \frac{\partial \tilde{w}}{\partial \tilde{y}} - \overline{\rho \tilde{w}' \tilde{v}'} \right) \tag{74}$$

In equations (73) and (74), P denotes the pressure, μ denotes the molecular viscosity, and K_1 and K_2 denote the geodesic curvatures of the curves $\tilde{x}$ = constant and $\tilde{z}$ = constant, respectively, and are defined by

$$K_1 = \frac{-1}{h_1 h_2} \frac{\partial h_2}{\partial \tilde{x}} \tag{75}$$

$$K_2 = -\frac{1}{h_1 h_2} \frac{\partial h_1}{\partial \tilde{z}} \tag{76}$$

The third component momentum equation, the normal (i.e., $\tilde{y}$) momentum equation, is given by

$$\frac{\partial P}{\partial \tilde{y}} = 0 \tag{77}$$

The energy equation is given by

$$\rho \frac{\tilde{u}}{h_1} \frac{\partial H}{\partial \tilde{x}} + \rho \frac{\tilde{w}}{h_2} \frac{\partial H}{\partial \tilde{z}} + \overline{\rho \tilde{v}} \frac{\partial H}{\partial \tilde{y}}$$

$$= \frac{\partial}{\partial \tilde{y}} \left[\frac{\mu}{Pr} \frac{\partial H}{\partial \tilde{y}} + \mu \left(1 - \frac{1}{Pr} \right) \frac{\partial}{\partial \tilde{y}} \left(\frac{\tilde{u}^2 + \tilde{w}^2}{2} \right) - \overline{\rho \tilde{v}' H'} \right] \tag{78}$$

where H denotes the mean total enthalpy per unit mass, H' denotes the corresponding time fluctuation component, and Pr denotes the laminar Prandtl number. It is assumed that the $\tilde{y}$-component of velocity is small compared to the $\tilde{x}$- and $\tilde{z}$-components, so that the mean total enthalpy can be expressed as

$$H = h + \frac{\tilde{u}^2 + \tilde{w}^2}{2} \tag{79}$$

where h is the mean static enthalpy per unit mass.

Boundary conditions for the above equations of motion may be written as

$$\left.\begin{aligned} \tilde{y} = 0: \quad & \tilde{u} = 0, \ \tilde{w} = 0, \ \tilde{v} = \tilde{v}_w(\tilde{x}, \tilde{z}) \\ & H = H_w(\tilde{x}, \tilde{z}), \text{ or } \left(\frac{\partial H}{\partial \tilde{y}} \right) = H'_w(\tilde{x}, \tilde{z}) \end{aligned}\right\} \tag{80}$$

$$\left.\begin{aligned} \tilde{y} = \delta: \quad & \tilde{u} = \tilde{u}_e(\tilde{x}, \tilde{z}), \ \tilde{w} = \tilde{w}_e(\tilde{x}, \tilde{z}) \\ & \tilde{H} = \tilde{H}_e(\tilde{x}, \tilde{z}) \end{aligned}\right\} \tag{81}$$

where δ denotes the boundary layer thickness, the subscript w denotes wall conditions, and the subscript e denotes boundary layer edge conditions.

The $\tilde{x}$- and $\tilde{z}$-component momentum equations reduce to the following expressions at the boundary layer edge:

$$\rho_e \frac{\tilde{u}_e}{h_1}\frac{\partial \tilde{u}_e}{\partial \tilde{x}} + \rho_e \frac{\tilde{w}_e}{h_2}\frac{\partial \tilde{u}_e}{\partial \tilde{z}} - \rho_e \tilde{u}_e \tilde{w}_e K_2 + \rho_e \tilde{w}_e^2 K_1 = -\frac{1}{h_1}\frac{\partial P}{\partial \tilde{x}} \qquad (82)$$

$$\rho_e \frac{\tilde{u}_e}{h_1}\frac{\partial \tilde{w}_e}{\partial \tilde{x}} + \rho_e \frac{\tilde{w}_e}{h_2}\frac{\partial \tilde{w}_e}{\partial \tilde{z}} - \rho_e \tilde{u}_e \tilde{w}_e K_1 + \rho_e \tilde{u}_e^2 K_2 = -\frac{1}{h_2}\frac{\partial P}{\partial \tilde{z}} \qquad (83)$$

3. BOUNDARY LAYER ATTACHMENT LINE EQUATIONS

The cross flow velocity component (i.e., $\tilde{w}$) is identically zero on a plane of flow symmetry. The flow on such a plane is usually referred to as attachment line flow. The attachment line is a streamline on the body on which both the cross flow velocity component and the cross flow pressure gradient are identically zero. The cross flow momentum equation will be singular on a flow symmetry plane since both $\tilde{w}$ and K_2 vanish there. The singularity may be removed by first differentiating the cross flow momentum equation with respect to $\tilde{z}$ and then employing that result in the analysis.

Performing the required differentiation and noting the appropriate symmetry conditions yields the following system of equations for the attachment-line flow:

$$\frac{\partial}{\partial \tilde{x}}(\rho h_2 \tilde{u}) + \rho h_1 \tilde{w}_z + \frac{\partial}{\partial \tilde{y}}(h_1 h_2 \overline{\rho \tilde{v}}) = 0 \tag{84}$$

$$\rho \frac{\tilde{u}}{h_1}\frac{\partial \tilde{u}}{\partial \tilde{x}} + \overline{\rho \tilde{v}}\frac{\partial \tilde{u}}{\partial \tilde{y}} = -\frac{1}{h_1}\frac{\partial P}{\partial \tilde{x}} + \frac{\partial}{\partial \tilde{y}}\left[\mu \frac{\partial \tilde{u}}{\partial \tilde{y}} - \overline{\rho(\tilde{u}'\tilde{v}')}\right] \tag{85}$$

$$\rho \frac{\tilde{u}}{h_1}\frac{\partial \tilde{w}_z}{\partial \tilde{x}} + \overline{\rho \tilde{v}}\frac{\partial \tilde{w}_z}{\partial \tilde{y}} + \frac{\rho}{h_2}\tilde{w}_z^2 - \rho \tilde{u}\tilde{w}_z K_1 + \rho \tilde{u}^2 \frac{\partial K_2}{\partial z}$$

$$= -\frac{1}{h_2}\frac{\partial^2 p}{\partial \tilde{z}^2} + \frac{\partial}{\partial \tilde{y}}\left[\mu \frac{\partial \tilde{w}_z}{\partial \tilde{y}} - \overline{\rho(\tilde{w}'\tilde{v}')}_z\right] \tag{86}$$

$$\rho \frac{\tilde{u}}{h_1}\frac{\partial H}{\partial \tilde{x}} + \overline{\rho \tilde{v}}\frac{\partial H}{\partial \tilde{y}} = \frac{\partial}{\partial \tilde{y}}\left[\frac{\mu}{Pr}\frac{\partial H}{\partial \tilde{y}} + \mu(1 - 1/Pr)\frac{\partial}{\partial \tilde{y}}\left(\frac{\tilde{u}^2}{2}\right) - \overline{\rho \tilde{v}'\tilde{H}'}\right] \tag{87}$$

where $\tilde{w}_z = \partial \tilde{w}/\partial \tilde{z}$. Equations (84) to (87) represent the continuity, streamwise momentum, cross flow momentum, and energy equations, respectively.

Equations (84) to (87) are subject to the following boundary conditions:

$$\left.\begin{aligned} \tilde{y} = 0: \quad & \tilde{u} = 0,\ \tilde{w}_z = 0,\ \tilde{v} = \tilde{v}_w(\tilde{x}, \tilde{z}) \\ & H = H_w(\tilde{x}, \tilde{z}),\ \text{or}\ \left(\frac{\partial H}{\partial \tilde{y}}\right) = H_w'(\tilde{x}, \tilde{z}) \end{aligned}\right\} \tag{88}$$

$$\left.\begin{aligned} \tilde{y} = \delta: \quad & \tilde{u} = \tilde{u}_e(\tilde{x}, \tilde{z}),\ \tilde{w}_z = \tilde{w}_{ze}(\tilde{x}, \tilde{z}) \\ & H = H_e(\tilde{x}, \tilde{z}) \end{aligned}\right\} \tag{89}$$

The edge condition equation for the attachment line flow is given by

$$\rho_e \tilde{u}_e \frac{\partial \tilde{u}_e}{\partial \tilde{x}} = -\frac{\partial P}{\partial \tilde{x}} \tag{90}$$

4. THERMODYNAMIC MODEL AND MOLECULAR TRANSPORT PROPERTIES

The thermodynamic model and molecular transport property representations for the boundary layer flow analysis are identical to those used for the supersonic core flow analysis. Consequently, equations (24), (25), (29), and (30) are employed in the boundary layer computation.

5. THREE-DIMENSIONAL TURBULENCE MODEL

Assumptions must be made for the Reynolds stress terms in the boundary layer governing equations in order to compute turbulent flows. In the present investigation, turbulent closure is achieved by employing eddy viscosity and mixing length formulations. It should be noted that the associated computer program is written in a modular form which allows for the rapid substitution of alternate turbulence models whether they be algebraic or higher-order transport equation models.

The present model is based on the Boussinesq eddy viscosity concept. With this assumption, the Reynolds stress terms in equations (73), (74), and (78) are represented by

$$-\rho\overline{\tilde{u}'\tilde{v}'} = \rho\varepsilon_x \frac{\partial\tilde{u}}{\partial\tilde{y}} \tag{91}$$

$$-\rho\overline{\tilde{w}'\tilde{v}'} = \rho\varepsilon_z \frac{\partial\tilde{w}}{\partial\tilde{y}} \tag{92}$$

$$-\rho\overline{H'\tilde{v}'} = \rho\varepsilon_\theta \frac{\partial H}{\partial\tilde{y}} \tag{93}$$

In equations (91) to (93), ε_x and ε_z represent the turbulent eddy viscosities for the streamwise and cross flow directions, respectively, and ε_θ represents the turbulent eddy thermal conductivity. For the present study, isotropic turbulence has been assumed, thus

$$\varepsilon_x = \varepsilon_z. \tag{94}$$

A two-layer turbulence model (20) is employed in the present study where

$$\varepsilon_x = \varepsilon_z = \varepsilon_i \qquad (0 \le \tilde{y} \le \tilde{y}_T) \tag{95}$$

$$\varepsilon_x = \varepsilon_z = \varepsilon_o \qquad (\tilde{y}_T \le \tilde{y} \le \delta) \tag{96}$$

where ε_i and ε_o are the inner and outer region eddy viscosities, respectively, and $\tilde{y}_T$ is the value of the $\tilde{y}$-coordinate where $\varepsilon_i = \varepsilon_o$. For the inner layer, the following mixing length expression is used

$$\varepsilon_i = \delta_{TR}\, L^2 \left[\left(\frac{\partial\tilde{u}}{\partial\tilde{y}}\right)^2 + \left(\frac{\partial\tilde{w}}{\partial\tilde{y}}\right)^2\right]^{1/2} \tag{97}$$

where L is the mixing length, and δ_{TR} is a parameter accounting for the transition from laminar to turbulent flow. The mixing length is given by

$$L = \kappa\tilde{y}[1 - \exp(-\tilde{y}/A)] \tag{98}$$

where κ is the von Karman parameter, which is taken to be a constant at the value

$$\kappa = 0.40 \tag{99}$$

and A is defined by

$$A = A^+ \frac{\nu}{N}\sqrt{\frac{\rho}{\rho_w}} \Big/ \tilde{u}_\tau \tag{100}$$

In equation (100), ν denotes the kinematic viscosity, the w subscript denotes wall conditions, A^+ is the van Driest damping factor given by

$$A^+ = 26.0 \tag{101}$$

and $\tilde{u}_\tau$ is given by

$$\tilde{u}_\tau = \left(\frac{\tau_{ws}}{\rho_w}\right)^{\frac{1}{2}} \tag{102}$$

where τ_{ws} is the shear stress at the wall. The parameter N in equation (100) takes different forms depending on whether or not there is mass transfer at the wall. For impermeable walls, N is expressed as

$$N = \left[1 - 11.8 \frac{\mu_w}{\mu_e} \left(\frac{\rho_e}{\rho_w}\right)^2 p^+\right]^{\frac{1}{2}} \tag{103}$$

where

$$p^+ = \frac{\nu_e \tilde{u}_s}{\tilde{u}_\tau^3} \frac{\partial \tilde{u}_s}{\partial \tilde{s}} \tag{104}$$

where $\tilde{u}_s$ is the velocity in the external streamline direction $\tilde{s}$. If wall mass transfer exists, then N is given by

$$N = \left[\frac{\mu}{\mu_e} \left(\frac{\rho_e}{\rho_w}\right)^2 \frac{p^+}{\tilde{v}_w^+} \left\{1 - \exp\left(11.8 \frac{\mu_w}{\mu} \tilde{v}_w^+\right)\right\}\right.$$

$$\left. + \exp\left(11.8 \frac{\mu_w}{\mu} \tilde{v}_w^+\right)\right]^{\frac{1}{2}} \tag{105}$$

where

$$\tilde{v}_w^+ = \frac{\tilde{v}_w}{\tilde{u}_\tau} \tag{106}$$

For the outer region, the eddy viscosity is given by the velocity defect relation

$$\varepsilon_o = \delta_{TR} \alpha \left| \int_0^\infty \left[(\tilde{u}_e^2 + \tilde{w}_e^2)^{\frac{1}{2}} - (\tilde{u}^2 + \tilde{w}^2)^{\frac{1}{2}}\right] d\tilde{y} \right| \tag{107}$$

where α is taken to be constant at the value

$$\alpha = 0.0168 \tag{108}$$

The expression for the turbulent thermal conductivity ε_θ involves the turbulent Prandtl number Pr_t and is given by

$$\varepsilon_\theta = \frac{\varepsilon}{Pr_t} \tag{109}$$

where

$$\varepsilon = \left[\varepsilon_x^2 + \varepsilon_z^2\right]^{\frac{1}{2}} \tag{110}$$

The parameter δ_{TR} incorporated into equations (97) and (107) is an intermittency factor accounting for the transition from laminar to turbulent flow. The assumed representations for δ_{TR} are presented in Appendix G.

SECTION VI

TRANSFORMATION OF THE BOUNDARY LAYER EQUATIONS

1. INTRODUCTION

The boundary layer equations may be solved in either physical variables or transformed variables. Solving the equations when they have been expressed in transformed variables has a distinct computational advantage in that larger steps can be taken in the $\tilde{x}$- and $\tilde{z}$-directions. This is because the solution profiles do not vary as much when using transformed variables as they do when using physical variables. The transformation used in the present study also stretches the body normal coordinate and removes a large portion of the boundary layer thickness variation for laminar flows. It also has the same advantages for turbulent flows, although there is a greater variation in boundary layer thickness for turbulent cases.

2. TRANSFORMED BOUNDARY LAYER EQUATIONS

The transformation used in the present investigation was proposed by Moore (11). A two-component vector potential is defined such that

$$\rho h_2 \tilde{u} = \frac{\partial \psi}{\partial \tilde{y}} \tag{111}$$

$$\rho h_1 \tilde{w} = \frac{\partial \phi}{\partial \tilde{y}} \tag{112}$$

and

$$h_1 h_2 \overline{\rho\tilde{v}} = -\left(\frac{\partial\psi}{\partial\tilde{x}} + \frac{\partial\phi}{\partial\tilde{z}}\right) + h_1 h_2 (\rho\tilde{v})_w \quad , \tag{113}$$

The last term in equation (113) accounts for mass transfer at the wall and is identically zero for impermeable walls. The governing equations are now transformed according to the formal transformation

$$(\tilde{x}, \tilde{y}, \tilde{z}) \rightarrow (\tilde{x}, \eta, \tilde{z}) \tag{114}$$

where

$$\tilde{x} = \tilde{x} \tag{115}$$

$$\tilde{z} = \tilde{z} \tag{116}$$

$$d\eta = \left(\frac{\tilde{u}_e}{\rho_e \mu_e \tilde{x}}\right)^{\frac{1}{2}} \rho\, d\tilde{y} \tag{117}$$

where η is the stretched normal coordinate. The functions ψ and ϕ take the forms

$$\psi = (\rho_e \mu_e \tilde{u}_e \tilde{x})^{\frac{1}{2}}\, h_2\, f(\tilde{x}, \eta, \tilde{z}) \tag{118}$$

$$\phi = (\rho_e \mu_e \tilde{u}_e \tilde{x})^{\frac{1}{2}}\, h_1 \left(\frac{\tilde{w}_e}{\tilde{u}_e}\right) g(\tilde{x}, \eta, \tilde{z}) \tag{119}$$

where f and g are to be determined by the analysis.

Equation (71) is satisfied identically when equations (111) to (113) are substituted into it. Substituting equations (111) to (113) into equations (73), (74), and (78) results in the following system of equations:

$$\left[C(1+\varepsilon_x^+)f''\right]' + P_2 f f'' + P_3 g f'' + \frac{N}{h_1}\left[\frac{\rho_e}{\rho} - (f')^2\right]$$

$$+ P_4\left[\frac{\rho_e}{\rho} - (g')^2\right] + P_5\left[g'f' - \frac{\rho_e}{\rho}\right] - T f''$$

$$= \frac{\tilde{x}}{h_1}\left(f'\frac{\partial f'}{\partial \tilde{x}} - f''\frac{\partial f}{\partial \tilde{x}}\right) + \frac{\tilde{w}_e}{\tilde{u}_e}\frac{\tilde{x}}{h_2}\left(g'\frac{\partial f'}{\partial \tilde{z}} - f''\frac{\partial g}{\partial \tilde{z}}\right) \qquad (120)$$

$$\left[C(1+\varepsilon_z^+)g''\right]' + P_2 f g'' + P_3 g g'' + P_6\left[\frac{\rho_e}{\rho} - (f')^2\right]$$

$$+ \frac{\tilde{w}_e}{\tilde{u}_e}\frac{P}{h_2}\left[\frac{\rho_e}{\rho} - (g')^2\right] + P_7\left[g'f' - \frac{\rho_e}{\rho}\right] - T g''$$

$$= \frac{\tilde{x}}{h_1}\left(f'\frac{\partial g'}{\partial \tilde{x}} - g''\frac{\partial f}{\partial \tilde{x}}\right) + \frac{\tilde{w}_e}{\tilde{u}_e}\frac{\tilde{x}}{h_2}\left(g'\frac{\partial g'}{\partial \tilde{z}} - g''\frac{\partial g}{\partial \tilde{z}}\right) \qquad (121)$$

$$\left\{C\left[\left(1+\varepsilon^+\frac{Pr}{Pr_t}\right)\frac{\theta'}{Pr} + \frac{\tilde{u}_e^2}{H_e}\left(1-\frac{1}{Pr}\right)\left(f'f'' + \frac{\tilde{w}_e^2}{\tilde{u}_e^2}g'g''\right)\right]\right\}'$$

$$+ P_2 f\theta' + P_3 g\theta' - T\theta'$$

$$= \frac{\tilde{x}}{h_1}\left(f'\frac{\partial \theta}{\partial \tilde{x}} - \theta'\frac{\partial f}{\partial \tilde{x}}\right) + \frac{\tilde{w}_e}{\tilde{u}_e}\frac{\tilde{x}}{h_2}\left(g'\frac{\partial \theta}{\partial \tilde{z}} - \theta'\frac{\partial g}{\partial \tilde{z}}\right) \qquad (122)$$

where the primes denote differentiation with respect to η.

Equations (120) to (122) represent the streamwise momentum, cross flow momentum, and energy equations, respectively. The following parameter definitions are used for equations (120) to (122):

$$f' = \tilde{u}/\tilde{u}_e \tag{123}$$

$$g' = \tilde{w}/\tilde{w}_e \tag{124}$$

$$\theta = H/H_e \tag{125}$$

$$R_x = \tilde{u}_e\tilde{x}/\nu_e \tag{126}$$

$$M = \frac{\tilde{x}}{\tilde{u}_e}\frac{\partial\tilde{u}_e}{\partial\tilde{x}} \tag{127}$$

$$N = \frac{\tilde{x}}{\tilde{u}_e}\frac{\partial\tilde{u}_e}{\partial\tilde{z}} \tag{128}$$

$$P = \frac{\tilde{x}}{\tilde{w}_e}\frac{\partial\tilde{w}_e}{\partial\tilde{z}} \tag{129}$$

$$Q = \frac{\tilde{x}}{\tilde{w}_e}\frac{\partial\tilde{w}_e}{\partial\tilde{x}} \tag{130}$$

$$S = \frac{\tilde{x}}{\rho_e\mu_e}\frac{\partial}{\partial\tilde{x}}(\rho_e\mu_e) \tag{131}$$

$$R = \frac{\tilde{x}}{\rho_e\mu_e}\frac{\partial}{\partial\tilde{z}}(\rho_e\mu_e) \tag{132}$$

$$P_2 = (1 + M + S - 2K_1 h_1 \tilde{x})/2h_1 \tag{133}$$

$$P_3 = \frac{\tilde{w}_e}{\tilde{u}_e} \frac{1}{2h_2} (2P - N + R - 2K_2 h_2 \tilde{x}) \tag{134}$$

$$P_4 = \left(\frac{\tilde{w}_e}{\tilde{u}_e}\right)^2 K_1 \tilde{x} \tag{135}$$

$$P_5 = -\frac{\tilde{w}_e}{\tilde{u}_e} \frac{1}{h_2} (-K_2 h_2 \tilde{x} + N) \tag{136}$$

$$P_6 = \frac{\tilde{u}_e}{\tilde{w}_e} K_2 \tilde{x} \tag{137}$$

$$P_7 = (K_1 h_1 \tilde{x} - Q)/h_1 \tag{138}$$

$$\varepsilon_x^+ = \frac{\varepsilon_x}{\nu} \tag{139}$$

$$\varepsilon_z^+ = \frac{\varepsilon_z}{\nu} \tag{140}$$

$$\varepsilon_\theta^+ = \frac{\varepsilon_\theta}{\nu} \tag{141}$$

$$\varepsilon^+ = \left[(\varepsilon_x^+)^2 + (\varepsilon_z^+)^2\right]^{1/2} \tag{142}$$

$$Pr_t = \varepsilon^+/\varepsilon_\theta^+ \tag{143}$$

$$C = \frac{\rho\mu}{\rho_e\mu_e} \tag{144}$$

$$T = \frac{(\rho\tilde{v})_w}{\rho_e\tilde{u}_e} R_x^{\frac{1}{2}} \tag{145}$$

The appropriate boundary conditions are given by

$$\left.\begin{aligned} \eta = 0: \quad & f = 0, \quad g = 0, \quad f' = 0, \quad g' = 0 \\ & \theta = \theta_w \quad \text{or} \quad \theta' = \theta'_w \end{aligned}\right\} \tag{146}$$

$$\eta = \eta_\delta: \quad f' = 1, \quad g' = 1, \quad \theta = 1 \tag{147}$$

3. TRANSFORMED ATTACHMENT LINE EQUATIONS

The attachment line equations can be transformed in a similar manner to that just outlined. Again, define a two-component vector potential

$$\rho h_2\tilde{u} = \frac{\partial\psi}{\partial\tilde{y}} \tag{148}$$

$$\rho h_1\tilde{w}_z = \frac{\partial\phi}{\partial\tilde{y}} \tag{149}$$

$$h_1h_2\overline{\rho\tilde{v}} = -\left(\frac{\partial\psi}{\partial\tilde{x}} + \phi\right) + h_1h_2(\rho\tilde{v})_w \tag{150}$$

Equations (114) to (118) are again used, however ϕ is now defined as

$$\phi = (\rho_e\mu_e\tilde{u}_e\tilde{x})^{\frac{1}{2}} h_1 \frac{\tilde{w}_{ze}}{\tilde{u}_e} g(\tilde{x}, \eta, \tilde{z}) \tag{151}$$

Substituting the above relationships into equations (85), (86), and (87) yields

$$\left[C(1+\varepsilon_x^+)f''\right]' + P_2 f f'' + \frac{P_1}{h_2} g f'' + \frac{M}{h_1}\left[\frac{\bar{\rho}_e}{\rho} - (f')^2\right] - T f''$$

$$= \frac{\tilde{x}}{h_1}\left(f' \frac{\partial f'}{\partial \tilde{x}} - f'' \frac{\partial f}{\partial \tilde{x}}\right) \tag{152}$$

$$\left[C(1+\varepsilon_z^+)\, g''\right]' + P_2 f g'' + \frac{P_1}{h_2} g g'' + P_8\left(f'g' - \frac{\rho_e}{\rho}\right)$$

$$+ \frac{P_1}{h_2}\left[\frac{\bar{\rho}_e}{\rho} - (g')^2\right] + P_9\left[\frac{\bar{\rho}_e}{\rho} - (f')^2\right] - T g''$$

$$= \frac{\tilde{x}}{h_1}\left(f' \frac{\partial g'}{\partial \tilde{x}} - g'' \frac{\partial f}{\partial \tilde{x}}\right) \tag{153}$$

$$\left\{C\left[\left(1 + \varepsilon^+ \frac{Pr}{Pr_t}\right)\frac{\theta'}{Pr} + \frac{\tilde{u}_e^2}{H_e}\left(1 - \frac{1}{Pr}\right) f f''\right]\right\}' + P_2 f\theta'$$

$$+ \frac{P_1}{h_2} g\theta' - T\theta' = \frac{\tilde{x}}{h_1}\left(f' \frac{\partial \theta}{\partial \tilde{x}} - \theta' \frac{\partial f}{\partial \tilde{x}}\right) \tag{154}$$

Equations (152) to (154) represent the streamwise momentum, cross flow momentum, and energy equations, respectively. The following new parameter definitions are employed:

$$f' = \tilde{u}/\tilde{u}_e \tag{155}$$

$$g' = \tilde{w}_z/\tilde{w}_{ze} \tag{156}$$

$$\theta = H/H_e \tag{157}$$

$$P_i = \frac{\tilde{x}}{\tilde{u}_e}\frac{\partial \tilde{w}_e}{\partial \tilde{z}} \tag{158}$$

$$P_8 = \left(K_1 h_1 \tilde{x} - \frac{\tilde{x}}{\tilde{w}_{ze}}\frac{\partial \tilde{w}_{ze}}{\partial \tilde{x}}\right)\frac{1}{h_1} \tag{159}$$

$$P_9 = \frac{\tilde{x}\tilde{u}_e}{\tilde{w}_{ze}}\frac{\partial K_2}{\partial \tilde{z}} \tag{160}$$

The appropriate boundary conditions are given by

$$\left.\begin{aligned} \eta = 0: \quad & f = 0, \quad g = 0, \quad f' = 0, \quad g' = 0 \\ & \theta = \theta_w \quad \text{or} \quad \theta' = \theta_w' \end{aligned}\right\} \tag{161}$$

$$\eta = \eta_\delta: \quad f' = 1, \quad g' = 1, \quad \theta = 1 \quad \} \tag{162}$$

SECTION VII

NUMERICAL SOLUTION OF THE BOUNDARY LAYER EQUATIONS

1. INTRODUCTION

The transformed parabolic boundary layer equations presented in Section VI are solved numerically using a second-order implicit finite difference algorithm in which marching is performed in the $\tilde{x}$-direction. The numerical algorithm that is employed in the present investigation is based on the Keller box scheme (12) originally used by Cebeci and Keller for the computation of two-dimensional boundary layer flows (13). An extension of that scheme to three-dimensional flows has been reported by Cebeci, Khattab, and Stewartson (14). The finite difference procedure given in Reference (14) is capable of computing both positive and negative cross flows.

The finite difference algorithm used for the boundary layer computation is briefly outlined in the present section. In order to compute this flow, three different types of differencing schemes are employed. The choice of which scheme to use depends upon whether the cross flow velocity is positive, negative, or identically zero (plane of symmetry flow). Since the respective difference equations are quite lengthy, only a summary of the most pertinent equations is presented in this section. A detailed development of those equations is given in Appendix I.

2. ATTACHMENT LINE FLOW

The numerical algorithm employed in the boundary layer computation is based on solving a system of first-order partial differential equations. The transformed streamwise momentum, cross flow momentum, and energy equations for the attachment line flow, given by equations (152) to (154), respectively, can be written as a first-order system by defining the following variables:

$$f' = u \tag{163}$$

$$u' = v = f'' \tag{164}$$

$$g' = w \tag{165}$$

$$w' = t = g'' \tag{166}$$

$$\theta' = \Delta \tag{167}$$

where the primes denote differentiation with respect to η. Introducing equations (163) to (167) into equations (152) to (154) yields the following system of first-order equations:

$$bv' + (b' + P_2 f + P_1 g/h_2 - T)v$$

$$+ \frac{M}{h_1}(\lambda - u^2) = \frac{\tilde{x}}{h_1}\left(u\frac{\partial u}{\partial \tilde{x}} - v\frac{\partial f}{\partial \tilde{x}}\right) \tag{168}$$

$$ct' + (c' + P_2 f + P_1 g/h_2 - T)t + P_8(uw - \lambda) + \frac{P_1}{h_2}(\lambda - w^2)$$

$$+ P_g(\lambda - u^2) = \frac{\tilde{x}}{h_1}\left(u\frac{\partial w}{\partial \tilde{x}} - t\frac{\partial f}{\partial \tilde{x}}\right) \tag{169}$$

$$d\Delta' + (d' + P_2 f + P_1 g/h_2 - T)\Delta + e'fv$$

$$+ e(f'v + fv') = \frac{\tilde{x}}{h_1}\left(u\frac{\partial\theta}{\partial\tilde{x}} - \Delta\frac{\partial f}{\partial\tilde{x}}\right) \tag{170}$$

In equations (168) to (170), the following parameter definitions are employed:

$$b = C(1 + \varepsilon_x^+) \tag{171}$$

$$c = C(1 + \varepsilon_z^+) \tag{172}$$

$$d = C\left(1 + \varepsilon^+\frac{Pr}{Pr_t}\right)\Big/Pr \tag{173}$$

$$e = C\frac{\tilde{u}_e^2}{He}(1 - 1/Pr) \tag{174}$$

$$\lambda = \rho_e/\rho \tag{175}$$

Equations (163) to (170) are solved using the computational network illustrated in Figure 10. In Figure 10, the computational cell step sizes are given by

$$\eta_j = \eta_{j-1} + h_{j-1} \tag{176}$$

$$\tilde{x}_n = \tilde{x}_{n-1} + k_{n-1} \tag{177}$$

where h_{j-1} and k_{n-1} are the mesh lengths in the η- and $\tilde{x}$-coordinate directions, respectively. Both h_j and k_n may be varied in the calculation as deemed suitable. A variable η step size capability

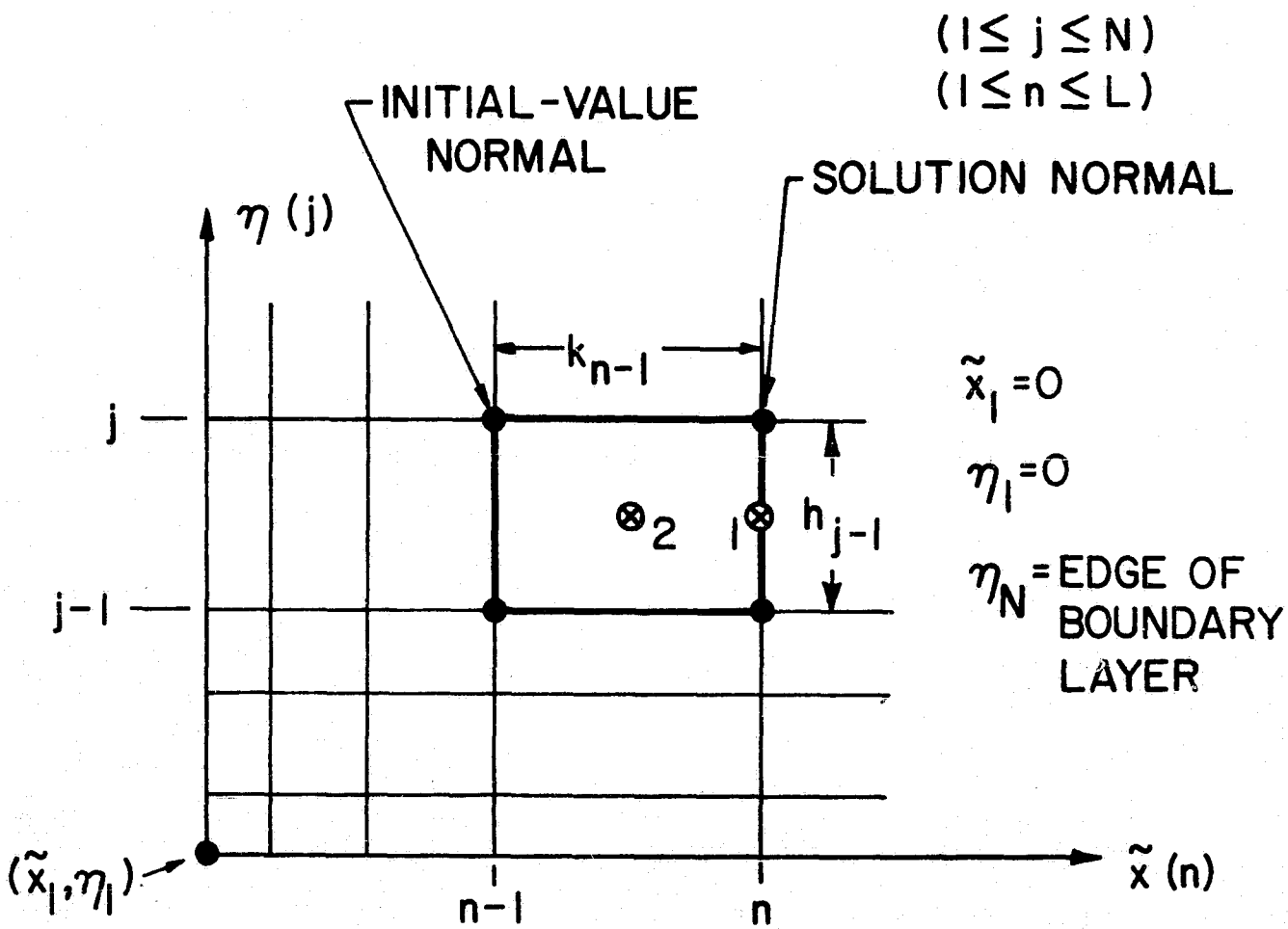

FIGURE 10. ATTACHMENT LINE FLOW COMPUTATIONAL NETWORK.

has been incorporated into the computer program by using the following relations:

$$h_j = K\, h_{j-1} \tag{178}$$

$$\eta_j = \sum_{i=1}^{j-1} h_i = \sum_{i=1}^{j-1} K^{i-1}\, h_1 \tag{179}$$

The computational grid point distribution for the η-coordinate is then determined by specifying the constant step size ratio factor K and the initial step size h_1.

The finite difference expressions used to approximate equations (163) to (170) are now presented in terms of the computational point network presented in Figure 10. The five parameter definition equations, equations (163) to (167), are approximated by using centered difference and averaging expressions taken about point (1) in Figure 10, which is located midway between the points $(\tilde{x}_n, \eta_j)$ and $(\tilde{x}_n, \eta_{j-1})$. Performing the differencing yields:

$$f_j^n - f_{j-1}^n - \frac{h_{j-1}}{2}\,(u_j^n + u_{j-1}^n) = 0 \tag{180}$$

$$u_j^n - u_{j-1}^n - \frac{h_{j-1}}{2}\,(v_j^n + v_{j-1}^n) = 0 \tag{181}$$

$$g_j^n - g_{j-1}^n - \frac{h_{j-1}}{2}\,(w_j^n + w_j^{n-1}) = 0 \tag{182}$$

$$w_j^n - w_{j-1}^n - \frac{h_{j-1}}{2}\,(t_j^n + t_j^{n-1}) = 0 \tag{183}$$

$$\theta_j^n - \theta_{j-1}^n - \frac{h_{j-1}}{2}\left(\Delta_j^n + \Delta_{j-1}^n\right) = 0 \tag{184}$$

The finite difference approximations to equations (168) to (170) are obtained by using centered difference and averaging expressions taken about point (2) in Figure 10, which is the midpoint of the computational cell. This procedure yields the following equations:

$$\bar{b}_{j*}\left[\frac{\bar{v}_j - \bar{v}_{j-1}}{h_{j-1}}\right] + \left[\frac{\bar{b}_j - \bar{b}_{j-1}}{h_{j-1}} + (\overline{P_2})\bar{f}_{j*} + \left(\frac{\overline{P_1}}{h_2}\right)\bar{g}_{j*} - (\bar{T})\right]\bar{v}_{j*}$$

$$+ \left(\frac{M}{h_1}\right)\left[\bar{\lambda}_{j*} - \overline{(u_{j*})^2}\right]$$

$$= \left(\frac{\tilde{x}}{h_1}\right)\left[\bar{u}_{j*}\left[\frac{\bar{u}_n - \bar{u}_{n-1}}{k_{n-1}}\right] - \bar{v}_{j*}\left[\frac{\bar{f}_n - \bar{f}_{n-1}}{k_{n-1}}\right]\right] \tag{185}$$

$$\bar{c}_{j*}\left[\frac{\bar{t}_j - \bar{t}_{j-1}}{h_{j-1}}\right] + \left[\frac{\bar{c}_j - \bar{c}_{j-1}}{h_{j-1}} + (\overline{P_2})\bar{f}_{j*} + \left(\frac{\overline{P_1}}{h_2}\right)\bar{g}_{j*}\right]\bar{t}_{j*}$$

$$+ (\overline{P_8})\left(\bar{u}_{j*}\bar{w}_{j*} - \bar{\lambda}_{j*}\right) + \left(\frac{\overline{P_1}}{h_2}\right)\left[\bar{\lambda}_{j*} - \overline{(w_{j*})^2}\right]$$

$$+ (\overline{P_9})\left[\bar{\lambda}_{j*} - \overline{(u_{j*})^2}\right] - (\bar{T})\,\bar{t}_{j*}$$

$$= \left(\frac{\tilde{x}}{h_1}\right)\left[\bar{u}_{j*}\left[\frac{\bar{w}_n - \bar{w}_{n-1}}{k_{n-1}}\right] - \bar{t}_{j*}\left[\frac{\bar{f}_n - \bar{f}_{n-1}}{k_{n-1}}\right]\right] \tag{186}$$

$$\overline{d}_{j*}\left[\frac{\overline{\Delta}_j - \overline{\Delta}_{j-1}}{h_{j-1}}\right] + \left[\frac{\overline{d}_j - \overline{d}_{j-1}}{h_{j-1}} + (\overline{P_2})\overline{f}_{j*} + \left(\frac{\overline{P_1}}{h_2}\right)\overline{g}_{j*} - (\overline{T})\right]\overline{\Delta}_{j*}$$

$$+ \left[\frac{\overline{e}_j - \overline{e}_{j-1}}{h_{j-1}}\right]\overline{f}_{j*}\overline{v}_{j*} + \overline{e}_{j*}\left[\overline{v}_{j*}\left[\frac{\overline{f}_j - \overline{f}_{j-1}}{h_{j-1}}\right] + \overline{f}_{j*}\left[\frac{\overline{v}_j - \overline{v}_{j-1}}{h_{j-1}}\right]\right]$$

$$= \left(\frac{\overline{\tilde{x}}}{h_1}\right)\left[\overline{u}_{j*}\left[\frac{\overline{\theta}_n - \overline{\theta}_{n-1}}{k_{n-1}}\right] - \overline{\Delta}_{j*}\left[\frac{\overline{f}_n - \overline{f}_{n-1}}{k_{n-1}}\right]\right] \qquad (187)$$

In equations (185) to (187), the following averaging notations are used:

$$(\overline{\alpha}) = \frac{1}{2}(\alpha^n + \alpha^{n-1}) \qquad (188)$$

$$\overline{\alpha}_j = \frac{1}{2}(\alpha_j^n + \alpha_j^{n-1}) \qquad (189)$$

$$\overline{\alpha}_n = \frac{1}{2}(\alpha_j^n + \alpha_{j-1}^n) \qquad (190)$$

$$\overline{\alpha}_{j*} = \frac{1}{4}(\alpha_j^n + \alpha_{j-1}^n + \alpha_j^{n-1} + \alpha_{j-1}^{n-1}) \qquad (191)$$

where α denotes a general function. Equation (188) is used solely for variables which are functions of $\tilde{x}$ and $\tilde{z}$ only.

Equations (180) to (187) form a system of 8(N - 1) equations when written for N points along the solution normal. An additional eight expressions can be obtained from the boundary conditions given below.

$$\left.\begin{aligned} \eta = \eta_1 = 0: \quad & f = 0, \quad g = 0, \quad u = 0, \quad w = 0 \\ & \theta = \theta_w, \qquad \text{or} \qquad \Delta = \Delta_w \end{aligned}\right\} \tag{192}$$

$$\left.\eta = \eta_N: \quad u = 1, \quad w = 1, \quad \theta = 1 \right\} \tag{193}$$

This then yields a total of 8N expressions for the 8N unknowns along the attachment line solution normal provided that the flow properties at station $\tilde{x}_{n-1}$ are known.

The system of difference equations is solved using Newton's method. In this method, the solution for any variable f at iteration (k + 1) is found from the solution at iteration (k) plus a perturbation. Thus,

$$\left[f_j^n\right]^{(k+1)} = \left[f_j^n\right]^{(k)} + \left[\delta f_j^n\right]^{(k)} \tag{194}$$

where f_j^n denotes any dependent variable and δf_j^n denotes its perturbation. The difference equations are obtained by substituting expressions like equation (194) into equations (180) to (187) and then neglecting quadratic and higher-order terms in the perturbation quantities. This produces a system of linear simultaneous equations for the perturbation quantities which is block tridiagonal in form and which is solved using an efficient direct matrix-factorization algorithm. The details of the solution procedure are presented in Appendix I.

3. POSITIVE CROSS FLOW

The transformed streamwise momentum, cross flow momentum, and energy equations for three-dimensional flow, given by equations (120),

(121), and (122), respectively, can be written as a system of first-order equations by again using equations (163) to (167). Introducing those parameter definitions yields the following first-order system for equations (120) to (122):

$$bv' + (b' + P_2 f + P_3 g - T)v + \frac{M}{h_1}(\lambda - u^2) + P_4(\lambda - w^2)$$

$$+ P_5(uw - \lambda) = \frac{\tilde{x}}{h_1}\left(u\frac{\partial u}{\partial \tilde{x}} - v\frac{\partial f}{\partial \tilde{x}}\right) + \left(\frac{\tilde{w}_e \tilde{x}}{\tilde{u}_e h_2}\right)\left(w\frac{\partial u}{\partial \tilde{z}} - v\frac{\partial g}{\partial \tilde{z}}\right) \qquad (195)$$

$$ct' + (c' + P_2 f + P_3 g - T)t + P_6(\lambda - u^2) + \left(\frac{\tilde{w}_e}{\tilde{u}_e}\frac{P}{h_2}\right)(\lambda - w^2)$$

$$+ P_7(uw - \lambda) = \frac{\tilde{x}}{h_1}\left(u\frac{\partial w}{\partial \tilde{x}} - t\frac{\partial f}{\partial \tilde{x}}\right) + \left(\frac{\tilde{w}_e \tilde{x}}{\tilde{u}_e h_2}\right)\left(w\frac{\partial w}{\partial \tilde{z}} - t\frac{\partial g}{\partial \tilde{z}}\right) \qquad (196)$$

$$d\Delta' + (d' + P_2 f + P_3 g - T)\Delta + e'\left[uv + \left(\frac{\tilde{w}_e}{\tilde{u}_e}\right)^2 wt\right]$$

$$+ e(uv' + u'v) + e\left(\frac{\tilde{w}_e}{\tilde{u}_e}\right)^2 (wt' + w't)$$

$$= \frac{\tilde{x}}{h_1}\left(u\frac{\partial \theta}{\partial \tilde{x}} - \Delta\frac{\partial f}{\partial \tilde{x}}\right) + \left(\frac{\tilde{w}_e \tilde{x}}{\tilde{u}_e h_2}\right)\left(w\frac{\partial \theta}{\partial \tilde{z}} - \Delta\frac{\partial g}{\partial \tilde{z}}\right) \qquad (197)$$

In equations (195), (196), and (197), the parameters b, c, d, e, and λ are again given by equations (171) to (175).

Equations (163) to (167) and equations (195) to (197) are solved for positive cross-flow velocities ($\tilde{w} > 0$) using the computational

network illustrated in Figure 11. The computational cell step sizes are again given by equations (176) and (177), and by

$$\tilde{z}_i = \tilde{z}_{i-1} + r_{i-1} \tag{198}$$

where r_{i-1} is the cell mesh length in the $\tilde{z}$-coordinate direction.

The finite difference equations used to approximate equations (163) to (167) are obtained by using centered difference and averaging expressions taken about point (1) in Figure 11, which is located midway between the points $(\tilde{x}_n, n_j, \tilde{z}_i)$ and $(\tilde{x}_n, n_{j-1}, \tilde{z}_i)$. This procedure yields the following equations:

$$f_j^{n,i} - f_{j-1}^{n,i} - \frac{h_{j-1}}{2}\left(u_j^{n,i} + u_{j-1}^{n,i}\right) = 0 \tag{199}$$

$$u_j^{n,i} - u_{j-1}^{n,i} - \frac{h_{j-1}}{2}\left(v_j^{n,i} + v_{j-1}^{n,i}\right) = 0 \tag{200}$$

$$g_j^{n,i} - g_{j-1}^{n,i} - \frac{h_{j-1}}{2}\left(w_j^{n,i} + w_{j-1}^{n,i}\right) = 0 \tag{201}$$

$$w_j^{n,i} - w_{j-1}^{n,i} - \frac{h_{j-1}}{2}\left(t_j^{n,i} + t_{j-1}^{n,i}\right) = 0 \tag{202}$$

$$\theta_j^{n,i} - \theta_{j-1}^{n,i} - \frac{h_{j-1}}{2}\left(\Delta_j^{n,i} + \Delta_{j-1}^{n,i}\right) = 0 \tag{203}$$

The finite difference approximations to equations (120), (121), and (122) are obtained by using centered difference and averaging expressions taken about point (2) in Figure 11, which is the midpoint of the computational cell. This procedure yields the following equations:

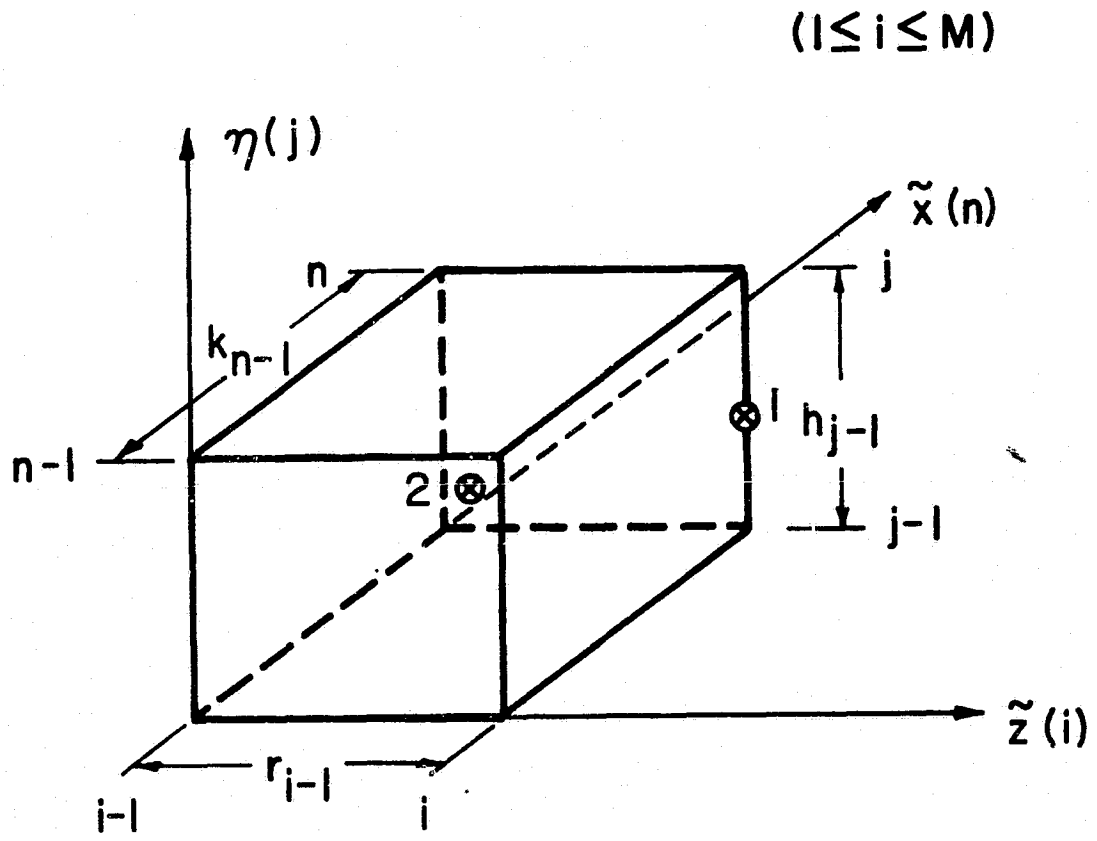

FIGURE II. THREE-DIMENSIONAL POSITIVE CROSS FLOW COMPUTATIONAL NETWORK.

$$\overline{b}_{j*}\left[\frac{\overline{v}_j - \overline{v}_{j-1}}{h_{j-1}}\right] + \left[\frac{\overline{b}_j - \overline{b}_{j-1}}{h_{j-1}} + (\overline{P_2})\overline{f}_{j*} + (\overline{P_3})\overline{g}_{j*} - (\overline{T})\right]\overline{v}_{j*}$$

$$+ \left(\frac{\overline{M}}{h_1}\right)\left[\overline{\lambda}_{j*} - (\overline{u}_{j*})^2\right] + (\overline{P_4})\left[\overline{\lambda}_{j*} - (\overline{w}_{j*})^2\right] + (\overline{P_5})(\overline{u}_{j*}\overline{w}_{j*} - \overline{\lambda}_{j*})$$

$$= \left(\frac{\overline{\tilde{x}}}{h_1}\right)\left[\overline{u}_{j*}\left(\frac{\overline{u}_n - \overline{u}_{n-1}}{k_{n-1}}\right) - \overline{v}_{j*}\left(\frac{\overline{f}_n - \overline{f}_{n-1}}{k_{n-1}}\right)\right]$$

$$+ \left(\frac{\overline{\tilde{w}_e \tilde{x}}}{\tilde{u}_e h_2}\right)\left[\overline{w}_{j*}\left(\frac{\overline{u}_i - \overline{u}_{i-1}}{r_{i-1}}\right) - \overline{v}_{j*}\left(\frac{\overline{g}_i - \overline{g}_{i-1}}{r_{i-1}}\right)\right] \qquad (204)$$

$$\overline{c}_{j*}\left[\frac{\overline{t}_j - \overline{t}_{j-1}}{h_{j-1}}\right] + \left[\frac{\overline{c}_j - \overline{c}_{j-1}}{h_{j-1}} + (\overline{P_2})\overline{f}_{j*} + (\overline{P_3})\overline{g}_{j*} - (\overline{T})\right]\overline{t}_{j*}$$

$$+ (\overline{P_6})\left[\overline{\lambda}_{j*} - (\overline{u}_{j*})^2\right] + \left(\frac{\overline{\tilde{w}_e P}}{\tilde{u}_e h_2}\right)\left[\overline{\lambda}_{j*} - (\overline{w}_{j*})^2\right]$$

$$+ (\overline{P_7})(\overline{u}_{j*}\overline{w}_{j*} - \overline{\lambda}_{j*}) = \left(\frac{\overline{\tilde{x}}}{h_1}\right)\left[\overline{u}_{j*}\left(\frac{\overline{w}_n - \overline{w}_{n-1}}{k_{n-1}}\right) - \overline{t}_{j*}\left(\frac{\overline{f}_n - \overline{f}_{n-1}}{k_{n-1}}\right)\right]$$

$$+ \left(\frac{\overline{\tilde{w}_e \tilde{x}}}{\tilde{u}_e h_2}\right)\left[\overline{w}_{j*}\left(\frac{\overline{w}_i - \overline{w}_{i-1}}{r_{i-1}}\right) - \overline{t}_{j*}\left(\frac{\overline{g}_i - \overline{g}_{i-1}}{r_{i-1}}\right)\right] \qquad (205)$$

$$\bar{d}_{j*}\left(\frac{\bar{\Delta}_j - \bar{\Delta}_{j-1}}{h_{j-1}}\right) + \left[\frac{\bar{d}_j - \bar{d}_{j-1}}{h_{j-1}} + (\bar{P}_2)\bar{f}_{j*} + (\bar{P}_3)\bar{g}_{j*} - (\bar{T})\right]\bar{\Delta}_{j*}$$

$$+ \frac{\bar{e}_j - \bar{e}_{j-1}}{h_{j-1}}\left[\bar{u}_{j*}\bar{v}_{j*} + \left(\frac{\tilde{\bar{w}}_e}{\tilde{u}_e}\right)^2 \bar{w}_{j*}\bar{t}_{j*}\right]$$

$$+ \bar{e}_{j*}\left[\bar{u}_{j*}\left(\frac{\bar{v}_j - \bar{v}_{j-1}}{h_{j-1}}\right) + \bar{v}_{j*}\left(\frac{\bar{u}_j - \bar{u}_{j-1}}{h_{j-1}}\right)\right]$$

$$+ \bar{e}_{j*}\left(\frac{\tilde{\bar{w}}_e}{\tilde{u}_e}\right)^2\left[\bar{w}_{j*}\left(\frac{\bar{t}_j - \bar{t}_{j-1}}{h_{j-1}}\right) + \bar{t}_{j*}\left(\frac{\bar{w}_j - \bar{w}_{j-1}}{h_{j-1}}\right)\right]$$

$$= \left(\frac{\tilde{\bar{x}}}{h_1}\right)\left[\bar{u}_{j*}\left(\frac{\bar{\theta}_n - \bar{\theta}_{n-1}}{k_{n-1}}\right) - \bar{\Delta}_{j*}\left(\frac{\bar{f}_n - \bar{f}_{n-1}}{k_{n-1}}\right)\right]$$

$$+ \left(\frac{\tilde{\bar{w}}_e\tilde{\bar{x}}}{\tilde{u}_e h_2}\right)\left[\bar{w}_{j*}\left(\frac{\bar{\theta}_i - \bar{\theta}_{i-1}}{r_{i-1}}\right) - \bar{\Delta}_{j*}\left(\frac{\bar{g}_i - \bar{g}_{i-1}}{r_{i-1}}\right)\right] \qquad (206)$$

In equations (204), (205), and (206), the following averaging notations are used:

$$(\bar{\alpha}) = \frac{1}{4}\left(\alpha^{n,i} + \alpha^{n,i-1} + \alpha^{n-1,i} + \alpha^{n-1,i-1}\right) \qquad (207)$$

$$\bar{\alpha}_j = \frac{1}{4}\left(\alpha_j^{n,i} + \alpha_j^{n,i-1} + \alpha_j^{n-1,i} + \alpha_j^{n-1,i-1}\right) \qquad (208)$$

$$\bar{\alpha}_n = \frac{1}{4}\left(\alpha_j^{n,i} + \alpha_j^{n,i-1} + \alpha_{j-1}^{n,i} + \alpha_{j-1}^{n,i-1}\right) \qquad (209)$$

$$\bar{\alpha}_i = \frac{1}{4}\left(\alpha_j^{n,i} + \alpha_j^{n-1,i} + \alpha_{j-1}^{n,i} + \alpha_{j-1}^{n-1,i}\right) \qquad (210)$$

$$\bar{\alpha}_{j*} = \frac{1}{8}\left(\alpha_j^{n,i} + \alpha_{j-1}^{n,i} + \alpha_j^{n-1,i} + \alpha_{j-1}^{n-1,i} + \alpha_j^{n,i-1} + \alpha_{j-1}^{n,i-1} + \alpha_j^{n-1,i-1} + \alpha_{j-1}^{n-1,i-1}\right) \tag{211}$$

where α denotes a general function. Equation (207) is used solely for variables which are functions of $\tilde{x}$ and $\tilde{z}$ only.

Boundary conditions for equations (199) to (206) are given by equations (192) and (193). Taken with the boundary conditions, equations (199) to (206) form a system of 8N equations for 8N unknowns along the boundary layer normal located at $\tilde{x} = \tilde{x}_n$ and $\tilde{z} = \tilde{z}_i$, provided that the properties at stations $(\tilde{x}_n, \tilde{z}_{i-1})$, $(\tilde{x}_{n-1}, \tilde{z}_i)$, and $(\tilde{x}_{n-1}, \tilde{z}_{i-1})$ are known. The system of difference equations is again solved using Newton's method with a direct matrix solution procedure. The details of the solution procedure are given in Appendix I.

4. NEGATIVE CROSS FLOW

The previous section presented the finite difference algorithm used for the computation of three-dimensional boundary layer flow when the cross flow velocity component is positive. Due to numerical stability considerations, more fully explained in Appendix I, alterations to the above scheme must be made when attempting to compute boundary layer flows with a negative cross flow velocity component. These modifications are briefly discussed in this section.

The pertinent governing equations for reversed cross flow cases are again given by equations (163) to (167) and equations (195) to

(197). These equations are solved for negative cross flow cases using the computational network illustrated in Figure 12. The computational cell step sizes in the n- and $\tilde{x}$-coordinate directions are again given by equations (176) and (177), respectively. The computational cell is, however, now staggered in the $\tilde{z}$-coordinate direction with the respective step sizes being given by

$$\tilde{z}_i = \tilde{z}_{i-1} + r_{i-1} \tag{212}$$

$$\tilde{z}_{i+1} = \tilde{z}_i + r_i \tag{213}$$

The finite difference equations used to approximate equations (163) to (167) are obtained by using centered difference and averaging expressions taken about point (1) in Figure 12, which is located midway between the points $(\tilde{x}_n, n_j, \tilde{z}_i)$ and $(\tilde{x}_n, n_{j-1}, \tilde{z}_i)$. This procedure again yields equations (199) to (203). The finite difference approximations to equations (195) to (197) are obtained by using centered difference and averaging expressions taken about points (2), (3), and (4) in Figure 12, which are the midpoints of the three faces of the computational cell. This procedure yields the following system of equations:

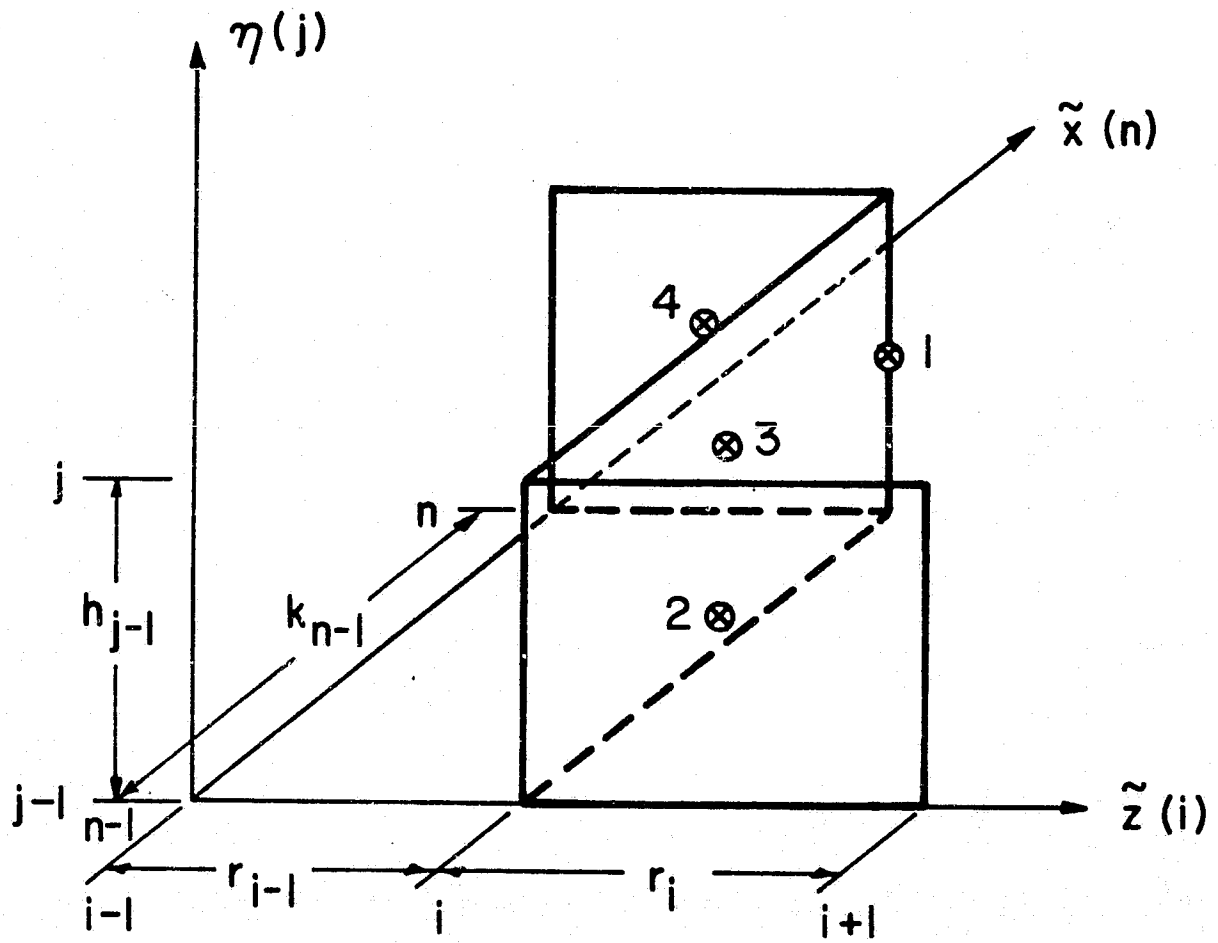

FIGURE 12. THREE-DIMENSIONAL NEGATIVE CROSS FLOW COMPUTATIONAL NETWORK.

$$\overline{b}_{j*}\left(\frac{\overline{v}_j - \overline{v}_{j-1}}{h_{j-1}}\right) + \left[\frac{\overline{b}_j - \overline{b}_{j-1}}{h_{j-1}} + (\overline{P}_2)\overline{f}_{j*} + (\overline{P}_3)\overline{g}_{j*} - (\overline{T})\right]\overline{v}_{j*}$$

$$+ \left(\frac{M}{h_1}\right)\left[\overline{\lambda}_{j*} - (\overline{u}_{j*})^2\right] + (\overline{P}_4)\left[\overline{\lambda}_{j*} - (\overline{w}_{j*})^2\right] + (\overline{P}_5)\left(\overline{u}_{j*}\overline{w}_{j*} - \overline{\lambda}_{j*}\right)$$

$$= \left(\frac{\tilde{x}}{h_1}\right)\left[\overline{u}_{j*}\left(\frac{\overline{u}_n - \overline{u}_{n-1}}{k_{n-1}}\right) - \overline{v}_{j*}\left(\frac{\overline{f}_n - \overline{f}_{n-1}}{k_{n-1}}\right)\right]$$

$$+ \left(\frac{\overline{\tilde{w}_e \tilde{x}}}{\tilde{u}_e h_2}\right)\left[\xi\left(w\frac{\partial u}{\partial \tilde{z}} - v\frac{\partial g}{\partial \tilde{z}}\right)\Big|_2 + (1-\xi)\left(w\frac{\partial u}{\partial \tilde{z}} - v\frac{\partial g}{\partial \tilde{z}}\right)\Big|_4\right] \qquad (214)$$

$$\overline{c}_{j*}\left(\frac{\overline{t}_j - \overline{t}_{j-1}}{h_{j-1}}\right) + \left[\frac{\overline{c}_j - \overline{c}_{j-1}}{h_{j-1}} + (\overline{P}_2)\overline{f}_{j*} + (\overline{P}_3)\overline{g}_{j*} - (\overline{T})\right]\overline{t}_{j*}$$

$$+ (\overline{P}_6)\left[\overline{\lambda}_{j*} - (\overline{u}_{j*})^2\right] + \left(\frac{\overline{\tilde{w}_e P}}{\tilde{u}_e h_2}\right)\left[\overline{\lambda}_{j*} - (\overline{w}_{j*})^2\right] + (\overline{P}_7)\left(\overline{u}_{j*}\overline{w}_{j*} - \overline{\lambda}_{j*}\right)$$

$$= \left(\frac{\tilde{x}}{h_1}\right)\left[\overline{u}_{j*}\left(\frac{\overline{w}_n - \overline{w}_{n-1}}{k_{n-1}}\right) - \overline{t}_{j*}\left(\frac{\overline{f}_n - \overline{f}_{n-1}}{k_{n-1}}\right)\right]$$

$$+ \left(\frac{\overline{\tilde{w}_e \tilde{x}}}{\tilde{u}_e h_2}\right)\left[\xi\left(w\frac{\partial w}{\partial \tilde{z}} - t\frac{\partial g}{\partial \tilde{z}}\right)\Big|_2 + (1-\xi)\left(w\frac{\partial w}{\partial \tilde{z}} - t\frac{\partial g}{\partial \tilde{z}}\right)\Big|_4\right] \qquad (215)$$

$$\bar{d}_{j*}\left[\frac{\bar{\Delta}_j - \bar{\Delta}_{j-1}}{h_{j-1}}\right] + \left[\frac{\bar{d}_j - \bar{d}_{j-1}}{h_{j-1}} + (\bar{P}_2)\bar{f}_{j*} + (\bar{P}_3)\bar{g}_{j*} - (\bar{T})\right]\bar{\Delta}_{j*}$$

$$+ \left[\frac{\bar{e}_j - \bar{e}_{j-1}}{h_{j-1}}\right]\left[\bar{u}_{j*}\bar{v}_{j*} + \left(\frac{\overline{\tilde{w}_e}}{\tilde{u}_e}\right)^2 \bar{w}_{j*}\bar{t}_{j*}\right]$$

$$+ \bar{e}_{j*}\left[\bar{u}_{j*}\left(\frac{\bar{v}_j - \bar{v}_{j-1}}{h_{j-1}}\right) + \bar{v}_{j*}\left(\frac{\bar{u}_j - \bar{u}_{j-1}}{h_{j-1}}\right)\right]$$

$$+ \bar{e}_{j*}\left(\frac{\overline{\tilde{w}_e}}{\tilde{u}_e}\right)^2\left[\bar{w}_{j*}\left(\frac{\bar{t}_j - \bar{t}_{j-1}}{h_{j-1}}\right) + \bar{t}_{j*}\left(\frac{\bar{w}_j - \bar{w}_{j-1}}{h_{j-1}}\right)\right]$$

$$= \left(\frac{\overline{\tilde{x}}}{h_1}\right)\left[\bar{u}_{j*}\left(\frac{\bar{\theta}_n - \bar{\theta}_{n-1}}{k_{n-1}}\right) - \bar{\Delta}_{j*}\left(\frac{\bar{f}_n - \bar{f}_{n-1}}{k_{n-1}}\right)\right]$$

$$+ \left(\frac{\overline{\tilde{w}_e \tilde{x}}}{\tilde{u}_e h_2}\right)\left[\xi\left(w\frac{\partial\theta}{\partial\tilde{z}} - \Delta\frac{\partial g}{\partial\tilde{z}}\right)\Big|_2 + (1-\xi)\left(w\frac{\partial\theta}{\partial\tilde{z}} - \Delta\frac{\partial g}{\partial\tilde{z}}\right)\Big|_4\right] \qquad (216)$$

In equations (214), (215), and (216), the following averaging notations are used:

$$(\bar{\alpha}) = \frac{1}{2}\left(\alpha^{n,i} + \alpha^{n-1,i}\right) \qquad (217)$$

$$\bar{\alpha}_j = \frac{1}{2}\left(\alpha_j^{n,i} + \alpha_j^{n-1,i}\right) \qquad (218)$$

$$\bar{\alpha}_n = \frac{1}{2}\left(\alpha_j^{n,i} + \alpha_{j-1}^{n,i}\right) \qquad (219)$$

$$\bar{\alpha}_{j*} = \frac{1}{4}\left(\alpha_j^{n,i} + \alpha_{j-1}^{n,i} + \alpha_j^{n-1,i} + \alpha_{j-1}^{n-1,i}\right) \qquad (220)$$

where α denotes a general function. Equation (217) is used solely for variables which are functions of $\tilde{x}$ and $\tilde{z}$ only. The final terms in equations (214), (215), and (216) are centered at points (2) and (4), and ξ is given by

$$\xi = \frac{\tilde{z}_{i+1} - \tilde{z}_i}{\tilde{z}_{i+1} - \tilde{z}_{i-1}} \tag{221}$$

Equations (214) to (216) are substituted for equations (204) to (206) whenever the local cross-flow velocity component becomes negative.

SECTION VIII

SHOCK WAVE-BOUNDARY LAYER INTERACTION ANALYSIS

1. INTRODUCTION

The boundary layer finite difference algorithm, presented in Section VII, is employed to compute all of the forebody/centerbody and cowl boundary layer flow except for that in the immediate vicinity of the shock wave-boundary layer interaction regions. The flow in an interaction region exhibits an elliptical character in that downstream disturbances may propagate upstream through the subsonic portion of the boundary layer. Because of this phenomenon, it is not possible to adequately model the flow in an interaction region using a parabolic system of governing differential equations which cannot account for upstream influence. An accurate numerical simulation of the interaction flow necessitates using a three-dimensional compressible Navier-Stokes analysis which incorporates the appropriate outflow boundary conditions. Although such an analysis is possible, the attendant increase in computer execution time would be prohibitive. Recognizing this, a three-dimensional integral analysis was selected for determining the interaction region flow in the present investigation. The analysis presented herein solves integral forms of the continuity, streamwise momentum, and cross-flow momentum equations while assuming that the boundary layer flow is isoenergetic immediately downstream of the shock wave reflection. The analysis used in the present study represents an extension of the methods given in References (23), (24), and (25).

The shock wave-boundary layer integral analysis is briefly discussed in this section. It is presented in greater detail in Appendix J.

2. INTEGRAL ANALYSIS

The three-dimensional integral conservation equations are applied to a series of control volumes where each control volume comprises a circumferential segment of the three-dimensional shock wave-boundary layer interaction region, as illustrated in Figure 13. A given control volume is bounded by the current boundary layer initial-value and solution surfaces in the streamwise ($\tilde{x}$) direction, and by the wall and the boundary layer edge surfaces in the normal ($\tilde{y}$) direction.

Following the suggestion of Paynter (25), the conservation equations are applied in a plane which is orthogonal to both the wall and to the space curve defined by the intersection of the shock wave with the wall. This plane is shown in Figure 14 passing through the point (P), and can be defined by the orthonormal triad of vectors $\hat{t}$, $\hat{n}_b$, and $\hat{\sigma}$. The unit vector $\hat{t}$ is tangent to the space curve at point (P), the unit vector $\hat{n}_b$ is orthogonal to the solid boundary at point (P), and the unit vector $\hat{\sigma}$ is orthogonal to both $\hat{t}$ and $\hat{n}_b$ at point (P) and is given by

$$\hat{\sigma} = \hat{n}_b \times \hat{t} \tag{222}$$

The tangential unit vector $\hat{t}$ can be determined from

$$\hat{t} = \left(\frac{dx}{ds}\right)\hat{i} + \left(\frac{dy}{ds}\right)\hat{j} + \left(\frac{dz}{ds}\right)\hat{k} \tag{223}$$

where ds is the differential arc length along the space curve and can be expressed as

$$(ds)^2 = (dx)^2 + (dy)^2 + (dz)^2 \tag{224}$$

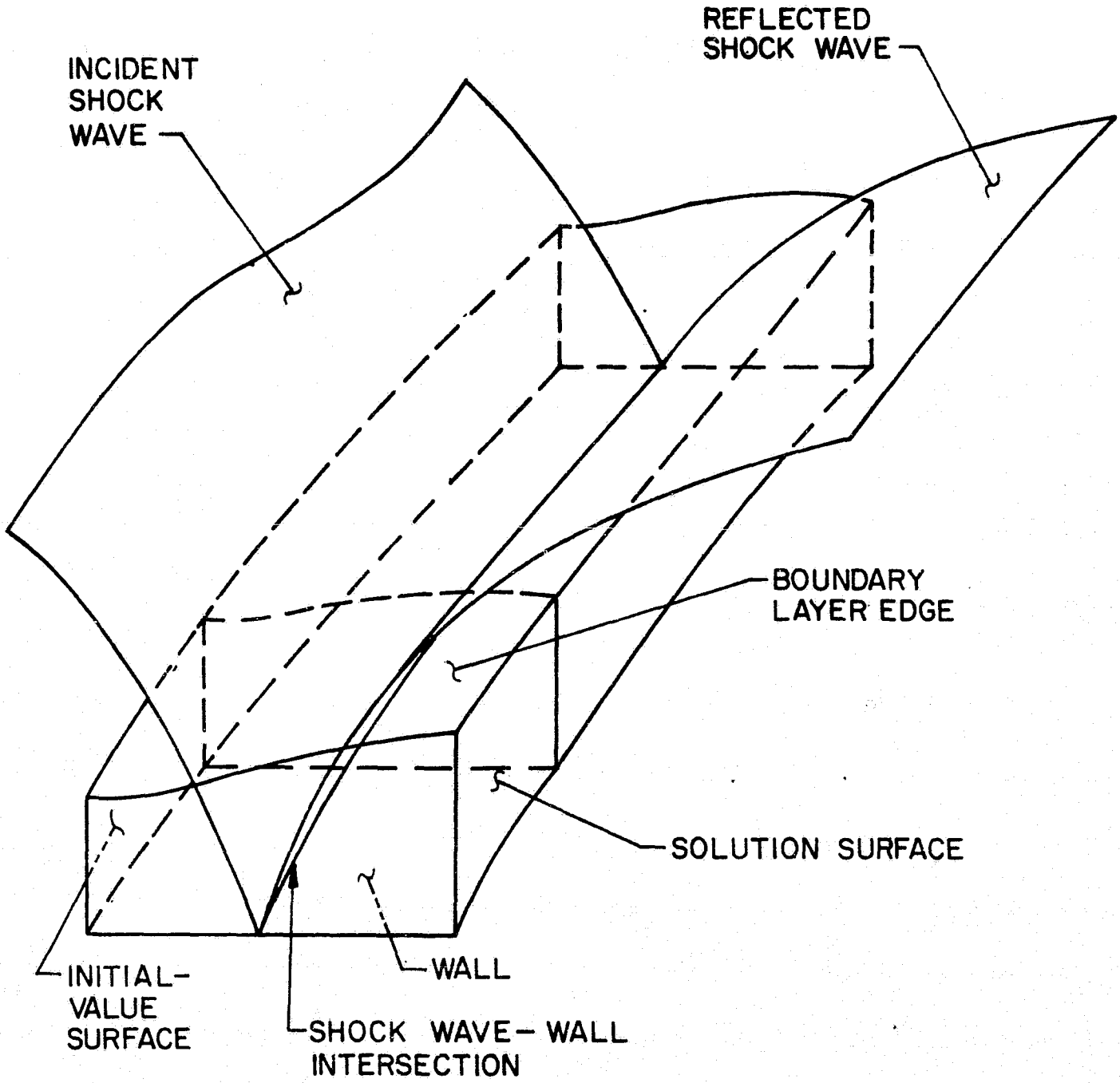

FIGURE 13. SHOCK WAVE- BOUNDARY LAYER INTERACTION REGION

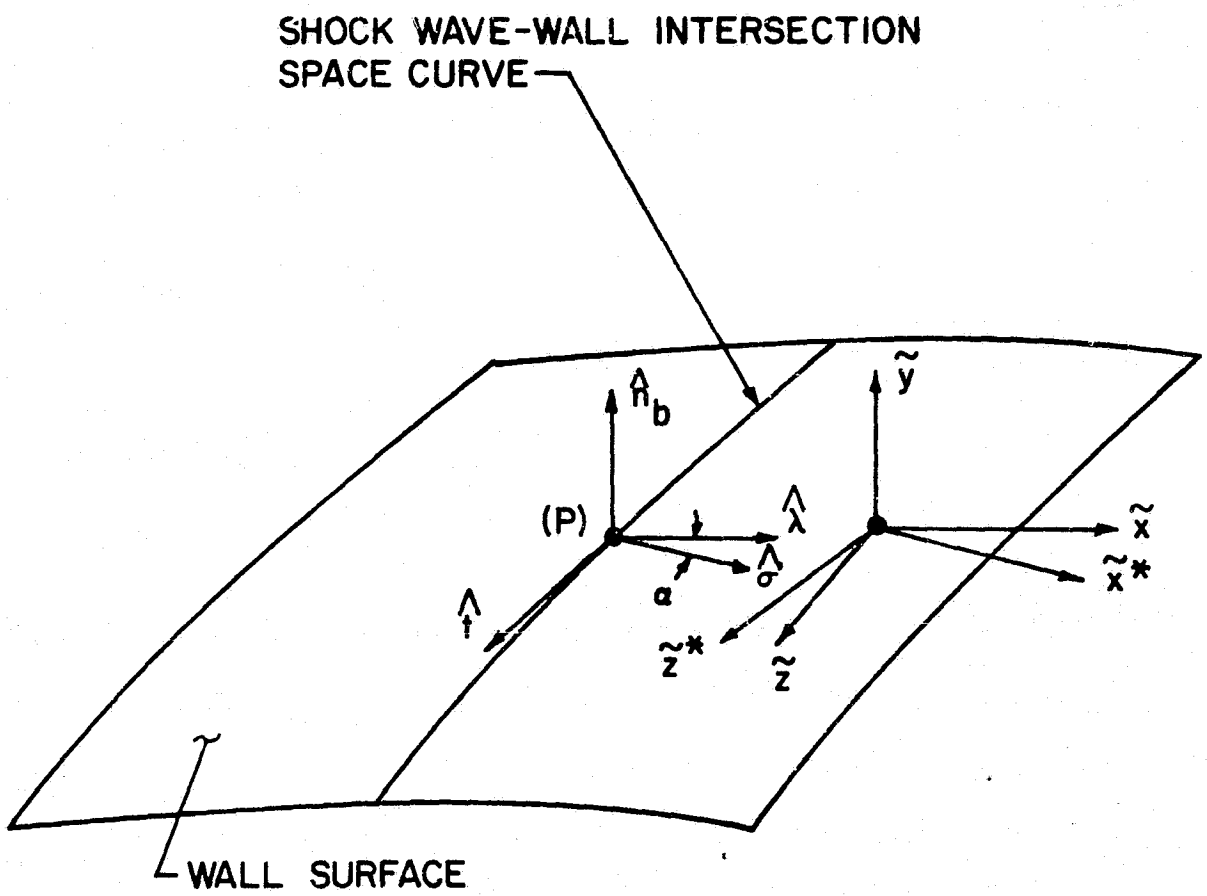

FIGURE 14. UNIT VECTOR SPECIFICATION FOR SHOCK WAVE-BOUNDARY LAYER INTERACTION ANALYSIS

After the unit vector $\hat{\sigma}$ has been determined, the angle α subtended by $\hat{\sigma}$ and $\hat{\lambda}$ may be obtained, where $\hat{\lambda}$ is a unit vector tangent to the body and which lies in the meridional plane of point (P). A coordinate rotation may then be employed to obtain the upstream boundary layer velocity components in the plane containing $\hat{n}_b$ and $\hat{\sigma}$. The body tangent curvilinear coordinates contained in and orthogonal to the plane of $\hat{n}_b$ and $\hat{\sigma}$ are denoted by $\tilde{x}^*$ and $\tilde{z}^*$, respectively (see Figure 14). The boundary layer velocity components in the $\tilde{x}^*$- and $\tilde{z}^*$-coordinate directions are denoted by $\tilde{u}^*$ and $\tilde{w}^*$, respectively, with $\tilde{u}_e^*$ and $\tilde{w}_e^*$ being the respective boundary layer edge velocity components.

After the velocity components at the initial-value surface have been transformed into the $(\tilde{x}^*, \tilde{y}, \tilde{z}^*)$-coordinate system, the integral conservation equations are applied to determine the boundary layer property profiles on the downstream side of the interaction region. A cross-section of the control surface used in the integral analysis is depicted in Figure 15, where the initial-value surface corresponds to station 1 and the solution surface corresponds to station 2. The respective boundary layer thicknesses are denoted by δ_1 and δ_2.

The conservation equations consist of integral forms of the continuity equation, the streamwise $(\tilde{x}^*)$ momentum equation, and the cross-flow $(\tilde{z}^*)$ momentum equation. The energy equation is approximated by the assumption that the total enthalpy at station 2 is constant in the $\tilde{y}$-direction, and is equal to the average total enthalpy at station 1. The integral conservation equations take the form

$$\int_o^{\delta_1} \rho\tilde{u}^* d\tilde{y} = \int_o^{\delta_2} \rho\tilde{u}^* d\tilde{y} + \dot{m}_{bleed} \tag{225}$$

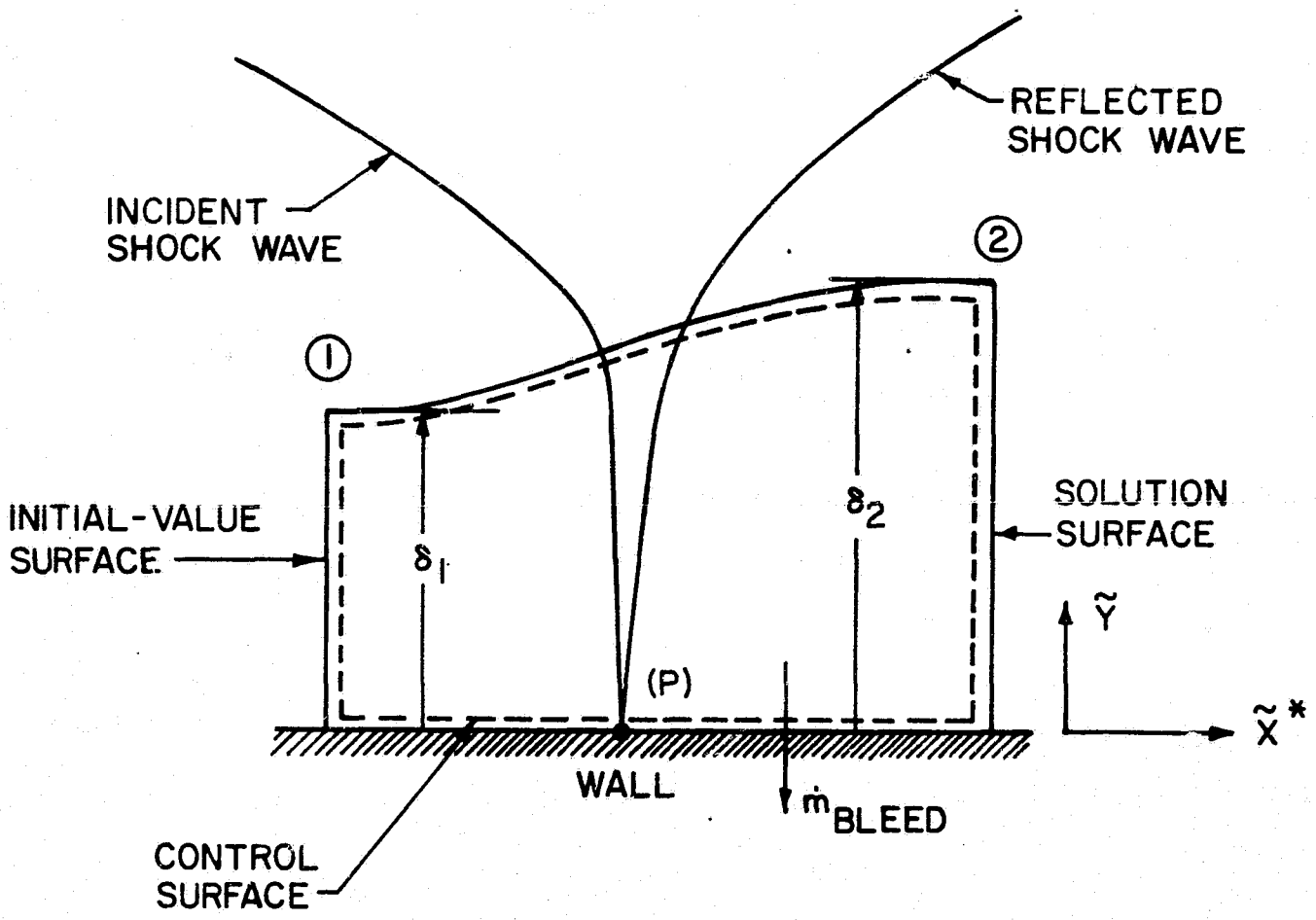

FIGURE 15. INTERACTION REGION CONTROL SURFACE

$$P_1\delta_2 - P_2\delta_2 + \overline{P}(\delta_2 - \delta_1) = \int_0^{\delta_2} \rho(\tilde{u}^*)^2 d\tilde{y} - \int_0^{\delta_1} \rho(\tilde{u}^*)^2 d\tilde{y} \tag{226}$$

$$\int_0^{\delta_1} \rho\tilde{u}^*\tilde{w}^* d\tilde{y} = \int_0^{\delta_2} \rho\tilde{u}^*\tilde{w}^* d\tilde{y} \tag{227}$$

$$\overline{H}_1 = H_2 \tag{228}$$

where equations (225) to (228) represent the continuity, streamwise momentum, cross-flow momentum, and energy equations, respectively. In the above equations, P_1 and P_2 represent the static pressure at stations 1 and 2, respectively, and are assumed to be constant in the $\tilde{y}$-direction, and $\overline{P}$ is an appropriately weighted average pressure acting on the upper surface of the control volume. The mean density and total enthalpy are again denoted by ρ and H, respectively, and $\dot{m}_{bleed}$ is the bleed mass flow rate. It was assumed in writing the above expressions, that negligible mass is entrained into the boundary layer between stations 1 and 2, that viscous shear stress effects may be neglected, and that mass bleed occurs normal to the wall.

Since the upstream flow properties have been determined by application of the finite difference algorithm, the integrals appearing in equations (225) to (228) that are evaluated at station 1 may be determined directly by numerical quadrature. To evaluate the integrals at station 2 requires that representations for the downstream velocity profiles be chosen. In the present investigation, the following turbulent power law profiles have been selected

$$\tilde{u}^* = \tilde{u}_e^* \eta^{\beta_1} \tag{229}$$

$$\tilde{w}^* = \tilde{w}_e^* \eta^{\beta_2} \tag{230}$$

where

$$\eta = \tilde{y}/\delta \tag{231}$$

and the exponents β_1 and β_2 are in the range

$$0 < \beta_1 < 1 \tag{232}$$

$$0 < \beta_2 < 1 \tag{233}$$

The mean total enthalpy H may be expressed in terms of the mean static enthalpy h as

$$H = h + \frac{1}{2}\left[(\tilde{u}_e^*)^2 \eta^{2\beta_1} + (\tilde{w}_e^*)^2 \eta^{2\beta_2}\right] \tag{234}$$

Since both β_1 and β_2 are bounded and $(\tilde{w}_e^*)^2 << (\tilde{u}_e^*)^2$, equation (234) may be approximated as

$$h \cong H - \frac{1}{2}(\tilde{u}_e^*)^2 \eta^{2\beta_1} \tag{235}$$

For a simple system in thermodynamic equilibrium, the following expression can be written

$$\rho = \rho(h, P) \tag{236}$$

where for a thermally and calorically perfect gas

$$\rho = K/h \tag{237}$$

with

$$K = \frac{\gamma}{\gamma - 1} P \tag{238}$$

Using the above relations allows the downstream integrals in equations (225), (226), and (227) to be written for a thermally and calorically perfect gas as

$$\int_0^{\delta_2} \rho\tilde{u}^* d\tilde{y} = K_2\delta_2\tilde{u}^*_{e_2}\int_0^1 \frac{\eta^{\beta_1}\, d\eta}{\left[H_2-\frac{1}{2}(\tilde{u}^*_{e_2})^2\,\eta^{2\beta_1}\right]} \tag{239}$$

$$\int_0^{\delta_2} \rho(\tilde{u}^{*2}) d\tilde{y} = K_2\delta_2(\tilde{u}^*_{e2})^2 \int_0^1 \frac{\eta^{2\beta_1} d\eta}{\left[H_2-\frac{1}{2}(\tilde{u}^*_{e_2})^2\eta^{2\beta_1}\right]} \tag{240}$$

$$\int_0^{\delta_2} \rho\tilde{u}^*\tilde{w}^* d\tilde{y} = K_2\delta_2\tilde{u}^*_{e_2}\,\tilde{w}^*_{e_2}\int_0^1 \frac{\eta^{\beta_1}\eta^{\beta_2} d\eta}{\left[H_2-\frac{1}{2}(\tilde{u}^*_{e_2})^2\eta^{2\beta_1}\right]} \tag{241}$$

To obtain the downstream property profiles, initial estimates are made for the exponents β_1 and β_2. Then equations (225), (226), and (228) are solved simultaneously while incorporating equations (239) and (240) for the downstream integrals. This produces a system of two equations for the downstream unknown quantities δ_2 and β_1. These equations are solved using a Newton-Raphson iteration scheme with β_1 serving as the perturbation quantity. After convergence has been obtained for δ_2 and β_1, equation (241) is incorporated into equation (227), with the resulting expression being solved using a Newton-Raphson iteration scheme employing β_2 as the perturbation quantity.

Determining the downstream boundary layer thickness δ_2 and the power law exponents β_1 and β_2 completely defines the downstream property field since H_2 was determined from equation (228). After the downstream velocity components $\tilde{u}_2^*$ and $\tilde{w}_2^*$ have been calculated, the velocity components $\tilde{u}_2$ and $\tilde{w}_2$ can be determined by a coordinate rotation.

By applying the above analysis to a series of control volumes, the

flow properties downstream of the shock wave-boundary layer interaction region may be determined for the entire computed sector. This solution is then used as initial data for restarting the finite difference boundary layer computation.

SECTION IX

OVERALL NUMERICAL ALGORITHM

1. INTRODUCTION

In this section, brief discussions are presented on the overall algorithm control logic, generation of the initial data, boundary conditions, regulation of the marching step size, computation of the transport forcing functions, and numerical stability. A detailed discussion of the overall numerical algorithm is presented in Appendix K.

2. COMPUTATION OF THE SUPERSONIC CORE FLOW

The overall numerical algorithm for the supersonic core flow computation consists of the repetitive application of the various characteristic unit processes to generate the global solution for given boundary conditions and a specified set of initial data.

The contours of the forebody/centerbody and the cowl, in addition to any planes of flow symmetry, constitute the boundaries of the computational flow regime. For the external flow field integration, the bow shock wave also represents a computational boundary.

The supersonic flow initial data are specified on a plane of constant x. The x-coordinate axis is the longitudinal axis of the centerbody and the cowl (see Figure 1). Moreover, the mean flow direction is assumed to be in the x-coordinate direction.

An inverse marching scheme is employed in the supersonic flow numerical algorithm. The solution is obtained on a family of space-like planes of constant x. The solution points on each plane represent the

intersection points of continuous streamlines which are propagated from the data points specified on the initial-value plane. In addition to the streamline solution points, solution points are also obtained at the intersection of the external and internal shock waves with the solution plane, and for the internal flow field, on the space curves where the internal shock wave intersects the solid boundaries. These space curves are defined by the locus of shock wave solution points.

Except in the vicinity of a shock wave reflection with a solid boundary, the axial (x) distance between the current initial-value plane and the current solution plane is determined by the application of the Courant-Friedrichs-Lewy (CFL) stability criterion (8). In the vicinity of a shock wave reflection with a solid boundary, the axial distance between successive solution planes is chosen so that the entire shock wave-solid boundary intersection falls between two adjacent solution planes.

The external supersonic flow about the forebody is computed first. The external flow field integration requires the periodic addition of streamlines in order to retain a well dispersed computational mesh. Furthermore, periodic deletion of selected streamlines is also required so that the number of computational points lies within bounds.

The internal supersonic flow field can be computed with or without the discrete fitting of the internal shock wave system. The option in which shock waves are not discretely fitted may be used in cases in which the internal shock waves are quite weak in strength, and thereby an acceptable solution can be obtained by smearing the internal discontinuities.

3. COMPUTATION OF THE BOUNDARY LAYER FLOW

The overall numerical algorithm for the boundary layer flow computation consists of the repetitive application of the attachment line flow,

three-dimensional flow, and shock wave-boundary layer interaction region flow subalgorithms to generate the global solution for given boundary conditions and a specified set of initial data.

The contours of the forebody/centerbody and the cowl, in addition to the planes of flow symmetry, constitute the boundaries of the computational flow regime.

The boundary layer flow initial data are specified on body normal rays of constant $\tilde{x}$. The $\tilde{x}$-coordinate axis is the streamwise curvilinear coordinate coincident with the body and contained in a given meridional plane (see Figure 9). The mean boundary flow direction is assumed to be in the $\tilde{x}$-coordinate direction. Separate sets of initial data are required to initiate the forebody/centerbody and cowl boundary layer computations.

The implicit finite difference algorithm is applied to compute all of the boundary layer flow except for that in the shock wave-boundary layer interaction regions where the integral analysis is employed. The finite difference algorithm first applies the attachment line flow subalgorithm to calculate the boundary layer flow on the windward and leeward planes of symmetry. The three-dimensional flow subalgorithm is then applied to compute the boundary layer flow between the planes of flow symmetry starting at the windward meridian and marching to the leeward meridian for a given solution surface. The boundary layer solution is obtained on an orthogonal curvilinear mesh conforming to the local surface curvature. As opposed to the bicharacteristic supersonic flow solution, individual streamlines are not followed in the boundary layer computation. The boundary layer external flow properties are determined by interpolation of the supersonic flow solution.

When a shock wave-boundary layer interaction region has been encountered, the three-dimensional integral analysis is applied to compute the property profiles on the downstream side of the interaction region. The boundary layer properties on the upstream side of the interaction region are supplied by application of the implicit finite difference algorithm. The external flow properties are obtained from the supersonic core flow solution.

The streamwise step size used in the boundary layer computation is selected to correspond to the axial marching step determined from the Courant-Friedrichs-Lewy stability criterion used in the supersonic flow computation. As a consequence, the supersonic flow and boundary layer flow solutions are determined at the same axial stations.

4. SUPERSONIC FLOW INITIAL DATA

The supersonic flow initial data are specified on a plane of constant x (see Figure 1). The flow must be supersonic at every point on this plane. For uniqueness and existence of a genuine solution, the values of the dependent variables prescribed on this surface must have at least continuous first partial derivatives.

If the forebody flow field is to be computed, the supersonic flow initial-value plane must be specified at an axial (x) station that is upstream of the forebody flow computational regime (see Figure 1). The last solution plane of the forebody flow field computation is adjusted to lie at the axial station of the cowl lip, and constitutes the initial-value plane for the internal flow field computation. The cowl lip is assumed to be contained in a plane of constant x. Furthermore, the bow shock wave must fall outside of the cowl lip, or, in the limit, intersect the cowl lip exactly. The internal flow cannot be calculated if the bow

shock wave is ingested into the annulus. The points on the solution plane at the cowl lip axial station are redistributed to obtain a ring of solution points coincident with the cowl lip.

If the forebody is conical ahead of the axial station where the supersonic flow initial-value plane is specified, an approximate flow property field on this plane may be internally generated in the computer program. The internally generated initial data are obtained by an approximate technique which employs the Taylor-Maccoll solution for the flow about a circular cone at zero incidence. A superposition method is then used to obtain an approximation for the flow about a circular cone at nonzero angle of attack by neglecting the cross flow effects. Alternatively, a more exact solution for the initial data for flow about a circular cone at incidence may be obtained by employing the results of Jones (28). The Jones algorithm has been incorporated into the computer program developed in the present study.

If the forebody is not conical ahead of the axial station of the initial-value plane, then the initial data must be specified by the user. If available, experimental data may be employed.

5. BOUNDARY LAYER FLOW INITIAL DATA

The boundary layer flow initial data are specified at stations of constant $\tilde{x}$ (see Figure 9). Separate sets of initial data must be specified to initiate the forebody/centerbody and cowl boundary layer computations. For uniqueness and existence of a genuine solution, the prescribed initial data must have at least continuous first partial derivatives.

The forebody/centerbody boundary layer flow initial data must be specified at the same axial station at which the supersonic flow initial data are specified. If the forebody is conical ahead of the axial station where

the computation is to be started, then the initial data may be generated using the implicit finite difference algorithm developed by Adams (29), which is applicable to determining the boundary layer flow for a circular cone at incidence. The Adams algorithm has been incorporated into the computer program developed in the present investigation. Use of the Adams algorithm requires specification of the wall temperature.

If the forebody is not conical ahead of the axial station where the computation is to begin, then the initial data must be specified by the user. Experimental data may be employed, if available.

The cowl boundary layer initial data must be specified at the axial location of the first supersonic flow solution plane inside the annulus (the boundary layer thickness at the cowl lip is identically zero). The cowl boundary layer initial data may be internally generated in the computer program using an approximate technique described in Appendix K. Alternatively, arbitrary initial data may be specified by the user.

6. FLOW SYMMETRY

Four flow symmetry options have been incorporated into the supersonic flow algorithm. The most general case is when no planes of symmetry exist. This option is used to compute the flow field for fully three-dimensional inlets at incidence. The second case is when one plane of flow symmetry exists. This option is used for computing the flow field for axisymmetric inlets at angles of attack. This second case of flow symmetry is the one most likely to arise in the class of problems being considered in the present investigation. The third case is when two planes of flow symmetry exist. This option is used to compute the flow field for three-dimensional inlets with two planes of geometric symmetry at zero angle of attack. The final option is when the flow is axisymmetric. This option is used to

compute the flow field in axisymmetric inlets at zero incidence.

One flow symmetry option has been incorporated into the boundary layer flow algorithm. This is for the case of one plane of flow symmetry.

7. SOLID BOUNDARY SURFACES

The computer program developed in the present investigation assumes that both the forebody/centerbody and the cowl are axisymmetric. For the purposes of geometry description, the axial (x) domain is divided into a number of intervals. In any interval, the body radius r may be specified by either tabular input, or by supplying the coefficients in the cubic polynomial

$$r(x) = a_i + b_i(x - x_i) + c_i(x - x_i)^2 + d_i(x - x_i)^3 \qquad (242)$$

where the subscript i denotes the i th interval, r(x) is the body radius at axial position x ($x_i \leq x < x_{i+1}$), and the coefficients a_i, b_i, c_i, and d_i are obtained by curve fitting the body contour. Since equation (242) is a cubic, slope and curvature can be matched at the junction point between two adjacent intervals (i.e., spline fits can be employed).

More arbitrary geometries may be readily incorporated into the analysis by replacement of the existing geometry module.

8. TEMPERATURE AND MASS TRANSFER BOUNDARY CONDITIONS

The boundary layer computation requires specification of the temperature or the normal temperature derivative at the wall. Constant temperature or temperature derivative boundary conditions may be specified. Alternatively, an arbitrary wall temperature or temperature derivative

distribution may be specified by tabular input. Quadratic interpolation is employed to obtain the temperature boundary condition at the required axial stations when the tabular input option is employed.

Mass transfer boundary conditions are specified by entering the axial locations of the boundary layer bleed zones and the mass flux within each zone.

9. INTEGRATION STEP SIZE REGULATION

Except in the vicinity of a reflection of the internal shock wave with a solid boundary, the axial marching step between successive supersonic flow solution planes is determined by the application of the Courant-Friedrichs-Lewy (CFL) stability criterion (8). The CFL stability criterion mandates that the domain of dependence of the differential equations be contained within the convex hull of the finite difference network. That is, the Mach cone must be inside the outer periphery of the nine initial-value plane field points used in formulating the bivariate interpolation polynomial, equation (51). The allowable axial step is given by

$$\Delta x = [u^2/(cq)][1 - (c/q)(q^2/u^2 - 1)^{1/2}]R_{min} \qquad (243)$$

where Δx is the marching step, and R_{min} is the distance between the streamline intersection point with the initial-value plane and the nearest point on the convex hull of the finite difference network. Equation (243) is applied at every streamline point on the initial-value plane, with the actual integration step being chosen as the Δx value at the most restrictive point. Equation (243) is applied only to streamline points. The shock wave points are excluded. Moreover, in the internal flow field

integration, the shock wave points are ignored in defining the convex hull of the finite difference network when applying the stability criterion to a streamline point.

In the vicinity of a reflection of the internal shock wave with a solid boundary, the axial step is controlled by the constraint that the shock wave-solid body intersection is contained entirely between two adjacent solution planes. The fit point stencils used in formulating the various interpolation polynomials are appropriately expanded, in this case, so that the CFL stability criterion is satisfied.

As noted previously, the marching step used in the boundary layer computation ($\Delta\tilde{x}$) corresponds to the axial step determined by the CFL stability criterion (Δx). Although there also exists a marching step stability limitation in the boundary layer computation, discussed in Appendix I, the CFL stability criterion is usually the more restrictive of the two.

10. CALCULATION OF THE TRANSPORT FORCING FUNCTIONS

The numerical procedure developed in the present investigation has the capability to include the influence of molecular transport in the supersonic flow solution by treating the viscous and thermal diffusion terms in the governing partial differential equations as forcing functions, or correction terms, in the method of characteristics scheme. The computer program has the capability to include the influence of viscous and thermal diffusion in the computation of the supersonic external flow about the forebody, and in the computation of the supersonic internal flow field in which shock waves are not discretely fitted. The program option in which shock waves are discretely fitted in the supersonic internal flow field does not have the capability to include the influence of molecular

transport in the computation, but rather assumes the supersonic flow to be inviscid and adiabatic. The detailed calculation procedures used for obtaining the transport forcing terms are presented in Appendix F.

11. NUMERICAL STABILITY

A stability analysis of the nonlinear supersonic flow finite difference algorithm including molecular transport was not attempted. Instead, a stability analysis for isentropic flow was conducted. Stability of the generalized analysis was then verified by actual numerical calculations.

Ransom, Hoffman, and Thompson (9) conducted a von Neumann linear stability analysis of the basic interior point scheme which indicated that interpolated flow properties, instead of the actual known values, should be used at the streamline-initial-value plane intersection point [point (5) in Figure 3]. The present supersonic flow analysis uses interpolated flow properties at all points in the initial-value plane.

Stability of the boundary layer flow algorithm was verified by actual numerical calculations.

SECTION X

COMPUTATIONAL RESULTS

1. INTRODUCTION

Selected computational results are presented in this section to illustrate application of the analysis. The results presented are divided into two major categories: external flow about the forebody, and internal flow in which the internal shock wave system has been computed. Both axisymmetric flow and three-dimensional flow results are shown. For the internal flow field in which shock waves have been fitted, some comparisons with experimental data and existing computational methods are made. Additional supersonic flow results may be found in Reference (1).

2. EXTERNAL FLOW RESULTS

For the purpose of testing the external flow integration procedure, the flow field about a right circular cone at incidence was computed. The supersonic flow for this case is a conical flow in that the solution is constant along rays emanating from the vertex of the cone (i.e., there is no characteristic length, so the solution has no dependency on x). At zero angle of attack, the solution depends only on the angle subtended by a given ray and the x-axis. At nonzero incidence, an azimuthal variation also exists. To obtain the required initial data, the results of Jones (28) were employed. The computed results should maintain the conical nature of the flow field.

Figure 16 presents numerical results obtained for a 10.0° half-angle cone at 2.5° angle of attack α with a free-stream Mach number M_∞ of 3.0. The computation employed 21 circumferential stations in the computed sector (half-plane), and the number of radial stations on the initial-value plane was 11. The computed static pressure P normalized by the free-stream static pressure P_∞ is plotted versus the axial position x normalized by the cowl lip radius R_c. The pressure distributions on the rays formed by the forebody and the bow shock wave on both the leeward and windward planes of symmetry are shown. Since the flow is conical, the solution should remain constant along each of these four rays at the respective pressure values at the appropriate points on the initial-value plane. The initial-value plane pressures are denoted by the straight line segments. The method of characteristics solution is shown at a discrete number of axial stations, each station corresponding to the axial location of a given solution plane. The bicharacteristic solution maintains the conical nature of the flow field.

It should be noted that the increase in pressure across the leeward side of the bow shock wave is minimal. As the angle of incidence is further increased, the strength of the bow shock wave on the leeward side is reduced until the point is reached where the angle of attack is equal to the cone half-angle. At this point, no shock wave exists on the leeward meridional plane. Further increase in the angle of incidence causes a flow expansion to occur on the leeward side. Since the present analysis assumes that a shock wave exists about the entire forebody, the case where a flow expansion occurs on the leeward side cannot be computed.

Boundary layer computations where performed for a 10.0° half-angle cone at 1.0° angle of attack α with a free-stream Mach number M_∞ of 2.5. This

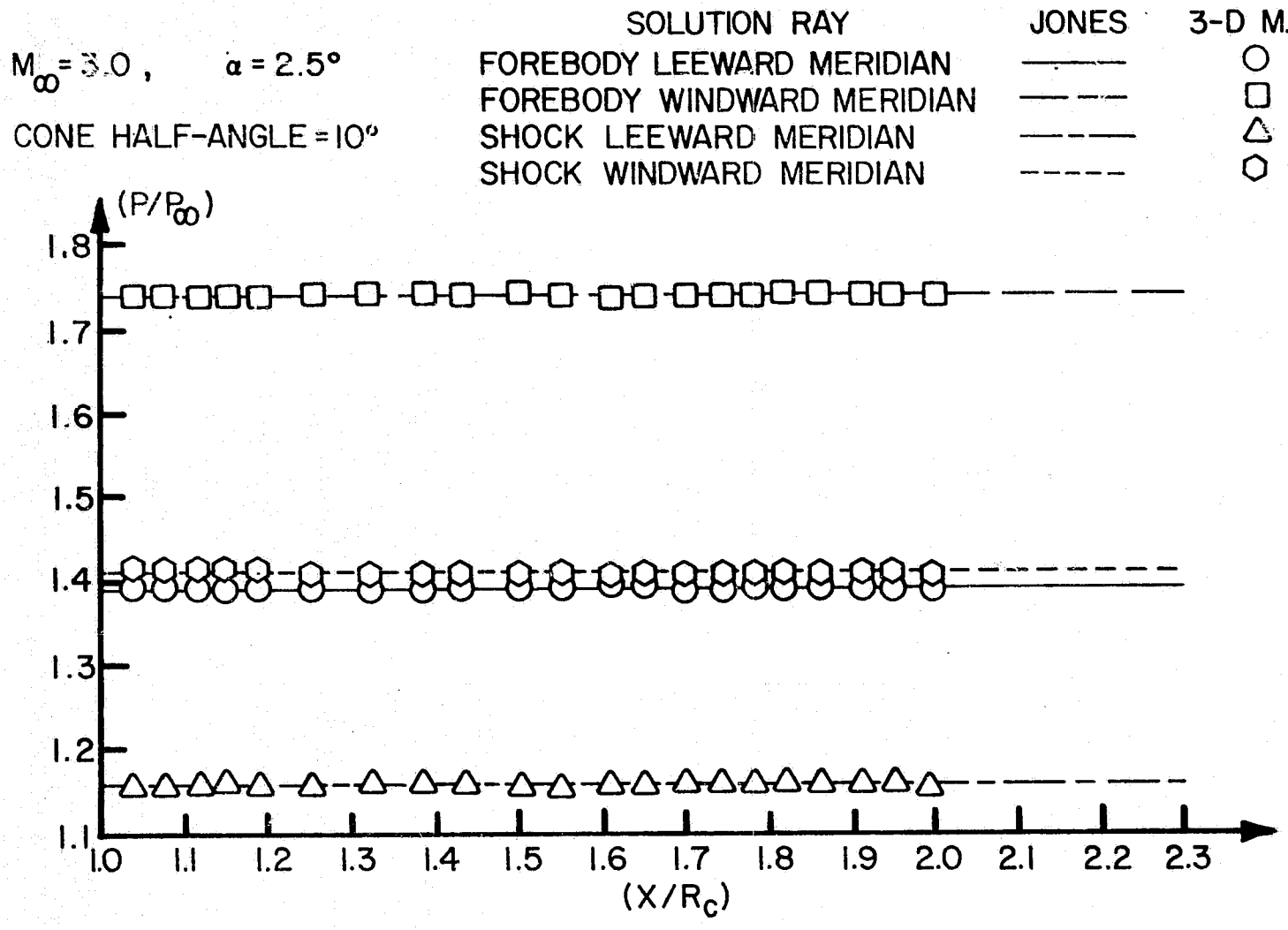

FIGURE 16. PRESSURE DISTRIBUTIONS FOR EXTERNAL FLOW

computation employed 15 circumferential stations for both the supersonic external flow and the boundary layer flow. Twenty radial stations were employed in the boundary layer computation. Figure 17 presents the computed boundary layer velocity profiles at a station where $x/R_c=2.0$, and where the polar angle ϕ measured from the windward meridian is 90.0°. The normalized streamwise and cross flow velocity components, denoted by $(\tilde{u}/\tilde{u}_e)$ and $(\tilde{w}/\tilde{w}_e)$, respectively, are plotted versus the distance $\tilde{y}$ measured normal to the wall. Figure 18 presents the normalized static temperature (T/T_e) profile for the same boundary layer station. The boundary layer initial data were obtained using the Adams algorithm (29). A constant wall temperature boundary condition was employed in the computation. The wall temperature was selected to equal the free-stream stagnation temperature. Moreover, laminar flow was assumed.

3. INTERNAL FLOW RESULTS

Internal flow calculations were performed for the Boeing Mach 3.5 supersonic mixed-compression inlet documented in Reference (30). The centerbody and cowl coordinates of this inlet are listed in Table 1. The boundary contours are illustrated in Figure 19 for the design case of zero centerbody translation. This inlet has a forebody which is conical (the forebody is not shown in Figure 19). Consequently, all of the numerical solutions were started at the cowl lip axial station. The supersonic flow initial data were obtained by employing the results of Jones (28). The forebody/centerbody boundary layer initial data were obtained using the Adams algorithm (29). The cowl boundary layer initial data were obtained using the approximate analysis described in Appendix K.

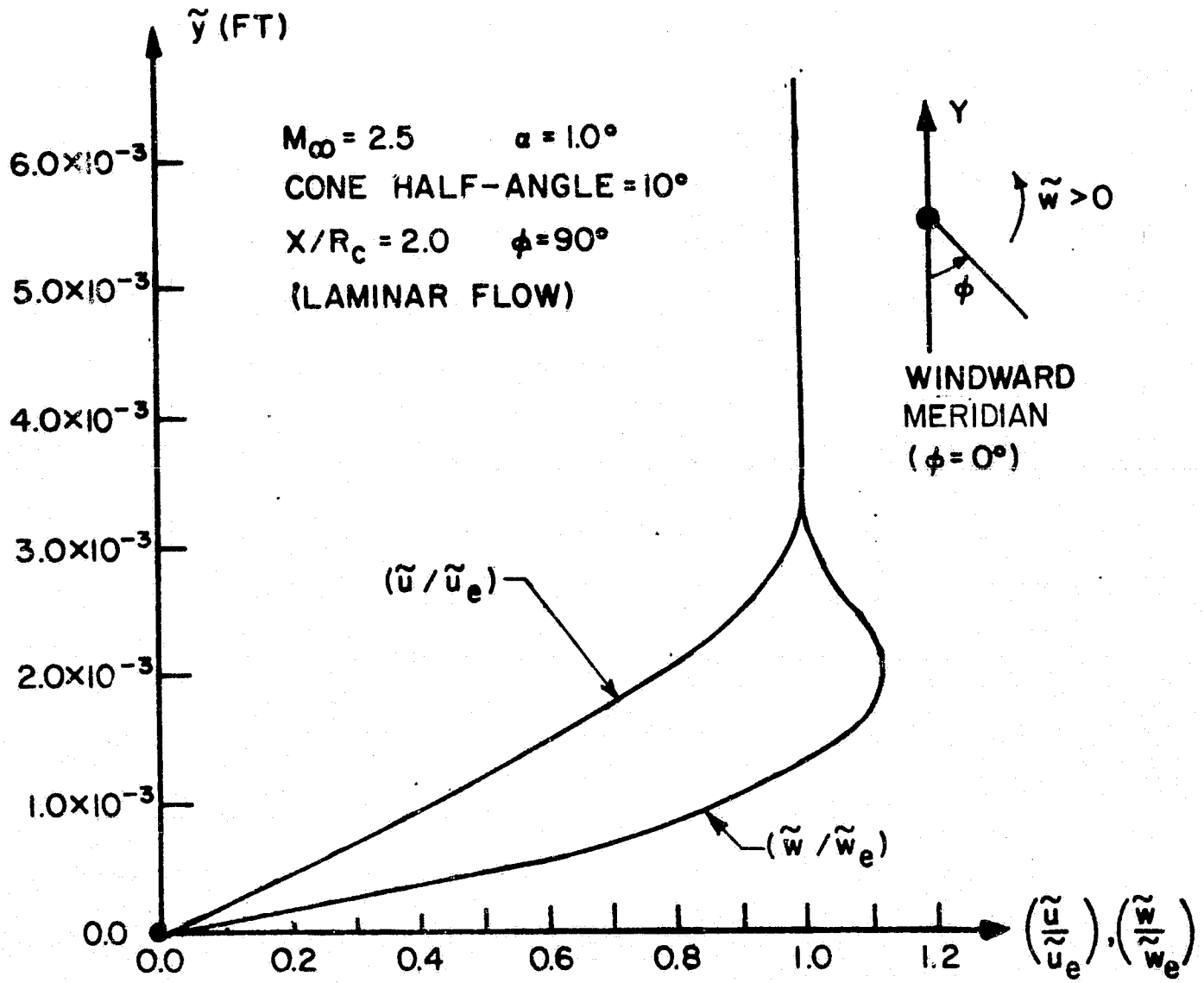

FIGURE 17. BOUNDARY LAYER VELOCITY PROFILES FOR EXTERNAL FLOW.

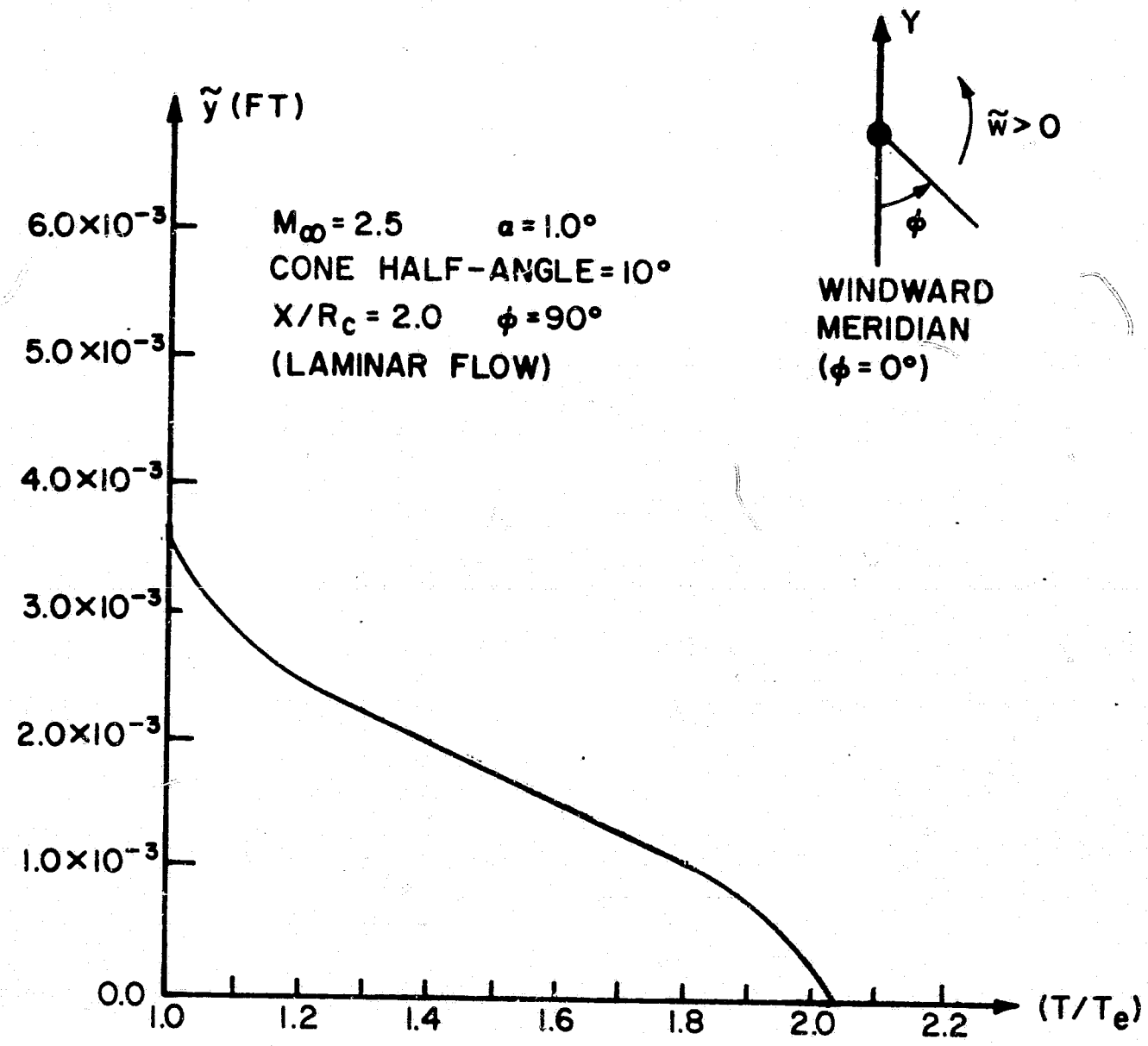

FIGURE 18. BOUNDARY LAYER STATIC TEMPERATURE PROFILE FOR EXTERNAL FLOW.

TABLE 1

MACH 3.5 INLET COORDINATES

CENTERBODY		COWL	
x/R_c	r/R_c	x/R_c	r/R_c
0.0	0.0	2.86	1.0
4.0	0.70532	3.1	1.004188
4.1	0.7228	3.2	1.0054
4.2	0.7387	3.4	1.0051
4.3	0.7512	3.6	0.99996
4.4	0.759	3.8	0.9882
4.5	0.7625	4.0	0.9681
4.55	0.763	4.1	0.954
4.6	0.7625	4.2	0.9364
4.65	0.7611	4.25	0.9261
4.7	0.7585	4.3	0.9154
4.8	0.7504	4.4	0.8949
4.9	0.7391	4.5	0.8768
5.1	0.7120	4.55	0.8695
5.3	0.6829	4.6	0.864
5.5	0.6525	4.65	0.86
5.6	0.6362	4.7	0.8572
5.7	0.618	4.8	0.8533
5.8	0.5973	4.9	0.8511
5.9	0.5744	5.0	0.8502
6.0	0.5467	5.1	0.85
		5.6	0.85
		5.8	0.8574
		5.9	0.8646
		6.0	0.8735

x : Axial Position

r : Radial Position

R_c: Radius of Cowl Lip

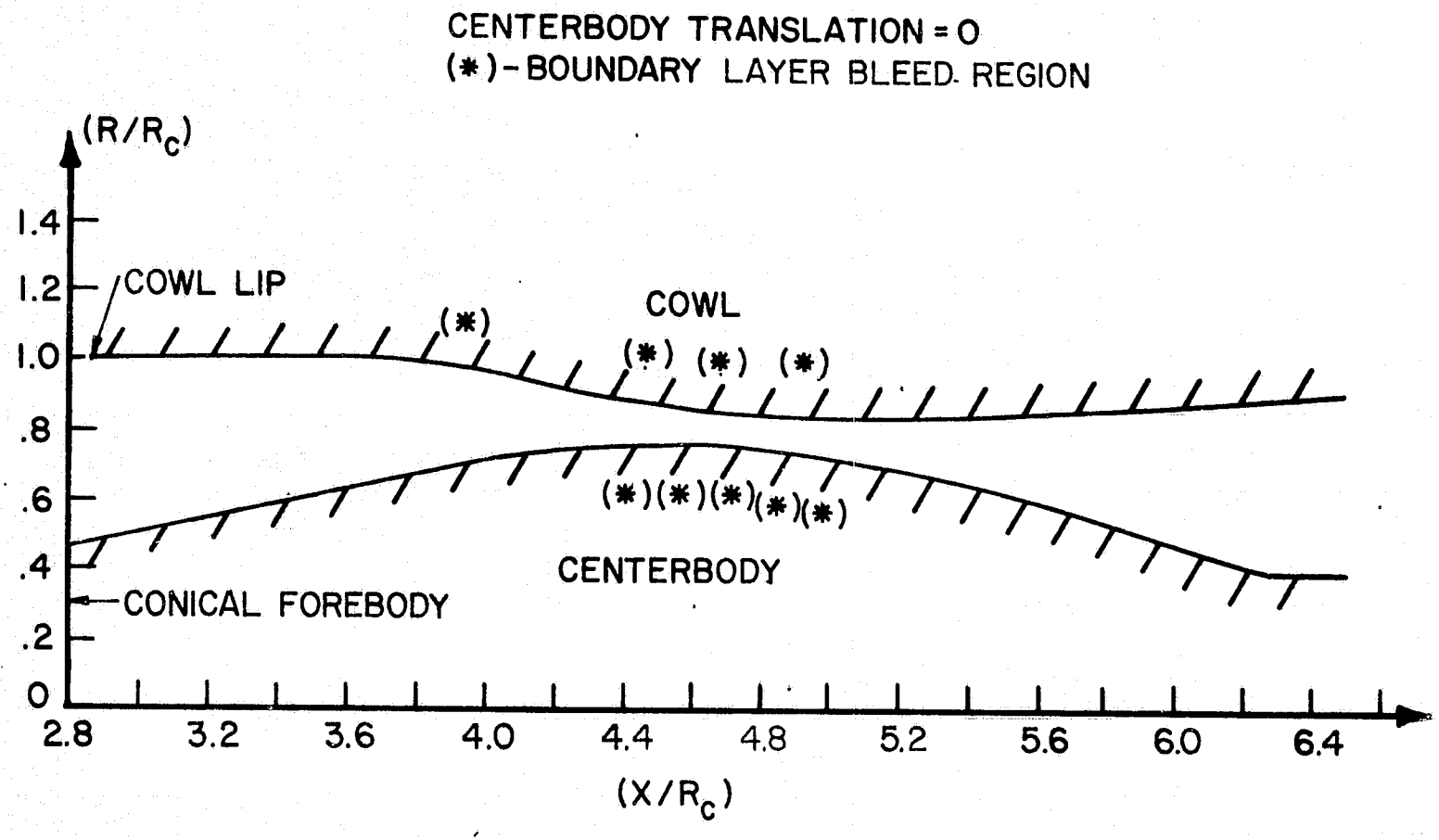

FIGURE 19. BOEING MACH 3.5 MIXED-COMPRESSION INLET CENTERBODY AND COWL CONTOURS

The first supersonic core flow results employing the internal flow computational algorithm in which shock waves are discretely fitted are for the design conditions of M_∞ = 3.5, zero centerbody translation, and zero incidence (α=0°). At the design point, the bow shock wave intersects the cowl lip exactly at zero incidence. Since the flow field is axisymmetric at zero incidence, it can be computed using a two-dimensional method. Comparisons of the supersonic core flow results obtained from the present analysis with those obtained from a two-dimensional method of characteristics scheme (31) for the zero incidence design point conditions are shown in Figures 20 and 21. In these figures, the static pressure P normalized by the free-stream stagnation pressure P_{T_∞} is plotted versus the axial position x normalized by the cowl lip radius R_c. Pressure distributions are shown for both the centerbody and the cowl. The results obtained by the two-dimensional method of characteristics algorithm are indicated by solid lines, and the results obtained by the present analysis are indicated by the dashed lines. Fifty radial stations were used in the two-dimensional method of characteristics solution. Figure 20 illustrates the case where a total of 11 radial stations (9 streamline points and an upstream and downstream shock wave point) were employed in the three-dimensional method of characteristics solution. Good overall agreement is observed. A slight smearing of the pressure distribution downstream of the second intersection of the shock wave with the centerbody and a slight shifting of the shock wave-solid body intersections are present in the three-dimensional algorithm's results. The smearing of the pressure distribution is primarily a consequence of the coarse mesh size used in the three-dimensional scheme's solution. Figure 21 illustrates the solution obtained by the three-dimensional analysis when a total of 21 radial stations were used in the computation. In this case, the agreement between

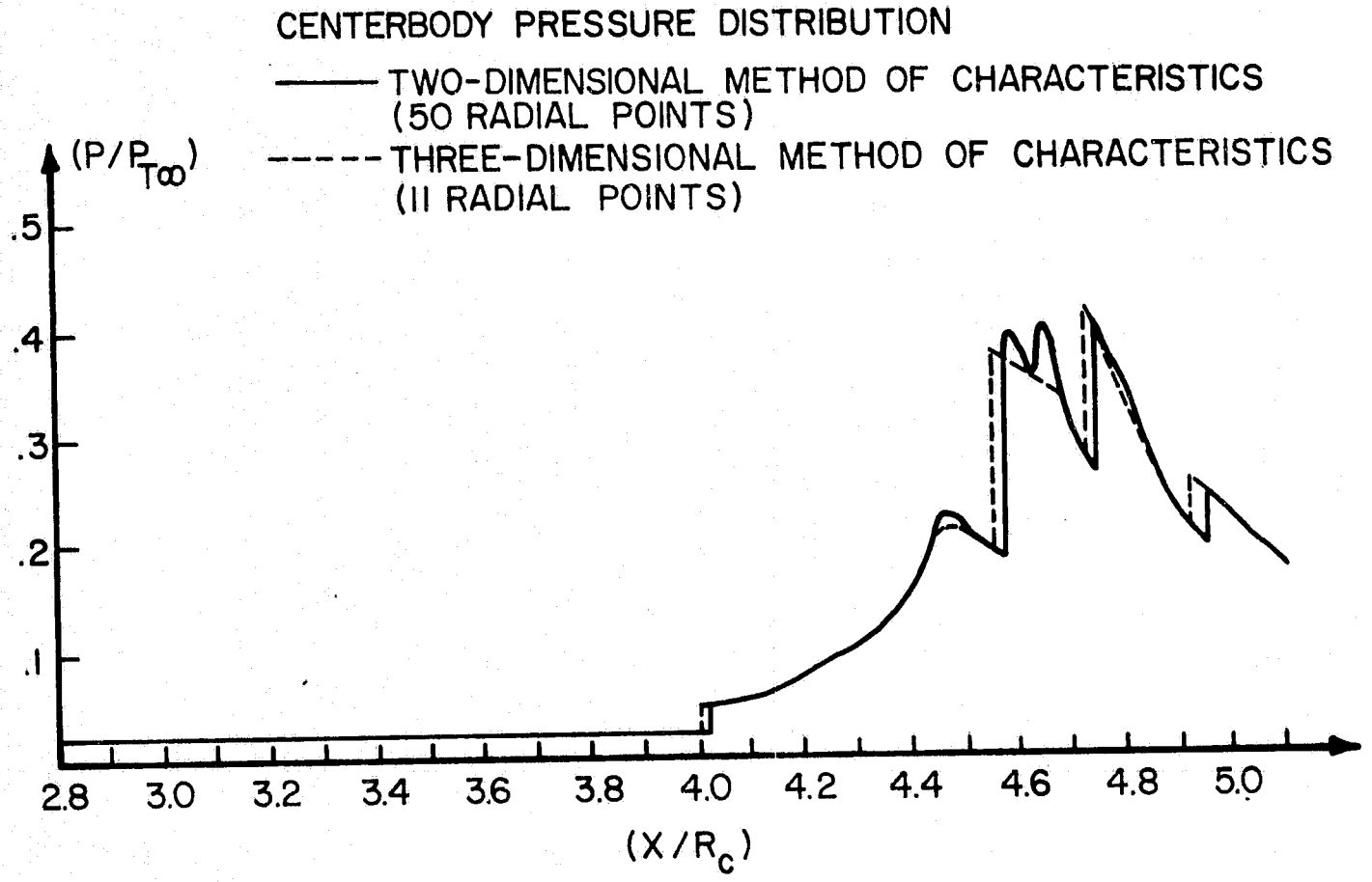

FIGURE 20. COMPARISON OF THE TWO- AND THREE-DIMENSIONAL METHODS OF CHARACTERISTICS FOR $M_\infty = 3.5$, $\alpha = 0°$, TRANSLATION = 0

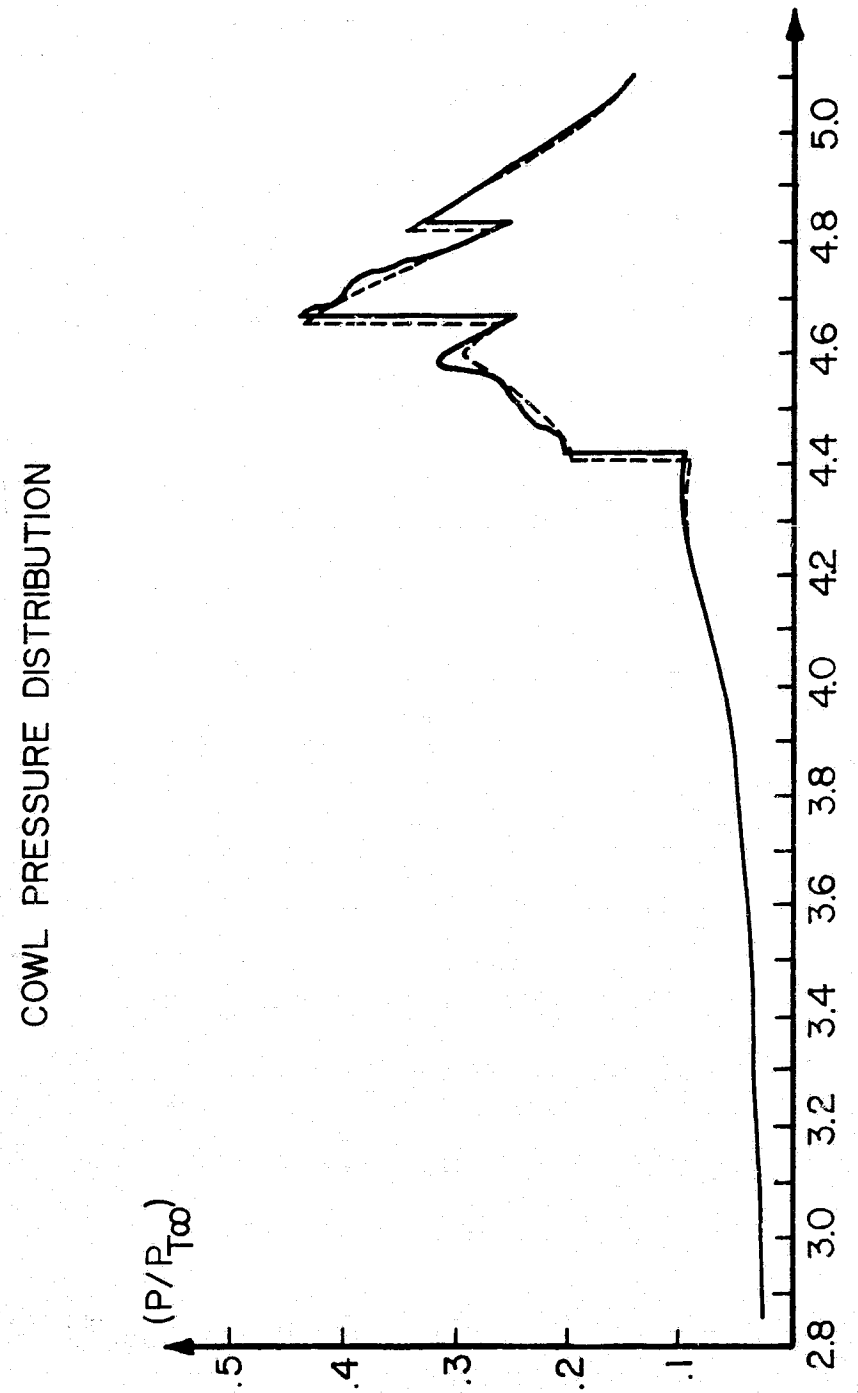

FIGURE 20. (CONTINUED)

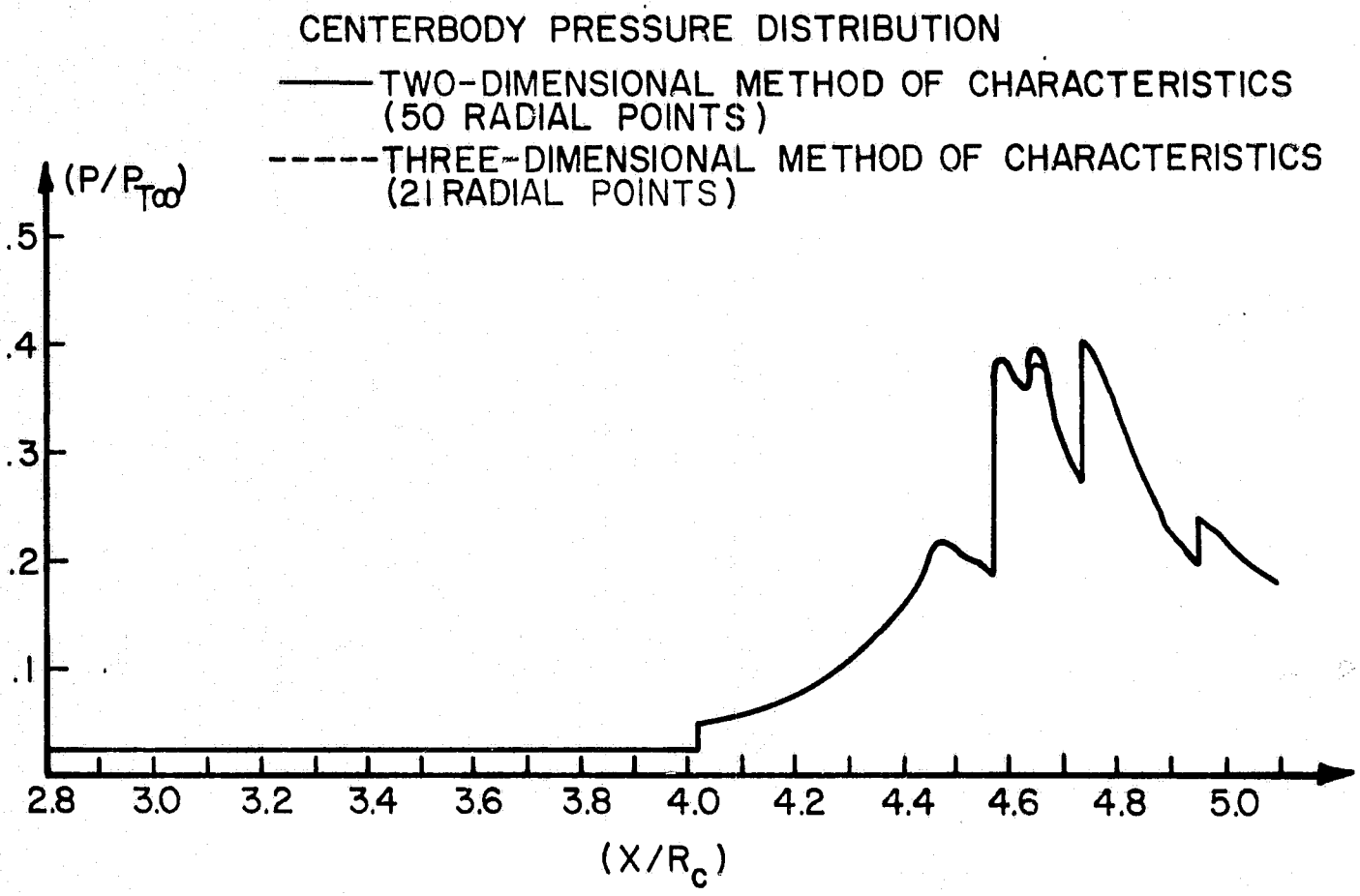

FIGURE 21. COMPARISON OF THE TWO- AND THREE-DIMENSIONAL METHODS OF CHARACTERISTICS FOR $M_\infty = 3.5$, $\alpha = 0°$, TRANSLATION = 0

COWL PRESSURE DISTRIBUTION

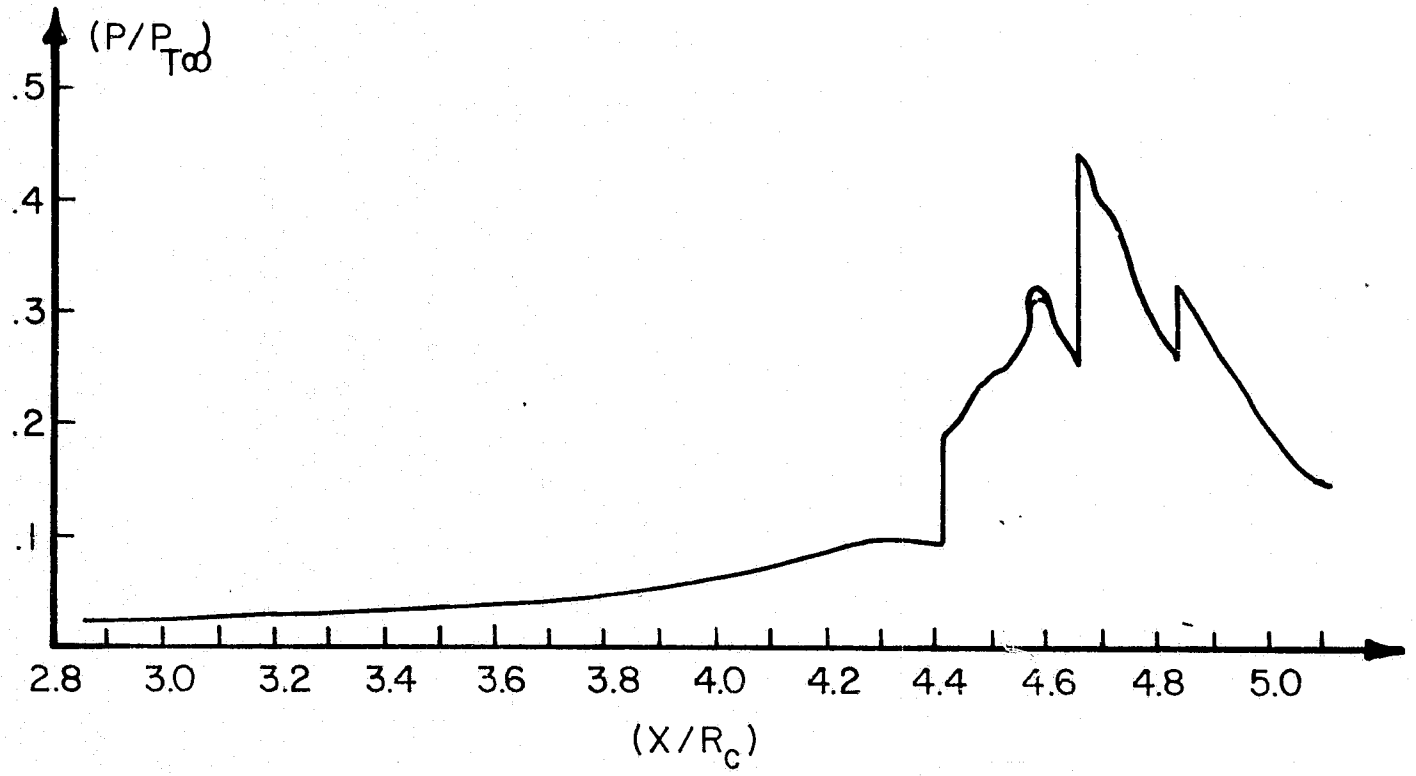

FIGURE 21. (CONTINUED)

the three-dimensional analysis and the two-dimensional analysis is excellent. The pressure distribution behind the second shock wave-centerbody intersection is predicted very well. The axial locations of the shock wave-solid boundary intersections also agree very well. For this computation, the maximum deviation in the computed mass flow rate at any solution plane from that at the cowl lip solution plane was approximately 0.77 percent.

Comparisons of the results of the present analysis with experimental data (32) for the Boeing Mach 3.5 inlet for $\alpha=0°$ are shown in Figure 22. Generally speaking, good agreement is observed. Mass bleed effects were not accounted for in this particular computation, rather an impermeable wall was assumed.

At a given free-stream Mach number, the centerbody assembly must be translated forward of its design point position as the angle of incidence is increased to maintain supersonic flow through the geometric throat of the annulus. The forward translation of the centerbody causes the cross-sectional area of the geometric throat to increase. Moreover, as the free-stream Mach number is reduced from the design point value, even further forward translation of the centerbody is required. The prescribed nondimensional centerbody translation will be denoted by $\Delta x/R_c$ in the following discussion.

Results are presented below for the off-design condition of $M_\infty=2.5$ with a centerbody translation of $\Delta x/R_c=0.855$. Supersonic core flow results for this case are presented in Figures 23 to 26. Figure 23 illustrates the computed centerbody and cowl pressure distributions for an incidence angle of $\alpha=0°$. Although the centerbody has been translated forward, the coordinate system origin is maintained at the forebody tip. Consequently, the internal flow computational regime begins at $x/R_c=3.715$. Generally speaking, the strength of the internal shock wave system for this case is somewhat reduced as compared

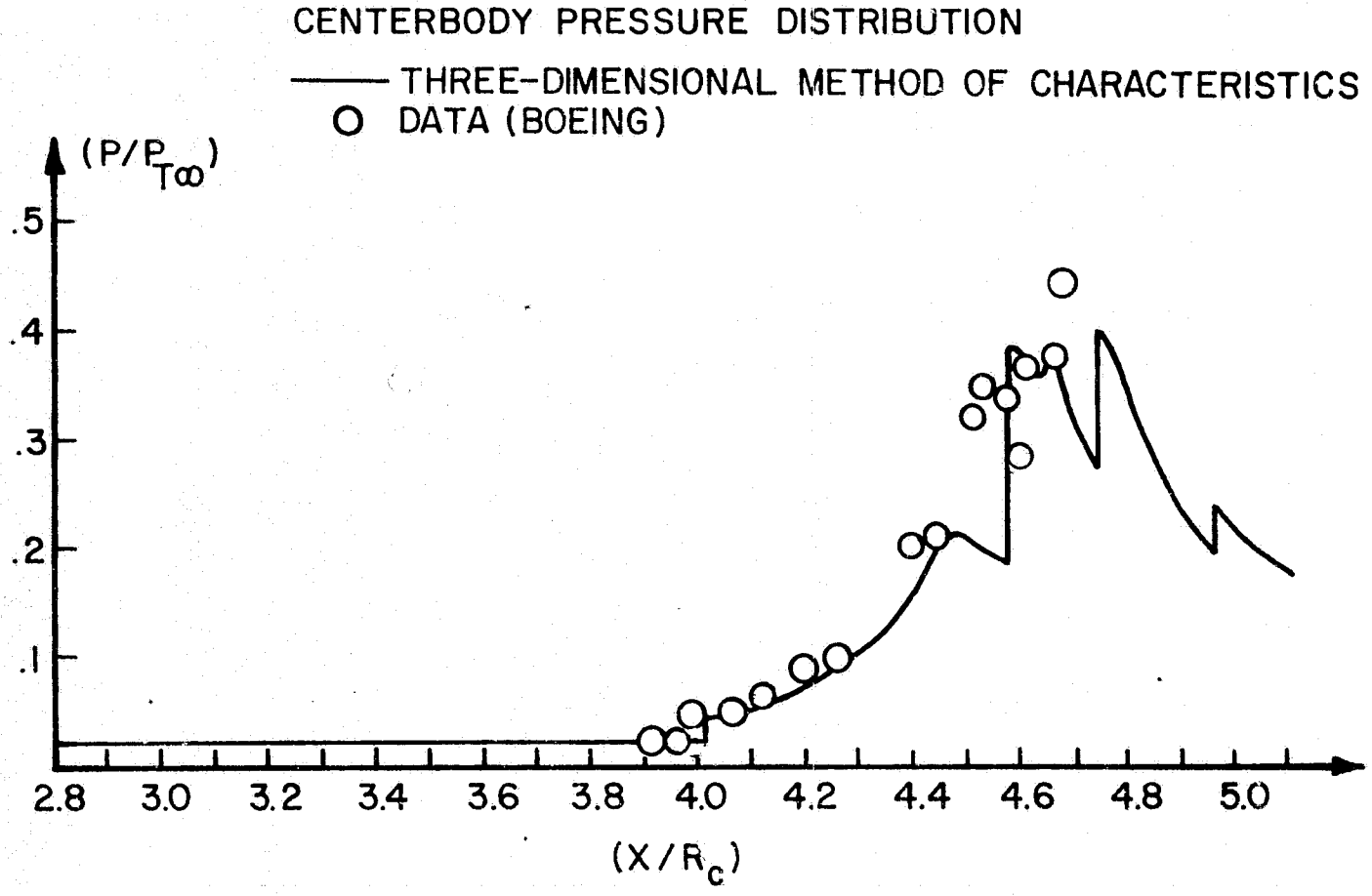

FIGURE 22. COMPARISON OF THE THREE-DIMENSIONAL METHOD OF CHARACTERISTICSWITH EXPERIMENTAL DATA FOR $M_\infty = 3.5$, $\alpha = 0°$, TRANSLATION =0

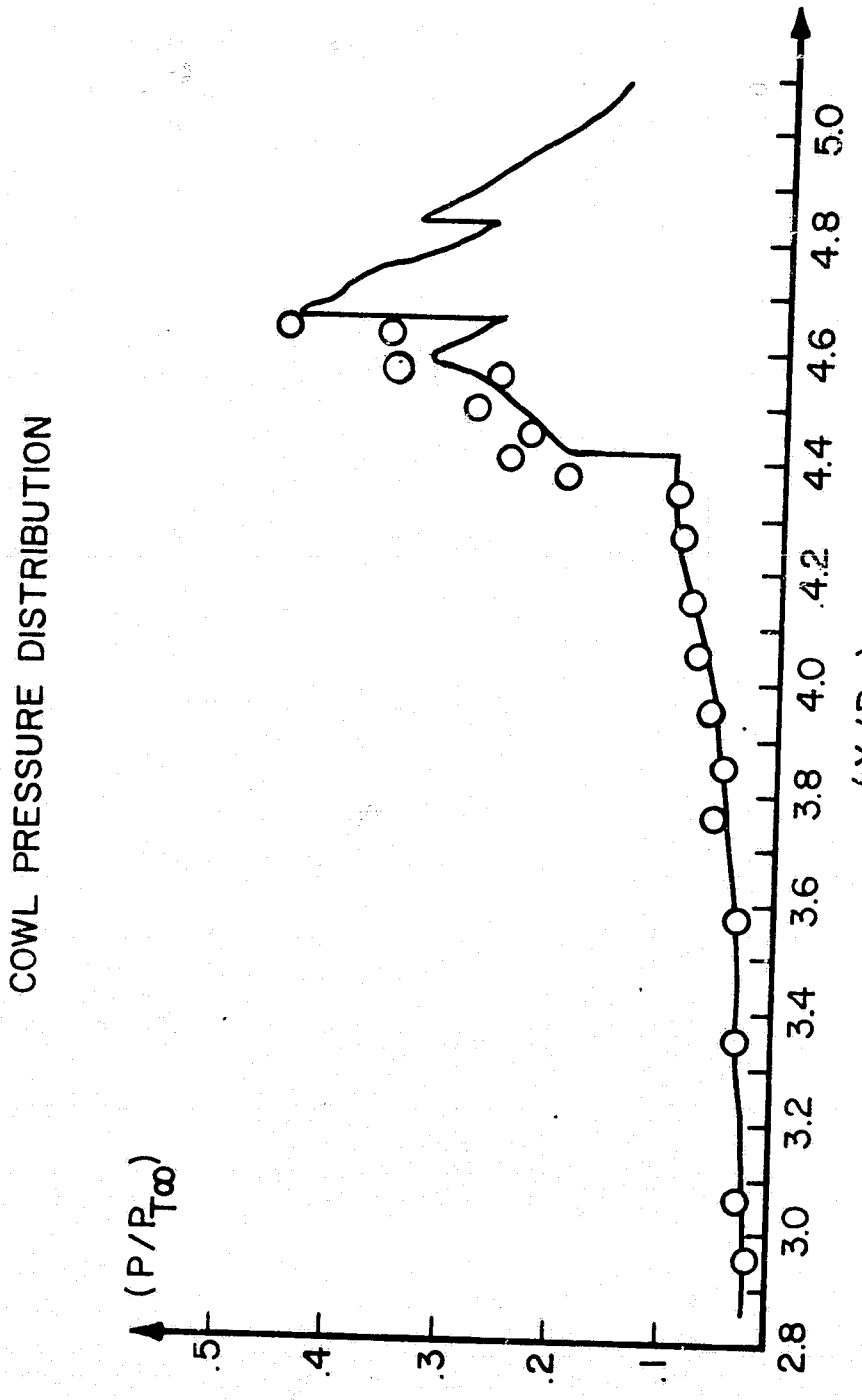

FIGURE 22. (CONTINUED)

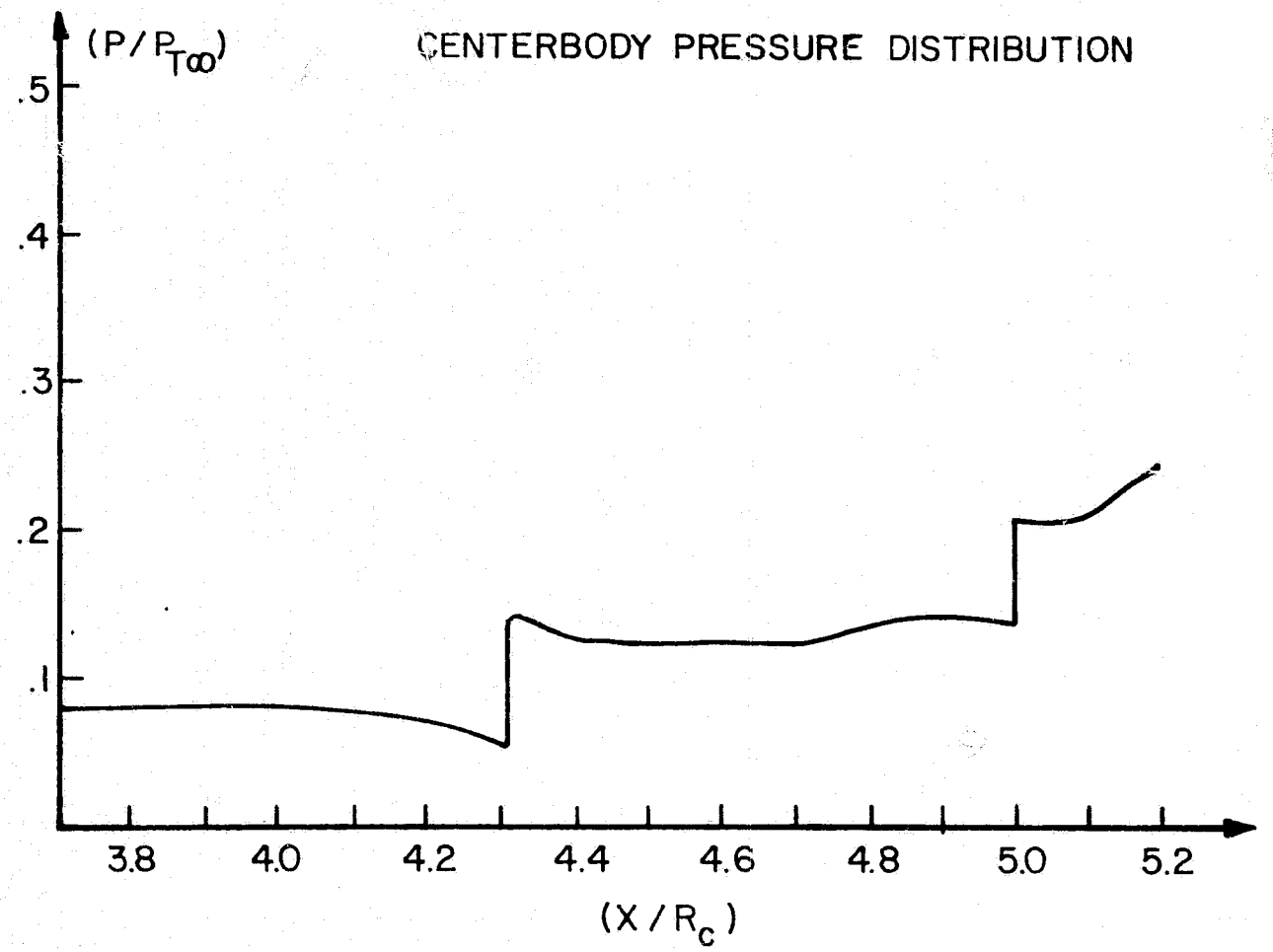

FIGURE 23. THREE-DIMENSIONAL METHOD OF CHARACTERISTICS SOLUTION FOR $M_\infty = 2.5$, $\alpha = 0°$, $\Delta X/R_c = .855$

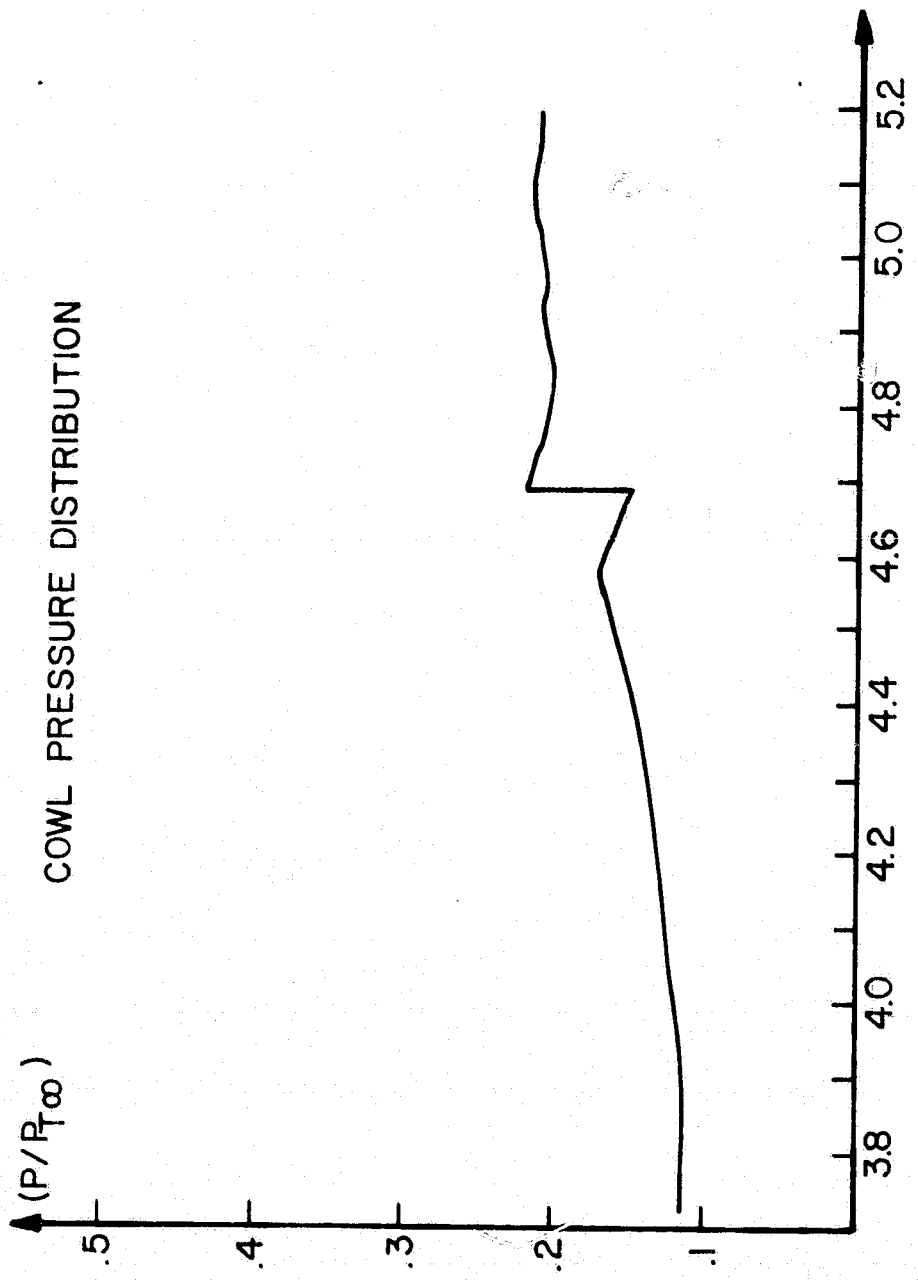

FIGURE 23. (CONTINUED)

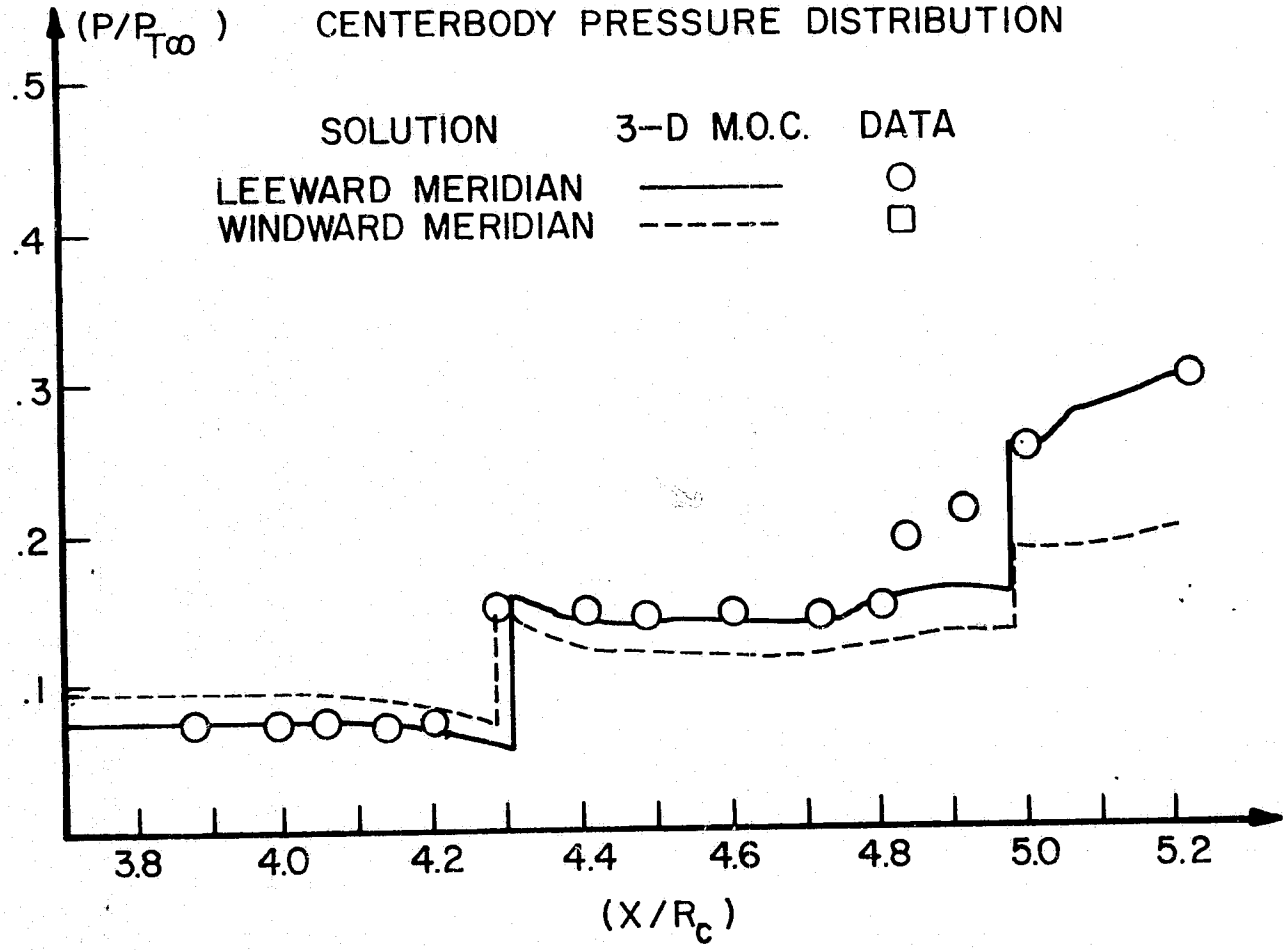

FIGURE 24. COMPARISON OF THREE-DIMENSIONAL METHOD OF CHARACTERISTICS SOLUTION WITH EXPERIMENTAL DATA FOR $M_\infty = 2.5$, $\alpha = 3°$, $\Delta X/R_c = .855$

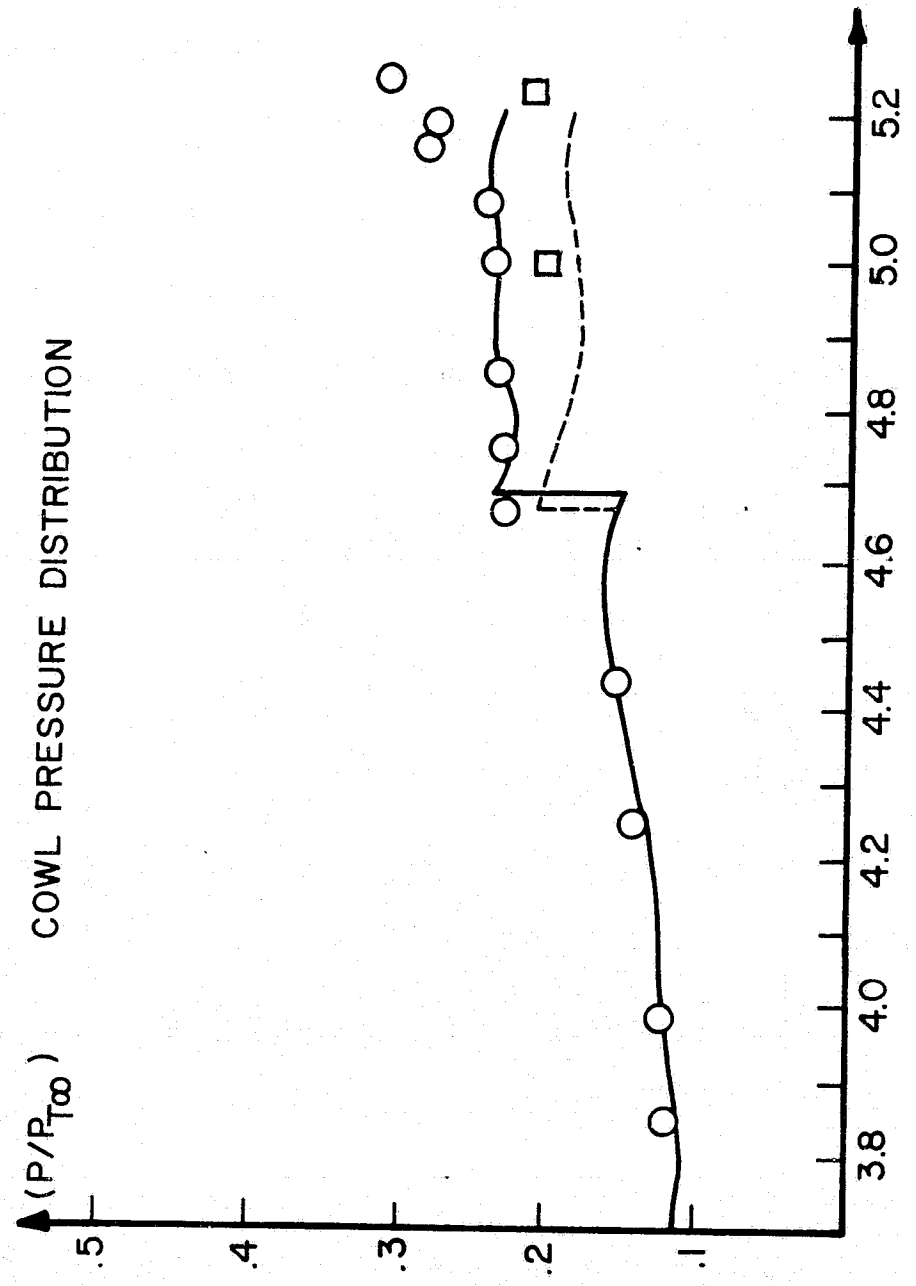

FIGURE 24. (CONTINUED)

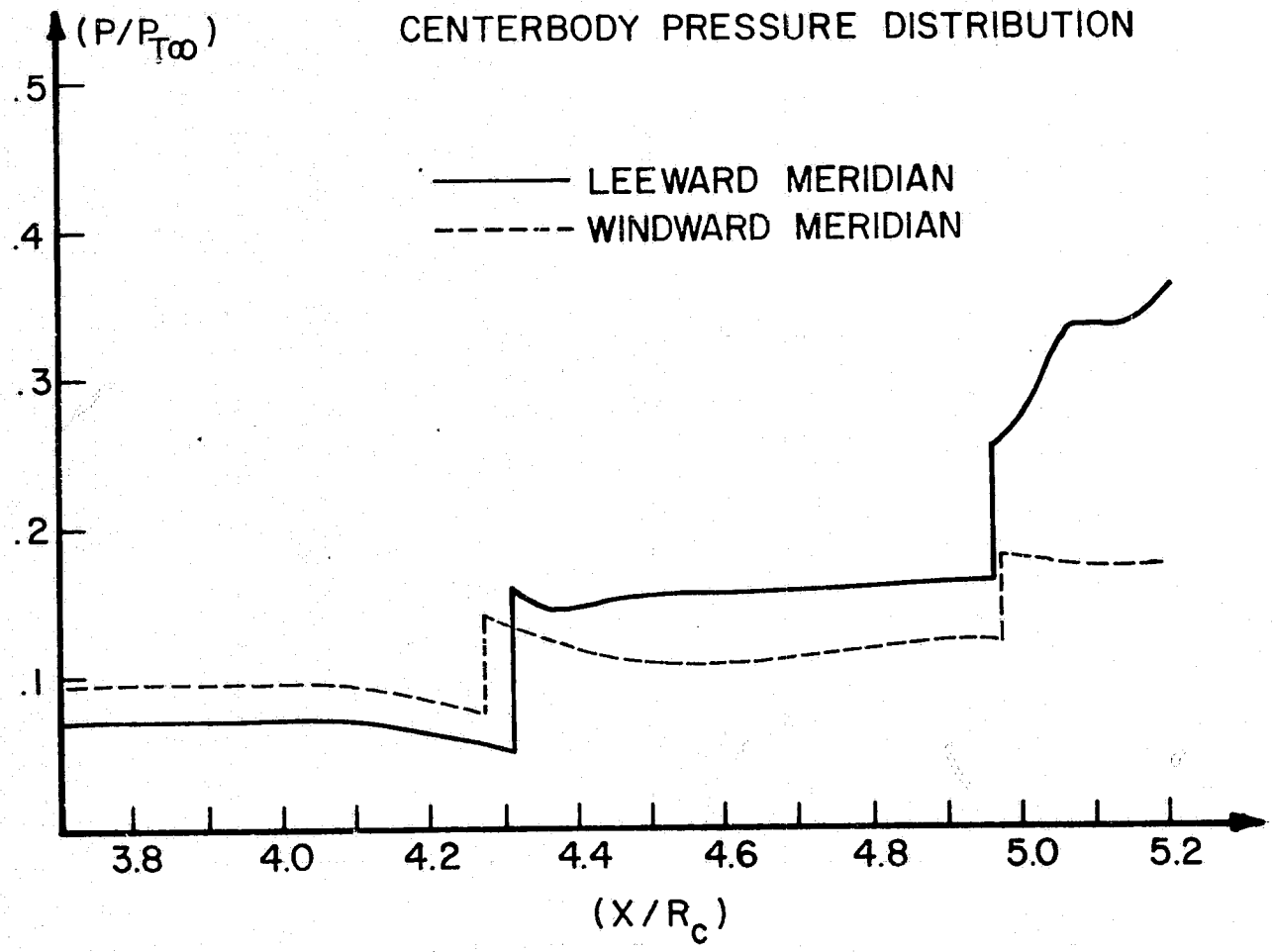

FIGURE 25. THREE-DIMENSIONAL METHOD OF CHARACTERISTICS SOLUTION FOR $M_\infty = 2.5$, $\alpha = 5°$, $\Delta X/R_c = .855$

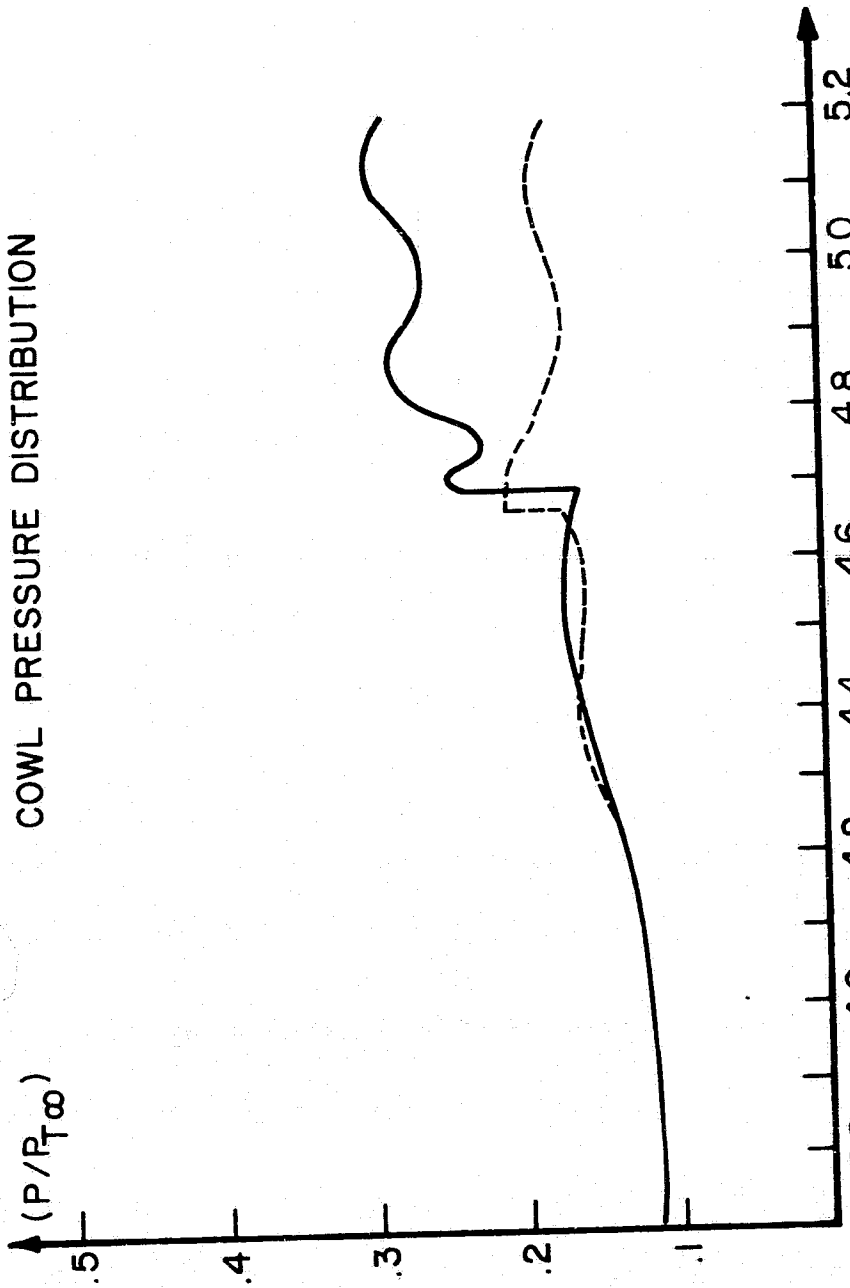

FIGURE 25. (CONTINUED)

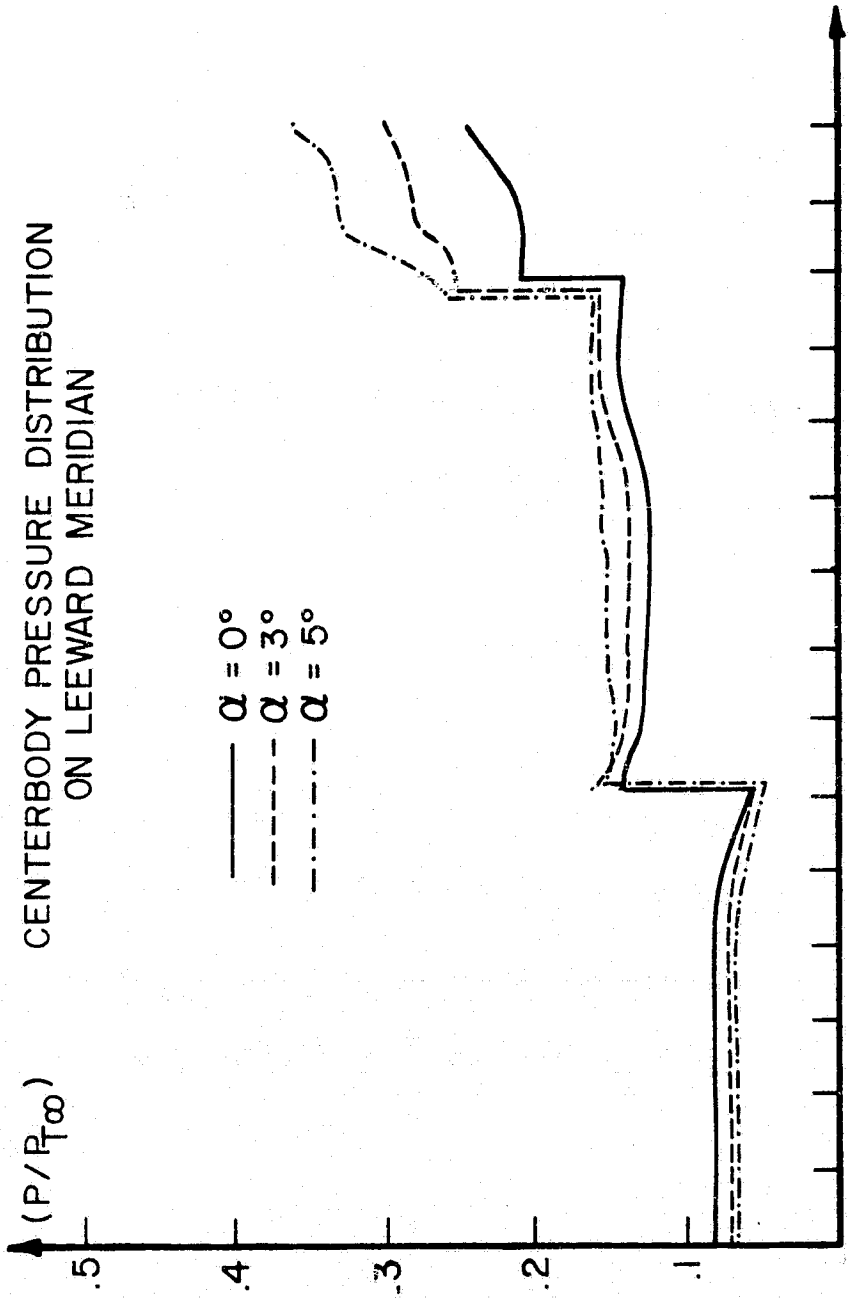

FIGURE 26. COMPUTED CENTERBODY PRESSURE DISTRIBUTIONS FOR $M_\infty = 2.5$, $\Delta X/R_C = .855$ WITH $\alpha = 0°, \alpha = 3°$, AND $\alpha = 5°$

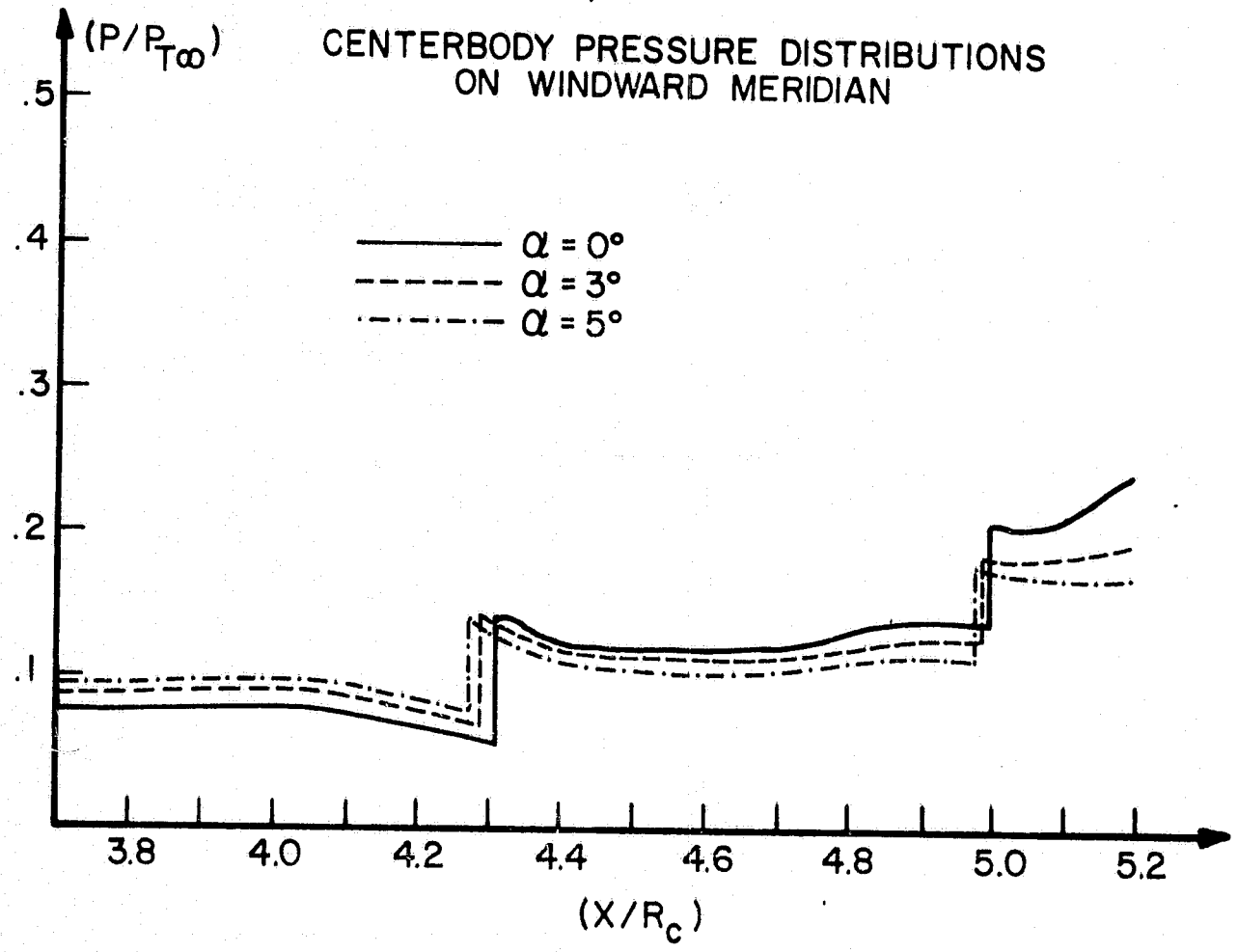

FIGURE 26. (CONTINUED)

to the design point case. Figure 24 illustrates the computed pressure distributions and some experimental data for an incidence angle of α=3.0°. Pressure distributions for the centerbody and the cowl on both the leeward and the windward meridians are shown. Compared to the α=0° case, the strength of the internal shock wave system is increased on the leeward side but reduced on the windward side. Experimental data are presented for the centerbody pressure on the leeward meridian and for the cowl pressure on both the leeward and windward meridians. Generally speaking, good overall agreement between theory and experiment is obtained. For these three-dimensional computations, 21 circumferential stations and 11 radial stations (9 streamline points and an upstream and downstream shock wave point) were employed in the computed sector (half-plane). The maximum deviation of the mass flow rate at any solution plane from the mass flow rate at the cowl lip solution plane for the α=3.0° case was 0.44 percent. The computed pressure distributions on the centerbody and the cowl for both the leeward and windward meridians for the incidence angle of α=5.0° are shown in Figure 25. The leeward meridian shock wave strength has been increased over the α=3.0° case, whereas the shock wave strength on the windward meridian has been reduced. The maximum deviation in mass flow rate for the α=5.0° case was 0.89 percent. Finally, to illustrate the effect of increasing angle of attack on the centerbody pressure distribution, the centerbody results of Figures 23, 24, and 25 are superimposed in Figure 26. The results presented in Figures 23 to 25 are for impermeable wall boundary conditions.

Additional supersonic internal flow results for the Mach 3.5 inlet at other off-design conditions may be found in Reference 1. Comparisons of the present algorithm with the results of the shock-capturing algorithm developed by Presley (33) also may be found in Reference 1. The analysis presented in Reference 33 is based on the use of the explicit MacCormack finite difference operator (34).

Internal flow boundary layer calculations were performed for the Mach 3.5 inlet again for the case of an off-design centerbody translation of $\Delta x/R_C=0.855$. All boundary layer computations were performed for an incidence angle $\alpha=1.0°$, and each computation employed 15 circumferential stations and 20 radial stations in the boundary layer computed sector. Both the forebody/centerbody and cowl boundary layers were determined using impermeable wall boundary conditions. A constant wall temperature boundary condition was employed with the specified wall temperature being equal to the free-stream stagnation temperature. Initial data for the forebody/centerbody boundary layer computation were obtained by application of the Adams algorithm (29). Initial data for the cowl boundary layer compuation were obtained using the approximate technique described in Appendix K.

Initial attempts at computing the internal boundary layers were made assuming entirely laminar flow. The numerical integration algorithm, however, indicated cowl boundary layer separation at an axial distance that was approximately midway between the cowl lip and annulus throat when a purely laminar flow was specified. An ensuing computation was performed specifying transitional flow onset locations slightly downstream of the entrance to the annulus. For the forebody/centerbody boundary layer, the transitional flow onset location was specified at $\tilde{x}/R_C\tilde{=}4.0$. For the cowl boundary layer, the transitional flow onset location was specified at $\tilde{x}/R_C\tilde{=}0.3$. Here, $\tilde{x}$ is the streamwise curvilinear coordinate measured from the forebody tip for the forebody/centerbody boundary layer calcualtion, and measured from the cowl lip for the cowl boundary layer computation.

Computed velocity profiles for the internal flow forebody/centerbody boundary layer calculation are presented in Figure 27. In Figure 27, the streamwise

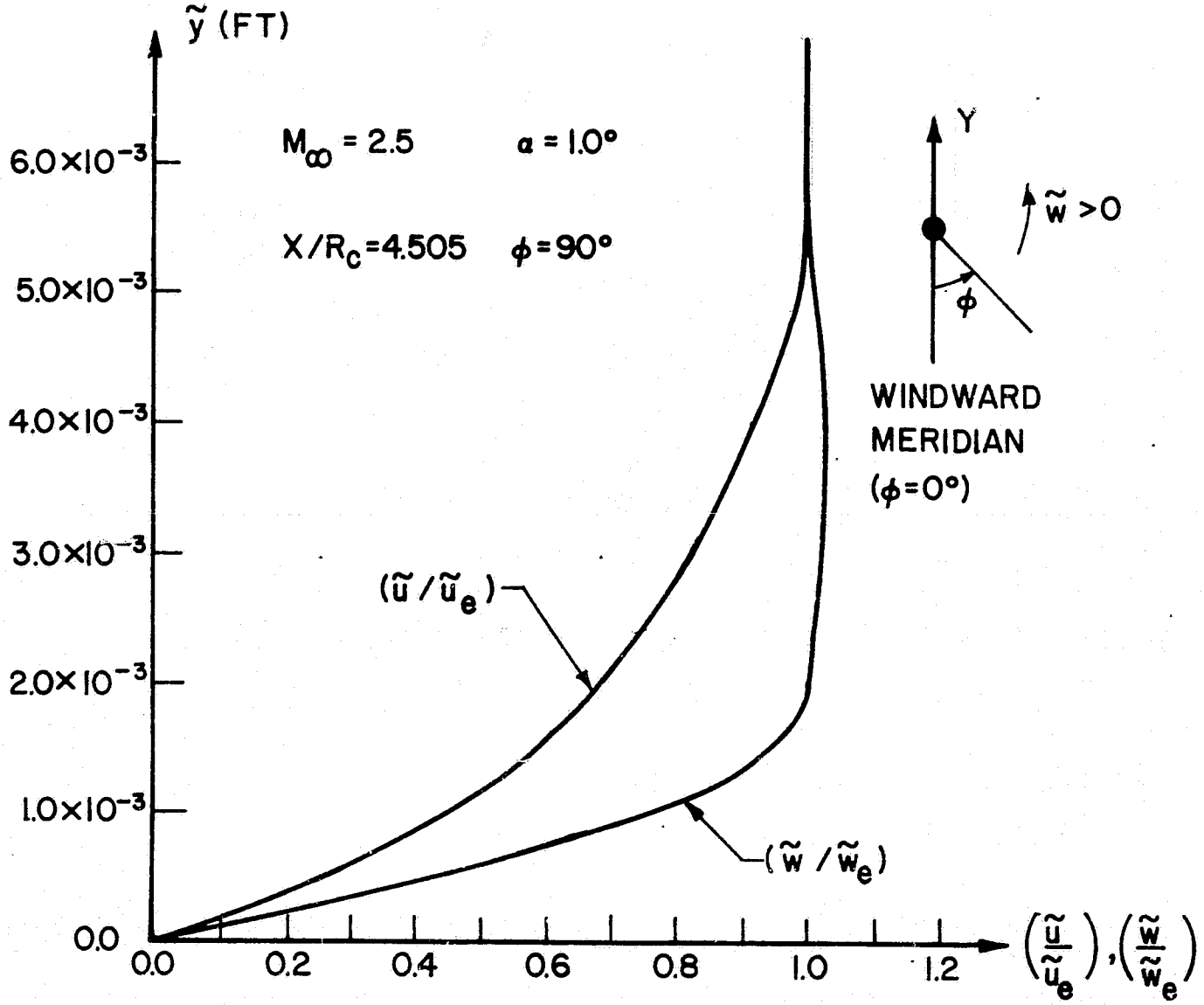

FIGURE 27. CENTERBODY BOUNDARY LAYER VELOCITY PROFILES FOR INTERNAL FLOW.

($\tilde{u}/\tilde{u}_e$) and cross-flow ($\tilde{w}/\tilde{w}_e$) velocity profiles are plotted against the distance $\tilde{y}$ measured normal to the wall. These results are for a boundary layer station that is at the axial location x/R_c=4.505 and at the polar angle ϕ=90° where the angle ϕ is measured from the windward meridian. The corresponding static temperature profile at this location is illustrated in Figure 28.

Computed velocity profiles for the cowl boundary layer calculation are presented in Figure 29 for a station located at x/R_c=4.505 and ϕ=90°. Again, the streamwise and cross-flow velocity profiles are plotted against the normal distance $\tilde{y}$. The corresponding static temperature profile is presented in Figure 30.

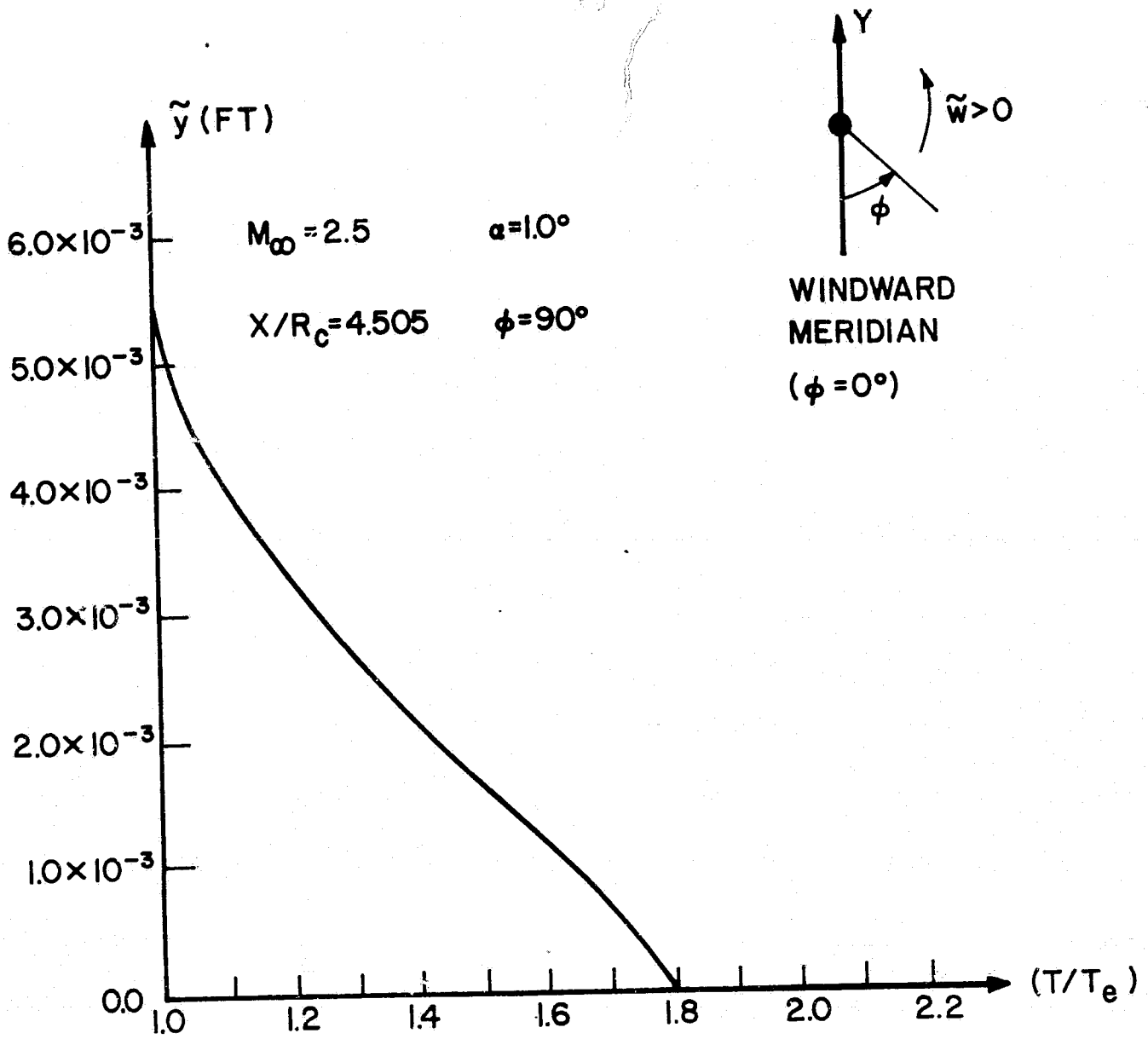

FIGURE 28. CENTERBODY BOUNDARY LAYER STATIC TEMPERATURE PROFILE FOR INTERNAL FLOW.

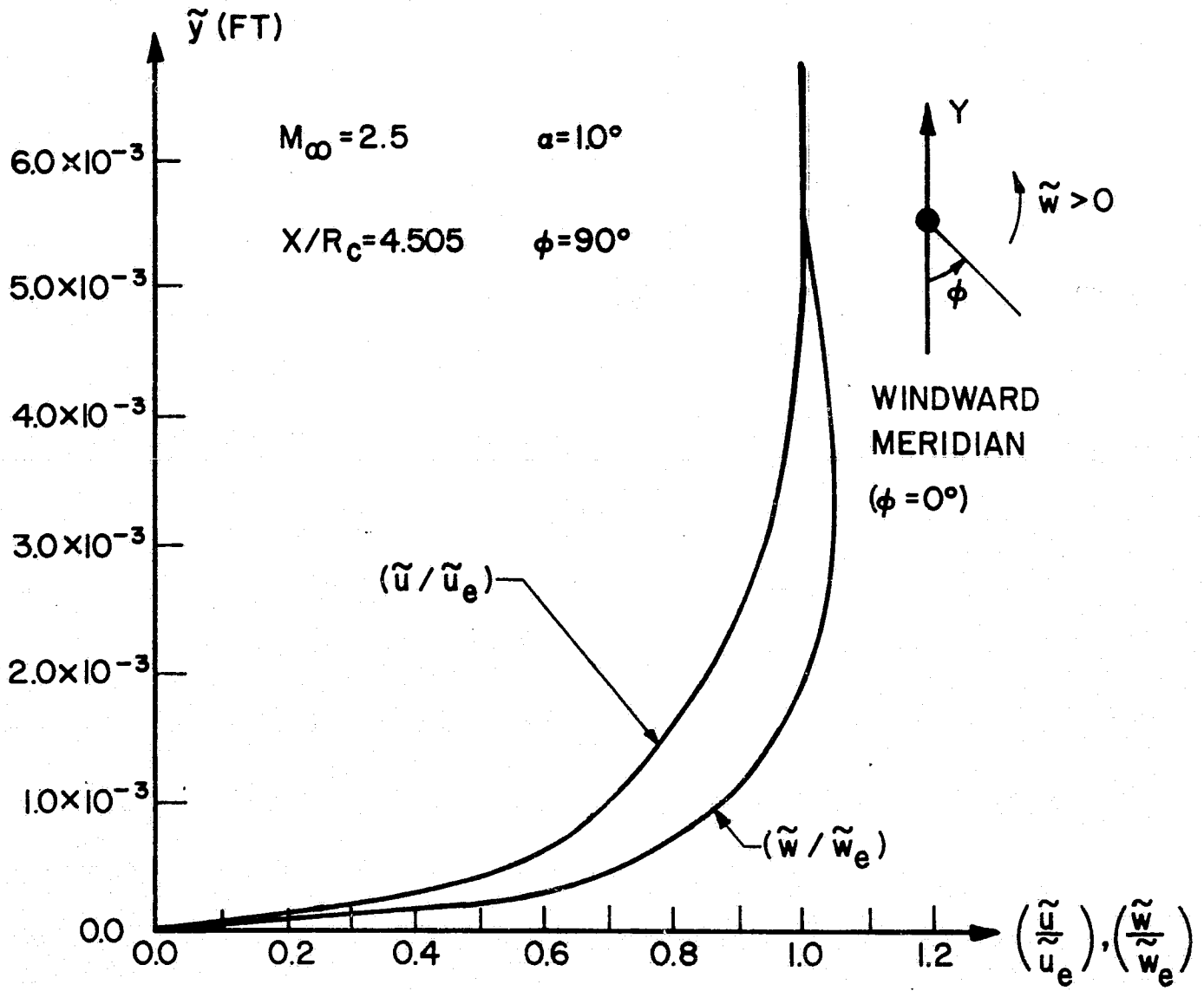

FIGURE 29. COWL BOUNDARY LAYER VELOCITY PROFILES.

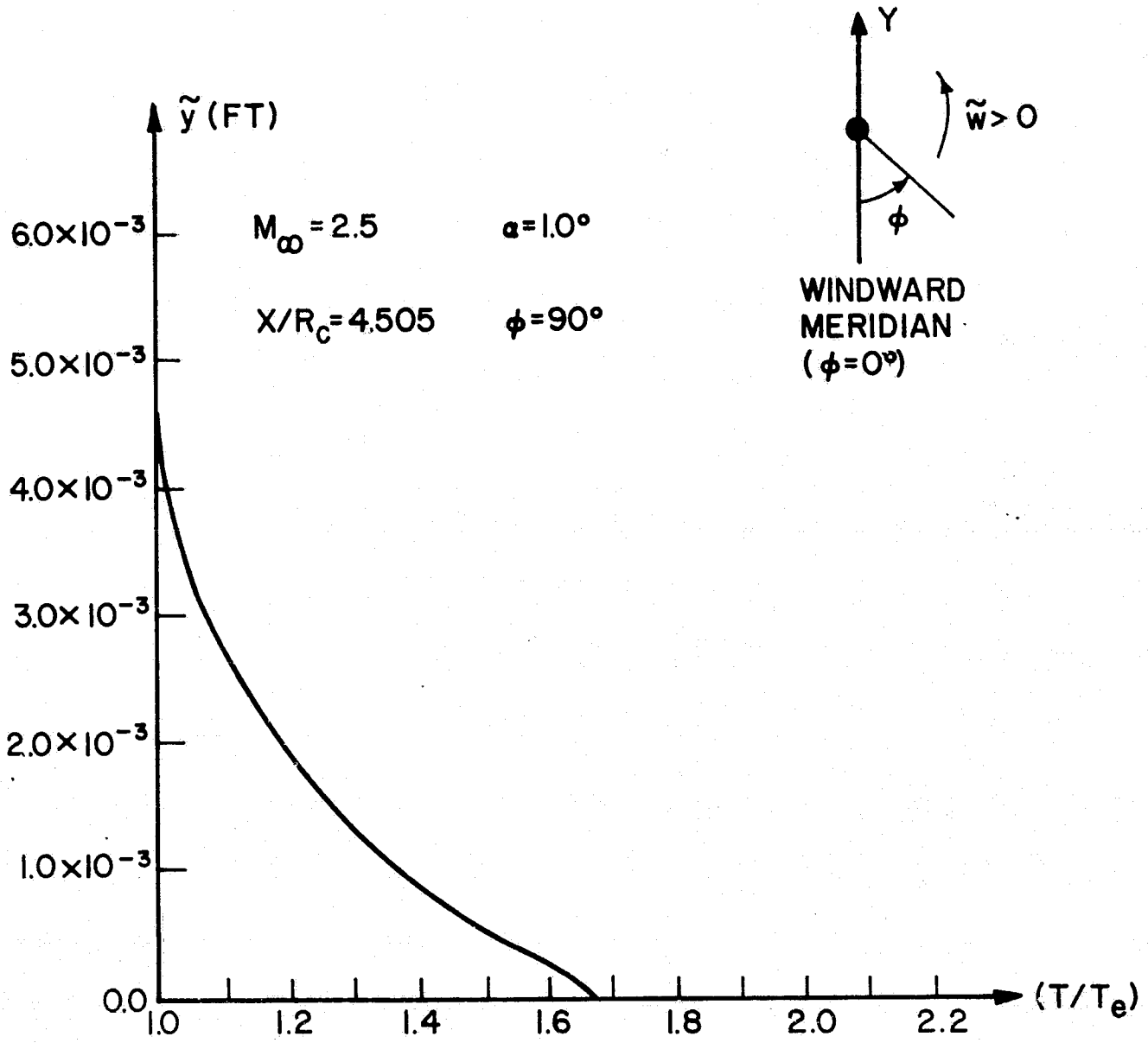

FIGURE 30. COWL BOUNDARY LAYER STATIC TEMPERATURE PROFILE.

SECTION XI

CONCLUSIONS AND RECOMMENDATIONS

The flow field in a supersonic mixed-compression aircraft inlet at non-zero angle of attack has been computed using a zonal solution algorithm which divides the flow field into different computational regimes. The computational regimes consist of a supersonic core flow, boundary layer flows adjacent to both the forebody/centerbody and cowl contours, and flow in the shock wave-boundary layer interaction regions. Separate analyses are used for each of the different computational regions.

The culmination of the present research effort is a production type computer program which has the capability to predict the flow field in a variety of axisymmetric mixed-compression aircraft inlets. A number of conclusions concerning the present analysis can be made:

1. The external flow field about the forebody can be accurately calculated if a bow shock wave of reasonably strong strength exists.
2. For axisymmetric flows, the solution obtained by the present analysis agrees well with the solution obtained by the two-dimensional method of characteristics.
3. Except in the regions of strong viscous interaction, the results of the present analysis agree well with experimental data.

Although the inlets analyzed were axisymmetric inlets, the computer program can be readily modified to analyze geometries which have noncircular cross-sections. Moreover, the inclusion of finite rate chemical reactions

in the thermodynamic model is reasonably straightforward. The analysis can be modified to compute the external flow about a stepped cone and to compute the internal flow when the bow shock wave has been ingested into the annulus.

Recommendations for enhancing the accuracy of the present analysis include improvement of the cowl boundary layer initial-data generation algorithm, refinement of the shock wave-boundary layer interaction region analysis, and incorporation of displacement thickness effects into the supersonic core flow solution.

APPENDIX A

GOVERNING EQUATIONS FOR THE SUPERSONIC CORE FLOW

1. INTRODUCTION

The major assumptions constituting the gas dynamic model for the supersonic core flow are:

1. steady flow
2. negligible body forces
3. thermodynamic equilibrium (i.e., mechanical, thermal, and chemical equilibrium)
4. no mass diffusion
5. negligible radiative heat transfer and no internal heat generation other than viscous dissipation
6. viscous and thermal diffusion effects of secondary importance in determining the solution

The governing equations for the assumed flow model are written in Cartesian coordinates and consist of the continuity equation, the component momentum equations, the energy equation, the thermal and caloric equations of state, and the appropriate representations for the molecular transport properties. These relations are presented in this appendix.

2. DIFFERENTIAL EQUATIONS OF MOTION

The general continuity equation* (3) is

*Repeated indices imply summation over the range of 1 to 3 unless otherwise noted.

$$\frac{D\rho}{Dt} + \rho \frac{\partial u_i}{\partial x_i} = 0 \qquad (A.1)$$

where t denotes time, ρ is the density, x_i (i=1,2,3) denotes the three rectangular coordinates x, y, and z, respectively, and u_i (i=1,2,3) denotes the corresponding velocity components u, v, and w, respectively. The operator D( )/Dt in equation (A.1) is the material derivative given by

$$\frac{D(\ )}{Dt} = \frac{\partial(\ )}{\partial t} + u_j \frac{\partial(\ )}{\partial x_j} \qquad (A.2)$$

For steady three-dimensional flow, equation (A.1) may be written in expanded form as

$$\rho u_x + \rho v_y + \rho w_z + u\rho_x + v\rho_y + w\rho_z = 0 \qquad (A.3)$$

where the subscripts x, y, and z denote partial differention with respect to the corresponding direction.

The appropriate momentum equation is the Navier-Stokes equation (3), which written in component form is

$$\rho \frac{Du_i}{Dt} = B_i - \frac{\partial P}{\partial x_i} + \frac{\partial}{\partial x_j}\left[\mu\left(\frac{\partial u_i}{\partial x_j} + \frac{\partial u_j}{\partial x_i}\right)\right] - \frac{2}{3}\frac{\partial}{\partial x_i}\left(\mu \frac{\partial u_j}{\partial x_j}\right) + \frac{\partial}{\partial x_i}\left(\eta \frac{\partial u_j}{\partial x_j}\right) \qquad (i=1,2,3) \qquad (A.4)$$

where B_i denotes the ith component of the body force, P is the pressure, μ denotes the dynamic viscosity, and η is the second coefficient of viscosity.

A major assumption of the present analysis is that the effects of viscous and thermal diffusion are of secondary importance in determining the solution as compared to the inertial effects. Consistent with this assumption of inertial dominance, the viscous and thermal diffusion terms in the governing differential equations will be treated as forcing or correction terms in the method of characteristic scheme to be presented. In the following, the viscous and thermal transport terms will be placed on the right-hand sides of the respective governing equations. The convective terms will be placed on the left-hand sides, and will be considered as constituting the principal parts of these equations. Thus, writing equation (A.4) with the assumptions of steady flow, negligible body forces, $\eta = 0$ [Stokes's hypothesis (4)]. and inertial dominance gives

$$\rho u_j \frac{\partial u_i}{\partial x_j} + \frac{\partial P}{\partial x_i} = F_i \qquad (i=1,2,3) \qquad (A.5)$$

where

$$F_i = \frac{\partial}{\partial x_j}\left[\mu\left(\frac{\partial u_i}{\partial x_j} + \frac{\partial u_j}{\partial x_i}\right)\right] - \frac{2}{3}\frac{\partial}{\partial x_i}\left(\mu \frac{\partial u_j}{\partial x_j}\right) \qquad (i=1,2,3) \qquad (A.6)$$

Treating the viscosity as a variable, equations (A.5) and (A.6) can be written in expanded form for each of the three coordinate directions as

$$\rho u u_x + \rho v u_y + \rho w u_z + P_x = F_x \qquad (A.7)$$

$$\rho u v_x + \rho v v_y + \rho w v_z + P_y = F_y \qquad (A.8)$$

$$\rho u w_x + \rho v w_y + \rho w w_z + P_z = F_z \qquad (A.9)$$

where

$$F_x = \mu_x\left[\frac{4}{3}u_x - \frac{2}{3}(v_y + w_z)\right] + \mu_y(u_y + v_x) + \mu_z(u_z + w_x)$$
$$+ \mu\left[\frac{4}{3}u_{xx} + u_{yy} + u_{zz} + \frac{1}{3}(v_{xy} + w_{xz})\right] \qquad (A.10)$$

$$F_y = \mu_y\left[\frac{4}{3}v_y - \frac{2}{3}(u_x + w_z)\right] + \mu_x(v_x + u_y) + \mu_z(v_z + w_y)$$
$$+ \mu\left[\frac{4}{3}v_{yy} + v_{xx} + v_{zz} + \frac{1}{3}(u_{yx} + w_{yz})\right] \qquad (A.11)$$

$$F_z = \mu_z\left[\frac{4}{3}w_z - \frac{2}{3}(u_x + v_y)\right] + \mu_x(w_x + u_z) + \mu_y(w_y + v_z)$$
$$+ \mu\left[\frac{4}{3}w_{zz} + w_{xx} + w_{yy} + \frac{1}{3}(u_{zx} + v_{zy})\right] \qquad (A.12)$$

Finally, it remains to obtain an appropriate form of the energy equation. It is assumed in the present analysis that the working gas can be represented as a simple system in thermodynamic equilibrium. Under this assumption the thermodynamic relation (5)

$$Tds = dh - \frac{dP}{\rho} \qquad (A.13)$$

is valid, where T denotes the absolute temperature, s is the entropy per unit mass, and h is the enthalpy per unit mass. For a simple system, specification of any two independent thermodynamic properties defines the thermodynamic state of the system (5). Thus,

$$P = P(\rho,s) \qquad (A.14)$$

Employing the concept of the total derivative, and introducing the material derivative operator given by equation (A.2), the following relation may be obtained from equation (A.14).

$$\frac{DP}{Dt} = \left(\frac{\partial P}{\partial \rho}\right)_s \frac{D\rho}{Dt} + \left(\frac{\partial P}{\partial s}\right)_\rho \frac{Ds}{Dt} \tag{A.15}$$

The sonic speed a is defined by

$$a^2 = \left(\frac{\partial P}{\partial \rho}\right)_s \tag{A.16}$$

Thus, equation (A.15) may be written as

$$\frac{DP}{Dt} - a^2 \frac{D\rho}{Dt} = F_e \tag{A.17}$$

where

$$F_e = \left(\frac{\partial P}{\partial s}\right)_\rho \frac{Ds}{Dt} \tag{A.18}$$

The material derivative of entropy in equation (A.18) may be expressed in terms of a thermal conduction function and a viscous dissipation function. Consider the energy equation in the following form (3).

$$\rho \frac{De}{Dt} = \frac{\partial}{\partial x_i}\left(\kappa \frac{\partial T}{\partial x_i}\right) + \frac{P}{\rho}\frac{D\rho}{Dt} + \Phi \tag{A.19}$$

In equation (A.19), e denotes the internal energy per unit mass, κ is the thermal conductivity, and Φ represents the viscous dissipation function which for $\eta = 0$ is given by

$$\Phi = \frac{1}{2}\mu \left(\frac{\partial u_i}{\partial x_j} + \frac{\partial u_j}{\partial x_i} - \frac{2}{3}\frac{\partial u_k}{\partial x_k}\delta_{ij}\right)^2 \tag{A.20}$$

where δ_{ij} is the Kronecker delta. Using the definition of enthalpy ($h = e + P/\rho$) in equation (A.13) yields

$$Tds = de - \frac{P}{\rho^2} d\rho \tag{A.21}$$

From equation (A.21) the material derivative of internal energy may be written as

$$\frac{De}{Dt} = T \frac{Ds}{Dt} + \frac{P}{\rho^2} \frac{D\rho}{Dt} \tag{A.22}$$

Introducing equation (A.22) into equation (A.19) yields

$$\rho T \frac{Ds}{Dt} = \frac{\partial}{\partial x_i} \left(\kappa \frac{\partial T}{\partial x_i} \right) + \Phi \tag{A.23}$$

Substituting equation (A.23) into equation (A.18) gives

$$F_e = \xi \left[\frac{\partial}{\partial x_i} \left(\kappa \frac{\partial T}{\partial x_i} \right) + \Phi \right] \tag{A.24}$$

where

$$\xi = \frac{1}{\rho T} \left(\frac{\partial P}{\partial s} \right)_\rho \tag{A.25}$$

By treating the thermal conductivity as a variable, and assuming steady three-dimensional flow, equations (A.17) and (A.24) may be written as

$$uP_x + vP_y + wP_z - a^2(u\rho_x + v\rho_y + w\rho_z) = F_e \tag{A.26}$$

where

$$\begin{aligned} F_e = \xi \Big\{ & \kappa(T_{xx} + T_{yy} + T_{zz}) + \kappa_x T_x + \kappa_y T_y + \kappa_z T_z \\ & + \mu \Big[2\left(u_x^2 + v_y^2 + w_z^2 + u_y v_x + u_z w_x + v_z w_y \right) + v_x^2 + w_x^2 \\ & + u_y^2 + w_y^2 + u_z^2 + v_z^2 - \frac{2}{3}(u_x + v_y + w_z)^2 \Big] \Big\} \end{aligned} \tag{A.27}$$

As in the component momentum equations, the viscous and thermal diffusion terms in the energy equation have been placed on the right-hand side and will be treated as forcing functions in the method of characteristics scheme to be presented. The left-hand side is composed of the convective terms which are considered to constitute the principal part of this equation.

3. THERMODYNAMIC MODEL

Before a solution to the system of governing partial differential equations can be obtained, the temperature T, sonic speed a, thermodynamic parameter ξ, viscosity μ, and thermal conductivity κ must be expressed in terms of the dependent variables P and ρ. The representations for T, a, and ξ are discussed in this section. The relations for μ and κ are presented in the next section.

The general functional forms of the temperature T, sonic speed a, and thermodynamic parameter ξ may be expressed as

$$T = T(P,\rho) \tag{A.28}$$

$$a = a(P,\rho) \tag{A.29}$$

$$\xi = \xi(P,\rho) \tag{A.30}$$

For multicomponent systems, with either frozen or equilibrium chemical composition, the functional relationships for T, a, and ξ are obtained from thermochemical calculations. In the case of a thermally and calorically perfect gas, the functional relationships for T, a, and ξ are simple analytical expressions given by

$$T = P/\rho R \tag{A.31}$$

$$a = (\gamma P/\rho)^{1/2} \tag{A.32}$$

$$\xi = \gamma - 1 \tag{A.33}$$

where γ is the specific heat ratio, and R is the gas constant.

In the computer program developed in the present investigation, the temperature, sonic speed, and thermodynamic parameter ξ are calculated in a separate subroutine. The assumed thermodynamic model is that of a thermally and calorically perfect gas, thus, equations (A.31) to (A.33) are employed. Substitution of a replacement subroutine for the existing one allows other thermodynamic models to be specified.

4. TRANSPORT PROPERTIES

Representations are required for the viscosity, the thermal conductivity, and their spatial gradients. Both viscosity and thermal conductivity are functions of temperature and pressure. Hence,

$$\mu = \mu(T,P) \tag{A.34}$$

$$\kappa = \kappa(T,P) \tag{A.35}$$

Using equations (A.34) and (A.35), the spatial derivatives of viscosity and thermal conductivity may be written as

$$\frac{\partial \mu}{\partial x_i} = \left(\frac{\partial \mu}{\partial T}\right)_P \frac{\partial T}{\partial x_i} + \left(\frac{\partial \mu}{\partial P}\right)_T \frac{\partial P}{\partial x_i} \tag{A.36}$$

$$\frac{\partial \kappa}{\partial x_i} = \left(\frac{\partial \kappa}{\partial T}\right)_P \frac{\partial T}{\partial x_i} + \left(\frac{\partial \kappa}{\partial P}\right)_T \frac{\partial P}{\partial x_i} \tag{A.37}$$

Hence, spatial derivatives of pressure and temperature are also required. Spatial derivatives of pressure and density are employed in the basic integration scheme (even for the inviscid flow case). Thus, those derivatives are already available. Spatial derivatives of temperature can be expressed in terms of spatial derivatives of pressure and density by differentiating the thermal equation of state, equation (A.28).

The pressure dependency indicated in equations (A.34) and (A.35) is usually quite weak, and often both the viscosity and the thermal conductivity are assumed to be functions of temperature only. Thus,

$$\mu = \mu(T) \tag{A.38}$$

$$\kappa = \kappa(T) \tag{A.39}$$

The Sutherland formula (4) is a good representation for equation (A.38).

$$\mu = \mu_o \left(\frac{T}{T_o}\right)^{1.5} \left(\frac{T_o + S}{T + S}\right) \tag{A.40}$$

In equation (A.40), μ_o is the viscosity at the reference temperature T_o, and S is a constant. Equation (A.39) can be represented by

$$\kappa = \frac{\mu c_p}{Pr} \tag{A.41}$$

where c_p is the constant pressure specific heat, and Pr is the laminar Prandtl number which is assumed to be constant in the analysis.

In the computer program, the viscosity, the thermal conductivity, and their spatial derivatives are computed in a separate subroutine. The assumed functional forms of viscosity and thermal conductivity are given by equations (A.40) and (A.41), respectively. Different formulations for the transport properties can be implemented into the computer program by supplying an appropriate replacement subroutine.

APPENDIX B

DERIVATION OF THE EQUATIONS FOR THE CHARACTERISTIC SURFACES AND THE COMPATIBILITY RELATIONS

1. INTRODUCTION

Systems of hyperbolic partial differential equations in n independent variables have the property that there exist surfaces in n-space on which linear combinations of the original differential equations can be formed that contain derivatives only in the surfaces themselves. Differentiation in these surfaces is performed in (n-1)-space. The resulting differential operators are interior operators which are known as compatibility relations. The surfaces are called characteristic surfaces. A compatibility relation is valid only when it is applied on its corresponding characteristic surface. Furthermore, data cannot be arbitrarily specified on a characteristic surface, but instead must satisfy the compatibility relation.

The method of characteristics is based on replacing the original system of partial differential equations with an equivalent number of compatibility relations applied on the appropriate characteristic surfaces. In flows with two independent variables, the method of characteristics has the advantage of reducing the solution of a system of partial differential equations to the solution of a system of ordinary differential equations. In three-dimensional flow, however, the resulting compatibility relations are still partial differential equations in two independent directions.

In this appendix, the equations for the characteristic surfaces and the corresponding compatibility relations are derived for steady three-dimensional flow. For a complete discussion of hyperbolic partial differential equations in three independent variables, refer to Courant and Hilbert (15). An excellent presentation of the method of characteristics for three-dimensional flow is given in Zucrow and Hoffman (16).

2. EQUATIONS OF MOTION

The partial differential equations of motion for steady three-dimensional flow consist of the three component momentum equations, the continuity equation, and the energy equation. Those equations are developed in Appendix A, and are repeated below for reference.

$$\rho u u_x + \rho v u_y + \rho w u_z + P_x = F_x \tag{B.1}$$

$$\rho u v_x + \rho v v_y + \rho w v_z + P_y = F_y \tag{B.2}$$

$$\rho u w_x + \rho v w_y + \rho w w_z + P_z = F_z \tag{B.3}$$

$$\rho u_x + \rho v_y + \rho w_z + u\rho_x + v\rho_y + w\rho_z = 0 \tag{B.4}$$

$$uP_x + vP_y + wP_z - a^2(u\rho_x + v\rho_y + w\rho_z) = F_e \tag{B.5}$$

In equations (B.1) to (B.5), u, v, and w denote the x, y, and z components of velocity, respectively, ρ is the density, P is the pressure, a is the sonic speed, and the subscripts x, y, and z denote partial differentiation in the corresponding direction. The nonhomogeneous terms F_x, F_y, F_z, and F_e are the forcing terms in the x, y, and z component momentum equations and the energy equation, respectively. Written in this form, with the left-hand sides constituting the prinicpal

parts, equations (B.1) to (B.5) may be classified as a system of quasi-linear nonhomogeneous partial differential equations of first order. The system is hyperbolic (i.e., has real characteristic surfaces) if the flow is supersonic.

3. CHARACTERISTIC SURFACES

The general compatibility relation, which is a linear combination of the governing partial differential equations, is formed by multiplying equations (B.1) to (B.5) by the arbitrary variables ω_i (i=1 to 5), respectively, and summing. This yields

$$\omega_1(\rho u u_x + \rho v u_y + \rho w u_z + P_x) + \omega_2(\rho u v_x + \rho v v_y + \rho w v_z + P_y)$$
$$+ \omega_3(\rho u w_x + \rho v w_y + \rho w w_z + P_z) + \omega_4(\rho u_x + \rho v_y + \rho w_z$$
$$+ u\rho_x + v\rho_y + w\rho_z) + \omega_5[uP_x + vP_y + wP_z$$
$$- a^2(u\rho_x + v\rho_y + w\rho_z)] = \omega_1 F_x + \omega_2 F_y + \omega_3 F_z + \omega_5 F_e \qquad (B.6)$$

Equation (B.6) may be written as

$$\rho(u\omega_1 + \omega_4)u_x + \rho v\omega_1 u_y + \rho w\omega_1 u_z + \rho u\omega_2 v_x + \rho(v\omega_2 + \omega_4)v_y$$
$$+ \rho w\omega_2 v_z + \rho u\omega_3 w_x + \rho v\omega_3 w_y + \rho(w\omega_3 + \omega_4)w_z$$
$$+ (\omega_1 + u\omega_5)P_x + (\omega_2 + v\omega_5)P_y + (\omega_3 + w\omega_5)P_z$$
$$+ u(\omega_4 - a^2\omega_5)\rho_x + v(\omega_4 - a^2\omega_5)\rho_y + w(\omega_4 - a^2\omega_5)\rho_z$$
$$= \omega_1 F_x + \omega_2 F_y + \omega_3 F_z + \omega_5 F_e \qquad (B.7)$$

By noting the coefficients of the partial derivatives in equation (B.7), the following vectors may be defined.

$$\overline{W}_1 = [\rho(u\omega_1 + \omega_4),\ \rho v\omega_1,\ \rho w\omega_1] \tag{B.8}$$

$$\overline{W}_2 = [\rho u\omega_2,\ \rho(v\omega_2 + \omega_4),\ \rho w\omega_2] \tag{B.9}$$

$$\overline{W}_3 = [\rho u\omega_3,\ \rho v\omega_3,\ \rho(w\omega_3 + \omega_4)] \tag{B.10}$$

$$\overline{W}_4 = [(\omega_1 + u\omega_5),\ (\omega_2 + v\omega_5),\ (\omega_3 + w\omega_5)] \tag{B.11}$$

$$\overline{W}_5 = [u(\omega_4 - a^2\omega_5),\ v(\omega_4 - a^2\omega_5),\ w(\omega_4 - a^2\omega_5)] \tag{B.12}$$

The directional derivative of a function f in some direction $\overline{\ell} = (\ell_x, \ell_y, \ell_z)$ is given by

$$\frac{df}{d\ell} = \ell_x \frac{\partial f}{\partial x} + \ell_y \frac{\partial f}{\partial y} + \ell_z \frac{\partial f}{\partial z} \tag{B.13}$$

By considering equations (B.8) to (B.13), equation (B.7) may be written as

$$\frac{du}{dW_1} + \frac{dv}{dW_2} + \frac{dw}{dW_3} + \frac{dP}{dW_4} + \frac{d\rho}{dW_5} = \omega_1 F_x + \omega_2 F_y + \omega_3 F_z + \omega_5 F_e \tag{B.14}$$

where du/dW_1 is the directional derivative of u in the $\overline{W}_1$ direction, etc.

On a characteristic surface, equation (B.14) reduces to an interior operator, that is, differentiation takes place in the surface itself. For this to occur, the vectors $\overline{W}_i$ (i=1 to 5) must all lie in the elemental plane which is tangent to the characteristic surface at the point in consideration. This means that the vectors $\overline{W}_i$ (i=1 to 5) are

linearly dependent. Let the normal to the characteristic surface be denoted by $\overline{N} = (N_x, N_y, N_z)$. Hence, on the characteristic surface

$$\overline{N} \cdot \overline{W}_i = 0 \qquad (i=1 \text{ to } 5) \tag{B.15}$$

Equation (B.15) yields five linear homogeneous equations which may be written in matrix form as follows

$$\begin{bmatrix} \rho U & 0 & 0 & \rho N_x & 0 \\ 0 & \rho U & 0 & \rho N_y & 0 \\ 0 & 0 & \rho U & \rho N_z & 0 \\ N_x & N_y & N_z & 0 & U \\ 0 & 0 & 0 & U & -a^2 U \end{bmatrix} \begin{bmatrix} \omega_1 \\ \omega_2 \\ \omega_3 \\ \omega_4 \\ \omega_5 \end{bmatrix} = 0 \tag{B.16}$$

where

$$U = uN_x + vN_y + wN_z \tag{B.17}$$

Since the system given by equation (B.16) is homogeneous, a nontrivial solution exits only if the coefficient matrix is singular, which means its determinant must be zero. Evaluating the determinant and equating it to zero yields

$$(\rho U)^3 \left[U^2 - a^2(N_x^2 + N_y^2 + N_z^2)\right] = 0 \tag{B.18}$$

Equation (B.18) is the characteristic equation for the original system of equations, equations (B.1) to (B.5). The form of equation (B.18) is that of a repeated linear factor and a quadratic factor.

Equating the two factors in equation (B.18) to zero yields the equations of two real nonintersecting cones formed by the envelope of the characteristic normals at a point. Setting the linear factor in equation (B.18) to zero gives (the case of $\rho = 0$ is immediately dismissed)

$$uN_x + vN_y + wN_z = 0 \tag{B.19}$$

Equation (B.19) represents a degenerate cone formed by the envelope of characteristic normals at a point, each normal being orthogonal to the local velocity vector. Hence, equation (B.19) represents a plane normal to a streamline. The characteristic surface is the reciprocal cone to this degenerate cone of normals, and, hence, is also degenerate, consisting of line segments tangent to the streamlines. Characteristic surfaces with normal components satisfying equation (B.19) are called stream surfaces. The envelope of all stream surfaces at a point is a single pencil of planes whose axis is a streamline. A streamline may be represented by the following equations

$$dx/dt = u \qquad dy/dt = v \qquad dz/dt = w \tag{B.20}$$

where t is the time of travel of a fluid particle along the streamline.

Equating the quadratic factor in equation (B.18) to zero gives

$$(uN_x + vN_y + wN_z)^2 - a^2(N_x^2 + N_y^2 + N_z^2) = 0 \tag{B.21}$$

Equation (B.21) represents the quadric surface of a right circular cone formed by the envelope of characteristic normals at a point. In gas dynamics this cone is usually referred to as the cone of normals, and is a real cone if $q > a$, where q is the velocity magnitude. Equation (B.21) may be written as

$$un_x + vn_y + wn_z = a \tag{B.22}$$

where $\hat{n} = (n_x, n_y, n_z)$ is the unit normal to the characteristic surface. Equation (B.22) was obtained by arbitrarily selecting the positive root, and the results which follow are consistent with that selection. Characteristic surfaces whose normal components satisfy equation (B.21), or equation (B.22), are called wave surfaces.

Equation (B.21) is the equation for the cone of normals, which is a quadric surface. In general, a quadric surface may be expressed as*

$$A_{ij}dx_i dx_j = 0 \tag{B.23}$$

where x_i (i=1,2,3) denotes the three cartesian coordinates x, y, and z, respectively, and A is a nine element coefficient matrix of order two. A normal vector is a directed line segment, so

$$N_i = \sigma\, dx_i \qquad (i=1,2,3) \tag{B.24}$$

where N_i is the ith component of the normal vector, and σ is a constant proportional to the length of the normal. By considering equations (B.23) and (B.24), equation (B.21) may be written as

$$(u_i u_j - a^2\delta_{ij})dx_i dx_j = 0 \tag{B.25}$$

where u_i (i=1,2,3) denotes the three velocity components u, v, and w, respectively, and δ_{ij} is the Kronecker delta.

---

*Repeated indices imply summation over the range of 1 to 3 unless otherwise noted.

The characteristic cone, which is the envelope of all wave surfaces at a point, is the reciprocal cone to the cone of normals given by equation (B.21), or equation (B.25). The geometrical relationship between these surfaces is shown in Figure B.1. If the general form of the equation of the cone of normals is given by equation (B.23), then the reciprocal cone is given by (9)

$$A^{-1}_{ij} dx_i dx_j = 0 \tag{B.26}$$

where A^{-1} is the inverse of the nine element symmetric matrix A in equation (B.23). Using equation (B.25) to determine A from which A^{-1} may be determined, equation (B.26) for the characteristic cone may be written as

$$[u_i u_j - (q^2 - a^2)\delta_{ij}]dx_i dx_j = 0 \tag{B.27}$$

Equation (B.27) represents a real cone if $q > a$. Writing equation (B.27) in expanded form yields

$$[u^2 - (q^2 - a^2)]dx^2 + [v^2 - (q^2 - a^2)]dy^2 + [w^2 - (q^2 - a^2)]dz^2$$

$$+ 2uv(dx)(dy) + 2uw(dx)(dz) + 2vw(dy)(dz) = 0 \tag{B.28}$$

The characteristic cone given by equation (B.28) is known as the Mach cone and represents the envelope of all wave surfaces at a point. The line of tangency between a partricular wave surface and the Mach cone is known as a bicharacteristic. Integration of equation (B.28) gives the curved cone known as the Mach conoid.

In summary, for steady three-dimensional flow there are two families of characteristic surfaces: stream surfaces and wave surfaces

FIGURE B.I. RELATION BETWEEN THE CONE OF NORMALS AND THE CHARACTERISTIC CONE (MACH CONE)

(see Figure B.2). The normal to a stream surface must satisfy equation (B.19), and, hence, the stream surface contains the local velocity vector. The envelope of all stream surfaces at a point is the streamline through the point. The normal to a wave surface must satisfy equation (B.21). The envelope of all wave surfaces at a point is the Mach cone. The line of contact between a particular wave surface and the Mach cone is called a bicharacteristic. At any point there are an infinite number of stream surfaces and wave surfaces.

4. SOLUTION FOR THE ω_i

On a characteristic surface, equation (B.14) reduces to an interior operator, that is, it becomes a compatibility relation. To obtain the exact form of the compatibility relation, the ω_i (i=1 to 5) must be determined.

For a stream surface, equation (B.19), repeated below, is valid.

$$uN_x + vN_y + wN_z = U = 0 \tag{B.19}$$

Substitution of equation (B.19) into the homogeneous system given by equation (B.16) yields

$$\begin{bmatrix} 0 & 0 & 0 & \rho N_x & 0 \\ 0 & 0 & 0 & \rho N_y & 0 \\ 0 & 0 & 0 & \rho N_z & 0 \\ N_x & N_y & N_z & 0 & 0 \\ 0 & 0 & 0 & 0 & 0 \end{bmatrix} \begin{bmatrix} \omega_1 \\ \omega_2 \\ \omega_3 \\ \omega_4 \\ \omega_5 \end{bmatrix} = 0 \tag{B.29}$$

FIGURE B.2. CHARACTERISTIC SURFACES

The coefficient matrix in equation (B.29) is rank two (rank is the number of nonzero rows in the row echelon form of a matrix). The number of independent nontrivial solutions for the ω_i is equal to the order of the coefficient matrix minus its rank, and hence, in this case, is three. From equation (B.29), $\omega_4 = 0$ for all solutions, ω_5 is arbitrary, while ω_1, ω_2, ω_3 satisfy the following equation.

$$\omega_1 N_x + \omega_2 N_y + \omega_3 N_z = 0 \tag{B.30}$$

A set of three possible solutions is

$$\omega_1 = \omega_2 = \omega_3 = \omega_4 = 0, \qquad \omega_5 = 1 \tag{B.31}$$

$$\omega_1 = u, \quad \omega_2 = v, \quad \omega_3 = w, \quad \omega_4 = \omega_5 = 0 \tag{B.32}$$

$$\omega_1 = S_x, \quad \omega_2 = S_y, \quad \omega_3 = S_z, \quad \omega_4 = \omega_5 = 0 \tag{B.33}$$

The vector $\overline{S} = (S_x, S_y, S_z)$ in equation (B.33) lies in the stream surface and is independent of the velocity vector.

On a wave surface, equation (B.21) is valid. That equation may be written as

$$U = a|\overline{N}| \tag{B.34}$$

where $|\overline{N}|$ is the magnitude of the normal to the wave surface. Substituting equation (B.34) into equation (B.16) yields

$$\begin{bmatrix} \rho a|\bar{N}| & 0 & 0 & \rho N_x & 0 \\ 0 & \rho a|\bar{N}| & 0 & \rho N_y & 0 \\ 0 & 0 & \rho a|\bar{N}| & \rho N_z & 0 \\ N_x & N_y & N_z & 0 & a|\bar{N}| \\ 0 & 0 & 0 & a|\bar{N}| & -a^3|\bar{N}| \end{bmatrix} \begin{bmatrix} \omega_1 \\ \omega_2 \\ \omega_3 \\ \omega_4 \\ \omega_5 \end{bmatrix} = 0 \qquad \text{(B.35)}$$

The coefficient matrix in equation (B.35) is rank four, and, hence, one independent nontrivial solution exists for the ω_i. The solutions for ω_1, ω_2, ω_3, and ω_5 may be expressed in terms of ω_4. Arbitrarily selecting $\omega_4 = -1$ yields

$$\omega_1 = n_x/a, \quad \omega_2 = n_y/a, \quad \omega_3 = n_z/a, \quad \omega_4 = -1,$$

$$\omega_5 = -1/a^2 \qquad \text{(B.36)}$$

where $\hat{n} = (n_x, n_y, n_z)$ is the unit normal to the wave surface.

5. COMPATIBILITY RELATIONS

The compatibility relations are obtained by substituting the solutions for the ω_i into equation (B.6). The compatibility relations valid along the stream surfaces are obtained by substituting equations (B.31) to (B.33) into equation (B.6). The results are

$$uP_x + vP_y + wP_z - a^2(u\rho_x + v\rho_y + w\rho_z) = F_e \qquad \text{(B.37)}$$

$$\rho u(uu_x + vu_y + wu_z) + \rho v(uv_x + vv_y + wv_z) + \rho w(uw_x + vw_y + ww_z) + uP_x + vP_y + wP_z = uF_x + vF_y + wF_z \quad (B.38)$$

$$\rho S_x(uu_x + vu_y + wu_z) + \rho S_y(uv_x + vv_y + wv_z) + \rho S_z(uw_x + vw_y + ww_z) + S_xP_x + S_yP_y + S_zP_z = S_xF_x + S_yF_y + S_zF_z \quad (B.39)$$

Note that equation (B.37) is the same as equation (B.5), which shows that the energy equation is characteristic to begin with.

Equations (B.37) and (B.38) may be written in a form that represents differentiation in the streamline direction only. From equation (B.13), noting that for a streamline $\ell_x = u$, $\ell_y = v$, and $\ell_z = w$, the directional derivative along a streamline is given by

$$\frac{d(\ )}{dt} = u\frac{\partial(\ )}{\partial x} + v\frac{\partial(\ )}{\partial y} + w\frac{\partial(\ )}{\partial z} \quad (B.40)$$

where t is the time of travel of a fluid particle along the streamline. Using equation (B.40), equations (B.37) and (B.38) may be rewritten as

$$\frac{dP}{dt} - a^2\frac{d\rho}{dt} = F_e \quad (B.41)$$

$$\rho u\frac{du}{dt} + \rho v\frac{dv}{dt} + \rho w\frac{dw}{dt} + \frac{dP}{dt} = uF_x + vF_y + wF_z \quad (B.42)$$

The compatibility equation that is valid along wave surfaces is obtained by substituting equation (B.36) into equation (B.6). The result is

$$\rho a n_x(uu_x + vu_y + wu_z) + \rho a n_y(uv_x + vv_y + wv_z)$$

$$+ \rho a n_z(uw_x + vw_y + ww_z) + (an_x - u)P_x + (an_y - v)P_y$$

$$+ (an_z - w)P_z - \rho a^2(u_x + v_y + w_z) = \lambda \qquad (B.43)$$

where

$$\lambda = a(n_x F_x + n_y F_y + n_z F_z) - F_e \qquad (B.44)$$

Equation (B.43) may be written in a form that contains differentiation in the bicharacteristic direction. A bicharacteristic is a ray or generator of the Mach cone. The Mach cone is the reciprocal cone to the cone of normals (see Figure B.1). As a consequence, a bicharacteristic is orthogonal to the surface of the cone of normals. The equation for the cone of normals is given by equation (B.21). Substitution of equation (B.24) into equation (B.21) yields the equation for the surface of the cone of normals in standard form [$f(x,y,z)$ = constant]. Differentiation of this expression to obtain the gradient yields the direction of the bicharacteristic. This gives $\ell_x = (u - an_x)$, $\ell_y = (v - an_y)$, and $\ell_z = (w - an_z)$ in equation (B.13), so that differentiation in the bicharacteristic direction is given by

$$\frac{d(\ )}{dt} = (u - an_x)\frac{\partial(\ )}{\partial x} + (v - an_y)\frac{\partial(\ )}{\partial y} + (w - an_z)\frac{\partial(\ )}{\partial z} \qquad (B.45)$$

In equation (B.45), t is the time of travel of a fluid particle along the streamline that is the axis of the Mach cone. The relationship between the vectors $\overline{\ell}$, $\overline{V}$, and $\hat{n}$ is shown in Figure B.3.

ORIGINAL PAGE IS
OF POOR QUALITY

FIGURE B.3. RELATIONSHIP BETWEEN VECTORS $\bar{l}, \hat{n}$, and $\bar{V}$

The term

$$\pm\{\rho a^2[n_x^2 u_x + n_y^2 v_y + n_z^2 w_z + (u_y + v_x)n_x n_y + (u_z + w_x)n_x n_z + (v_z + w_y)n_y n_z]\}$$

may be added to and subtracted from equation (B.43), and then by employing equation (B.45) the following form of the wave surface compatibility relation may be obtained.

$$\rho a n_x \frac{du}{dt} + \rho a n_y \frac{dv}{dt} + \rho a n_z \frac{dw}{dt} - \frac{dP}{dt} = \lambda - \rho a^2[(n_x^2 - 1)u_x + (n_y^2 - 1)v_y + (n_z^2 - 1)w_z + n_x n_y(u_y + v_x) + n_x n_z(u_z + w_x) + n_y n_z(v_z + w_y)] \qquad (B.46)$$

The terms in brackets in equation (B.46) are known as cross derivatives and represent differentiation in the wave surface in a direction normal to the bicharacteristic direction.

Equations (B.29) and (B.35) determine the number of independent differential compatibility relations valid along a particular stream surface and a particular wave surface, respectively. At any point there exist an infinite number of stream surfaces and wave surfaces. However, the number of independent compatibility relations cannot exceed the number of independent equations of motion. Hence, it is necessary to determine which of the possible combinations of compatibility relations are independent. Rusanov (6), using a proof in the space of characteristic normals, has shown that for steady three-dimensional isentropic flow two of the stream surface compatibility relations and

the single wave surface compatibility relation applied along three different wave surfaces form an independent set of characteristic equations. Rusanov's results may be extended to the present problem since the principal parts of equations (B.1) to (B.5) are the same as those for isentropic flow. Thus, for the present problem, an independent set of compatibility equations consists of equations (B.41) and (B.42) applied along a streamline, and equation (B.43) [or equation (B.46)] applied along three different wave surfaces.

6. BUTLER'S PARAMETERIZATION OF THE CHARACTERISTIC EQUATIONS

The numerical algorithm that is employed in the present investigation is based on a second-order scheme devised by D.S. Butler (7). This scheme has been used by Ransom, Hoffman, and Thompson (9) to compute isentropic steady three-dimensional nozzle flows, and by Cline and Hoffman (17) to compute chemically-reacting steady three-dimensional nozzle flows.

In this section, Butler's parameterization of the characteristic equations is presented. The discussion below is limited to the particular application of Butler's method to the present problem. An excellent review of Butler's general method is given in Ransom, Hoffman, and Thompson (9).

For Butler's scheme to be applicable, the characteristic determinant must be composed of a quadratic factor and a repeated linear factor. The determinant of the coefficient matrix in equation (B.16) is the characteristic determinant for the present problem, and by examination of equation (B.18) it is seen that it is composed of the required factors. The quadratic factor corresponds to the wave surfaces. The

envelope of all wave surfaces at a point is the Mach cone. The line of tangency between a particular wave surface and the Mach cone is a bicharacteristic. The linear factor corresponds to the stream surfaces. The axis of the envelope of all stream surfaces at a point is a streamline. Butler's method assumes that for the linear factor, differentiation can be expressed soley along the axis of the envelope of the corresponding characteristic surfaces. Examination of equations (B.41) and (B.42) demonstrates that this condition is applicable.

As discussed in the first section of this appendix, if the system of governing partial differential equations has differentiation occurring in n-space, then differentiation in the characteristic surfaces occurs in (n-1)-space (i.e., differentiation is performed in a manifold of one lower dimension). As a result, for three-dimensional flow (n=3), the general form of a compatibility relation valid along a characteristic surface may be written as

$$E_\nu(\partial u_\nu/\partial x_1') + F_\nu(\partial u_\nu/\partial x_2') = D \qquad (B.47)$$

where the repeated index ν implies summation over the range of 1 to 5, x_i' (i=1,2) denotes two independent directions in the characteristic surface, u_ν (ν=1 to 5) denotes the dependent variables, and E_ν, F_ν (ν=1 to 5), and D are general functions of x_i' and u_ν. For stream surfaces, differentiation may be expressed solely in the streamline direction [see equations (B.41) and (B.42)]. Consequently, in the following, the discussion will be limited to the wave surfaces.

For steady three-dimensional flow, Butler introduced the following parametric representation for a bicharacteristic.

$$dx_i = (u_i + c\alpha_i\cos\theta + c\beta_i\sin\theta)dt \quad (i=1,2,3) \tag{B.48}$$

In equation (B.48), x_i (i=1,2,3) denotes the three cartesian coordinates x, y, and z, respectively, u_i (i=1,2,3) denotes the corresponding velocity components u, v, and w, respectively, θ is a parametric angle denoting a particular element of the Mach cone and has the range $0 \leq \theta \leq 2\pi$, t is the time of travel of a fluid particle along the streamline that is the axis of the Mach cone, and c is defined by

$$c^2 = a^2q^2/(q^2 - a^2) \tag{B.49}$$

where q is the velocity magnitude and a is the sonic speed. The vectors α_i and β_i are parametric unit vectors with α_i, β_i, and u_i/q (i=1,2,3) forming an orthonormal set. A geometrical representation of this parameterization is given in Figure B.4.

The direction specified by equation (B.48) lies in the wave surface and is in the bicharacteristic direction. A direction in the wave surface and orthogonal to the bicharacteristic direction may be written in parametric form as

$$m_i = c\beta_i\cos\theta - c\alpha_i\sin\theta \quad (i=1,2,3) \tag{B.50}$$

Verification of the orthogonality of the directions given by equations (B.48) and (B.50) may be accomplished by forming the dot product $(m_i dx_i)$ and using the orthonormality relations

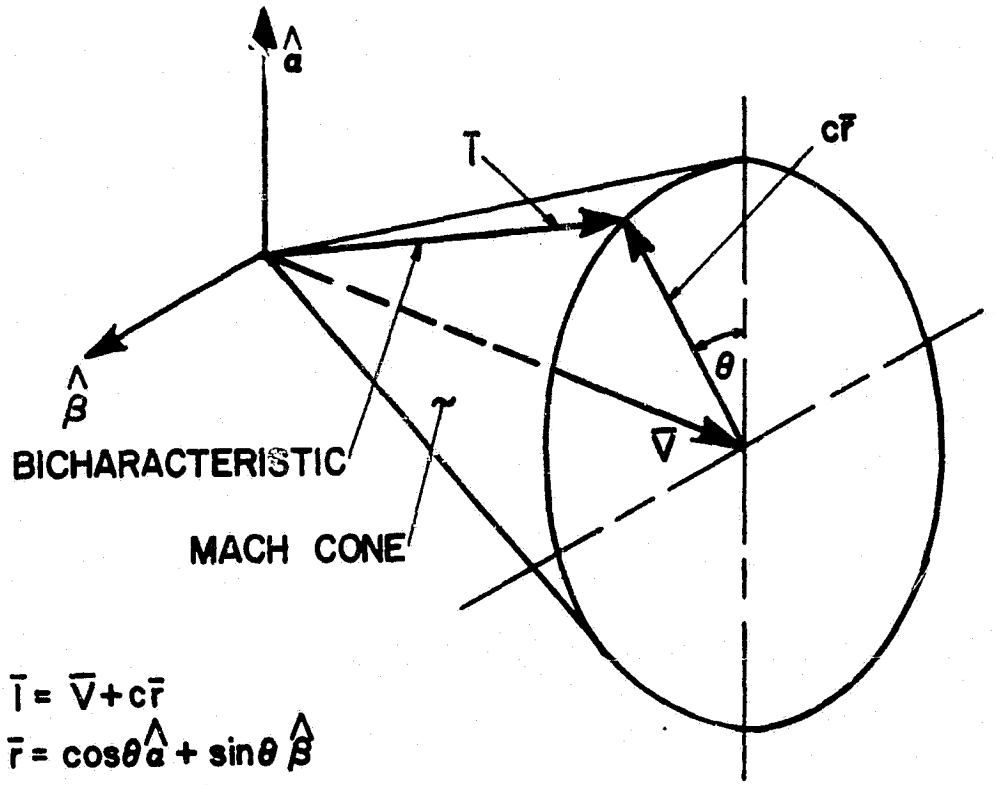

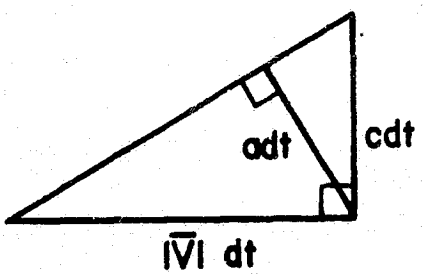

FIGURE B.4. BICHARACTERISTIC PARAMETERIZATION

$$u_i\alpha_i = u_i\beta_i = \alpha_i\beta_i = 0$$

$$\alpha_i\alpha_i = \beta_i\beta_i = u_iu_i/q^2 = 1 \qquad \text{(B.51)}$$

By considering equation (B.47) and selecting x_1' and x_2' as the directions given by equations (B.48) and (B.50), respectively, the following form of the wave surface compatibility relation is obtained.

$$A_\nu(u_i + c\alpha_i\cos\theta + c\beta_i\sin\theta)\frac{\partial u_\nu}{\partial x_i} =$$

$$B + C_\nu(c\beta_i\cos\theta - c\alpha_i\sin\theta)\frac{\partial u_\nu}{\partial x_i} \qquad \text{(B.52)}$$

In equation (B.52), A_ν, B, and C_ν are functions of θ, u_ν, and x_i. Employing equation (B.13), and noting from equation (B.48) that along a bicharacteristic

$$\ell_i = u_i + c\alpha_i\cos\theta + c\beta_i\sin\theta \qquad (i=1,2,3) \qquad \text{(B.53)}$$

equation (B.52) may be written as

$$A_\nu\frac{du_\nu}{d\ell} = B + C_\nu(c\beta_i\cos\theta - c\alpha_i\sin\theta)\frac{\partial u_\nu}{\partial x_i} \qquad \text{(B.54)}$$

where the operator $d(\ )/d\ell$ represents the directional derivative along the bicharacteristic. The general forms of the coefficients A_ν, B, and C_ν are given by Butler as

$$A_\nu = A_{1\nu} + A_{2\nu}\cos\theta + A_{3\nu}\sin\theta \qquad \text{(B.55)}$$

$$B = B_1 + B_2\cos\theta + B_3\sin\theta \qquad \text{(B.56)}$$

$$C_\nu = C_{1\nu} + C_{2\nu}\cos\theta + C_{3\nu}\sin\theta \tag{B.57}$$

where the $A_{k\nu}$, B_k, and $C_{k\nu}$ (k=1,2,3 and ν=1 to 5) are independent of θ.

In addition to the parametric wave surface compatibility relation, given by equation (B.54), Butler also developed a noncharacteristic relation which is applied along a streamline. This noncharacteristic relation is used in the numerical scheme in conjunction with the wave surface compatibility relation applied along four different bicharacteristics, and permits the formulation of three independent linear combinations of these five equations which do not contain cross derivatives at the solution point. The cross derivative terms [see equation (B.46)] represent differentiation in the wave surface but in a direction orthogonal to the bicharacteristic direction [i.e., differentiation in the direction given by equation (B.50)]. Butler presents the noncharacteristic relation in the form

$$A_{1\nu}\frac{du_\nu}{d\lambda} = B_1 + (C_{2\nu}c\beta_i - C_{3\nu}c\alpha_i)\frac{\partial u_\nu}{\partial x_i} \tag{B.58}$$

where the operator $d(\ )/d\lambda$ represents the directional derivative along the streamline. The coefficients $A_{1\nu}$, B_1, $C_{2\nu}$, and $C_{3\nu}$ (ν=1 to 5) in equation (B.58) are obtained by inspecting the form of equation (B.54) and then using equations (B.55), (B.56), and (B.57).

For the present problem, the actual form of the parametric wave surface compatibility relation, equation (B.54), may be obtained by substituting the appropriate parametric form of the wave surface unit normal into the compatibility relation, equation (B.43). The normal to the wave surface is also the normal to the Mach cone at a point common to both surfaces. The quadric surface of the Mach cone is

represented by equation (B.27), repeated below.

$$[u_i u_j - (q^2 - a^2)\delta_{ij}]dx_i dx_j = 0 \qquad (B.27)$$

Substituting the parametric form for dx_j, given by equation (B.48), into equation (B.27) yields

$$[u_i u_j - (q^2 - a^2)\delta_{ij}](u_j + c\alpha_j \cos\theta + c\beta_j \sin\theta)dx_i = 0 \qquad (B.59)$$

The ith component of the normal N_i to this surface is

$$N_i = [u_i u_j - (q^2 - a^2)\delta_{ij}](u_j + c\alpha_j \cos\theta + c\beta_j \sin\theta) \quad (i=1,2,3) \qquad (B.60)$$

Employing the orthonormality conditions given by equation (B.51), equation (B.60) may be written as

$$N_i = a^2[u_i - (q^2/c)(\alpha_i \cos\theta + \beta_i \sin\theta)] \quad (i=1,2,3) \qquad (B.61)$$

Dividing equation (B.61) by the magnitude of the normal $\left[|\overline{N}| = (N_i N_i)^{1/2}\right]$ and using equation (B.51), the parametric form of the wave surface unit normal is obtained.

$$n_i = (a/c)(cu_i/q^2 - \alpha_i \cos\theta - \beta_i \sin\theta) \quad (i=1,2,3) \qquad (B.62)$$

Substituting equation (B.62) and the orthonormality relation

$$\alpha_i \alpha_j + \beta_i \beta_j + u_i u_j / q^2 = \delta_{ij} \qquad (B.63)$$

into the wave surface compatibility relation, equation (B.43), gives the following parametric form of that equation

$$\frac{dP}{dt} + \rho c(\alpha_i \cos\theta + \beta_i \sin\theta)\frac{du_i}{dt} = \Phi - \rho c^2(\alpha_i \sin\theta - \beta_i \cos\theta)(\alpha_j \sin\theta - \beta_j \cos\theta)\frac{\partial u_i}{\partial x_j} \tag{B.64}$$

where

$$\Phi = -(c^2/a^2)\lambda \tag{B.65}$$

The operator d( )/dt in equation (B.64) denotes differentiation in the bicharacteristic direction.

It should be noted that the directional derivatives in equations (B.46) and (B.64) are not identical. The directional derivative in equation (B.46) is based on equation (B.45). Substitution of the parametric unit normal, given by equation (B.62), into equation (B.45) yields

$$\frac{d(\ )}{dt} = (a^2/c^2)(u_i + c\alpha_i \cos\theta + c\beta_i \sin\theta)\frac{\partial(\ )}{\partial x_i} \tag{B.66}$$

The directional derivative in equation (B.64) is given by

$$\frac{d(\ )}{dt} = (u_i + c\alpha_i \cos\theta + c\beta_i \sin\theta)\frac{\partial(\ )}{\partial x_i} \tag{B.67}$$

Hence, the two expressions differ by the factor (a^2/c^2).

Finally, it remains to determine the actual form of the noncharacteristic relation, equation (B.58). Denote u_ν (ν=1 to 5) and x_i (i=1,2,3) in equations (B.54) and (B.58) by

$$u_1 = u, \quad u_2 = v, \quad u_3 = w, \quad u_4 = P, \quad u_5 = \rho$$

$$x_1 = x, \quad x_2 = y, \quad x_3 = z \tag{B.68}$$

By inspection of equation (B.64), and use of equations (B.68), (B.55), (B.56), and (B.57), the noncharacteristic relation is seen to be

$$\frac{dP}{dt} = \sigma - \rho c^2(\alpha_i\alpha_j + \beta_i\beta_j)\frac{\partial u_i}{\partial x_j} \tag{B.69}$$

where

$$\sigma = (c^2/a^2)F_e - (c^2/q^2)(uF_x + vF_y + wF_z) \tag{B.70}$$

The operator d( )/dt in equation (B.69) denotes the directional derivative along a streamline.

In summary, Butler has developed a bicharacteristic parameterization given by equation (B.48). The corresponding parametric form of the wave surface compatibility relation is given by equation (B.64). Butler also developed a noncharacteristic relation, given by equation (B.69), which is applied along a streamline. These relations, along with the stream surface compatibility relations, equations (B.41) and (B.42), constitute the system of compatibility relations. The use of this system of equations in the various unit processes is presented in Appendix E.

APPENDIX C

INTERPOLATION

1. INTRODUCTION

In the course of computing the flow field, a number of situations arise which require interpolation. To this end, univariate, bivariate, and trivariate interpolation polynomials are employed in the numerical algorithm. These interpolation schemes are presented in this appendix.

2. UNIVARIATE INTERPOLATION

Univariate interpolation is required in geometry description, calculation of the transport forcing terms, and in determination of the properties along a space curve formed by the locus of shock wave solution points. Applications to geometry description and transport term computation are discussed in Appendices D and F, respectively. The application to the determination of properties along a shock wave is discussed here.

When a shock wave intersects either a solid boundary or a solution plane (a plane of constant x), a space curve is defined as illustrated in Figure C.1. Interpolated values of position, shock wave angle, and flow properties are required along this curve. For this purpose, the quadratic polynomial

$$f(\theta) = a_1 + a_2\theta + a_3\theta^2 \qquad (C.1)$$

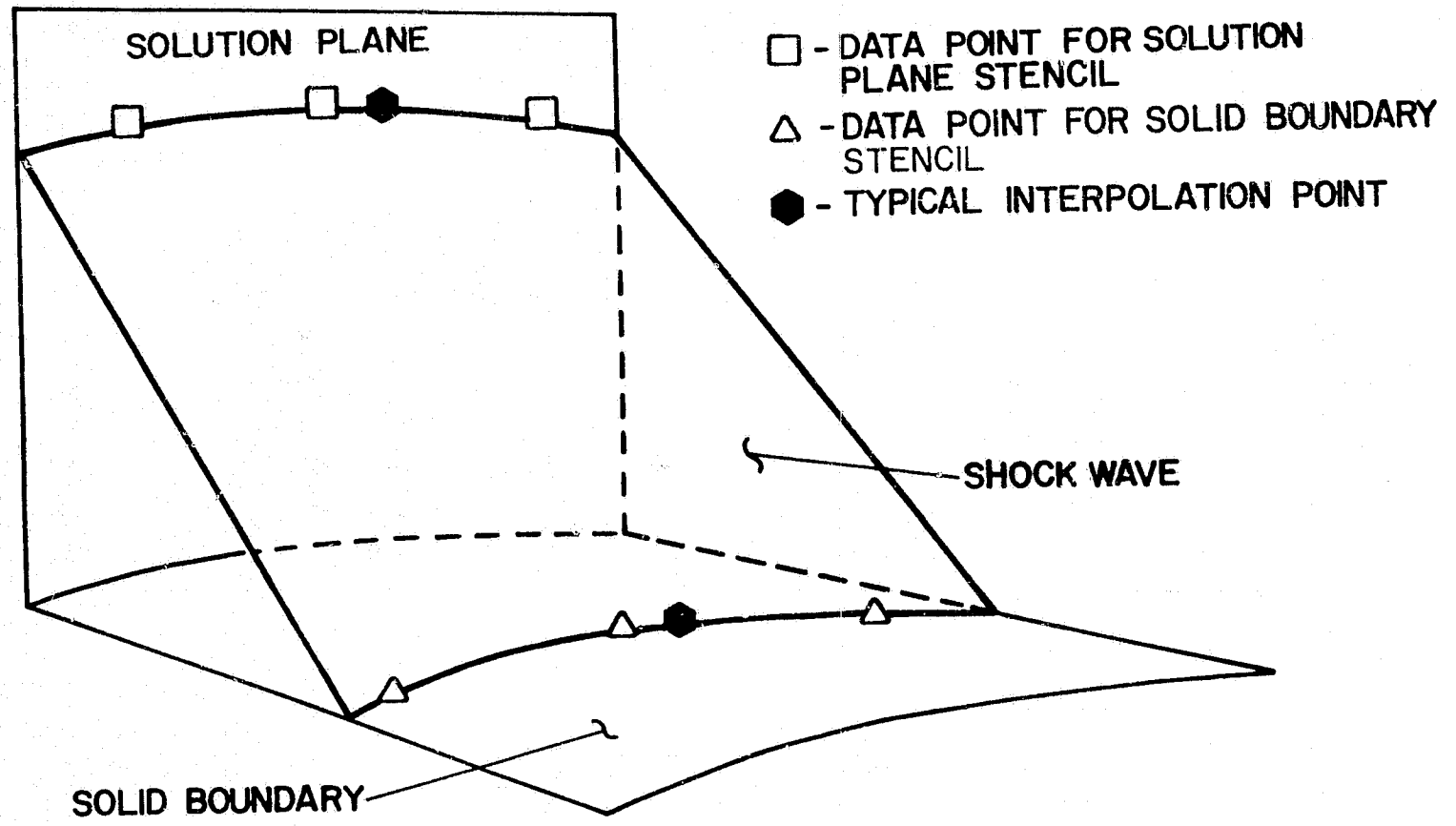

FIGURE C.1. POINT STENCILS FOR UNIVARIATE INTERPOLATION

is employed, where $f(\theta)$ denotes a general function expressed in terms of the polar angle θ given by

$$\theta = \tan^{-1}(z/y) \tag{C.2}$$

where y and z are the coordinates of a point on the space curve. The coefficients a_i (i=1,2,3) in equation (C.1) are determined by fitting this expression to three data points on the space curve, and, as a consequence, a system of three simultaneous linear equations must be solved for the coefficients a_i of each function representation. The solution to this system of equations is obtained using a Gaussian elimination method with complete pivoting (18).

Figure C.1 illustrates typical data point stencils used for determining coefficients in equation (C.1). The fit point array consists of a base point, which is the point closest to the position of the interpolated point, and the immediate neighbors of the base point.

3. BIVARIATE INTERPOLATION

Bivariate interpolation is required for property determination in a given solution plane (a plane of constant x). Two types of bivariate interpolation polynomials are employed in the numerical algorithm. They are a linear bivariate polynomial whose three coefficients are determined by fitting this expression to three data points, and a quadratic bivariate polynomial whose six coefficients are determined by a least squares fitting of nine data points.

The linear bivariate polynomial is used in the single application when a streamline-shock wave intersection point is sufficiently close to the current solution plane so that an interior point unit

process on the downstream side of the shock wave is not performed. In that case the projection of the streamline onto the solution plane and subsequent property interpolation in this plane is performed. The bivariate interpolation polynomial used in this case is

$$f(y,z) = a_1 + a_2 y + a_3 z \qquad (C.3)$$

where f(y,z) denotes a general function of the coordinates y and z. The coeffficients a_i (i=1,2,3) in equation (C.3) are determined by fitting this expression to three data points. This yields a system of three simultaneous linear equations for the coefficients a_i of each function representation. This system of equations is solved using a Gaussian elimination method with complete pivoting [as was done for equation (C.1)].

A typical data point stencil used for determining the coefficients in equation (C.3) is illustrated in Figure C.2. Two shock wave solution points and a field point constitute the fit point array.

In all other situations which require bivariate interpolation, the quadratic polynomial

$$f(y,z) = a_1 + a_2 y + a_3 z + a_4 yz + a_5 y^2 + a_6 z^2 \qquad (C.4)$$

is employed, where f(y,z) is a general function of the coordinates y and z. The coefficients a_i (i=1 to 6) in equation (C.4) are determined by a least squares fit of nine points. Using the standard theory of least squares (18), the system of normal equations which determines the coefficients in equation (C.4) is

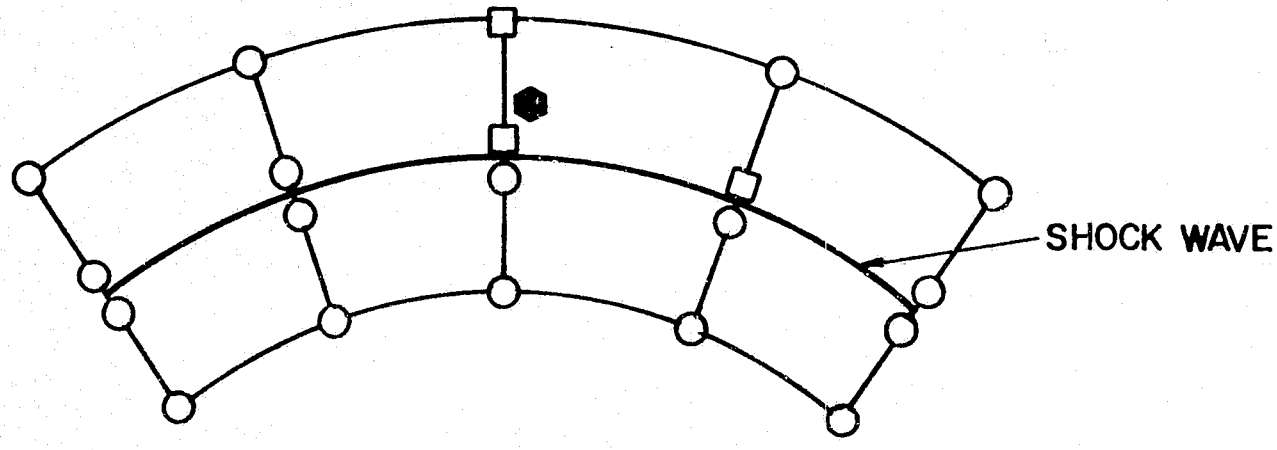

○ - SOLUTION POINT
□ - DATA POINT FOR INTERPOLATION STENCIL
⬢ - TYPICAL INTERPOLATION POINT

FIGURE C.2. POINT STENCIL FOR LINEAR BIVARIATE INTERPOLATION

$$9a_1 + \sum y_i a_2 + \sum z_i a_3 + \sum y_i z_i a_4 + \sum y_i^2 a_5 + \sum z_i^2 a_6 = \sum f_i \quad (C.5)$$

$$\sum y_i a_1 + \sum y_i^2 a_2 + \sum y_i z_i a_3 + \sum y_i^2 z_i a_4 + \sum y_i^3 a_5 + \sum y_i z_i^2 a_6 = \sum y_i f_i \quad (C.6)$$

$$\sum z_i a_1 + \sum y_i z_i a_2 + \sum z_i^2 a_3 + \sum y_i z_i^2 a_4 + \sum y_i^2 z_i a_5 + \sum z_i^3 a_6 = \sum z_i f_i \quad (C.7)$$

$$\sum y_i z_i a_1 + \sum y_i^2 z_i a_2 + \sum y_i z_i^2 a_3 + \sum y_i^2 z_i^2 a_4 + \sum y_i^3 z_i a_5 + \sum y_i z_i^3 a_6 = \sum y_i z_i f_i \quad (C.8)$$

$$\sum y_i^2 a_1 + \sum y_i^3 a_2 + \sum y_i^2 z_i a_3 + \sum y_i^3 z_i a_4 + \sum y_i^4 a_5 + \sum y_i^2 z_i^2 a_6 = \sum y_i^2 f_i \quad (C.9)$$

$$\sum z_i^2 a_1 + \sum y_i z_i^2 a_2 + \sum z_i^3 a_3 + \sum y_i z_i^3 a_4 + \sum y_i^2 z_i^2 a_5 + \sum z_i^4 a_6 = \sum z_i^2 f_i \quad (C.10)$$

In equations (C.5) to (C.10), the $\sum$ sign implies summation over the range of 1 to 9, while the subscript i denotes the ith data point (i=1 to 9). This system of simultaneous linear equations has a symmetric coefficient matrix and is solved using a Gaussian elimination method with pivoting in the main diagonal.

Figure C.3 illustrates typical data point stencils used in determining the coefficients in equation (C.4). Basically, there are two

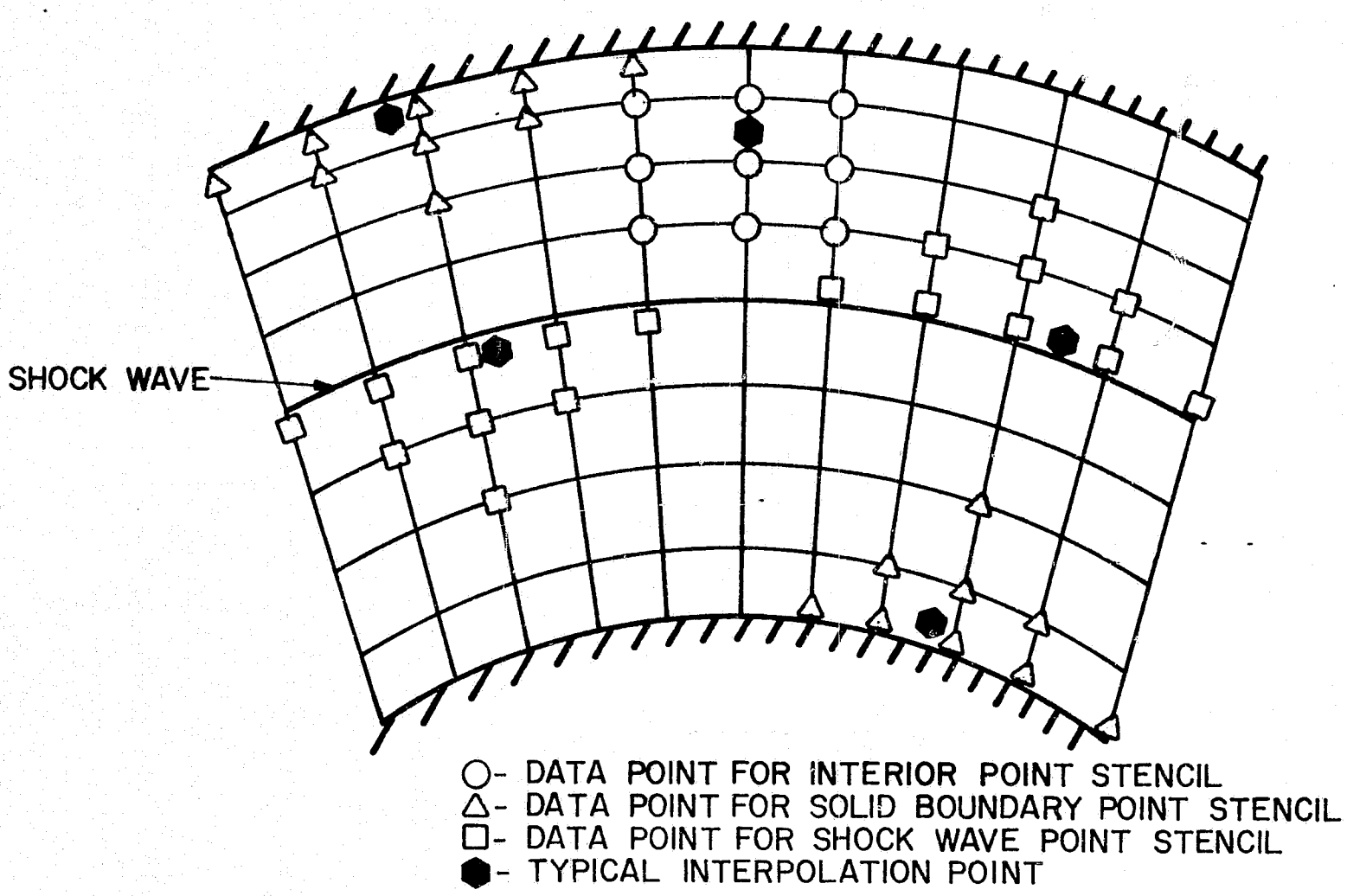

FIGURE C.3.
POINT STENCILS FOR QUADRATIC BIVARIATE INTERPOLATION

types of stencils: interior point and boundary point. Since the shock wave mathematically represents a discontinuity, the boundary point stencil must be employed when the interpolation base point (the data point closest to the interpolated point) is on the shock wave. The fit point array consists of the base point and its eight immediate neighbors. Special logic in the computer program is used to insure that no stencil bridges the shock wave.

4. TRIVARIATE INTERPOLATION

Trivariate interpolation is required for property determination on the surface of a solid boundary (a stream surface) and for property determination on the upstream and downstream sides of the shock wave. Two types of trivariate interpolation polynomials are employed in the numerical algorithm. They are a linear trivariate polynomial whose four coefficients are determined by fitting this expression to four data points, and a quadratic trivariate polynomial whose eight coefficients are determined by a least squares fitting of fourteen data points.

The linear trivariate polynomial is used in the single application for property determination on the upstream side of the shock wave surface. This polynomial has the form

$$f(x,y,z) = a_1 + a_2x + a_3y + a_4z \qquad (C.11)$$

where $f(x,y,z)$ is a general function of the coordinates x, y, and z. The coefficients a_i (i=1,2,3,4) in equation (C.11) are determined by fitting this expression to four data points. Hence, a system of four simultaneous linear equations must be solved for the coefficient a_i

of each function representation. This system of equations is solved using a Gaussian elimination method with complete pivoting [as was done for equations (C.1) and (C.3)].

A typical data point stencil used for determining the coefficients in equation (C.11) is illustrated in Figure C.4. Three data points are located on one space curve and one data point is located on the other space curve.

In all other situations which require trivariate interpolation, the quadratic polynomial

$$f(x,y,z) = a_1 + a_2 y + a_3 z + a_4 yz + a_5 y^2 + a_6 z^2 + a_7 xy + a_8 xz \tag{C.12}$$

is employed, where $f(x,y,z)$ is a general function dependent on the coordinates x, y, and z. The coefficients a_i (i=1 to 8) in equation (C.12) are determined by a least squares fit of fourteen data points. From the theory of least squares, the system of normal equations which determines the coefficients in equation (C.12) is

$$14a_1 + \sum y_i a_2 + \sum z_i a_3 + \sum y_i z_i a_4 + \sum y_i^2 a_5 + \sum z_i^2 a_6 + \sum x_i y_i a_7 + \sum x_i z_i a_8 = \sum f_i \tag{C.13}$$

$$\sum y_i a_1 + \sum y_i^2 a_2 + \sum y_i z_i a_3 + \sum y_i^2 z_i a_4 + \sum y_i^3 a_5 + \sum y_i z_i^2 a_6 + \sum x_i y_i^2 a_7 + \sum x_i y_i z_i a_8 = \sum y_i f_i \tag{C.14}$$

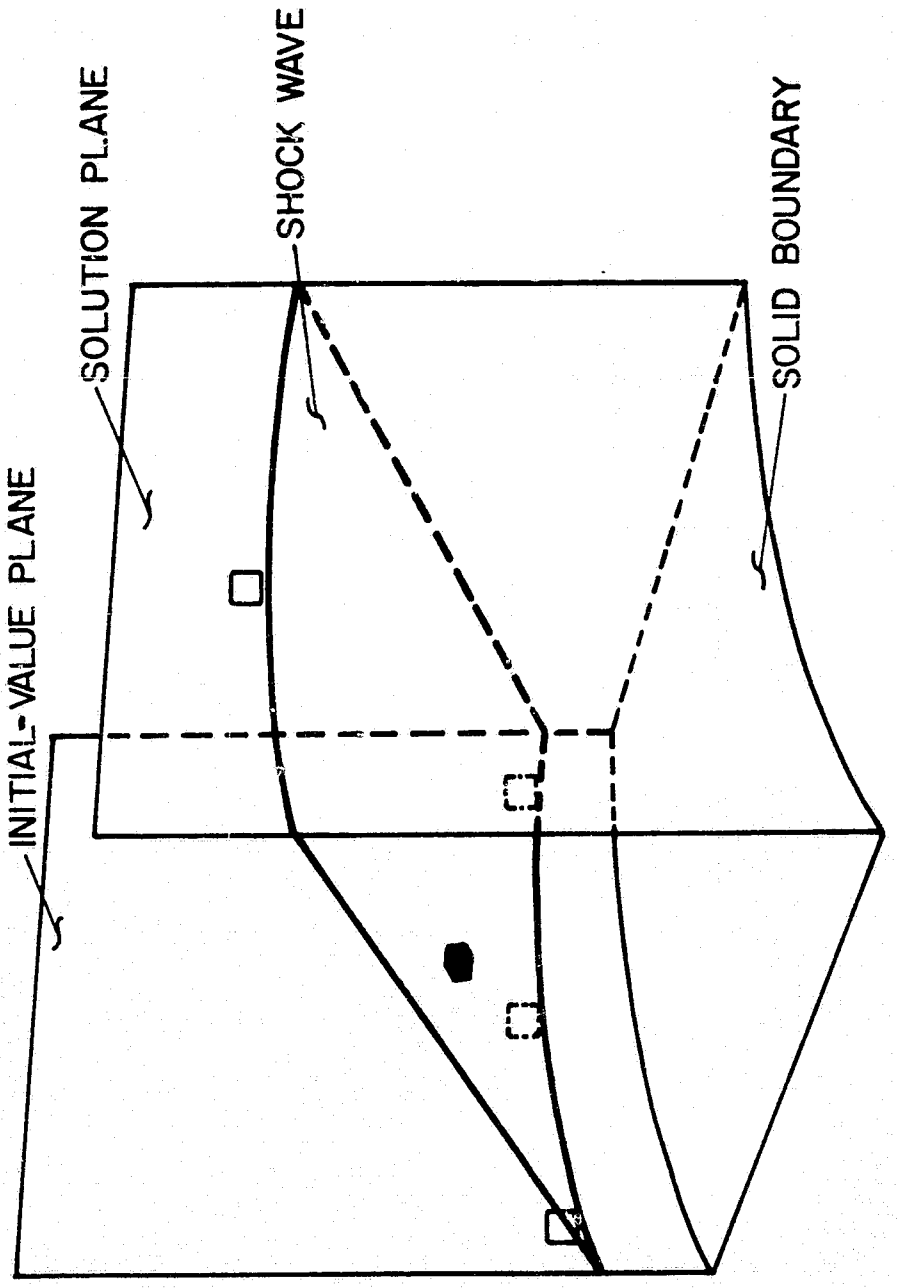

FIGURE C.4. POINT STENCIL FOR LINEAR TRIVARIATE INTERPOLATION

$$\sum z_i a_1 + \sum y_i z_i a_2 + \sum z_i^2 a_3 + \sum y_i z_i^2 a_4 + \sum y_i^2 z_i a_5 + \sum z_i^3 a_6 + \sum x_i y_i z_i a_7 + \sum x_i z_i^2 a_8 = \sum z_i f_i \qquad (C.15)$$

$$\sum y_i z_i a_1 + \sum y_i^2 z_i a_2 + \sum y_i z_i^2 a_3 + \sum y_i^2 z_i^2 a_4 + \sum y_i^3 z_i a_5 + \sum y_i z_i^3 a_6 + \sum x_i y_i^2 z_i a_7 + \sum x_i y_i z_i^2 a_8 = \sum y_i z_i f_i \qquad (C.16)$$

$$\sum y_i^2 a_1 + \sum y_i^3 a_2 + \sum y_i^2 z_i a_3 + \sum y_i^3 z_i a_4 + \sum y_i^4 a_5 + \sum y_i^2 z_i^2 a_6 + \sum x_i y_i^3 a_7 + \sum x_i y_i^2 z_i a_8 = \sum y_i^2 f_i \qquad (C.17)$$

$$\sum z_i^2 a_1 + \sum y_i z_i^2 a_2 + \sum z_i^3 a_3 + \sum y_i z_i^3 a_4 + \sum y_i^2 z_i^2 a_5 + \sum z_i^4 a_6 + \sum x_i y_i z_i^2 a_7 + \sum x_i z_i^3 a_8 = \sum z_i^2 f_i \qquad (C.18)$$

$$\sum x_i y_i a_1 + \sum x_i y_i^2 a_2 + \sum x_i y_i z_i a_3 + \sum x_i y_i^2 z_i a_4 + \sum x_i y_i^3 a_5 + \sum x_i y_i z_i^2 a_6 + \sum x_i^2 y_i^2 a_7 + \sum x_i^2 y_i z_i a_8 = \sum x_i y_i f_i \qquad (C.19)$$

$$\sum x_i z_i a_1 + \sum x_i y_i z_i a_2 + \sum x_i z_i^2 a_3 + \sum x_i y_i z_i^2 a_4 + \sum x_i y_i^2 z_i a_5 + \sum x_i z_i^3 a_6 + \sum x_i^2 y_i z_i a_7 + \sum x_i^2 z_i^2 a_8 = \sum x_i z_i f_i \qquad (C.20)$$

In equations (C.13) to (C.20), the $\sum$ sign implies summation over the range of 1 to 14, while the subscript i denotes the ith data point (i=1 to 14). This system of simultaneous linear equations has a symmetric coefficient matrix and is solved using a Gaussian elimination method with pivoting in the main diagonal [as was done for equation (C.4)].

Figure C.5 illustrates typical data point stencils used in determining the coefficients in equation (C.12). The fit point array consists of seven data points along each of the appropriate space curves on either the shock wave or the solid boundary.

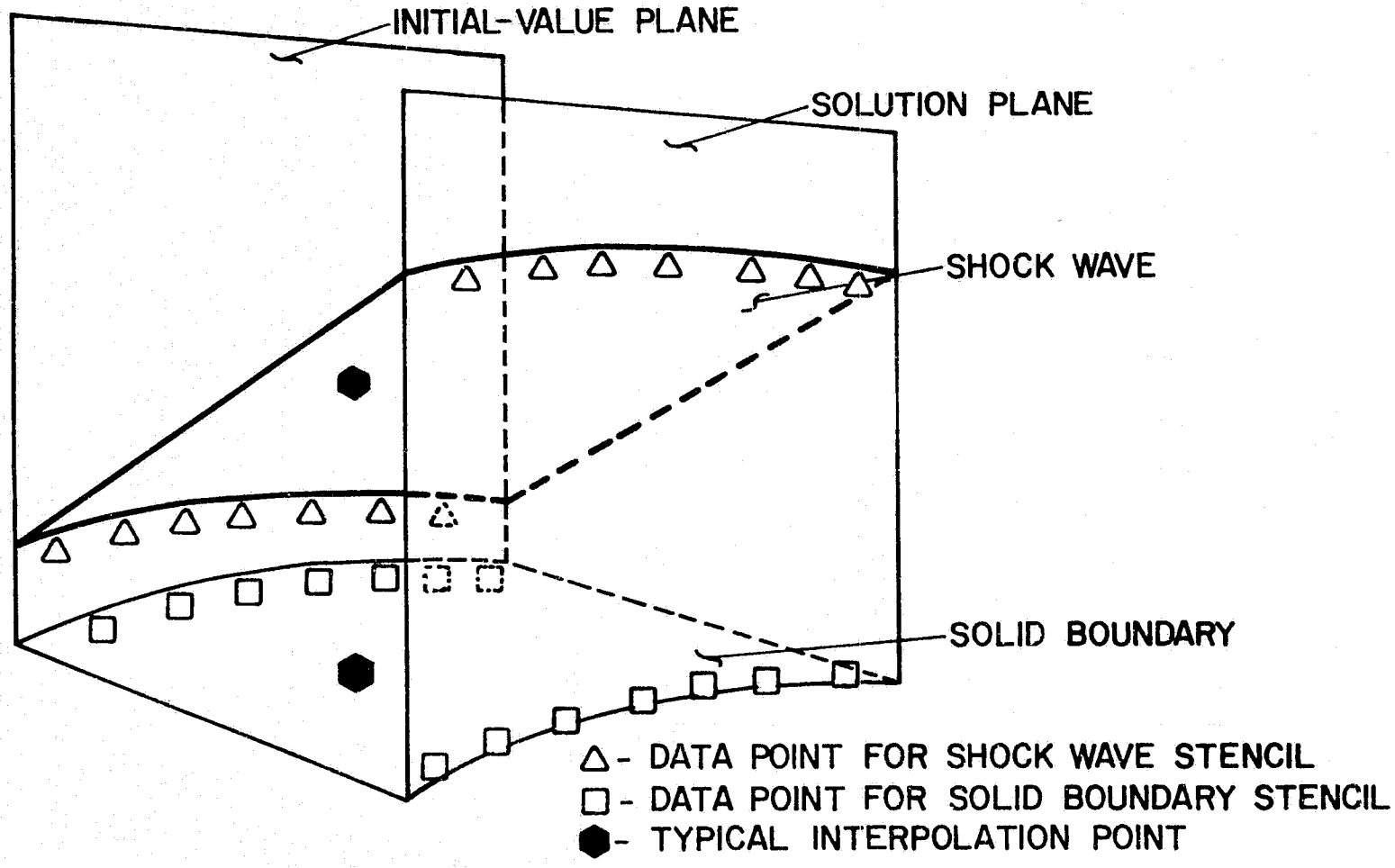

FIGURE C.5. POINT STENCILS FOR QUADRATIC TRIVARIATE INTERPOLATION

APPENDIX D

SURFACE REPRESENTATIONS, AND STREAMLINE- AND BICHARACTERISTIC-SURFACE INTERSECTIONS

1. INTRODUCTION

The procedures employed for representing the solid boundary and shock wave surfaces are presented in this appendix. The technique used for determining the intersection point of either a streamline with the shock wave, or a bicharacteristic with either the shock wave or the solid boundary, is also discussed.

2. SOLID BOUNDARY SURFACES

The centerbody and cowl surfaces are specified in the computer program by a separate geometry module that has the capability to describe a variety of axisymmetric contours. More arbitrary geometries, such as those having elliptical or superelliptical cross sections, may be considered by supplying an appropriate replacement module. In general, to specify a surface completely, its functional form [$f(x,y,z) = \text{constant}$] and its gradient at any point [$\nabla f(x,y,z)$] must be available.

The existing geometry module, which describes axisymmetric contours, divides the axial (x) domain into a number of intervals. In any interval, the body radius may be specified by either tabular input, or by supplying the coefficients in a cubic polynomial written as a

function of x. For the tabular input case, linear interpolation is performed to obtain the radius $r(x)$ between the points (x_i, r_i) and (x_{i+1}, r_{i+1}) where $(x_i \leq x < x_{i+1})$. Alternatively, employing the cubic polynomial

$$r(x) = a_i + b_i(x - x_i) + c_i(x - x_i)^2 + d_i(x - x_i)^3$$

$$(x_i \leq x < x_{i+1}) \qquad \text{(D.1)}$$

requires that the coefficients a_i, b_i, c_i, and d_i be supplied for the ith interval (these coefficients must be externally generated). Since equation (D.1) is a cubic, slope and curvature can be matched at the junction point between two adjacent intervals (i.e., spline fits can be employed).

3. SHOCK WAVE SURFACE

Some of the unit processes, which are described in Appendix E, require an analytical representation for the shock wave surface. During the course of the program development, a number of different representations were devised, including the fitting of both planar surfaces and quadric surfaces to locally approximate the shock wave surface. The quadric surface formulation displayed a tendency to produce a (local) surface with undulations. The planar surface representation did not exhibit this effect, and, for fine mesh spacings, produced results essentially the same as the representation that was ultimately selected for use in the numerical algorithm. However, the accuracy of the planar surface representation suffered at coarse mesh spacings. The shock wave surface formulation that was selected for use in the algorithm is presented below.

The shock wave surface is represented as a family of straight lines between two space curves, as illustrated in Figure D.1. The space curves represent either the intersection of the shock wave with a solution plane (which is a plane of constant x), or the intersection of the shock wave with a solid boundary (i.e., an interplanar ring of shock wave solution points). Each space curve is represented by the two quadratic expressions

$$r_i(\theta) = a_i + b_i\theta + c_i\theta^2 \qquad (i=1,2) \qquad (D.2)$$

$$x_i(\theta) = d_i + e_i\theta + f_i\theta^2 \qquad (i=1,2) \qquad (D.3)$$

where r_i is the radius of a point on space curve i (i=1,2), x_i is the corresponding axial position of a point on space curve i, and θ is the polar angle given by

$$\theta = \tan^{-1}(z/y) \qquad (D.4)$$

where y and z are the coordinates of a point on the space curve. In equations (D.2) and (D.3), the coefficients a_i to f_i (i=1,2) are determined by fitting these expressions to three known points on each space curve as described in Appendix C. When the space curve lies in a solution plane, x of course has no θ dependency.

Once equations (D.2) and (D.3) are determined for the two space curves, the shock wave surface is represented as an infinite family of straight lines between the two space curves, where each straight line falls in a meridional plane (i.e., a plane of constant θ). Consequently, for a given value of θ and x, the shock wave surface is represented by the linear interpolation formula

FIGURE D.1. SHOCK WAVE SURFACE REPRESENTATION

C-3

$$r(x,\theta) = \frac{(x - x_2(\theta))}{(x_1(\theta) - x_2(\theta))} r_1(\theta) + \frac{(x - x_1(\theta))}{(x_2(\theta) - x_1(\theta))} r_2(\theta) \quad (D.5)$$

In equation (D.5), $r(x,\theta)$ is the shock wave radius at axial position x and polar angle θ, $r_1(\theta)$ and $x_1(\theta)$ are given by equations (D.2) and (D.3), respectively, for one of the space curves, and $r_2(\theta)$ and $x_2(\theta)$ are given by equations (D.2) and (D.3), respectively, for the other space curve (see Figure D.1). A strong point of this representation is that a smooth (local) surface is produced because linear interpolation is performed for the shock wave radius in a meridional plane, while transverse curvature information is introduced through equations (D.2) and (D.3).

4. STREAMLINE- AND BICHARACTERISTIC-SURFACE INTERSECTIONS

A number of unit processes require determining the intersection point of either a streamline with the shock wave, or a bicharacteristic with either the shock wave or a solid boundary. The technique used is the same for all cases and is presented below.

A streamline or bicharacteristic may be represented by the equation

$$dx_i = \Gamma_i dt \qquad (i=1,2,3) \qquad (D.6)$$

where x_i (i=1,2,3) denotes the three cartesian coordinates x, y, and z, respectively, and t is a parameter proportional to the length of the streamline or bicharacteristic. For a streamline, the parameter Γ_i in equation (D.6) is given by

$$\Gamma_i = u_i \qquad (i=1,2,3) \tag{D.7}$$

where u_i (i=1,2,3) denotes the velocity components u, v, and w, respectively. For a bicharacteristic, Γ_i is given by

$$\Gamma_i = u_i + c\alpha_i\cos\phi + c\beta_i\sin\phi \qquad (i=1,2,3) \tag{D.8}$$

where α_i, β_i, ϕ, and c are the parameters employed in Butler's parameterization of the Mach cone (24), which is discussed in Appendix B.

Using equation (D.6), the following equation may be written.

$$dx/\Gamma_1 = dy/\Gamma_2 = dz/\Gamma_3 \tag{D.9}$$

Solving equation (D.9) simultaneously, the linear expressions

$$y = [y_k - (\Gamma_2/\Gamma_1)x_k] + (\Gamma_2/\Gamma_1)x \tag{D.10}$$

$$z = [z_k - (\Gamma_3/\Gamma_1)x_k] + (\Gamma_3/\Gamma_1)x \tag{D.11}$$

may be obtained, where x_k, y_k, and z_k are the coordinates of a known point on the streamline or bicharacteristic, while x, y, and z represent the coordinates of the point of intersection of the streamline or bicharacteristic with a surface (see Figure D.2).

An iterative procedure is employed to determine the coordinates x, y, and z. First, the values of Γ_i (i=1,2,3) are evaluated at the known point. Then, a trial value is assumed for the axial coordinate x. From equations (D.10) and (D.11), the corresponding coordinates y and z may be obtained. Then, the radius $r^* = (y^2 + z^2)^{1/2}$ and the polar angle $\theta = \tan^{-1}(z/y)$ of the assumed intersection point may be computed. From the assumed value for x and the calculated value for θ,

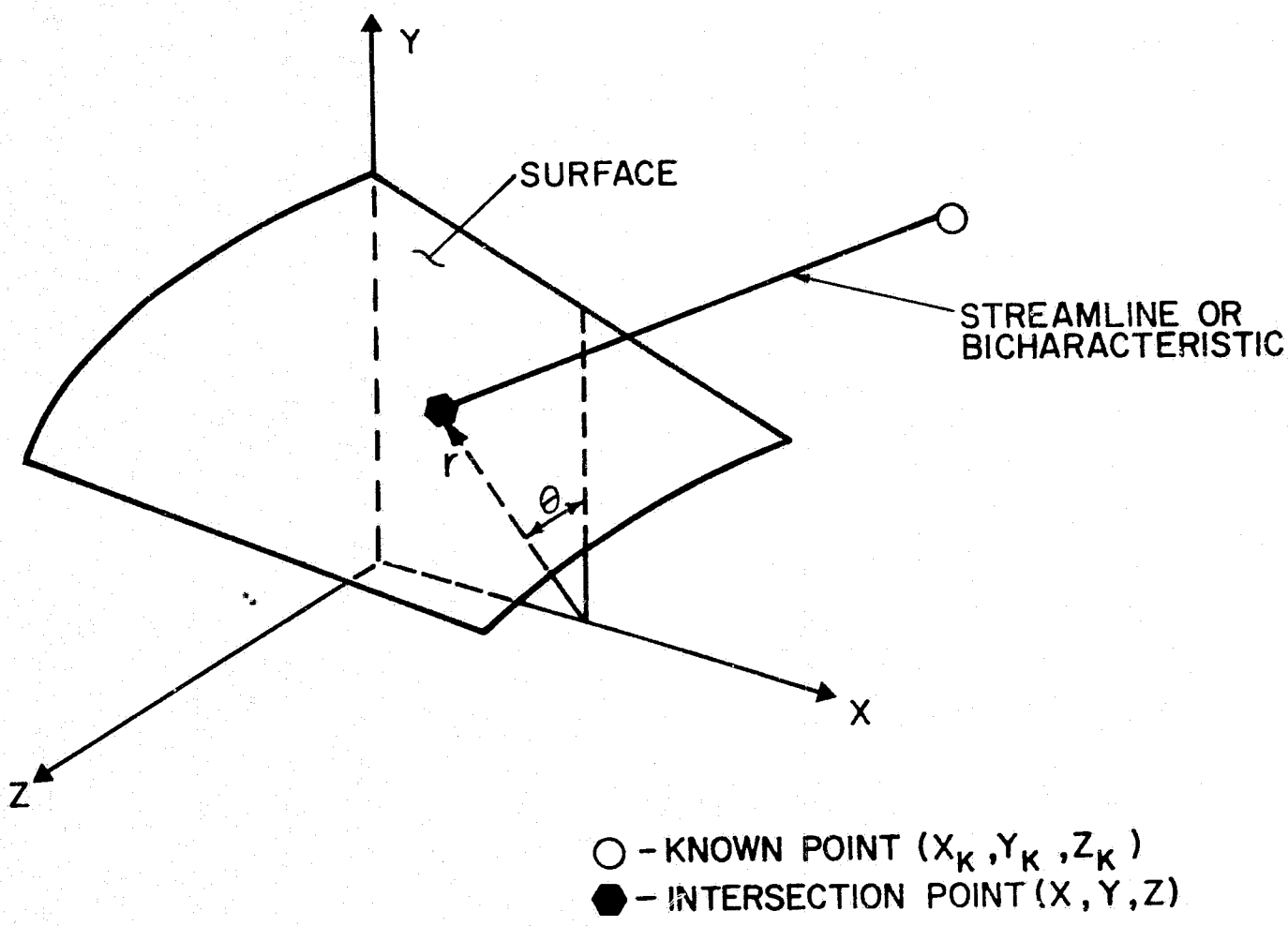

FIGURE D.2 INTERSECTION OF STREAMLINE OR BICHARACTERISTIC WITH A SURFACE.

the body radius r^{**} [determined from the tabular wall data or equation (D.1)] or the shock wave radius r^{**} [given by equation (D.5)] may be obtained. The difference between r^{*} and r^{**} is reduced to within a specified tolerance by employing a numerical relaxation technique (secant method) which iterates on x. Once convergence has been obtained, the values of Γ_i at the intersection point are computed using the trivariate interpolation method discussed in Appendix C. Appropriate averages of the values of Γ_i at the known point and the intersection point are then formed, and the entire process is repeated until overall convergence is obtained.

It should be noted that it is possible to use θ, instead of x, as the variable upon which the iterative scheme is based. The resulting formulation, however, is singular when the streamline or bicharacteristic lies in a meridional plane.

APPENDIX E

SUPERSONIC CORE FLOW UNIT PROCESSES

1. INTRODUCTION

Computation of the flow field requires that a variety of unit processes be employed. These subalgorithms may be classified into four major types: interior point, solid boundary point, field-shock wave point, and body-shock wave point. Computation of the external flow field about the forebody portion of the centerbody requires using the basic versions of the first three aforementioned algorithms. Computation of the internal flow field, with its attendant reflected shock wave system, requires using the basic interior point and solid boundary point algorithms plus modified versions of these routines, as well as the other unit processes. All of the unit processes are presented in this appendix.

2. SUMMARY OF THE CHARACTERISTIC EQUATIONS

The equations for the characteristic surfaces and the compatibility equations valid along these surfaces are developed in Appendix B. A summary of the pertinent results is given below.

For steady three-dimensional supersonic flow, compatibility equations may be written which are valid when applied along either streamlines or bicharacteristics. A streamline is represented by the equation

$$dx_i = u_i\, dt \qquad (i=1,2,3) \qquad (E.1)$$

where x_i (i=1,2,3) denotes the three cartesian coordinates x, y, and z, respectively, u_i (i=1,2,3) denotes the corresponding velocity components u, v, and w, respectively, and t is the time of travel of a fluid particle along the streamline. The compatibility equations valid along a streamline are given by*

$$\frac{dP}{dt} - a^2 \frac{d\rho}{dt} = F_e \qquad (E.2)$$

$$\frac{dP}{dt} + \rho u_i \frac{du_i}{dt} = u_i F_i \qquad (E.3)$$

where P denotes the pressure, ρ is the density, a is the sonic speed, F_i (i=1,2,3) denotes the transport forcing terms in the x, y, and z component momentum equations, respectively, and F_e is the transport forcing term in the energy equation. The operator d( )/dt in equations (E.2) and (E.3) represents differentiation in the streamline direction. The forcing terms F_i and F_e are defined by equations (A.6) and (A.27), respectively.

A bicharacteristic, which is a ray or generator of the Mach cone, is represented by

$$dx_i = (u_i + c\alpha_i \cos\theta + c\beta_i \sin\theta)dt \qquad (i=1,2,3) \qquad (E.4)$$

where θ is a parametric angle denoting a particular element of the Mach cone and has the range $0 \leq \theta \leq 2\pi$, t is the time of travel of a fluid

---

*Repeated indices imply summation over the range of 1 to 3 unless otherwise noted.

particle along the streamline that is the axis of the Mach cone, and c is defined by

$$c^2 = q^2a^2/(q^2 - a^2) \tag{E.5}$$

where q is the velocity magnitude. The vectors α_i and β_i in equation (E.4) are parametric unit vectors with α_i, β_i, and u_i/q (i=1,2,3) forming an orthonormal set. The compatibility equation valid along a bicharacteristic is given by

$$\frac{dP}{dt} + \rho c(\alpha_i \cos\theta + \beta_i \sin\theta)\frac{du_i}{dt} = \Phi - \rho c^2(\alpha_i \sin\theta - \beta_i \cos\theta)(\alpha_j \sin\theta - \beta_j \cos\theta)\frac{\partial u_i}{\partial x_j} \tag{E.6}$$

In equation (E.6), the operator d( )/dt represents differentiation in the bicharacteristic direction, and the parameter Φ is given by

$$\Phi = (c^2/a^2)(F_e - an_iF_i) \tag{E.7}$$

where n_i is the ith component of the wave surface unit normal and is given by

$$n_i = (a/c)(cu_i/q^2 - \alpha_i \cos\theta - \beta_i \sin\theta) \qquad (i=1,2,3) \tag{E.8}$$

In addition to the above relations, the following noncharacteristic relation is applied along a streamline

$$\frac{dP}{dt} = \sigma - \rho c^2(\alpha_i\alpha_j + \beta_i\beta_j)\frac{\partial u_i}{\partial x_j} \tag{E.9}$$

where the operator d( )/dt represents differentiation in the streamline direction, and the parameter σ is given by

$$\sigma = (c^2/a^2)F_e - (c^2/q^2)(u_i F_i) \qquad (E.10)$$

Equations (E.1) to (E.10) form the basis of the numerical integration method.

3. GENERAL COMMENTS CONCERNING THE UNIT PROCESSES

An inverse marching scheme is employed in the numerical algorithm. The solution is obtained on space-like planes of constant x, with the x-axis being the longitudinal axis of the centerbody and cowl. For the internal flow field, the solution is also obtained on the space curves which represent the intersection of the internal shock wave with the solid boundaries. These space curves are defined by the locus of shock wave solution points.

Except in the vicinity of a shock wave-solid boundary intersection, the distance between successive solution planes is determined by the application of the Courant-Friedrichs-Lewy (CFL) stability criterion, which is presented in Appendix K. The axial step in the vicinity of a shock wave-solid boundary intersection is controlled by special constraints which are also discussed in Appendix K.

Each of the unit processes is presented below. In general, a unit process is divided into a predictor step and a number of enusing corrector steps. In most cases, a unit process employs an outer iterative loop for determination of the flow properties at the solution point, and an inner iterative loop (or loops) for location of bicharacteristic-initial-value plane intersection points, etc. The terms "inner" and "outer" are used in this context in the following discussions.

4. INTERIOR POINT UNIT PROCESS

Figure E.1 is a depiction of the computational network used in the determination of the solution for a typical interior point. Points (1) to (5) are located on the initial-value plane which is a plane of constant x on which the solution is known. Points (1) to (4) represent the intersection points of four rearward-running bicharacteristics with the initial-value plane, and point (5) is the intersection point of the streamline with this plane. Point (6) is the interior solution point, which is located at the intersection of the forward projection of the streamline with the solution plane. The axial (x) distance between the initial-value plane and the solution plane is determined by either the application of the CFL stability criterion, or, in the vicinity of a shock wave-solid boundary intersection, by the special constraints discussed in Appendix K.

Interpolated values of the three velocity components u, v, and w, the pressure P, and the density ρ are required at the bicharacteristic-initial-value plane intersection points, points (1) to (4) in Figure E.1. For this purpose, the following bivariate interpolation polynomial is employed

$$f(y,z) = a_1 + a_2 y + a_3 z + a_4 yz + a_5 y^2 + a_6 z^2 \qquad \text{(E.11)}$$

where f(y,z) denotes a general function of the coordinates y and z. The coefficients a_i (i=1 to 6) in equation (E.11) are determined by a least squares fit of nine data points in the initial-value plane [point (5) and its eight immediate field point neighbors]. The detailed implementation of equation (E.11) is discussed in Appendix C.

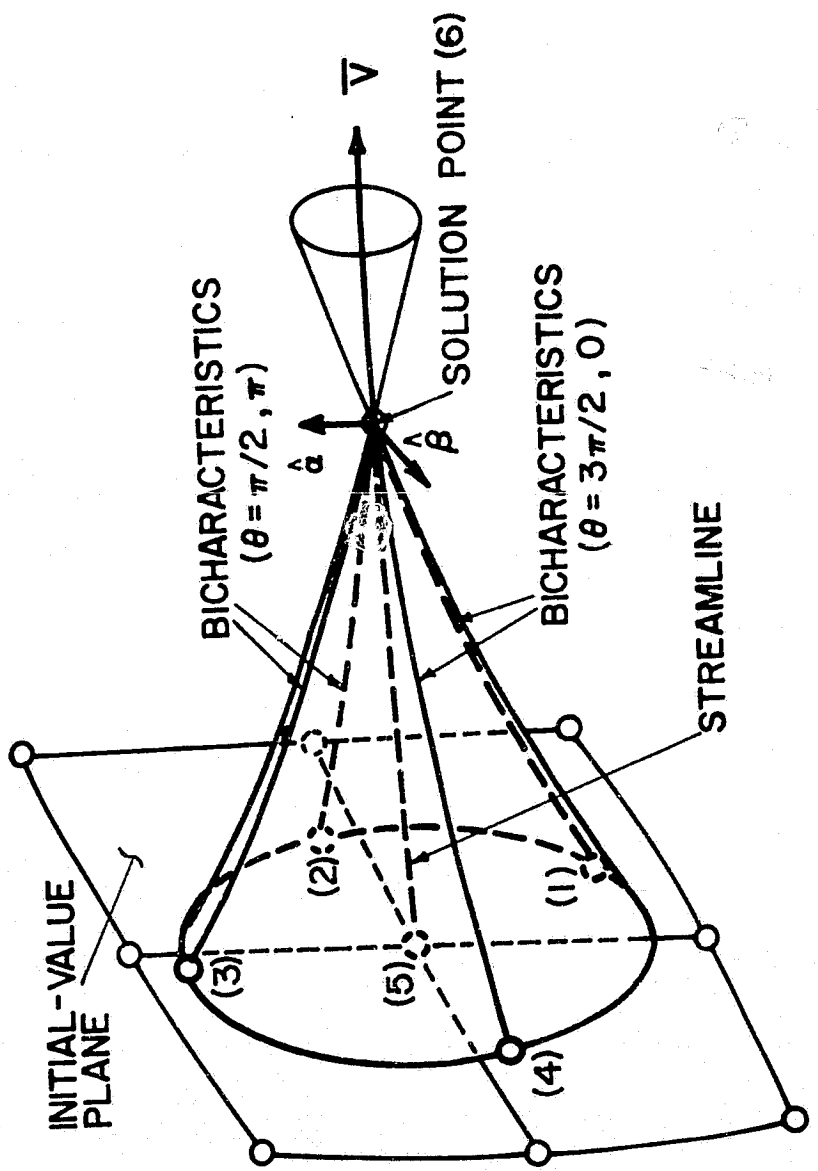

FIGURE E.I. INTERIOR POINT COMPUTATIONAL NETWORK

In addition to using interpolated values for the flow properties at points (1) to (4) in Figure E.1, interpolated values are also employed at point (5), the streamline base point, even though this is a field solution point. As shown by Ranson, et al. (9), this interpolation is required to produce a stable numerical scheme.

The interior point unit process is initiated by locating the solution point, point (6). This is accomplished by extending the streamline forward from point (5) to intersect the solution plane. The coordinates of point (6) are obtained using the following finite difference form of equation (E.1).

$$x_i(6) - x_i(5) = \frac{1}{2}[u_i(5) + u_i(6)][t(6) - t(5)] \qquad (i=1,2,3) \quad (E.12)$$

In applying equation (E.12) for the predictor (first outer iteration), $u_i(6)$ is equated to $u_i(5)$, whereas, for the corrector (ensuing outer iteration), the previously obtained value of $u_i(6)$ is used.

Equation (E.12) is first applied for i=1 (i.e., the x-coordinate direction). The axial step [x(6) - x(5)] is determined prior to the application of the unit process. Hence, the time parameter [t(6) - t(5)] may be obtained. Then, equation (E.12) is applied for i=2 and i=3 to determine y(6) and z(6).

At this point, four bicharacteristics are extended backward from the solution point to intersect the initial-value plane. This is accomplished by applying the following finite difference form of equation (E.4).

$$x_i(6) - x_i(k) = \frac{1}{2}\{[u_i(k) + u_i(6)] + [c(k) + c(6)][\alpha_i \cos\theta(k) + \beta_i \sin\theta(k)]\}[t(6) - t(k)] \qquad (i=1,2,3) \qquad (E.13)$$

In equation (E.13), k denotes the bicharacteristic intersection points in Figure E.1 and has the values 1, 2, 3, and 4 corresponding to the $\theta(k)$ values of 0, $\pi/2$, π, and $3\pi/2$, respectively. The bicharacteristic intersection points are determined in an inner iterative loop. That is, for every outer iteration that is performed to determine the flow properties at point (6), a number of inner iterations are performed to locate points (1) to (4). On the first inner iteration of the predictor (the first outer iteration), $u_i(k)$ and $c(k)$ are equated to $u_i(5)$ and $c(5)$, respectively, for each of the four bicharacteristics. On ensuing inner and outer iterations, the flow properties previously obtained at each of the bicharacteristic intersection points are used. The flow properties at these points are determined by employing the bivariate interpolation polynomial given by equation (E.11). Moreover, as was done for equation (E.12), for the predictor (the first outer iteration), the flow properties at point (6) in equation (E.13) are set equal to those at point (5), whereas, for the corrector (ensuing outer iterations), previously computed values of the flow properties are used at the solution point.

Equation (E.13) is first applied for i=1 (i.e., the x-coordinate direction). The axial step [x(6) - x(k)] is determined prior to the application of the unit process. Thus, the time parameter [t(6) - t(k)] may be obtained for each of the four bicharacteristics. Then, equation (E.13) is applied for i=2 and i=3 to determine y(k) and z(k) for each bicharacteristic.

The parametric unit vectors α_i and β_i appearing in equation (E.13) are arbitrarily fixed at the solution point, point (6). Butler (7), in his original work, held α_i and β_i constant along a bicharacteristic but varied θ in order to insure that the bicharacteristic remained tangent to the Mach cone. Ransom, et al. (9) held θ constant along a bicharacteristic but varied α_i and β_i to satisfy this tangency condition. As noted by Cline, et al. (17), Butler (19) later realized that it is not necessary to satisfy the tangency condition in order to achieve second-order accuracy in the resulting overall numerical algorithm. As a consequence, in the present analysis, both θ and the unit vectors α_i and β_i are held constant along the bicharacteristics. For the external flow field integration, α_i and β_i are selected to straddle the projection of the pressure gradient in the initial-value plane. For the internal flow field integration, α_i and β_i are chosen to straddle the meridional plane.

Once the positions of and the flow properties at points (1) to (4) have been determined for a given outer iteration, the transport forcing functions F_x, F_y, F_z, and F_e are computed at each of these points and at the streamline base point, point (5), as described in Appendix F. Approximations for the transport forcing functions at point (6) are also made at this stage as described in Appendix F. The system of nonlinear compatibility equations is then solved for the flow properties at point (6) as outlined below.

The compatibility equations valid along a streamline are given by equations (E.2) and (E.3). Writing those relations in finite difference form yields

$$[P(6) - P(5)]/[t(6) - t(5)] - \frac{1}{2}[a^2(5) + a^2(6)][\rho(6) - \rho(5)]/[t(6) - t(5)] = \frac{1}{2}[F_e(5) + F_e(6)] \quad (E.14)$$

$$[P(6) - P(5)]/[t(6) - t(5)] + \frac{1}{2}[\rho(5)u_i(5) + \rho(6)u_i(6)][u_i(6) - u_i(5)]/[t(6) - t(5)] = \frac{1}{2}[u_i(5)F_i(5) + u_i(6)F_i(6)] \quad (E.15)$$

The noncharacteristic equation, given by equation (E.9), is also applied along a streamline. Writing that equation in finite difference form gives

$$[P(6) - P(5)]/[t(6) - t(5)] = \frac{1}{2}[\sigma(5) + \sigma(6)] - \frac{1}{2}\rho(5)c^2(5)(\alpha_i\alpha_j + \beta_i\beta_j)\partial u_i/\partial x_j(5) - \frac{1}{2}\rho(6)c^2(6)(\alpha_i\alpha_j + \beta_i\beta_j)\partial u_i/\partial x_j(6) \quad (E.16)$$

In equation (E.16), σ is given by equation (E.10), and $\partial u_i/\partial x_j(k)$ denotes the appropriate partial derivative evaluated at point (k) in Figure E.1. Partial derivatives taken with respect to y and z are found by analytically differentiating equation (E.11). Partial derivatives taken with respect to x are then found by using the governing partial differential equations.

The compatibility equation valid along a bicharacteristic is given by equation (E.6). For θ values of 0, $\pi/2$, π, and $3\pi/2$, equation (E.6) becomes

$$\frac{dP}{dt_1} + \rho c\alpha_i \frac{du_i}{dt_1} = \Phi_1 - \rho c^2 \beta_i\beta_j \frac{\partial u_i}{\partial x_j} \quad (E.17)$$

$$\frac{dP}{dt_2} + \rho c \beta_i \frac{du_i}{dt_2} = \Phi_2 - \rho c^2 \alpha_i \alpha_j \frac{\partial u_i}{\partial x_j} \tag{E.18}$$

$$\frac{dP}{dt_3} - \rho c \alpha_i \frac{du_i}{dt_3} = \Phi_3 - \rho c^2 \beta_i \beta_j \frac{\partial u_i}{\partial x_j} \tag{E.19}$$

$$\frac{dP}{dt_4} - \rho c \beta_i \frac{du_i}{dt_4} = \Phi_4 - \rho c^2 \alpha_i \alpha_j \frac{\partial u_i}{\partial x_j} \tag{E.20}$$

In equations (E.17) to (E.20), the operator $d(\ )/dt_k$ denotes differentiation along the bicharacteristic corresponding to $\theta(k)$, and Φ_k is determined from equation (E.7). Writing equations (E.17) to (E.20) in finite difference form yields

$$\begin{aligned}
&[P(6) - P(1)]/[t(6) - t(1)] + \tfrac{1}{2}[\rho(1)c(1) \\
&\quad + \rho(6)c(6)]\alpha_i[u_i(6) - u_i(1)]/[t(6) - t(1)] \\
&\quad = \tfrac{1}{2}[\Phi_1(1) + \Phi_1(6)] - \tfrac{1}{2}\rho(1)c^2(1)\beta_i\beta_j\partial u_i/\partial x_j(1) \\
&\quad - \tfrac{1}{2}\rho(6)c^2(6)\beta_i\beta_j\partial u_i/\partial x_j(6)
\end{aligned} \tag{E.21}$$

$$\begin{aligned}
&[P(6) - P(2)]/[t(6) - t(2)] + \tfrac{1}{2}[\rho(2)c(2) \\
&\quad + \rho(6)c(6)]\beta_i[u_i(6) - u_i(2)]/[t(6) - t(2)] \\
&\quad = \tfrac{1}{2}[\Phi_2(2) + \Phi_2(6)] - \tfrac{1}{2}\rho(2)c^2(2)\alpha_i\alpha_j\partial u_i/\partial x_j(2) \\
&\quad - \tfrac{1}{2}\rho(6)c^2(6)\alpha_i\alpha_j\partial u_i/\partial x_j(6)
\end{aligned} \tag{E.22}$$

$$[P(6) - P(3)]/[t(6) - t(3)] - \frac{1}{2}[\rho(3)c(3) + \rho(6)c(6)]\alpha_i[u_i(6) - u_i(3)]/[t(6) - t(3)] = \frac{1}{2}[\Phi_3(3) + \Phi_3(6)] - \frac{1}{2}\rho(3)c^2(3)\beta_i\beta_j\partial u_i/\partial x_j(3) - \frac{1}{2}\rho(6)c^2(6)\beta_i\beta_j\partial u_i/\partial x_j(6) \quad \text{(E.23)}$$

$$[P(6) - P(4)]/[t(6) - t(4)] - \frac{1}{2}[\rho(4)c(4) + \rho(6)c(6)]\beta_i[u_i(6) - u_i(4)]/[t(6) - t(4)] = \frac{1}{2}[\Phi_4(4) + \Phi_4(6)] - \frac{1}{2}\rho(4)c^2(4)\alpha_i\alpha_j\partial u_i/\partial x_j(4) - \frac{1}{2}\rho(6)c^2(6)\alpha_i\alpha_j\partial u_i/\partial x_j(6) \quad \text{(E.24)}$$

It was noted in Appendix B that only three wave surface compatibility relations are independent. To obtain three independent relations, linear combinations of equations (E.21) to (E.24) and the noncharacteristic relation, equation (E.16), are formed in such a manner as to algebraically eliminate the cross derivative terms at the solution point [i.e., terms containing $\partial u_i/\partial x_j(6)$]. Subtracting equation (E.23) from equation (E.21) yields

$$[P(6) - P(1)]/[t(6) - t(1)] - [P(6) - P(3)]/[t(6) - t(3)]$$

$$+ \frac{1}{2}[\rho(1)c(1) + \rho(6)c(6)]\alpha_i[u_i(6) - u_i(1)]/[t(6) - t(1)]$$

$$+ \frac{1}{2}[\rho(3)c(3) + \rho(6)c(6)]\alpha_i[u_i(6) - u_i(3)]/[t(6) - t(3)]$$

$$= \frac{1}{2}[\Phi_1(1) + \Phi_1(6)] - \frac{1}{2}[\Phi_3(3) + \Phi_3(6)]$$

$$- \frac{1}{2}\rho(1)c^2(1)\beta_i\beta_j\partial u_i/\partial x_j(1) + \frac{1}{2}\rho(3)c^2(3)\beta_i\beta_j\partial u_i/\partial x_j(3) \quad (E.25)$$

Subtracting equation (E.24) from equation (E.22) yields

$$[P(6) - P(2)]/[t(6) - t(2)] - [P(6) - P(4)]/[t(6) - t(4)]$$

$$+ \frac{1}{2}[\rho(2)c(2) + \rho(6)c(6)]\beta_i[u_i(6) - u_i(2)]/[t(6) - t(2)]$$

$$+ \frac{1}{2}[\rho(4)c(4) + \rho(6)c(6)]\beta_i[u_i(6) - u_i(4)]/[t(6) - t(4)]$$

$$= \frac{1}{2}[\Phi_2(2) + \Phi_2(6)] - \frac{1}{2}[\Phi_4(4) + \Phi_4(6)]$$

$$- \frac{1}{2}\rho(2)c^2(2)\alpha_i\alpha_j\partial u_i/\partial x_j(2) + \frac{1}{2}\rho(4)c^2(4)\alpha_i\alpha_j\partial u_i/\partial x_j(4) \quad (E.26)$$

Adding equations (E.21) and (E.22) and subtracting equation (E.16) from the sum yields

$$[P(6) - P(1)]/[t(6) - t(1)] + [P(6) - P(2)]/[t(6) - t(2)]$$

$$- [P(6) - P(5)]/[t(6) - t(5)]$$

$$+ \frac{1}{2}[\rho(1)c(1) + \rho(6)c(6)]\alpha_i[u_i(6) - u_i(1)]/[t(6) - t(1)]$$

$$+ \frac{1}{2}[\rho(2)c(2) + \rho(6)c(6)]\beta_i[u_i(6) - u_i(2)]/[t(6) - t(2)]$$

$$= \frac{1}{2}[\Phi_1(1) + \Phi_1(6)] + \frac{1}{2}[\Phi_2(2) + \Phi_2(6)] - \frac{1}{2}[\sigma(5) + \sigma(6)]$$

$$- \frac{1}{2}\rho(1)c^2(1)\beta_i\beta_j\partial u_i/\partial x_j(1) - \frac{1}{2}\rho(2)c^2(2)\alpha_i\alpha_j\partial u_i/\partial x_j(2)$$

$$+ \frac{1}{2}\rho(5)c^2(5)(\alpha_i\alpha_j + \beta_i\beta_j)\partial u_i/\partial x_j(5) \qquad \text{(E.27)}$$

Equations (E.14), (E.15), (E.25), (E.26), and (E.27) are the five finite difference equations which are used to solve for the flow properties u(6), v(6), w(6), P(6), and ρ(6). Since these equations are nonlinear, an iterative scheme is required to obtain the solution. On the first outer iteration (the predictor), all of the flow properties at point (6) appearing in the coefficients of the derivatives in the above set of equations are set equal to the respective properties at point (5). This produces a system of simultaneous linear equations which is solved using a Gaussian elimination method with complete pivoting (18). On ensuing corrector applications (outer iterations), previously computed values for the flow properties at point (6) are employed in the scheme. This method is similar to the Euler predictor-corrector algorithm used to obtain the solution for initial-value problems for ordinary differential equations, and can be shown to have second-order accuracy either by direct numerical calculation (9) or by substituting an exact solution into the difference equations and expanding the resulting terms in a Taylor series and thereby determining the truncation error. The iterative scheme is terminated when all five flow properties at point (6) have converged to within specified tolerances.

5. SOLID BOUNDARY POINT UNIT PROCESS

Figure E.2 is a depiction of the computational network used in determining the solution for a typical point on a solid boundary. The point notation used in Figure E.2 is the same as that used in Figure E.1 (interior point scheme). In this unit process, however, point (4), corresponding to the bicharacteristic with $\theta = 3\pi/2$, falls outside of the flow field and cannot be employed. Furthermore, the streamline points (5) and (6) lie on the stream surface formed by the solid boundary. The formulations used for representing the solid boundaries are presented in Appendix D.

The boundary condition used in this unit process is simply that the flow velocity component normal to the wall equals a specified constant C. Let n_{bi} (i=1,2,3) denote the x, y, and z components, respectively, of the outward unit normal to the solid boundary surface. Then, the appropriate boundary condition may be written as

$$u_i(6)\ n_{bi}(6) = C \qquad \text{(E.28)}$$

The solid boundary point unit process is virtually identical to the interior point unit process, except that the wave surface compatibility equation valid along the bicharacteristic corresponding to $\theta = 3\pi/2$ is not employed. That equation is replaced by equation (E.28). Thus, the system of compatibility equations used for determining the solution at a solid boundary point consists of equations (E.14), (E.15), (E.25), (E.27), and (E.28). This system of equations is solved using the same iterative scheme that was employed in the interior point solution.

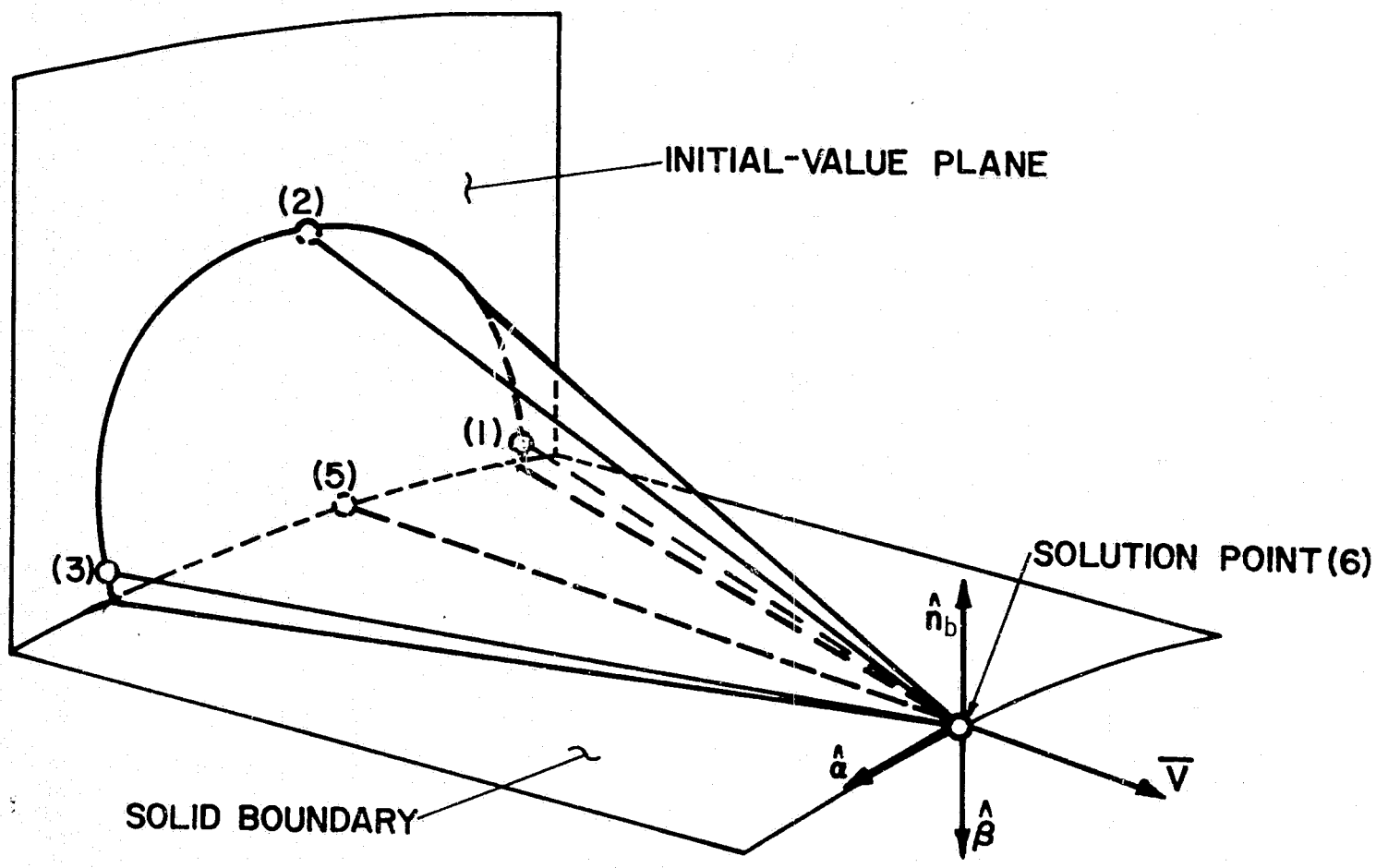

FIGURE E.2. SOLID BOUNDARY POINT COMPUTATIONAL NETWORK

The location of the solution point, point (6) in Figure E.2, obtained by applying the finite difference form of the streamline equation, equation (E.12), is adjusted along the projection of the body normal in the solution plane so that the solution point lies on the solid boundary. The orientation of the parametric unit vectors α_i and β_i is selected such that $\beta_i = - n_{bi}$ (i=1,2,3), and α_i (i=1,2,3) is found by employing the orthonormal relations between α_i, β_i, and u_i/q. This selection for the reference vector set produces a computational network in which the bicharacteristics corresponding to $\theta = 0$, $\pi/2$, and π intersect the initial-value plane for convex boundaries. For concave boundaries, those bicharacteristics intersect an extrapolation of the initial-value plane (the required extrapolation is assumed to have an error third-order in step size). The bicharacteristics corresponding to $\theta = 0$ and π lie in the elemental plane which is tangent to the solid boundary at point (6).

6. BOW SHOCK WAVE POINT UNIT PROCESS

A depiction of the computational network used in determining the solution for a typical bow shock wave point is given in Figure E.3. A segment of the shock wave surface extending from the initial-value plane to the solution plane is shown in this figure. The space curve (A) is defined by the intersection of the shock wave with the initial-value plane, whereas, space curve (B) is defined by the intersection of the shock wave with the solution plane. The axial distance between the initial-value plane and the solution plane is determined by the application of the CFL stability criterion.

The bow shock wave solution point is denoted by point (2) in Figure E.3. The flow properties upstream of the shock wave are known

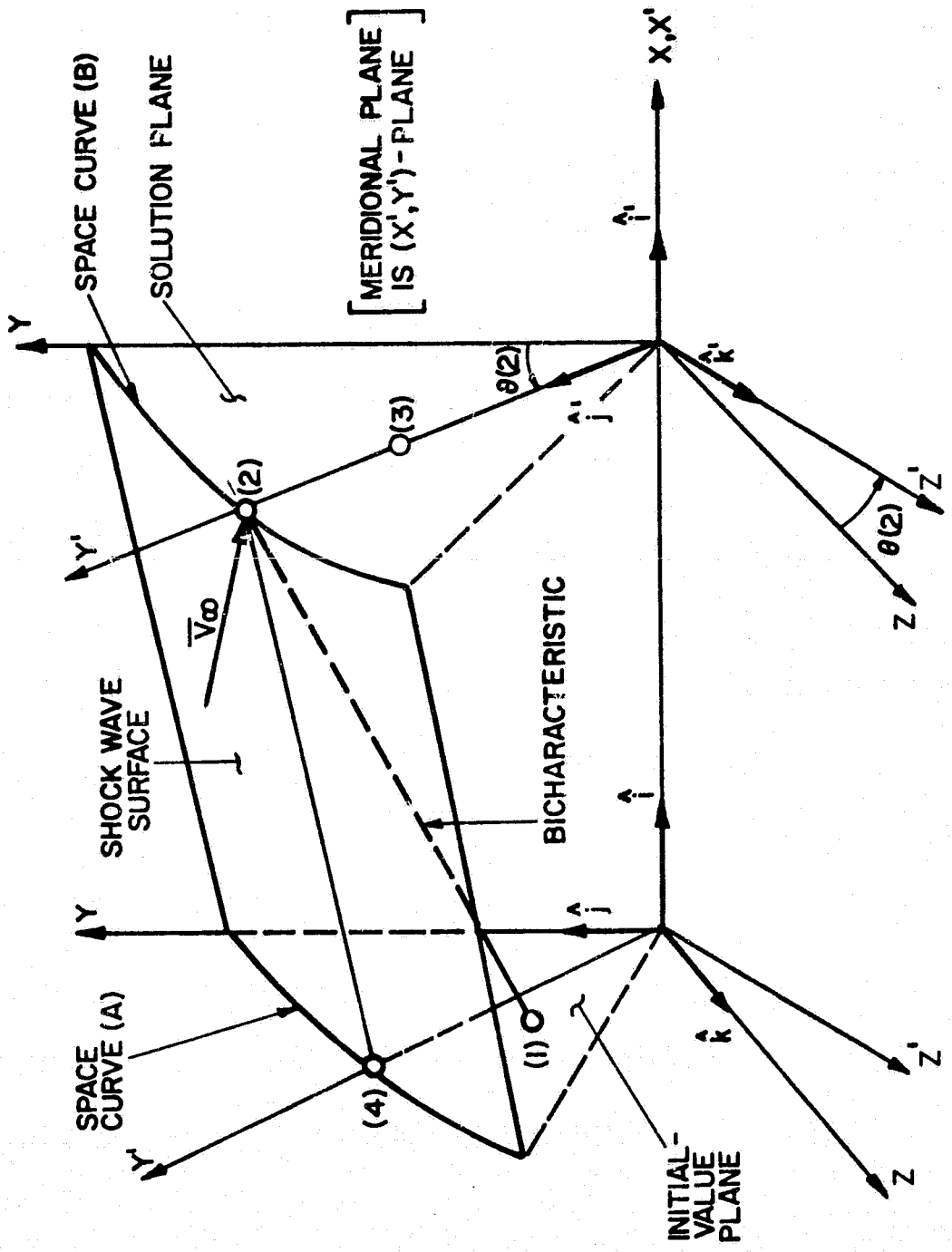

FIGURE E.3. BOW SHOCK WAVE POINT COMPUTATIONAL NETWORK

a priori. Hence, in the following discussion, the flow properties u(2), v(2), w(2), P(2), and $\rho(2)$ refer to the properties at point (2) downstream of the shock wave. Point (1) is the intersection point of a rearward-running bicharacteristic with the initial-value plane. This bicharacteristic is extended backward from the solution point. Point (3) is an interior point in the solution plane which is used to define the meridional plane in which the shock wave solution point lies. Point (4) is the intersection point of space curve (A) with the meridional plane which passes through points (2) and (3).

In this unit process, a local cartesian coordinate system is employed for the description of the orientation of the local shock wave surface. This local coordinate system has coordinates x', y', and z', where x' is coincident with the x-axis, y' is in the radial direction corresponding to the meridional plane which subtends an angle θ with the (x,y)-plane, and z' is normal to the (x',y')-plane (see Figure E.3). The unit vectors in the x, y, and z directions are denoted by $\hat{i}$, $\hat{j}$, and $\hat{k}$, respectively, whereas, the unit vectors in the x', y', and z' directions are denoted by $\hat{i}'$, $\hat{j}'$, and $\hat{k}'$, respectively. A vector quantity $\overline{A}$ may be represented in these coordinate systems by

$$\overline{A} = A_x\hat{i} + A_y\hat{j} + A_z\hat{k} \tag{E.29}$$

$$\overline{A} = A_{x'}\hat{i}' + A_{y'}\hat{j}' + A_{z'}\hat{k}' \tag{E.30}$$

The relationships between the respective components in equations (E.29) and (E.30) are given by

$$A_{x'} = A_x \tag{E.31}$$

$$A_{y'} = A_y\cos\theta + A_z\sin\theta \tag{E.32}$$

$$A_{z'} = A_z\cos\theta - A_y\sin\theta \tag{E.33}$$

$$A_x = A_{x'} \tag{E.34}$$

$$A_y = A_{y'}\cos\theta - A_{z'}\sin\theta \tag{E.35}$$

$$A_z = A_{z'}\cos\theta + A_{y'}\sin\theta \tag{E.36}$$

The orientation of the local shock wave surface is specified by a set of unit vectors referenced to the (x',y',z')-system. This set of unit vectors, illustrated in Figure E.4, consists of a unit vector $\hat{n}_s$ which is normal to the shock wave surface and two unit vectors $\hat{\ell}$ and $\hat{t}$ which are tangent to this surface. The tangential unit vector $\hat{t}$ lies in the meridional plane [(x',y')-plane], subtends an angle ϕ with the x'-axis, and is defined by the intersection of the shock wave with the meridional plane at point (P). The tangential unit vector $\hat{\ell}$ lies in the transverse plane [(y',z')-plane], subtends an angle α with the z'-axis, and is defined by the intersection of the shock wave with the transverse plane at point (P). The tangential vectors $\hat{t}$ and $\hat{\ell}$ are therefore given by

$$\hat{t} = \cos\phi\ \hat{i}' + \sin\phi\ \hat{j}' \tag{E.37}$$

$$\hat{\ell} = \sin\alpha\ \hat{j}' + \cos\alpha\ \hat{k}' \tag{E.38}$$

The shock wave normal unit vector, denoted by $\hat{n}_s$, is given by

$$\hat{n}_s = \hat{\ell} \times \hat{t}/|\hat{\ell} \times \hat{t}| \tag{E.39}$$

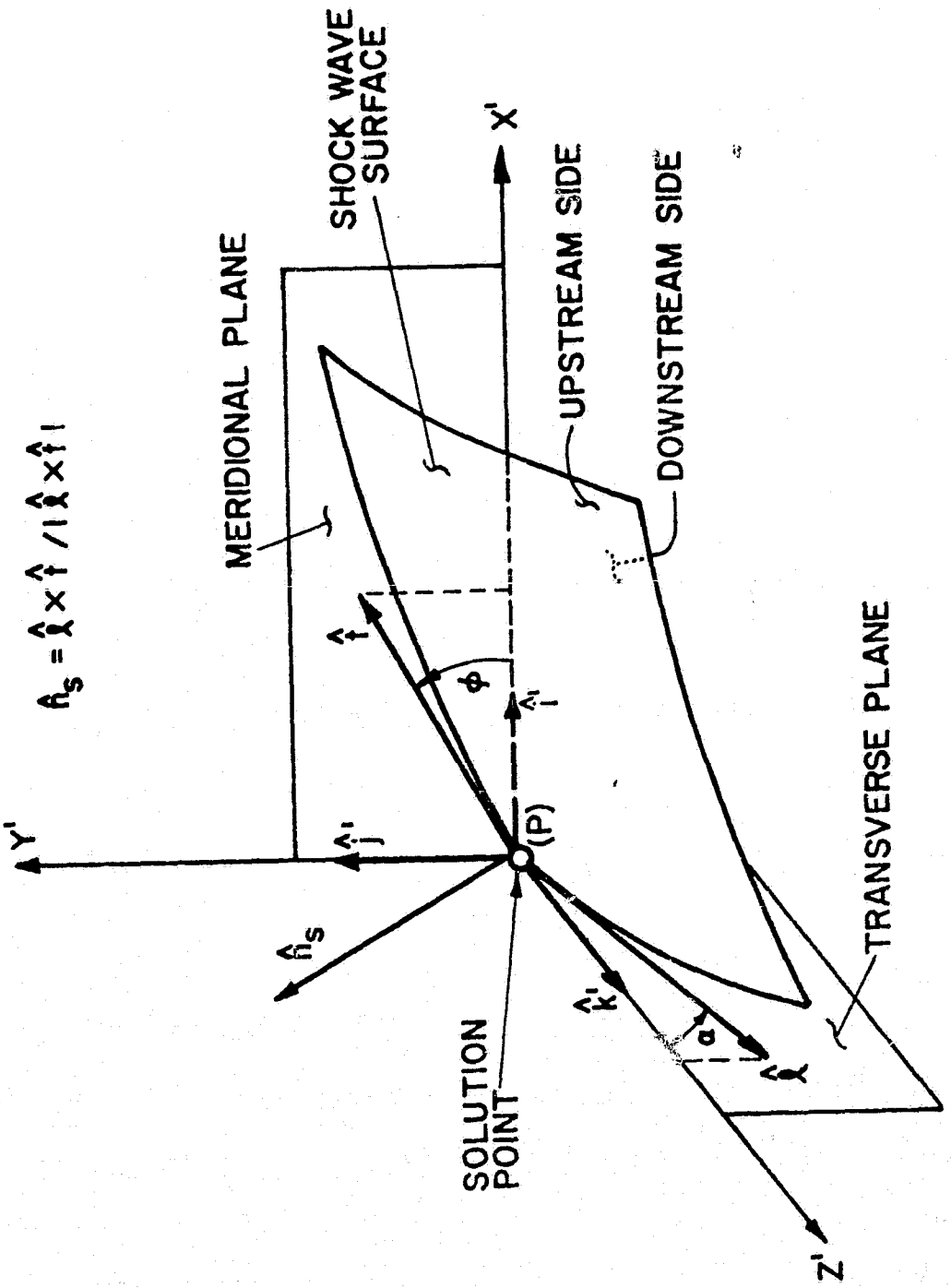

FIGURE E.4. UNIT VECTORS FOR SPECIFICATION OF SHOCK WAVE SURFACE ORIENTATION

The interior point and solid boundary point unit processes achieve second-order accuracy by using local iteration. In local iteration, a corrector application employs previously determined flow property values at the solution point, but does not require using flow property values at other points in the solution plane. The shock wave point unit process, however, requires that global iteration be performed in order to achieve second-order accuracy. In global iteration, a corrector application employs previously determined flow property values not only at the solution point, but also at neighboring points in the solution plane. As a consequence, before a corrector application in global iteration can be performed, the entire solution plane (or at least an appropriate section of it) must be determined by a prior calculation. In practice, since the interior point and solid boundary point schemes require local iteration only, the interior point and solid boundary points are computed first. Then, a prediction for each shock wave solution point is made, thereby giving a tentative solution for all of the shock wave points. Then, a global iteration is conducted for the shock wave solution points using the previously determined field points in the solution plane. In the following discussion, the term "predictor" will refer to the first application of the shock wave point unit process used to obtain an initial estimate of the solution without using field point data in the solution plane. The term "global corrector" will refer to the application of the shock wave point unit process which uses field point data in the solution plane. The shock wave point unit process is now outlined.

The shock wave point unit process is initiated by locating the solution point, point (2) in Figure E.3. The meridional plane in which the solution point lies is arbitrarily selected to contain point (3). Point (3) is the interior solution point adjacent to the shock wave surface whose location is determined prior to the application of the shock wave point unit process. The angle subtended by a meridional plane and the (x,y)-plane is denoted by θ. Then

$$\theta(2) = \theta(3) = \tan^{-1}[z(3)/y(3)] \tag{E.40}$$

Denote the radial position of a point by r. Then the radial position of point (2) is obtained from

$$r(2) = r(4) + [x(2) - x(4)] \tan\left\{\frac{1}{2}[\phi(2) + \phi(4)]\right\} \tag{E.41}$$

where $[x(2) - x(4)]$ is the axial distance between the initial-value plane and the solution plane and is determined by the CFL stability criterion. On the first application of equation (E.41), the shock wave angle $\phi(2)$ is equated to $\phi(4)$, whereas, on ensuing applications, the previously determined value of $\phi(2)$ is used. At point (4), the radial position r(4) and shock wave angle $\phi(4)$ are determined by interpolation using the quadratic univariate formulae

$$r(\theta) = a_1 + a_2\theta + a_3\theta^2 \tag{E.42}$$

$$\phi(\theta) = b_1 + b_2\theta + b_3\theta^2 \tag{E.43}$$

In equations (E.42) and (E.43), the coefficients a_i (i=1,2,3) and b_i (i=1,2,3) are determined by fitting these expressions to three local shock wave solution points on space curve (A) as described in Appendix C.

For the case of axisymmetric flow, or on a plane of flow symmetry in three-dimensional flow, point (4) coincides with a previously determined shock wave solution point so the interpolation would not be required. In general, however, point (4) does not coincide with a known point so the interpolation is necessary.

After the solution point has been located, the shock wave normal unit vector $\hat{n}_s$ at the solution point is found by forming the normalized cross product of the tangential unit vectors $\hat{\ell}$ and $\hat{t}$ [see equation (E.39)]. The tangential vector $\hat{t}$ is obtained by using the current value of $\phi(2)$ in equation (E.37). The tangential vector $\hat{\ell}$ is obtained by using the current value of $\alpha(2)$ in equation (E.38). For either space curve (A) or space curve (B), the value of $\alpha(2)$ may be obtained from

$$\alpha(2) = \tan^{-1}\left[\frac{1}{r}\frac{dr}{d\theta}\right]_{\theta(2)} \tag{E.44}$$

For a predictor application, the analytical form of $r(\theta)$ used in equation (E.44) is given by equation (E.42) applied along space curve (A), whereas, for a global corrector application, $r(\theta)$ is obtained from equation (E.42) applied along space curve (B).

After the shock wave normal unit vector has been determined, the local Hugoniot equations may be applied across the shock wave, thereby yielding a solution for the flow properties $u(2)$, $v(2)$, $w(2)$, $P(2)$, and $\rho(2)$. In general, the local Hugoniot equations take the form (16)

$$\rho_u \tilde{V}_{nu} = \rho_d \tilde{V}_{nd} \tag{E.45}$$

$$P_u + \rho_u \tilde{V}^2_{nu} = P_d + \rho_d \tilde{V}^2_{nd} \tag{E.46}$$

$$\tilde{V}_{tu} = \tilde{V}_{td} \tag{E.47}$$

$$\tilde{V}_{\ell u} = \tilde{V}_{\ell d} \tag{E.48}$$

$$h_u + q_u^2/2 = h_d + q_d^2/2 \tag{E.49}$$

$$h = h(P,\rho) \tag{E.50}$$

In equations (E.45) to (E.50), h is the enthalpy per unit mass, q is the velocity magnitude ($q^2 = u^2 + v^2 + w^2$), $\tilde{V}_n$ is the velocity component in the $-\hat{n}_s$ direction, $\tilde{V}_t$ is the velocity component in the $\hat{t}$ direction, $\tilde{V}_\ell$ is the velocity component in the $\hat{\ell}$ direction, and the subscripts u and d denote the properties on the upstream and downstream sides of the shock wave, repsectively. Equations (E.45) to (E.50) are solved simultaneously for the downstream flow properties. To obtain the velocity components $\tilde{V}_{nu}$, $\tilde{V}_{tu}$, and $\tilde{V}_{\ell u}$, the upstream velocity vector is first transformed from the (x,y,z)-system to the (x',y',z')-system using equations (E.31) to (E.33), after which the appropriate dot products are formed with $-\hat{n}_s$, $\hat{t}$, and $\hat{\ell}$. Similarly, the downstream velocity components $\tilde{V}_{nd}$, $\tilde{V}_{td}$, and $\tilde{V}_{\ell d}$ are transformed back to the (x,y,z)-system after the local Hugoniot equations have been applied.

In the computer program, the local Hugoniot equations are contained in a separate subroutine. The assumed thermodynamic model is that of a thermally and calorically perfect gas. Other thermodynamic models may be used by suitably modifying the existing subroutine or replacing it. For the assumed model of a thermally and calorically perfect gas, the pressure ratio across the shock wave is given by

$$\frac{P_d}{P_u} = \frac{2\gamma}{\gamma + 1} M_{nu}^2 - \frac{\gamma - 1}{\gamma + 1} \tag{E.51}$$

where M_{nu} is the incident normal Mach number given by

$$M_{nu} = \tilde{V}_{nu}/a_u \tag{E.52}$$

and γ is the specific heat ratio. Using the result of equation (E.51), the density ratio across the shock wave is given by

$$\frac{\rho_d}{\rho_u} = \frac{(\gamma + 1)/(\gamma - 1) + (P_u/P_d)}{1 + [(\gamma + 1)/(\gamma - 1)](P_u/P_d)} \tag{E.53}$$

With the downstream pressure and density determined, the downstream normal velocity component $\tilde{V}_{nd}$ may be obtained from equation (E.46), and the tangential downstream velocity components $\tilde{V}_{td}$ and $\tilde{V}_{\ell d}$ may be computed from equations (E.47) and (E.48). Transformation of the downstream velocity components back into the (x,y,z)-system yields the required flow properties at the solution point.

At this stage, a rearward-running bicharacteristic is extended from the solution point, point (2), back to the initial-value plane, intersecting this plane at point (1), as illustrated in Figure E.3. This is accomplished by employing the following finite difference form of equation (E.4) evaluated for the parametric angle $\theta = \pi/2$.

$$x_i(2) - x_i(1) = \frac{1}{2}\left\{[u_i(1) + u_i(2)] + [c(1) + c(2)]\beta_i\right\}[t(2) - t(1)] \qquad (i=1,2,3) \tag{E.54}$$

As in the interior point and solid boundary point schemes, an inner iteration is performed to locate point (1). On the first application

of equation (E.54), the flow properties at point (1) are equated to those at point (2), whereas, on ensuing applications, previously obtained values of the flow properties at point (1) are used. The flow property values at point (1) are found by employing the bivariate interpolation polynomial given by equation (E.11). The coefficients in equation (E.11) are obtained by a least squares fit of nine data points in the initial-value plane using a boundary-type stencil as described in Appendix C.

Equation (E.54) is first applied for i=1 (i.e., the x-coordinate direction). Since the axial step [x(2) - x(1)] is known from the application of the CFL stability criterion, the time parameter [t(2) - t(1)] may be determined. Then, equation (E.54) is applied for i=2 and i=3 to determine y(1) and z(1). For axisymmetirc flow, or for a plane of flow symmetry in three-dimensional flow, point (1) lies in the meridional plane which contains points (2) and (3). In general, however, for other flow situations, point (1) lies outside of this plane.

The orientation of the parametric unit vector β_i in equation (E.54) is arbitrarily selected such that

$$\beta_3/\beta_2 = \tan[\theta(2)] \tag{E.55}$$

This relation, in conjunction with the orthonormality conditions

$$\beta_i u_i(2) = 0 \tag{E.56}$$

$$\beta_i \beta_i = 1 \tag{E.57}$$

allows the values of β_i (i=1,2,3) to be determined. Since equation

(E.57) is a quadratic equation, a multiplicity of roots exist for the β_i (i=1,2,3). The roots are chosen such that point (1) lies underneath the shock wave in the initial-value plane. Once the values of β_i (i=1,2,3) are determined, the values of α_i (i=1,2,3) are found through use of the orthogonality relation between α_i, β_i, and u_i/q (i.e., $\hat{\alpha} = \hat{\beta} \times \overline{V}/q$).

After the position of and the flow properties at point (1) have been determined, the transport forcing functions F_x, F_y, F_z, and F_e are computed at point (1) as described in Appendix F. Approximations for the transport forcing functions are also made at point (2) at this time as described in Appendix F.

At this stage, the wave surface compatibility equation corresponding to the parametric angle $\theta = \pi/2$ is applied between points (1) and (2). From equation (E.6), the appropriate equation is

$$\frac{dP}{dt} + \rho c \beta_i \frac{du_i}{dt} = \Phi_{\pi/2} - \rho c^2 \alpha_i \alpha_j \frac{\partial u_i}{\partial x_j} \qquad \text{(E.58)}$$

where $\Phi_{\pi/2}$ is obtained from equation (E.7) for the parametric angle $\theta = \pi/2$. Writing equation (E.58) in finite difference form, solving for the pressure at point (2), and denoting this pressure by P*(2), the following equation is obtained.

$$\begin{aligned} P^*(2) = P(1) &+ \tfrac{1}{2}[\Phi_{\pi/2}(1) + \Phi_{\pi/2}(2)][t(2) - t(1)] \\ &- \tfrac{1}{2}[\rho(1)c^2(1)\alpha_i\alpha_j\partial u_i/\partial x_j(1) \\ &+ \rho(2)c^2(2)\alpha_i\alpha_j\partial u_i/\partial x_j(2)][t(2) - t(1)] \\ &- \tfrac{1}{2}[\rho(1)c(1) + \rho(2)c(2)]\beta_i[u_i(2) - u_i(1)] \end{aligned} \qquad \text{(E.59)}$$

Note that the cross-derivative terms $[\partial u_i/\partial x_j(k)]$ in equation (E.59) appear at both point (1) in the initial-value plane and at point (2) in the solution plane. In general, these terms can be evaluated by employing equation (E.11) fit to nine data points in the appropriate plane, differentiating this expression analytically to obtain partial derivatives with respect to y and z, and then using the governing partial differential equations to obtain the required partial derivatives with respect to x. On the predictor application of the shock wave point unit process, the flow property field in the solution plane is not known, so the cross-derivatives at point (2) are set equal to those at point (1). On a global corrector application of the shock wave point unit process, the cross deriatives at point (2) are evaluated in the manner just described.

The pressure P(2) is calculated from the local Hugoniot equations. The pressure P*(2) is calculated from equation (E.59). The difference between P(2) and P*(2) is driven to within a specified tolerance of zero by employing a one-dimensional secant iteration scheme which iterates on the shock wave angle $\phi(2)$. Two initial estimates of $\phi(2)$ ar equired to initiate the subiteration.

The shock wave point unit process is first applied as a predictor for each shock wave solution point. In this application, the value of α used in equation (E.38) is obtained by curve fitting points along space curve (A), and the cross-derivative terms at the shock wave solution point are equated to those terms at the bicharacteristic base

point in the initial-value plane, point (1). After a tentative solution is obtained for all of the shock wave points, a number of global corrector applications are performed. Here, the value of α used in equation (E.38) is based on data along space curve (B), and the cross-derivative terms at the shock wave solution point are evaluated at that point. The resulting overall scheme has second-order accuracy when the global correction is performed. The global iteration is terminated when successive values of α have converged at each of the shock wave solution points.

In the course of the program development, an alternative algorithm to the one just presented was devised in an attempt to compute the bow shock wave solution points. In this alternative scheme, a multiplicity of bicharacteristics were used, and, like the interior point or solid boundary point unit processes, linear combinations of the wave surface compatibility equations were formed as to algebraically eliminate the cross-derivative terms at the solution point. A two-dimensional Newton-Raphson method was devised for determining the angles ϕ and α explicitly, and second-order accuracy was achieved without resorting to global correction. This scheme was successful in computing axisymmetric flows, but an apparent instability arose when attempting to compute three-dimensional flow fields.

7. SOLID BODY-SHOCK WAVE POINT UNIT PROCESS

The solid body-shock wave point unit process is used to determine the flow properties downstream of the shock wave at a point where the shock wave intersects a solid boundary. This unit process is used to determine the solution for the points on the cowl on the downstream side

of the cowl lip shock wave, and for the points on the centerbody or cowl on the downstream side of an internal reflected shock wave. The method of computation is essentially the same for either application and is discussed below. The solution points on the downstream side of the incident shock wave at an internal shock wave reflection are computed using the field-shock wave point unit process which is presented later.

A depiction of the computational network used in the solid body-shock wave point unit process is presented in Figure E.5. A typical solid body-shock wave solution point is denoted by point (P) in this figure. At point (P), the outward unit normal vector to the solid boundary is denoted by $\hat{n}_b$. The locus of solid body-shock wave solution points represents the intersection of the shock wave with the solid boundary, and defines space curve (A) in Figure E.5. The intersection of the shock wave with the meridional plane passing through point (P) is denoted by space curve (B). The tangential unit vectors to space curves (A) and (B) at point (P) are denoted by $\hat{\ell}$ and $\hat{t}$, respectively. The unit normal vector to the shock wave at point (P) is denoted by $\hat{n}_s$.

As was done for the bow shock wave point unit process, the unit vectors $\hat{\ell}$, $\hat{t}$, and $\hat{n}_s$ are referenced to a local cartesian coordinate system (x',y',z'), where again x' is coincident with the x-axis, y' is in the radial direction along the meridian which subtends the angle θ with the (x,y)-plane, and z' is normal to the (x',y')-plane. The relations between the components of a vector in the (x,y,z)-system and in the (x',y',z')-system are given by equations (E.31) to (E.36). As in the bow shock wave point unit process, the tangential unit vector $\hat{t}$ lies

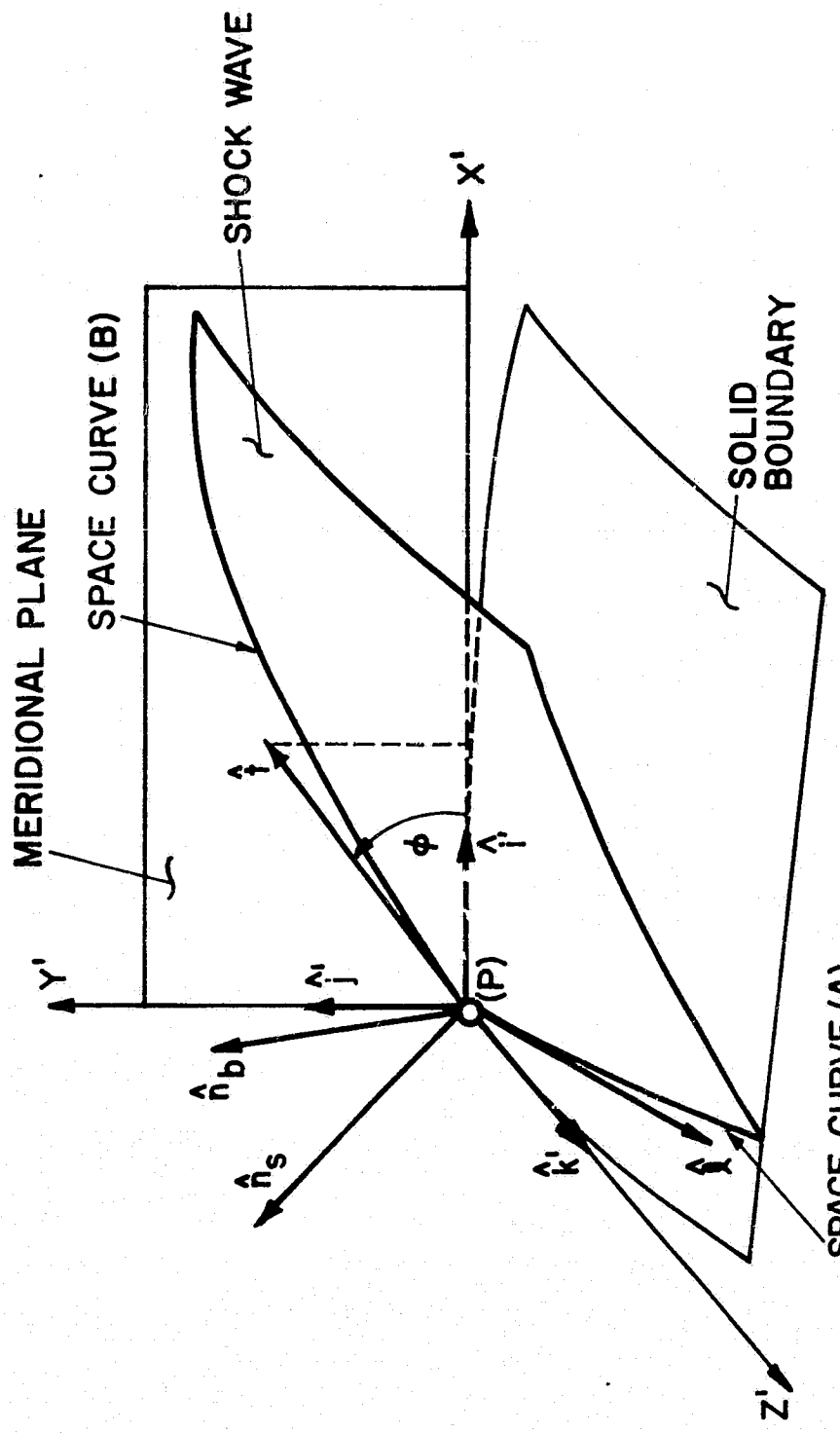

FIGURE E.5. SOLID BODY-SHOCK WAVE POINT COMPUTATIONAL NETWORK

in the meridional plane [(x',y')-plane] and subtends the angle ϕ with the x'-axis. Hence,

$$\hat{t} = \cos\phi\ \hat{i}' + \sin\phi\ \hat{j}' \tag{E.60}$$

Unlike the bow shock wave point unit process, however, the tangential unit vector $\hat{\ell}$ does not, in general, lie in the transverse plane [(y',z')-plane], but rather it may have a nonzero x'-component. This tangential vector along space curve (A) may be represented by

$$\hat{\ell} = \frac{dx'}{ds}\ \hat{i}' + \frac{dy'}{ds}\ \hat{j}' + \frac{dz'}{ds}\ \hat{k}' \tag{E.61}$$

where ds is the differential arc length given by

$$(ds)^2 = (dx')^2 + (dy')^2 + (dz')^2 \tag{E.62}$$

The derivatives in equation (E.61) are obtained by analytically differentiating the expressions

$$x'(\theta) = a_1 + a_2\theta + a_3\theta^2 \tag{E.63}$$

$$y'(\theta) = b_1 + b_2\theta + b_3\theta^2 \tag{E.64}$$

$$z'(\theta) = c_1 + c_2\theta + c_3\theta^2 \tag{E.65}$$

In equations (E.63) to (E.65), the coefficients a_i, b_i, and c_i (i=1,2,3) are obtained by fitting the respective expressions to three points on space curve (A) as described in Appendix C. For the cowl lip shock wave points, space curve (A) is defined by the cowl lip itself since the shock wave is assumed to be attached to the cowl lip. In this case, the x'-component in equation (E.61) is identically zero,

and, as a consequence, $\hat{\ell}$ lies in the transverse plane. Furthermore, if the cowl is axisymmetric, the y'-component is also identically zero. Alternatively, for computing the downstream properties at a reflected internal shock wave, space curve (A) is defined by the intersection of the incident shock wave with the solid boundary. Except for an axisymmetric flow field, or for a point on a plane of flow symmetry in three-dimensional flow, the x'-component in equation (E.61) is nonzero. With the tangential unit vectors determined, the shock wave normal unit vector $\hat{n}_s$ is obtained from equation (E.39).

The solid body-shock wave point unit process is initiated by determining the body normal unit vector $\hat{n}_b$ and the tangential unit vector $\hat{\ell}$ at point (P), expressing both of these vectors in the (x',y',z')-system. Then, an initial estimate is made for the value of ϕ in equation (E.60), and, by use of equation (E.39), the shock wave normal unit vector is obtained. In exactly the same manner as was done in the bow shock wave point unit process, the downstream flow properties at point (P) are computed by use of equations (E.45) to (E.53). At this stage, the velocity normal to the body V_{nb} at point (P) is computed from the equation

$$V_{nb} = u'_d n_{bx'} + v'_d n_{by'} + w'_d n_{bz'} \qquad (E.66)$$

where u'_d, v'_d, and w'_d are the downstream velocity components at point (P), and $n_{bx'}$, $n_{by'}$, and $n_{bz'}$ are the components of the body normal unit vector, both vectors being expressed in terms of the (x',y',z') coordinates. The body normal velocity V_{nb} is reduced to within a tolerance of a specified constant by varying the angle ϕ using a one-dimensional secant iteration procedure. Two initial estimates of ϕ are

required for starting the iterative procedure. Once convergence has been obtained, the downstream velocity components are transformed back into the (x,y,z)-coordinates using equations (E.34) to (E.36).

In the course of the program development, an alternative algorithm to the one just presented was devised to compute the solid body-shock wave points. That algorithm determined the shock normal vector (and thereby the downstream properties) by employing the shock wave relations which link the flow turning angle and the shock wave angle, both these angles being measured from the approach streamline direction in a plane defined by the approach velocity vector and the shock wave normal vector. Since the shock wave normal vector is required to define this plane, an iterative procedure for determining that vector is required in this method. This method was tested and produced results identical to the method described earlier. However, due to the greater complexity of the alternate method, it was not selected for use in the final algorithm.

8. SHOCK-MODIFIED INTERIOR POINT UNIT PROCESSES

In some situations during the computation of the internal flow, the interior point unit process must be applied in a modified form. One such application is illustrated in Figure E.6. In this situation, the Mach cone, with apex at the solution point, intersects not only the initial-value plane but also a solid boundary and an internal shock wave. The point notation used in Figure E.6 is the same as that used in the computational network of the basic interior point scheme, which is illustrated in Figure E.1. The solution point, denoted by point (6)

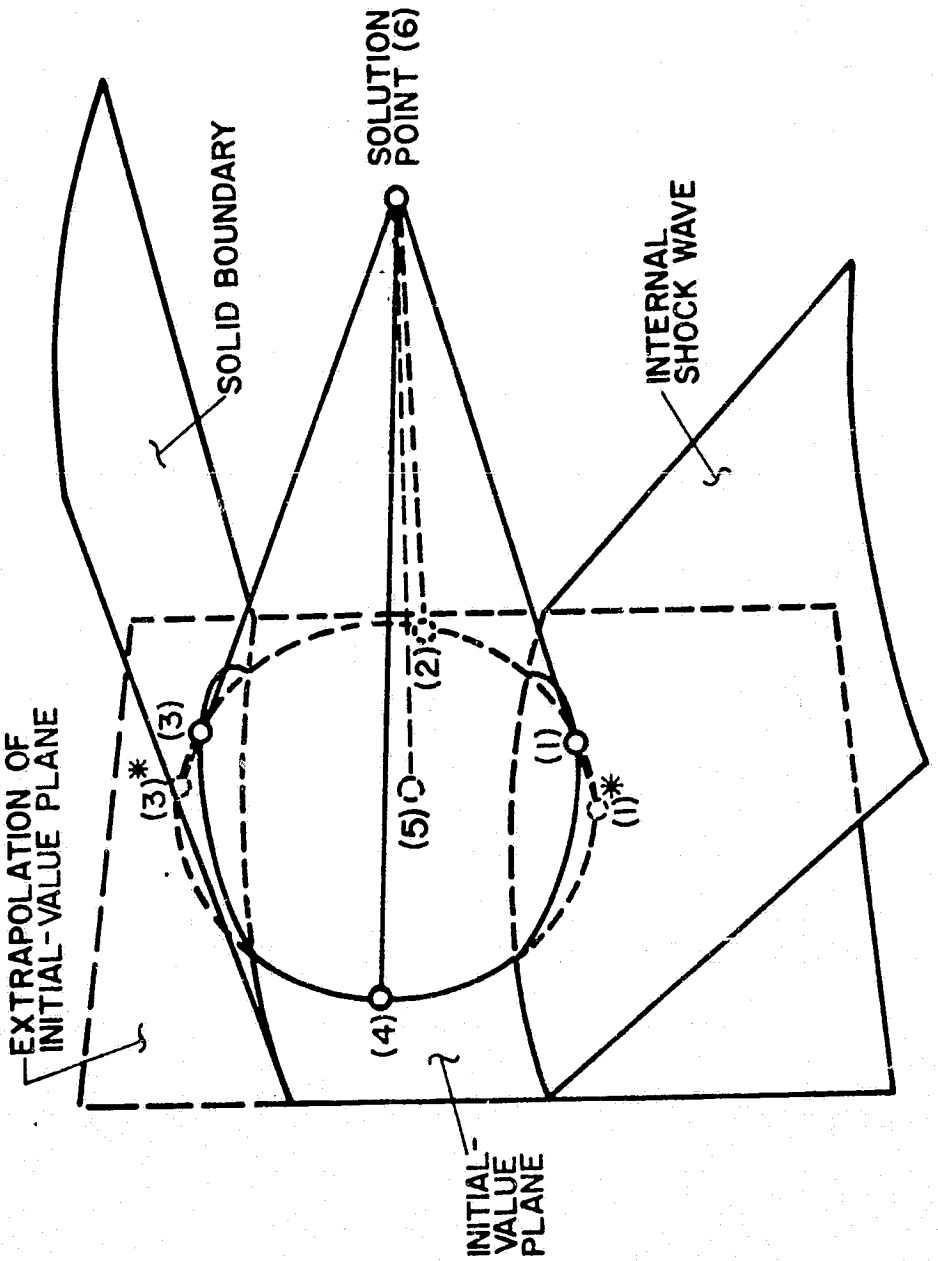

FIGURE E.6. SHOCK-MODIFIED INTERIOR POINT COMPUTATIONAL NETWORK (STREAMLINE BASE POINT ON INITIAL-VALUE PLANE)

in Figure E.6, lies on the current solution plane. Point (5) represents the streamline base point on the initial-value plane. As in the basic interior point unit process, points (1) to (4) represent the bicharacteristic base points. Point (1), in this case, lies on the surface of the internal shock wave, and point (3) lies on the solid boundary. Points (2) and (4) lie on the initial-value plane.

The axial distance between the initial-value plane and the solution plane is determined by either the CFL stability criterion or by the special constraints which apply when an internal shock wave intersects a solid boundary. Those procedures are discussed in Appendix K. In either case, the axial step is determined prior to the application of the unit processes.

In the overall algorithm for the computation of the internal flow, the order of integration is selected so that the shock wave solution points and the body solution points are determined before any attempt is made to obtain the solution at any of the interior field points which lie in the flow field sector that is downstream of the shock wave. As a consequence, the flow property fields on the downstream side of the shock wave and on the stream surface formed by the solid boundary are determined before the solution at an interior point, such as point (6) in Figure E.6, is attempted.

The procedure used to obtain the solution at point (6) in Figure E.6 is almost identical to the basic interior point unit process, which is presented in Section 4 of this appendix. The major difference between the two algorithms is that, in the present case, the bicharacteristic intersection points on the shock wave [point (1)] and on the

solid boundary [point (3)] must be determined in addition to those bi-characteristic intersection points [points (2) and (4)] on the initial-value plane. Along with the location of these points, flow property values and first partial derivatives of the flow properties at these points must also be obtained.

As in the basic interior point unit process, flow property values at points (2) and (4) on the initial-value plane are obtained using the bivariate interpolation polynomial given by equation (E.11). The coefficients in this equation are determined by a least squares fit of nine data points in the initial-value plane as discussed in Appendix C. Flow property values at point (1) on the shock wave surface or at point (3) on the solid boundary surface are obtained using the trivariate interpolation polynomial

$$f(x,y,z) = a_1 + a_2y + a_3z + a_4yz + a_5y^2 + a_6z^2 + a_7xy + a_8xz \qquad (E.67)$$

The coefficients a_i (i=1 to 8) in equation (E.67) are determined by a least squares fit of fourteen data points on either the downstream side of the shock wave for interpolation on that surface, or on the solid boundary for interpolation on that surface. The detailed implementation of equation (E.67) is presented in Appendix C.

An outline of the unit process used to determine the solution at point (6) in Figure E.6 is now presented. The computation is initiated by determining the location of the solution point, point (6), using equation (E.12) in a manner identical to the procedure employed in the basic interior point unit process. After the position of the solution

point has been obtained for a given outer iteration, the four bicharacteristics, corresponding to the values of the parametric angle $\theta = 0, \pi/2, \pi$, and $3\pi/2$ in equation (E.13), are extended rearward from the solution point to the initial-value plane. From the bicharacteristic-initial-value plane intersection point coordinates, denoted by $y^*(k)$ and $z^*(k)$ (k=1 to 4), the radius $r^*(k) = [y^*(k)^2 + z^*(k)^2]^{1/2}$ and the polar angle $\theta^*(k) = \tan^{-1}[z^*(k)/y^*(k)]$ of each intersection point are computed. The radius $r^*(k)$ is then compared to the shock wave radius r_s and the body radius r_b in the meridional plane defined by the polar angle $\theta^*(k)$. The shock wave radius is determined from the univariate interpolation polynomial

$$r_s(\theta) = a_1 + a_2\theta + a_3\theta^2 \qquad \text{(E.68)}$$

where the coefficients a_i (i=1,2,3) are determined by fitting this expression to three shock wave solution points in the initial-value plane as described in Appendix C. The solid body radius r_b is obtained by employing the formulations presented in Appendix D. For the orientation shown in Figure E.6, if $r_s \leq r^*(k) \leq r_b$, the bicharacteristic intersects the initial-value plane and the analysis proceeds as in the basic interior point unit process. If $r^*(k) < r_s$, the bicharacteristic intersects the internal shock wave. In this case, the bicharacteristic base point location on the surface of the shock wave is found by employing the bicharacteristic-surface intersection scheme presented in Appendix D. For a shock wave intersection, that scheme requires that equation (E.68) also be fitted to three shock wave solution points in the current solution plane. If $r^*(k) > r_b$, the bicharacteristic

intersects the solid boundary. The bicharacteristic base point location on the solid boundary is also obtained by using the iterative scheme presented in Appendix D. As in the basic interior point unit process, an inner iteration is performed for locating points (1) to (4). Interpolated values of the flow properties at the respective points are obtained by using either equation (E.11) or equation (E.67), whichever is applicable.

After the bicharacteristic base points, points (1) to (4), have been located, the first partial derivatives of the flow properties with respect to y and z at these points are obtained by analytically differentiating the appropriate interpolation polynomial. In a like manner, these derivatives are also obtained at the streamline base point, point (5). Then, using the governing partial differential equations, the x-partial derivatives of the flow properties are found at points (1) to (5). For any bicharacteristic which intersects the shock wave or the solid boundary, the time parameter [t(6) - t(k)] is found using equation (E.13) applied for i=1 (i.e., the x-coordinate direction) while employing the appropriate intersection coordinates. At this stage, the system of compatibility equations may be solved for the flow properties at point (6) in a manner identical to that employed in the basic interior point scheme.

The situation illustrated in Figure E.6 is quite general. In some instances, there are no bicharacteristic intersections with the solid boundary. Alternatively, there may be no intersections of the bicharacteristics with the internal shock wave. There may be two bicharacteristics intersecting with the shock wave, etc.

Another situation in which the interior point unit process must be applied in a modified form is illustrated in Figure E.7. In this figure, the Mach cone, with apex at the solution point, intersects both the initial-value plane and the internal shock wave. The point notation used in Figure E.7 is the same as that used in Figure E.6. However, in this case, the streamline base point, point (5), does not lie on the initial-value plane, but rather lies on the surface of the internal shock wave.

The location of the streamline base point is obtained by extending the streamline from the initial-value plane to the surface of the shock wave. The point of intersection of the streamline with the shock wave is determined by employing the iterative scheme which is presented in Appendix D for finding a streamline-surface intersection point. That procedure requires that equation (E.68) be applied to three known shock wave solution points in the initial-value plane and three shock wave solution points in the current solution plane. Furthermore, interpolated values of the velocity components are required on the upstream side of the shock wave at the point where the streamline intersects the shock wave. For this purpose, the following linear trivariate interpolation polynomial is employed.

$$f(x,y,z) = a_1 + a_2x + a_3y + a_4z \qquad \text{(E.69)}$$

The coefficients a_i (i=1 to 4) in equation (E.69) are determined by fitting this expression to four data points on the upstream side of the shock wave, as discussed in Appendix C.

After the streamline-shock wave intersection point has been determined, the following fraction is formed

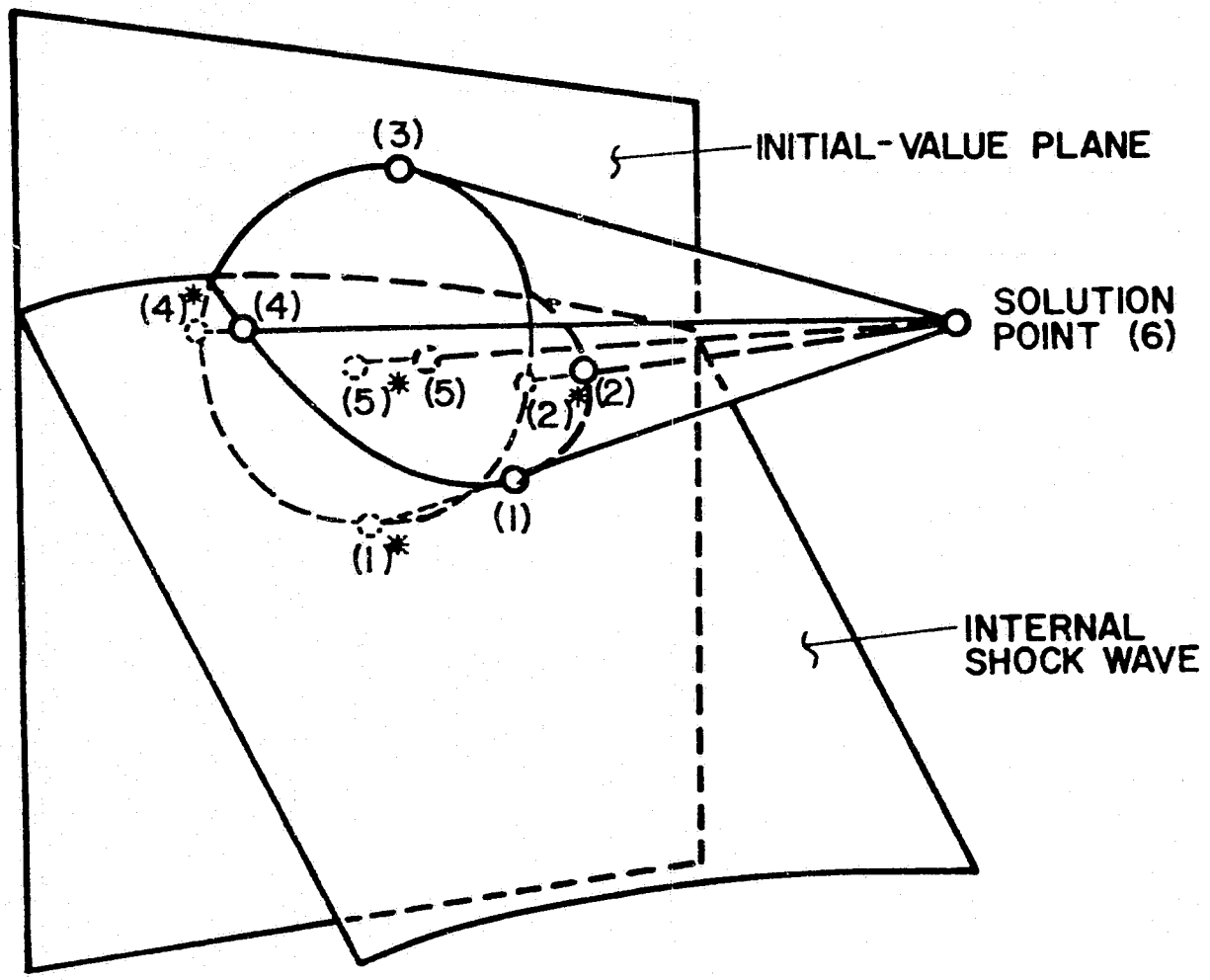

FIGURE E.7. SHOCK-MODIFIED INTERIOR POINT COMPUTATIONAL NETWORK (STREAMLINE BASE POINT ON SHOCK WAVE)

$$\varepsilon = [x_S - x(5)]/(x_S - x_I) \tag{E.70}$$

where x_I and x_S are the axial positions of the initial-value plane and the solution plane, respectively. If ε is greater than a specified minimum value, an interior point unit process is performed on the downstream side of the shock wave. This unit process is almost identical to that used for determining the solution at point (6) in Figure E.6. In this case, however, the streamline formula given by equation (E.12) is applied between the streamline-shock wave intersection point and the solution plane. Interpolated flow property values at point (5) are determined by applying equation (E.67) to fourteen data points on the downstream side of the shock wave.

If, on the other hand, ε is less than the specified minimum value, an interior point unit process on the downstream side of the shock wave is not performed. Instead, the streamline from point (5) is projected onto the solution plane, and the flow properties at the solution point are determined by interpolation in the solution plane. The streamline integration from point (5) to point (6) employs equation (E.12). The flow property values at point (5) are obtained from equation (E.67) applied to fourteen data points on the downstream side of the shock wave. Flow property values at the streamline-solution plane intersection point are determined from the linear bivariate polynomial

$$f(y,z) = a_1 + a_2 y + a_3 z \tag{E.71}$$

The coefficients a_i (i=1,2,3) in equation (E.71) are determined by fitting this expression to three data points in the current solution plane, as described in Appendix C. The order of integration for

determining the internal flow field is specified so that the downstream shock wave points and outer interior points in the downstream flow field sector are determined first. The location of the solution point, in this case, is determined by an iterative loop which is terminated when the y and z coordinates of the projected solution point have converged.

9. SHOCK-MODIFIED SOLID BOUNDARY POINT UNIT PROCESSES

In some situations, the solid boundary point unit process must be applied in a modified form. One such application is illustrated in Figure E.8. In this situation, a portion of the Mach cone, with apex at the solid body solution point, intersects both the initial-value plane and the internal shock wave. The point notation used in Figure E.8 is identical to that used in Figure E.2, which depicts the computational network for the standard body point unit process. The unit process employed in the present case is almost identical to the standard body point unit process. In the present case, however, the bicharacteristic-shock wave intersection is handled in a manner identical to that employed in the shock-modified interior point unit process presented in the previous section.

In some situations, the entire Mach cone intersects the shock wave, as illustrated in Figure E.9. This situation occurs at a body point on the solution plane that is immediately downstream of a solid body-shock wave reflection, or at a body point on the solution plane that is immediately behind the shock wave emanating from the cowl lip. In the former case, the shock wave-solid body intersection is a space curve in three-dimensions, whereas, in the latter case, the shock wave-solid

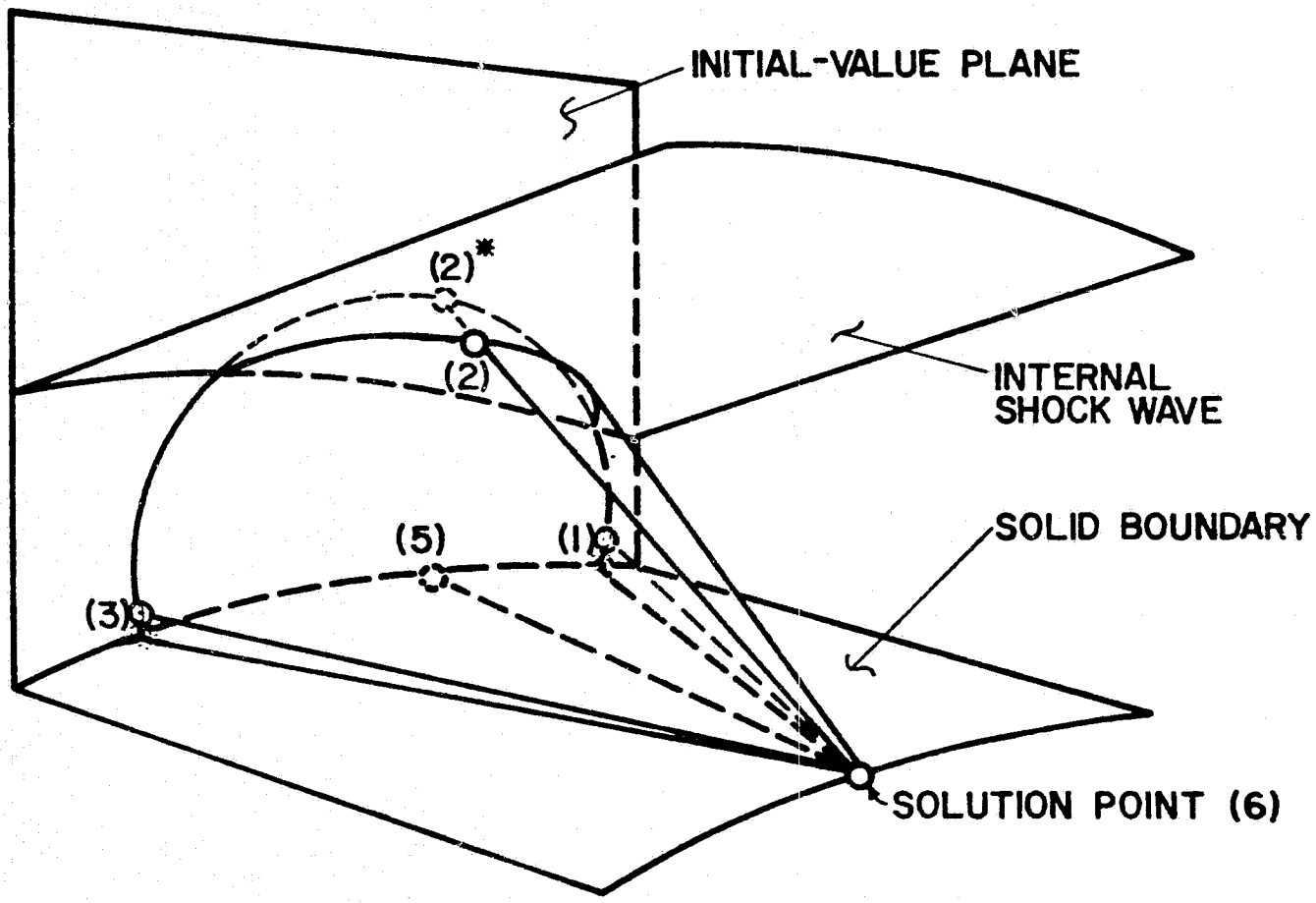

FIGURE E.8. SHOCK-MODIFIED SOLID BOUNDARY POINT COMPUTATIONAL NETWORK (TYPICAL APPLICATION)

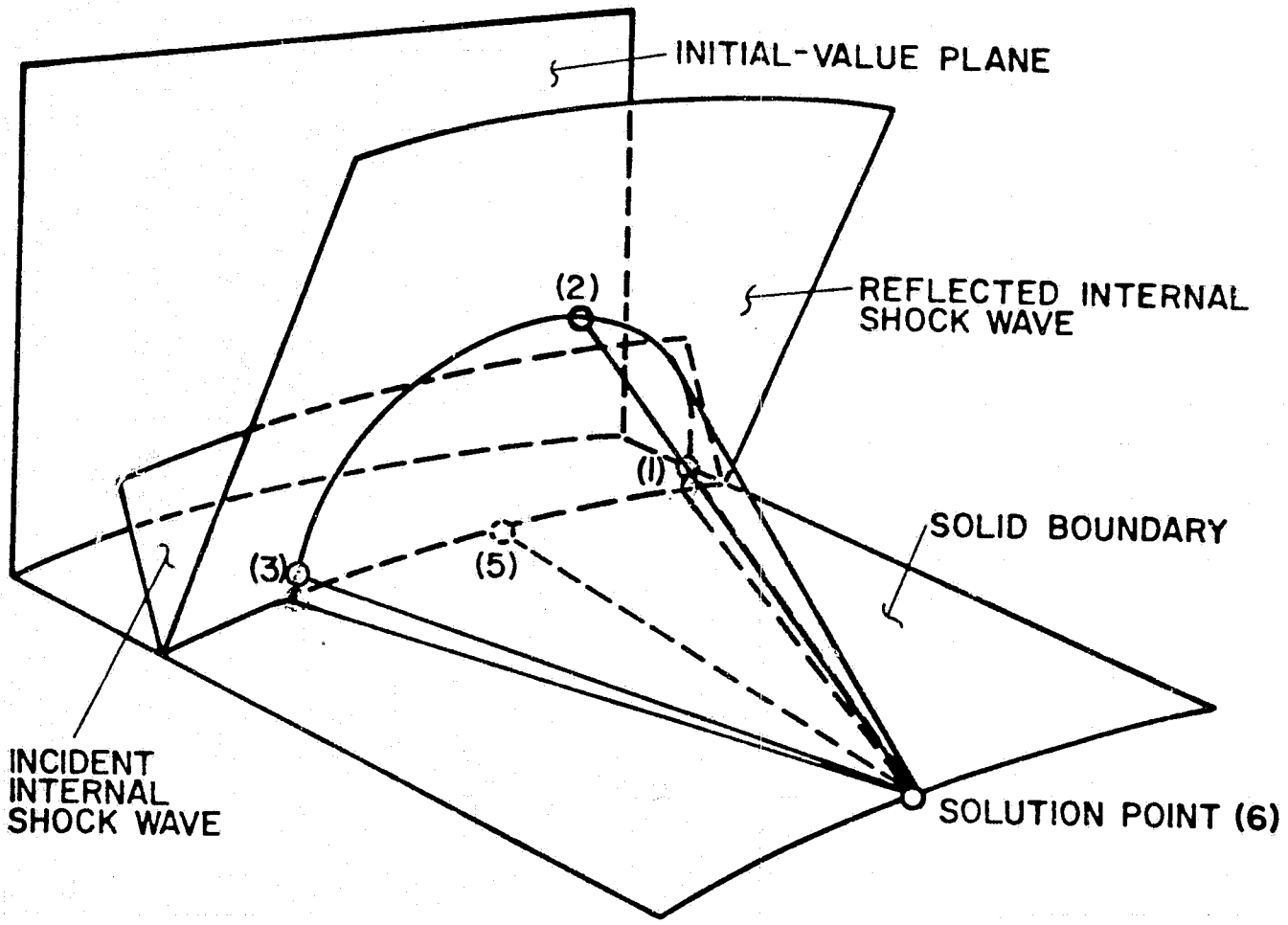

FIGURE E.9. SHOCK-MODIFIED SOLID BOUNDARY POINT COMPUTATIONAL NETWORK (POST SHOCK REFLECTION APPLICATION)

body intersection is a curve in a plane of constant x. The appropriate intersection algorithm is used as presented in Appendix D, and for the most part, procedures identical to those employed in the shock-modified interior point unit process are employed in this case.

10. INTERNAL FLOW FIELD-SHOCK WAVE POINT UNIT PROCESSES

Figure E.10 illustrates the overall computational network used in determining the solution for a typical shock wave point in the internal flow field. To determine the solution at the shock wave point, an interior point unit process must be performed to obtain the upstream flow properties at the location of the shock wave solution point. Figure E.10 illustrates both the computational network for the interior point unit process (denoted by primed numbers), and the computational network for the standard shock wave point unit process (denoted by unprimed numbers). The point notations employed in these computational networks are identical to those used in the corresponding standard unit processes.

The computational procedure employed for determining the solution for an internal flow field-shock wave point is almost identical to the bow shock wave point unit process. The major difference between the two procedures is that for an internal flow shock wave point, the upstream flow properties at the solution point are obtained from an interior point computation, rather than using free-stream data as in the bow shock wave point unit process. The required interior point unit process is essentially the same as the basic interior point unit process presented in Section 4 of this appendix. In the present case, however, the streamline is not extended from a field point in the

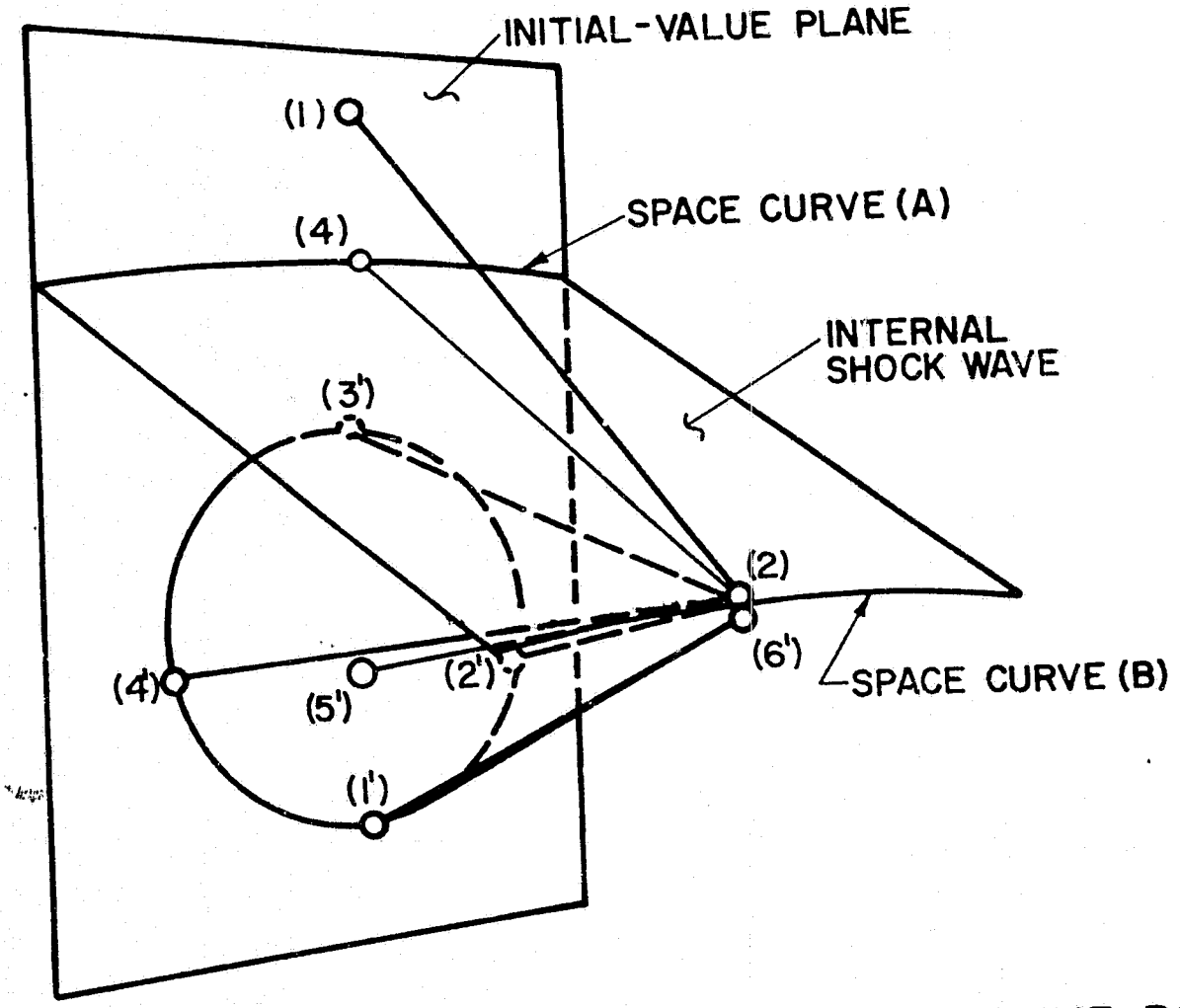

FIGURE E.10. INTERNAL FLOW FIELD-SHOCK WAVE POINT COMPUTATIONAL NETWORK (TYPICAL APPLICATION)

initial-value plane to the solution plane, but rather it is extended from the shock wave solution point back to the initial-value plane. The position of the shock wave solution point is determined by the shock wave point unit process. To initiate the interior point computation in the present case, flow property values are used from an adjacent field point in the flow field sector that is upstream of the shock wave in the solution plane. This modified interior point unit process requires searching the flow field sector upstream of the shock wave in the initial-value plane for the field point that is closest to the streamline-initial-value plane intersection point. This point is then used as the base point for the stencil of initial-value plane field points that are used in formulating the bivariate interpolation polynomial given by equation (E.11) (see Appendix C).

For the first solution plane inside the inlet, the downstream bicharacteristic base point, point (1) in Figure E.11, does not lie on the initial-value plane, but rather is located on the stream surface formed by the cowl boundary. To compute the pressure at point (2) from the wave surface compatibility relation, equation (E.59), the flow property values must be available at point (1), which requires that the flow property field must be known on the cowl surface. The body points on the cowl surface at the first internal flow solution plane, however, must be obtained from the unit process described in Section 9 of this appendix. That unit process requires that the flow property field on the downstream side of the shock wave be known. Hence, a simultaneous solid body point-shock wave point algorithm must be employed. This procedure was not developed in the present

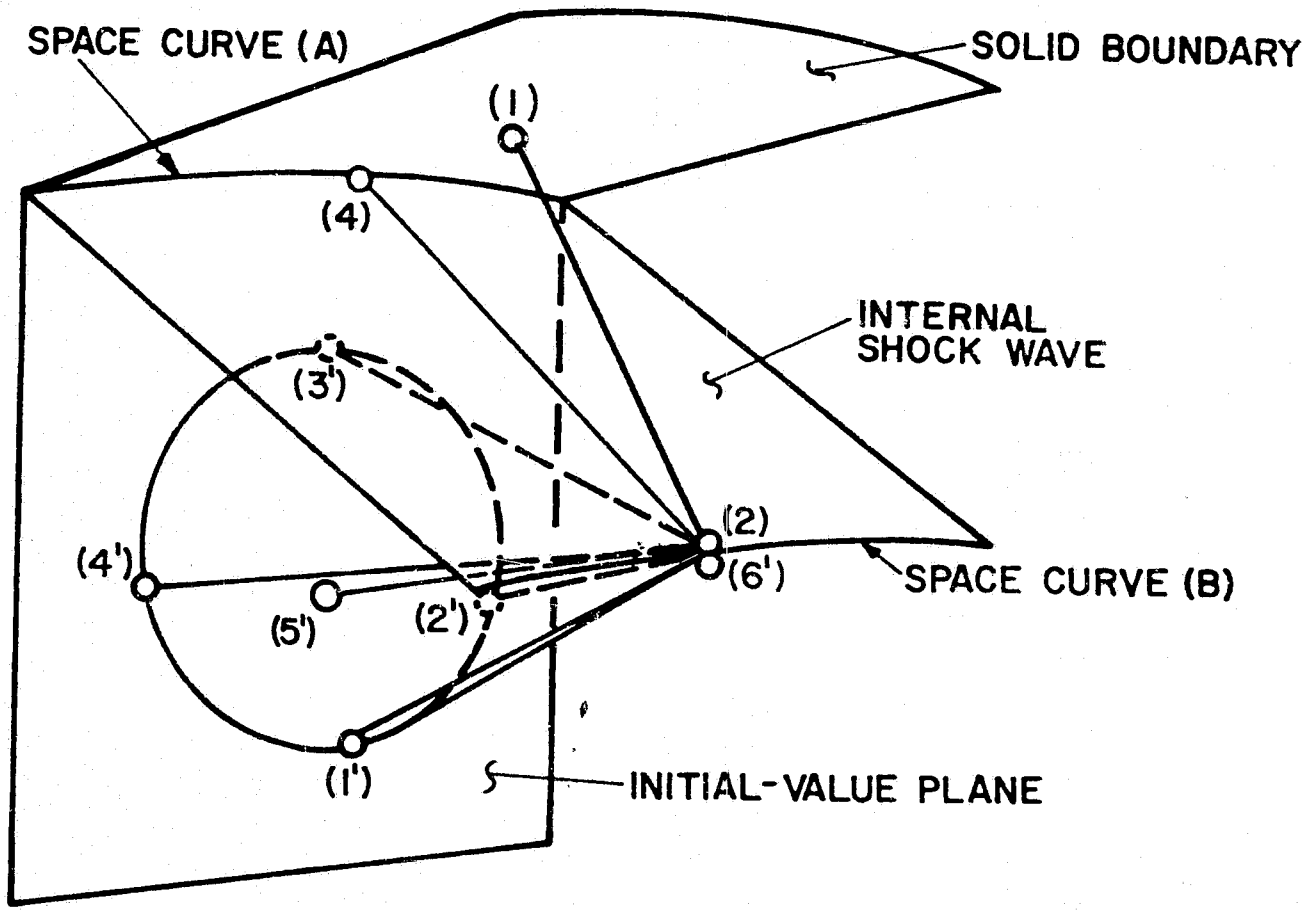

FIGURE E.11. INTERNAL FLOW FIELD-SHOCK WAVE POINT COMPUTATIONAL NETWORK (FIRST INTERNAL FLOW SOLUTION PLANE APPLICATION)

investigation. Rather, the shock wave points on the first internal flow solution plane are computed using a value of ϕ in equation (E.37) equal to the value of ϕ at the shock wave point in the initial-value plane which lies in the same meridional plane as the solution point. This provides a solution at each shock wave point on the first solution plane without employing the compatibility relation along the bicharacteristic. The body points on the cowl are then computed in the manner outlined in Section 9. On ensuing solution planes, except for the one immediately after a solid body-shock wave intersection, the bicharacteristic base point is located and the angle ϕ is iterated to convergence.

When the internal shock wave intersects a solid boundary, as illustrated in Figure E.12, a modification is required to the shock wave point unit process. In this case, instead of performing an interior point unit process to obtain the upstream flow properties at the solution point, a modified solid boundary point unit process must be employed. Moreover, the shock wave solution point, in this case, does not lie on the solution plane, but rather its position must be obtained by computing the intersection of the incident shock wave with the solid boundary.

Finally, it should be noted that in order to achieve strict second-order accuracy in the internal flow shock wave point solution, global correction must be performed [this involves evaluating the cross derivatives at the solution point and using updated values of α in equation (E.38)]. Time constraints in the present investigation did not permit the development of the global correction capability for

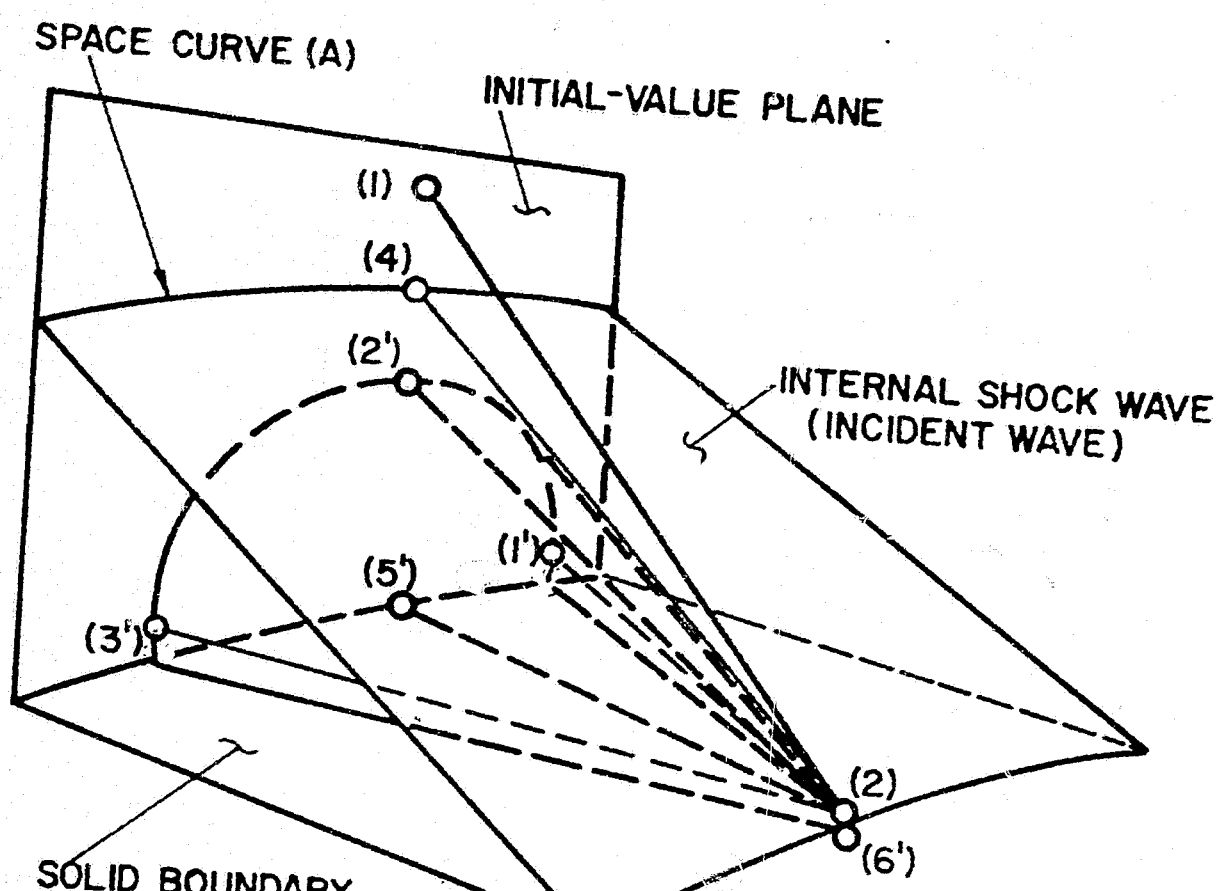

FIGURE E.12. INTERNAL FLOW FIELD-SHOCK WAVE POINT COMPUTATIONAL NETWORK (INCIDENT WAVE-BOUNDARY INTERSECTION APPLICATION)

the internal flow shock wave points. Hence, only local iteration can be performed for those points.

APPENDIX F

CALCULATION OF THE TRANSPORT TERMS

1. INTRODUCTION

The numerical procedure developed in this investigation has the capability to include the influence of molecular transport on the solution by treating the viscous and thermal diffusion terms in the governing equations as forcing functions, or correction terms, in the method of characteristics scheme. At present, the computer program has the capability to include the influence of viscous and thermal diffusion in the computation of the external flow field about the forebody, and in the computation of the internal flow field in which shock waves are not discretely traced. The program option which performs discrete fitting of the internal shock wave system does not have the capability to include the influence of molecular transport in the computation, but rather assumes the flow to be inviscid and adiabatic.

2. EXPRESSIONS FOR THE TRANSPORT TERMS

The expressions for the transport forcing functions are derived in Appendix A, and are summarized below.

$$F_x = \mu_x\left[\frac{4}{3}u_x - \frac{2}{3}(v_y + w_z)\right] + \mu_y(u_y + v_x) + \mu_z(u_z + w_x) + \mu\left[\frac{4}{3}u_{xx} + u_{yy} + u_{zz} + \frac{1}{3}(v_{xy} + w_{xz})\right] \qquad (F.1)$$

$$F_y = \mu_y\left[\frac{4}{3}v_y - \frac{2}{3}(u_x + w_z)\right] + \mu_x(v_x + u_y) + \mu_z(v_z + w_y)$$
$$+ \mu\left[\frac{4}{3}v_{yy} + v_{xx} + v_{zz} + \frac{1}{3}(u_{yx} + w_{yz})\right] \qquad (F.2)$$

$$F_z = \mu_z\left[\frac{4}{3}w_z - \frac{2}{3}(u_x + v_y)\right] + \mu_x(w_x + u_z) + \mu_y(w_y + v_z)$$
$$+ \mu\left[\frac{4}{3}w_{zz} + w_{xx} + w_{yy} + \frac{1}{3}(u_{zx} + v_{zy})\right] \qquad (F.3)$$

$$F_e = \xi\left\{\kappa(T_{xx} + T_{yy} + T_{zz}) + \kappa_x T_x + \kappa_y T_y + \kappa_z T_z\right.$$
$$+ \mu\left[2(u_x^2 + v_y^2 + w_z^2 + u_y v_x + u_z w_x + v_z w_y) + v_x^2 + w_x^2\right.$$
$$\left.\left. + u_y^2 + w_y^2 + u_z^2 + v_z^2 - \frac{2}{3}(u_x + v_y + w_z)^2\right]\right\} \qquad (F.4)$$

where

$$\xi = \frac{1}{\rho T}\left(\frac{\partial P}{\partial s}\right)_\rho \qquad (F.5)$$

In equations (F.1) to (F.5), u, v, and w denote the velocity components in the x, y, and z coordinate directions, respectively, P is the pressure, ρ denotes the density, T is the absolute temperature, s denotes the entropy per unit mass, μ represents the dynamic viscosity, and κ is the thermal conductivity. The subscripts x, y, and z on the right-hand sides of equations (F.1) to (F.4) denote partial differentiation in the corresponding coordinate direction, whereas F_x, F_y, and F_z on the left-hand sides denote the transport forcing functions in the x, y, and z component momentum equations, respectively. F_e is the transport forcing function in the energy equation.

3. COMPUTATION OF THE TRANSPORT FORCING FUNCTIONS

During the course of the program development, a number of methods were devised in an effort to obtain a good approximation to the transport forcing functions. One such method was based on employing a quadratic trivariate interpolation polynomial whose coefficients were determined by a least squares fitting of a number of known field points on the initial-value plane and the previous solution planes. This polynomial was employed to determine the five dependent properties u, v, w, P, and ρ. The spatial derivatives of the velocity components appearing in equations (F.1) to (F.4) were then obtained by analytically differentiating the respective interpolation polynomials. Spatial gradients of pressure and density were obtained in a similar manner. Then, by differentiation of the thermal equation state, temperature derivatives were expressed in terms of the pressure and density derivatives. The molecular transport properties and their spatial gradients were obtained using the procedures presented in Appendix A.

This method of calculating the transport forcing terms was considered to have good accuracy. The computer execution time required by this method, however, was felt to be unacceptable. This prohibitive execution time was primarily due to the least squares curve fitting of the trivariate interpolation polynomials. Consequently, a more efficient method with acceptable accuracy was sought for approximating the transport terms. The method which was selected is presented below.

For the interior point and solid boundary point unit processes, the transport terms must be computed at all points in the computational network (see Figures E.1 and E.2). For the bow shock

wave point unit process, the transport terms must be computed at the solution point and at the intersection point of the bicharacteristic with the initial-value plane (see Figure E.3). For each of these unit processes, partial derivatives of the dependent properties with respect to y and z in the initial-value plane are obtained by analytically differentiating the quadratic bivariate interpolation polynomial

$$f(y,z) = a_1 + a_2 y + a_3 z + a_4 yz + a_5 y^2 + a_6 z^2 \qquad (F.6)$$

The coefficients a_i (i=1 to 6) in equation (F.6) are determined by a least squares fit of nine data points in the initial-value plane as discussed in Appendix C. Equation (F.6) is applied for the five dependent flow properties u, v, w, P, and ρ. Spatial derivatives of pressure and density are required [even though they do not appear explicitly in equations (F.1) to (F.4)] because spatial derivatives of temperature are expressed in terms of pressure and density derivatives through differentiation of the thermal equation of state as discussed in Appendix A.

In the solution plane, partial derivatives of the dependent properties with respect to y and z are equated to the corresponding derivatives in the initial-value plane. For the interior point and boundary point schemes, the derivatives at the solution point are set equal to those at the streamline base point. For the bow shock wave point scheme, the solution point derivatives are equated to those at the bicharacteristic base point. The evaluation of these derivatives in the solution plane would require that a global iteration algorithm be employed. In this algorithm, the property field on the solution

plane would first be determined by a predictor application of the appropriate unit process at each point in the computed sector. Then, by fitting equation (F.6) to solution plane field points the appropriate partial derivatives could be obtained. In a similar manner, ensuing corrector applications would be performed until overall convergence was achieved. The attendant increase in algorithm complexity and computer execution time using this global iteration procedure, however, was felt to be unwarranted since the transport terms are assumed to be of secondary importance in determining the solution.

Partial derivatives with respect to x in equations (F.1) to (F.4) are obtained from the following quadratic univariate interpolation polynomial.

$$f(x) = a_1 + a_2 x + a_3 x^2 \qquad (F.7)$$

The coefficients a_i (i=1,2,3) in equation (F.7) are determined by fitting this expression to three data points. The first data point is located on the solution plane that is immediately upstream of the current initial-value plane, the second data point is on the initial-value plane, and the third data point is the solution point itself. For the interior point and boundary point unit processes, the fit points are located on the streamline which passes through the solution point. For the bow shock wave point unit process, the fit points are the shock wave solution points corresponding to the circumferential index of the solution point. Special logic in the computer program takes account of point deletion and addition in the forebody flow field computation and thereby insures that the appropriate fit points are selected. Of course, for a predictor application of either the interior point or

boundary point unit processes, property values at the solution point are equated to those at the streamline base point in the initial-value plane.

Equation (F.7) is applied for the five dependent flow properties u, v, w, P, and ρ. Analytical differentiation of equation (F.7) yields approximations to the x-partial derivatives. Differentiation of the thermal equation of state allows the spatial derivatives of temperature in the x-coordinate direction to be expressed in terms of the corresponding pressure and density derivatives. This formulation yields an x-partial derivative which is constant in a given x-plane.

Since equation (F.7) uses data on a previous solution plane, derivatives cannot be evaluted using this representation until at least one previous solution plane is available. Furthermore, the derivatives obtained using this formulation are only approximations to the x-partial derivatives since the y and z coordinates of each of the three fit points are not, in general, identical. Considering that the effects of molecular diffusion are assumed to be small, this approximation is acceptable.

The molecular transport properties and their spatial gradients are obtained using the procedures presented in Appendix A.

APPENDIX G

GOVERNING EQUATIONS FOR THE BOUNDARY LAYER FLOW

1. INTRODUCTION

The major assumptions constituting the fluid dynamic model for the boundary layer flow are:

1. steady flow,
2. negligible body forces,
3. thermodynamic equilibrium (i.e., mechanical, thermal, and chemical equilibrium),
4. negligible radiative heat transfer and no internal heat generation other than viscous dissipation, and
5. negligible pressure variation in the boundary layer normal direction.

The governing equations for the assumed flow model are written in an orthogonal body-fitted curvilinear coordinate system. They consist of the continuity equation, the component momentum equations, the energy equation, the thermal and caloric equations of state, and expressions for the molecular transport properties and turbulent eddy diffusities. These relations are presented in this appendix.

2. DIFFERENTIAL EQUATIONS OF MOTION

The governing equations for the three-dimensional boundary layer flow have been derived by Vaglio-Laurin (10) in orthogonal curvilinear

coordinates. For the present investigation, a body-fitted curvilinear coordinate system has been selected, which is comprised of geodesics and geodesic parallels. The coordinate system is illustrated in Figure G.1, and consists of the coordinates $\tilde{x}$, $\tilde{y}$, and $\tilde{z}$, where $\tilde{x}$ is coincident with the body surface and lies in a given meridional plane, $\tilde{y}$ is locally orthogonal to the body surface, and $\tilde{z}$ is orthogonal to both $\tilde{x}$ and $\tilde{y}$.

When employing the coordinate system of Figure G.1, the continuity equation may be written as

$$\frac{\partial}{\partial \tilde{x}} (\rho h_2 \tilde{u}) + \frac{\partial}{\partial \tilde{z}} (\rho h_1 \tilde{w}) + \frac{\partial}{\partial \tilde{y}} (h_1 h_2 \overline{\rho \tilde{v}}) = 0 \qquad (G.1)$$

In equation (G.1), $\tilde{u}$, $\tilde{v}$, and $\tilde{w}$ denote the mean velocity components in the $\tilde{x}$-, $\tilde{y}$-, and $\tilde{z}$-coordinate directions, respectively, and ρ denotes the mean density. The overbar ($\overline{\ }$) denotes a time averaged product with

$$\overline{\rho \tilde{v}} = \rho \tilde{v} + \overline{\rho' \tilde{v}'} \qquad (G.2)$$

where the primed quantities denote the respective time fluctuation components. In equation (G.1), the parameters h_1 and h_2 are metric coefficients which are generally dependent on $\tilde{x}$ and $\tilde{z}$, only. The metric coefficients for axisymmetric geometries are given by the simple expressions

$$h_1 = 1 \qquad (G.3)$$

$$h_2 = r = r(\tilde{x}) \qquad (G.4)$$

where r is the body radius at the position $\tilde{x}$.

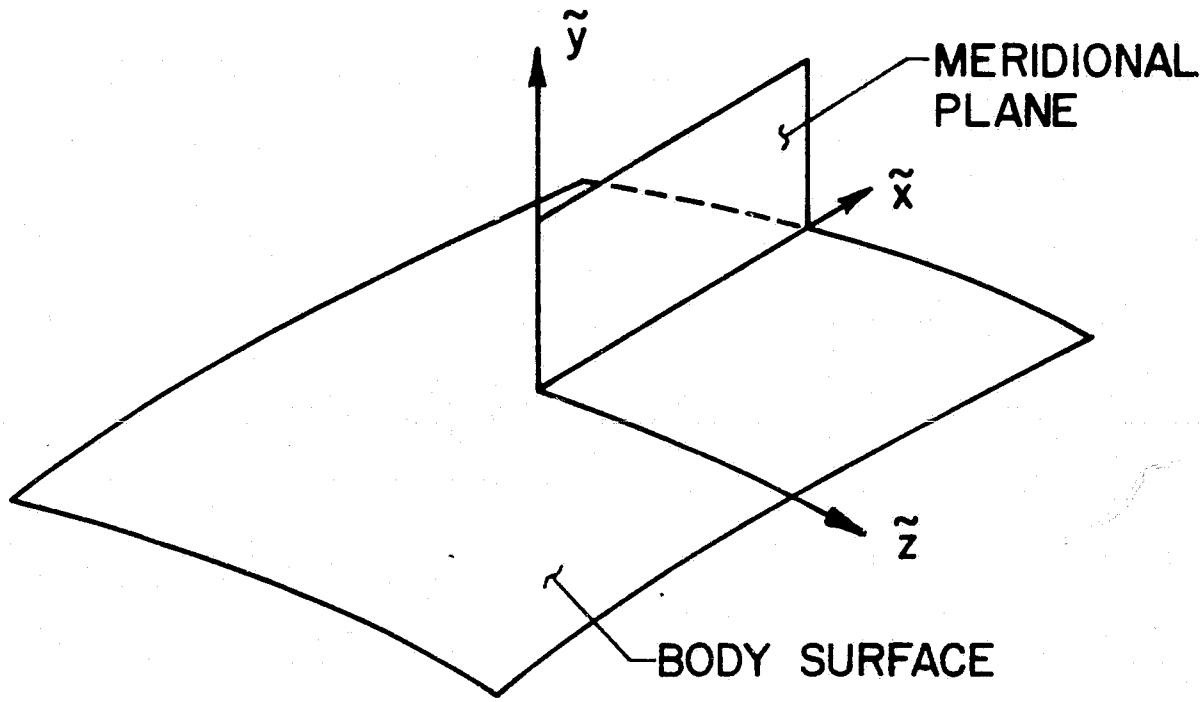

($\tilde{x}$ AND $\tilde{z}$ COINCIDENT WITH BODY SURFACE)

FIGURE G.I. ORTHOGONAL CURVILINEAR COORDINATE SYSTEM FOR BOUNDARY LAYER COMPUTATION.

The component momentum equations in the $\tilde{x}$ and $\tilde{z}$ directions are termed the streamwise and cross flow momentum equations, respectively. Those equations are given by, respectively,

$$\rho \frac{\tilde{u}}{h_1}\frac{\partial \tilde{u}}{\partial \tilde{x}} + \rho \frac{\tilde{w}}{h_2}\frac{\partial \tilde{u}}{\partial \tilde{z}} + \overline{\rho \tilde{v}}\frac{\partial \tilde{u}}{\partial \tilde{y}} - \rho \tilde{u}\tilde{w}K_2 + \rho \tilde{w}^2 K_1$$

$$= -\frac{1}{h_1}\frac{\partial P}{\partial \tilde{x}} + \frac{\partial}{\partial \tilde{y}}\left(\mu \frac{\partial \tilde{u}}{\partial \tilde{y}} - \overline{\rho \tilde{u}'\tilde{v}'}\right) \tag{G.5}$$

$$\rho \frac{\tilde{u}}{h_1}\frac{\partial \tilde{w}}{\partial \tilde{x}} + \rho \frac{\tilde{w}}{h_2}\frac{\partial \tilde{w}}{\partial \tilde{z}} + \overline{\rho \tilde{v}}\frac{\partial \tilde{w}}{\partial \tilde{y}} - \rho \tilde{u}\tilde{w}K_1 + \rho \tilde{u}^2 K_2$$

$$= -\frac{1}{h_2}\frac{\partial P}{\partial \tilde{z}} + \frac{\partial}{\partial \tilde{y}}\left(\mu \frac{\partial \tilde{w}}{\partial \tilde{y}} - \overline{\rho \tilde{w}'\tilde{v}'}\right) \tag{G.6}$$

where P denotes the mean static pressure, μ denotes the molecular viscosity, and K_1 and K_2 are geometric parameters known as the geodesic curvatures of the curves $\tilde{x}$ = constant and $\tilde{z}$ = constant, respectively. Both K_1 and K_2 are generally functions of $\tilde{x}$ and $\tilde{z}$, only, and are given by

$$K_1 = -\frac{1}{h_1 h_2}\frac{\partial h_2}{\partial \tilde{x}} \tag{G.7}$$

$$K_2 = -\frac{1}{h_1 h_2}\frac{\partial h_1}{\partial \tilde{z}} \tag{G.8}$$

For axisymmetric geometries, the geodesic curvature terms are given by

$$K_1 = -\frac{f}{r\sqrt{f^2 + 1}} \tag{G.9}$$

$$K_2 = 0 \tag{G.10}$$

with

$$f = \frac{dr}{dx} = \frac{dr(x)}{dx} \tag{G.11}$$

where r is the body radius, and x is the position measured along the longitudinal axis of the body.

The third momentum equation, which is the $\tilde{y}$- or normal momentum equation, is given by the classical expression

$$\frac{\partial P}{\partial \tilde{y}} = 0 \tag{G.12}$$

The energy equation is given by

$$\rho \frac{\tilde{u}}{h_1} \frac{\partial H}{\partial \tilde{x}} + \rho \frac{\tilde{w}}{h_2} \frac{\partial H}{\partial \tilde{z}} + \overline{\rho \tilde{v}} \frac{\partial H}{\partial \tilde{y}}$$

$$= \frac{\partial}{\partial \tilde{y}} \left[\frac{\mu}{Pr} \frac{\partial H}{\partial \tilde{y}} + \mu \left(1 - \frac{1}{Pr} \right) \frac{\partial}{\partial \tilde{y}} \left(\frac{\tilde{u}^2 + \tilde{w}^2}{2} \right) - \overline{\rho \tilde{v}' \tilde{H}'} \right] \tag{G.13}$$

where H denotes the mean total enthalpy per unit mass, H' denotes its time fluctuation component, and Pr is the molecular or laminar Prandtl number. The total enthalpy H is given by

$$H = h + \frac{\tilde{u}^2 + \tilde{w}^2}{2} \tag{G.14}$$

where h is the mean static enthalpy per unit mass. It is assumed in equation (G.14) that

$$(\tilde{u}^2 + \tilde{w}^2) >>> \tilde{v}^2 \tag{G.15}$$

and thereby $\tilde{v}$ can be neglected in defining the total enthalpy.

The boundary layer equations of motion are subject to the following boundary conditions:

$$\left.\begin{aligned} &\tilde{y} = 0: \quad \tilde{u} = 0, \quad \tilde{w} = 0, \quad \tilde{v} = \tilde{v}_w(\tilde{x},\tilde{z}) \\ &\qquad H = H_w(\tilde{x},\tilde{z}) \quad \text{or} \quad \left(\frac{\partial H}{\partial \tilde{y}}\right) = H'_w(\tilde{x},\tilde{z}) \end{aligned}\right\} \tag{G.16}$$

$$\left.\begin{aligned} &\tilde{y} = \delta: \quad \tilde{u} = \tilde{u}_e(\tilde{x},\tilde{z}), \quad \tilde{w} = \tilde{w}_e(\tilde{x},\tilde{z}) \\ &\qquad H = H_e(\tilde{x},\tilde{z}) \end{aligned}\right\} \tag{G.17}$$

where δ denotes the boundary thickness which is dependent upon $\tilde{x}$ and $\tilde{z}$, the subscript w denotes wall conditions, and the subscript e denotes boundary layer edge conditions. Note that equation (G.16) allows for distributed mass transpiration or bleed at the wall.

At the boundary layer edge, the $\tilde{x}$- and $\tilde{z}$-component momentum equations reduce to the following expressions:

$$\rho_e \frac{\tilde{u}_e}{h_1}\frac{\partial \tilde{u}_e}{\partial \tilde{x}} + \rho_e \frac{\tilde{w}_e}{h_2}\frac{\partial \tilde{u}_e}{\partial \tilde{z}} - \rho_e \tilde{u}_e \tilde{w}_e K_2 + \rho_e \tilde{w}_e^2 K_1 = -\frac{1}{h_1}\frac{\partial P}{\partial \tilde{x}} \tag{G.18}$$

$$\rho_e \frac{\tilde{u}_e}{h_1}\frac{\partial \tilde{w}_e}{\partial \tilde{x}} + \rho_e \frac{\tilde{w}_e}{h_2}\frac{\partial \tilde{w}_e}{\partial \tilde{z}} - \rho_e \tilde{u}_e \tilde{w}_e K_1 + \rho_e \tilde{u}_e^2 K_2 = -\frac{1}{h_2}\frac{\partial P}{\partial \tilde{z}} \tag{G.19}$$

3. BOUNDARY LAYER ATTACHMENT LINE EQUATIONS

On a plane of flow symmetry, the cross flow velocity ($\tilde{w}$) is identically zero, as is the cross flow pressure gradient ($\partial P/\partial \tilde{z}$). The flow on this plane is referred to as attachment line flow. The attachment line is a streamline on the body on which both $\tilde{w}$ and $\partial P/\partial \tilde{z}$ are identically zero. The cross flow momentum equation will be singular on a flow symmetry plane since both $\tilde{w}$ and K_2 vanish there. As suggested by Moore (11), a nonsingular equation may be obtained by first differentiating the cross flow momentum equation and then substituting into it the appropriate symmetry conditions. Performing the proper operations yields the following system of equations for the attachment line flow:

$$\frac{\partial}{\partial \tilde{x}}(\rho h_2 \tilde{u}) + \rho h_1 \tilde{w}_z + \frac{\partial}{\partial \tilde{y}}(h_1 h_2 \overline{\rho \tilde{v}}) = 0 \tag{G.20}$$

$$\rho \frac{\tilde{u}}{h_1}\frac{\partial \tilde{u}}{\partial \tilde{x}} + \overline{\rho \tilde{v}}\frac{\partial \tilde{u}}{\partial \tilde{y}} = -\frac{1}{h_1}\frac{\partial P}{\partial \tilde{x}} + \frac{\partial}{\partial \tilde{y}}\left[\mu \frac{\partial \tilde{u}}{\partial \tilde{y}} - \overline{\rho \tilde{u}'\tilde{v}'}\right] \tag{G.21}$$

$$\rho \frac{\tilde{u}}{h_1}\frac{\partial \tilde{w}_z}{\partial \tilde{x}} + \overline{\rho \tilde{v}}\frac{\partial \tilde{w}_z}{\partial \tilde{y}} + \frac{\rho}{h_2}\tilde{w}_z^2 - \rho \tilde{u}\tilde{w}_z K_1 + \rho \tilde{u}^2 \frac{\partial K_2}{\partial \tilde{z}}$$

$$= -\frac{1}{h_2}\frac{\partial^2 P}{\partial \tilde{z}^2} + \frac{\partial}{\partial \tilde{y}}\left[\mu \frac{\partial \tilde{w}_z}{\partial \tilde{y}} - \rho(\overline{\tilde{w}'\tilde{v}'})_z\right] \tag{G.22}$$

$$\rho \frac{\tilde{u}}{h_1}\frac{\partial H}{\partial \tilde{x}} + \overline{\rho \tilde{v}}\frac{\partial H}{\partial \tilde{y}} = \frac{\partial}{\partial \tilde{y}}\left[\frac{\mu}{Pr}\frac{\partial H}{\partial \tilde{y}} + \mu\left(1 - \frac{1}{Pr}\right)\frac{\partial}{\partial \tilde{y}}\left(\frac{\tilde{u}^2}{2}\right) - \overline{\rho \tilde{v}'H'}\right] \tag{G.23}$$

where $\tilde{w}_z = \partial\tilde{w}/\partial\tilde{z}$. Equations (G.20) to (G.23) represent the continuity, streamwise momentum, cross flow momentum, and energy equations, respectively.

Boundary conditions for the attachment line equations are given by

$$\left.\begin{aligned} \tilde{y} = 0: \quad & \tilde{u} = 0, \quad \tilde{w}_z = 0, \quad \tilde{v} = \tilde{v}_w(\tilde{x},\tilde{z}) \\ & H = H_w(\tilde{x},\tilde{z}) \quad \text{or} \quad \left(\frac{\partial H}{\partial \tilde{y}}\right) = H'_w(\tilde{x},\tilde{z}) \end{aligned}\right\} \tag{G.24}$$

$$\left.\begin{aligned} \tilde{y} = \delta: \quad & \tilde{u} = \tilde{u}_e(\tilde{x},\tilde{z}), \quad \tilde{w}_z = \tilde{w}_{ze}(\tilde{x},\tilde{z}) \\ & \tilde{H} = \tilde{H}_e(\tilde{x},\tilde{z}) \end{aligned}\right\} \tag{G.25}$$

At the boundary layer outer edge, equation (G.21) reduces to

$$\rho_e \tilde{u}_e \frac{\partial \tilde{u}_e}{\partial \tilde{x}} = -\frac{\partial P}{\partial \tilde{x}} \tag{G.26}$$

which is of the form of two-dimensional flow.

Note that the attachment line flow is quasi-two-dimensional in that the velocity vector lies in a plane. However, the solution is influenced by flow off that plane.

4. THERMODYNAMIC MODEL AND MOLECULAR TRANSPORT PROPERTIES

The thermodynamic model and molecular transport property representations are identical for the boundary flow and the supersonic core flow. As a consequence, the relations given in Sections 3 and 4 of Appendix A are applicable for the boundary layer flow.

5. THREE-DIMENSIONAL TURBULENCE MODEL

The computation of turbulent boundary layer flows requires that assumptions be made for the Reynolds stress terms in the governing equations of motion. Mathematical closure is achieved in the present study by using an eddy viscosity formulation along with mixing length and velocity defect concepts.

The computer program developed in the present investigation is written in a modular fashion and allows for the rapid substitution of alternate turbulence models. Either algebraic or transport-equation models may be incorporated into the program along with improved transition modeling functions.

The present turbulence model is algebraic and is based on the Boussinesq eddy viscosity concept. The Reynolds stresses in equations (G.5), (G.6), and (G.13) can be written under this assumption as

$$- \rho \overline{\tilde{u}'\tilde{v}'} = \rho\varepsilon_x \frac{\partial \tilde{u}}{\partial \tilde{y}} \tag{G.27}$$

$$- \rho \overline{\tilde{w}'\tilde{v}'} = \rho\varepsilon_z \frac{\partial \tilde{w}}{\partial \tilde{y}} \tag{G.28}$$

$$- \rho \overline{H'\tilde{v}'} = \rho\varepsilon_\theta \frac{\partial H}{\partial \tilde{y}} \tag{G.29}$$

where ε_x and ε_z are the turbulent eddy viscosities in the $\tilde{x}$- and $\tilde{z}$-coordinate directions, respectively, and ε_θ is the turbulent eddy thermal conductivity. Isotropic turbulence has been assumed in the present study, thereby

$$\varepsilon_x = \varepsilon_z \tag{G.30}$$

The present turbulence model is a two-layer representation (20) where

$$\varepsilon_x = \varepsilon_z = \varepsilon_i : (0 \leq \tilde{y} \leq \tilde{y}_t) \tag{G.31}$$

$$\varepsilon_x = \varepsilon_z = \varepsilon_o : (\tilde{y}_t \leq \tilde{y} \leq \delta) \tag{G.32}$$

In equations (G.31) and (G.32), ε_i and ε_o represent the inner and outer region eddy viscosities, respectively, and $\tilde{y}_t$ is the value of the normal coordinate determined by continuity of the eddy viscosity, that is, where $\varepsilon_i = \varepsilon_o$.

A mixing length representation is employed for the inner layer eddy viscosity

$$\varepsilon_i = \delta_{tr} L^2 \left[\left(\frac{\partial \tilde{u}}{\partial \tilde{y}} \right)^2 + \left(\frac{\partial \tilde{w}}{\partial \tilde{y}} \right)^2 \right]^{1/2} \tag{G.33}$$

where L is the mixing length, and δ_{tr} is a function accounting for the transition from laminar to turbulent flow. The mixing length L is given by

$$L = \kappa \tilde{y} [1 - \exp(-\tilde{y}/A)] \tag{G.34}$$

where κ is the von Karman constant given by

$$\kappa = 0.40 \tag{G.35}$$

and A is defined by

$$A = A^+ \frac{\nu}{N} \sqrt{\frac{\rho}{\rho_w}} \Big/ \tilde{u}_\tau \tag{G.36}$$

In equation (G.36), ν denotes the kinematic viscosity, the subscript w denotes wall conditions, A^+ is the van Driest damping factor which is given by

$$A^+ = 26.0 \tag{G.37}$$

and $\tilde{u}_\tau$ is given by

$$\tilde{u}_\tau = \left(\frac{\tau_{ws}}{\rho_w}\right)^{1/2} \tag{G.38}$$

where τ_{ws} is the shear stress at the wall. Equation (G.36) is valid for cases with and without distributed wall mass transfer. For impermeable walls, the parameter N in equation (G.36) is given by

$$N = \left[1 - 11.8 \frac{\mu_w}{\mu_e} \left(\frac{\rho_e}{\rho_w}\right)^2 p^+\right]^{1/2} \tag{G.39}$$

where

$$p^+ = \frac{\nu_e \tilde{u}_s}{\tilde{u}_\tau^3} \frac{\partial \tilde{u}_s}{\partial \tilde{s}} \tag{G.40}$$

where $\tilde{u}_s$ is the velocity in the external streamline direction $\tilde{s}$. For cases of wall transpiration or bleed, N is given by

$$N = \left\{\frac{\mu}{\mu_e} \left(\frac{\rho_e}{\rho_w}\right)^2 \frac{p^+}{\tilde{v}_w^+} \left[1 - \exp\left(11.8 \frac{\mu_w}{\mu} \tilde{v}_w^+\right)\right] + \exp\left(11.8 \frac{\mu_w}{\mu} \tilde{v}_w^+\right)\right\}^{1/2} \tag{G.41}$$

where $\tilde{v}_w^+$ is a mass transfer parameter given by

$$\tilde{v}_w^+ = \frac{\dot{v}_w}{\tilde{u}_\tau} \tag{G.42}$$

The outer region eddy viscosity is given by the velocity defect expression

$$\varepsilon_o = \delta_{tr}\alpha\left|\int_0^\infty\left[\left(\tilde{u}_e^2 + \tilde{w}_e^2\right)^{1/2} - \left(\tilde{u}^2 + \tilde{w}^2\right)^{1/2}\right]d\tilde{y}\right| \tag{G.43}$$

In equation (G.43), the parameter α is taken to be a constant at the value

$$\alpha = 0.0168 \tag{G.44}$$

The turbulent eddy thermal conductivity is expressed in terms of the turbulent eddy viscosity as

$$\varepsilon_\theta = \frac{\varepsilon}{Pr_t} \tag{G.45}$$

with

$$\varepsilon = \left(\varepsilon_x^2 + \varepsilon_z^2\right)^{1/2} = \sqrt{2}\,\varepsilon_x \tag{G.46}$$

where Pr_t is the turbulent Prandtl number which is assumed to be a constant in the analysis.

The parameter δ_{tr} in equations (G.33) and (G.43) is an intermittency factor which can account for the progressive transition from laminar to turbulent flow. The transition parameter δ_{tr} takes on the following values:

$$\left.\begin{aligned} \delta_{tr} &= 0: \quad \text{(laminar flow)} \\ \delta_{tr} &= 1: \quad \text{(turbulent flow)} \\ 0 < \delta_{tr} &< 1: \quad \text{(transitional flow)} \end{aligned}\right\} \qquad \text{(G.47)}$$

A number of transition models have been incorporated into the computer program. One model requires specification of the axial position where transition occurs, and the flow is assumed to instantaneously transition from laminar to turbulent using this model. An alternative model requires that two Reynolds numbers be specified: the first denoting the onset of transition, and the second denoting the onset of fully turbulent flow. Analytical functions are then used to model the parameter δ_{tr} in the transition region. A full description of the available transition models may be found in the user's manual.

APPENDIX H

TRANSFORMATION OF THE BOUNDARY LAYER EQUATIONS

1. INTRODUCTION

The boundary layer equations may be solved numerically in terms of the physical variables presented in Appendix G. Alternatively, the boundary layer equations may be first transformed using a normal coordinate stretching function and then numerically solved. An advantage of using the transformed variable formulation is that larger step sizes may be taken in the streamwise and cross flow coordinate directions, thereby improving computational efficiency. Use of the transformed variables removes much of the boundary layer property profile and thickness variation, especially for laminar flows. These same advantages exist for turbulent flows but to a lesser degree. The boundary layer equation transformation used in the present investigation is presented in this appendix.

2. TRANSFORMED BOUNDARY LAYER EQUATIONS

The boundary layer transformation used in the present investigation has been suggested by Moore (11). Following Moore, a two-component vector potential is defined such that

$$\rho h_2 \tilde{u} = \frac{\partial \psi}{\partial \tilde{y}} \tag{H.1}$$

$$\rho h_1 \tilde{w} = \frac{\partial \phi}{\partial \tilde{y}} \tag{H.2}$$

$$h_1 h_2 \overline{\rho \tilde{v}} = -\left(\frac{\partial \psi}{\partial \tilde{x}} + \frac{\partial \phi}{\partial \tilde{z}}\right) + h_1 h_2 (\rho \tilde{v})_w \tag{H.3}$$

In equations (H.1), (H.2), and (H.3), $\tilde{u}$, $\tilde{v}$, and $\tilde{w}$ denote the mean velocity components in the $\tilde{x}$-, $\tilde{y}$-, and $\tilde{z}$-curvilinear coordinate directions, respectively, ρ denotes the mean density, the overbar denotes a time averaged product, h_1 and h_2 represent metric coefficient parameters defined in Appendix G, ψ and ϕ denote the component potential functions, and the subscript w denotes wall conditions. The last term in equation (H.3) accounts for wall mass transfer and is identically zero for impermeable walls. Substituting equations (H.1), (H.2) and (H.3) into the continuity equation, given by equation (G.1), identically satisfies that equation.

The governing equations of motion are now reformulated according to the transformation

$$(\tilde{x}, \tilde{y}, \tilde{z}) \rightarrow (\tilde{x}, \eta, \tilde{z}) \tag{H.4}$$

with

$$\tilde{x} = \tilde{x} \tag{H.5}$$

$$\tilde{z} = \tilde{z} \tag{H.6}$$

$$d\eta = \left(\frac{\tilde{u}_e}{\rho_e \mu_e \tilde{x}}\right)^{\frac{1}{2}} \rho d\tilde{y} \tag{H.7}$$

where η is the stretched normal coordinate, μ is the dynamic viscosity, and the subscript e denotes boundary layer edge conditions. Under this transformation, the functions ψ and ϕ take the forms

$$\psi = (\rho_e \mu_e \tilde{u}_e \tilde{x})^{\frac{1}{2}} h_2 f(\tilde{x}, \eta, \tilde{z}) \tag{H.8}$$

$$\phi = (\rho_e \mu_e \tilde{u}_e \tilde{x})^{\frac{1}{2}} h_1 \left(\frac{\tilde{w}_e}{\tilde{u}_e}\right) g(\tilde{x}, \eta, \tilde{z}) \tag{H.9}$$

where the functions f and g are to be determined numerically in the analysis.

As noted earlier, the continuity equation given by equation (G.1) is identically satisfied by equations (H.1), (H.2), and (H.3). Substituting equations (H.1) to (H.9) into equations (G.5), (G.6), and (G.13) results in the following system of equations:

$$\left[C(1 + \varepsilon_x^+)f''\right]' + P_2 f f'' + P_3 g f'' + \frac{M}{h_1}\left[\frac{\rho_e}{\rho} - (f')^2\right]$$

$$+ P_4\left[\frac{\rho_e}{\rho} - (g')^2\right] + P_5\left[g'f' - \frac{\rho_e}{\rho}\right] - Tf''$$

$$= \frac{\tilde{x}}{h_1}\left(f' \frac{\partial f'}{\partial \tilde{x}} - f'' \frac{\partial f}{\partial \tilde{x}}\right) + \frac{\tilde{w}_e}{\tilde{u}_e}\frac{\tilde{x}}{h_2}\left(g' \frac{\partial f'}{\partial \tilde{z}} - f'' \frac{\partial g}{\partial \tilde{z}}\right) \tag{H.10}$$

$$\left[C(1 + \varepsilon_z^+)g''\right]' + P_2 fg'' + P_3 gg'' + P_6\left[\frac{\rho_e}{\rho} - (f')^2\right]$$

$$+ \frac{\tilde{w}_e}{\tilde{u}_e}\frac{P}{h_2}\left[\frac{\rho_e}{\rho} - (g')^2\right] + P_7\left[g'f' - \frac{\rho_e}{\rho}\right] - Tg''$$

$$= \frac{\tilde{x}}{h_1}\left(f'\frac{\partial g'}{\partial \tilde{x}} - g''\frac{\partial f}{\partial \tilde{x}}\right) + \frac{\tilde{w}_e}{\tilde{u}_e}\frac{\tilde{x}}{h_2}\left(g'\frac{\partial g'}{\partial \tilde{z}} - g''\frac{\partial g}{\partial \tilde{z}}\right) \qquad \text{(H.11)}$$

$$\left\{C\left[\left(1 + \varepsilon^+\frac{Pr}{Pr_t}\right)\frac{\theta'}{Pr} + \frac{\tilde{u}_e^2}{H_e}\left(1 - \frac{1}{Pr}\right)\left(f'f'' + \frac{\tilde{w}_e^2}{\tilde{u}_e^2}g'g''\right)\right]\right\}'$$

$$+ P_2 f\theta' + P_3 g\theta' - T\theta'$$

$$= \frac{\tilde{x}}{h_1}\left(f'\frac{\partial \theta}{\partial \tilde{x}} - \theta'\frac{\partial f}{\partial \tilde{x}}\right) + \frac{\tilde{w}_e}{\tilde{u}_e}\frac{\tilde{x}}{h_2}\left(g'\frac{\partial \theta}{\partial \tilde{z}} - \theta'\frac{\partial g}{\partial \tilde{z}}\right) \qquad \text{(H.12)}$$

where the primes denote differentiation with respect to η, H denotes the mean total enthalpy per unit mass, and Pr and Pr_t denote the laminar and turbulent Prandtl numbers, respectively. Equations (H.10), (H.11), and (H.12) represent the streamwise momentum, cross flow momentum, and energy equations, respectively. The following parameter definitions are used in equations (H.10), (H.11), and (H.12).

$$f' = \tilde{u}/\tilde{u}_e \qquad \text{(H.13)}$$

$$g' = \tilde{w}/\tilde{w}_e \qquad \text{(H.14)}$$

$$\theta = H/H_e \qquad \text{(H.15)}$$

$$R_x = \tilde{u}_e \tilde{x}/\nu_e \tag{H.16}$$

$$M = \frac{\tilde{x}}{\tilde{u}_e} \frac{\partial \tilde{u}_e}{\partial \tilde{x}} \tag{H.17}$$

$$N = \frac{\tilde{x}}{\tilde{u}_e} \frac{\partial \tilde{u}_e}{\partial \tilde{z}} \tag{H.18}$$

$$P = \frac{\tilde{x}}{\tilde{w}_e} \frac{\partial \tilde{w}_e}{\partial \tilde{z}} \tag{H.19}$$

$$Q = \frac{\tilde{x}}{\tilde{w}_e} \frac{\partial \tilde{w}_e}{\partial \tilde{x}} \tag{H.20}$$

$$S = \frac{\tilde{x}}{\rho_e \mu_e} \frac{\partial}{\partial \tilde{x}} (\rho_e \mu_e) \tag{H.21}$$

$$R = \frac{\tilde{x}}{\rho_e \mu_e} \frac{\partial}{\partial \tilde{z}} (\rho_e \mu_e) \tag{H.22}$$

$$P_2 = (1 + M + S - 2K_1 h_1 \tilde{x})/2h_1 \tag{H.23}$$

$$P_3 = \frac{\tilde{w}_e}{\tilde{u}_e} \frac{1}{2h_2} (2P - N + R - 2K_2 h_2 \tilde{x}) \tag{H.24}$$

$$P_4 = \left(\frac{\tilde{w}_e}{\tilde{u}_e}\right)^2 K_1 \tilde{x} \tag{H.25}$$

$$P_5 = - \frac{\tilde{w}_e}{\tilde{u}_e} \frac{1}{h_2} (-K_2 h_2 \tilde{x} + N) \tag{H.26}$$

$$P_6 = \frac{\tilde{u}_e}{\tilde{w}_e} K_2 \tilde{x} \tag{H.27}$$

$$P_7 = (K_1 h_1 \tilde{x} - Q)/h_1 \tag{H.28}$$

$$\varepsilon_x^+ = \frac{\varepsilon_x}{\nu} \tag{H.29}$$

$$\varepsilon_z^+ = \frac{\varepsilon_z}{\nu} \tag{H.30}$$

$$\varepsilon_\theta^+ = \frac{\varepsilon_\theta}{\nu} \tag{H.31}$$

$$\varepsilon^+ = \left[(\varepsilon_x^+)^2 + (\varepsilon_z^+)^2 \right]^{\frac{1}{2}} \tag{H.32}$$

$$Pr_t = \varepsilon^+ / \varepsilon_\theta^+ \tag{H.33}$$

$$C = \frac{\rho \mu}{\rho_e \mu_e} \tag{H.34}$$

$$T = \frac{(\rho \tilde{v})_w}{\rho_e \tilde{u}_e} R_x^{\frac{1}{2}} \tag{H.35}$$

In equations (H.13) to (H.35), ν denotes the kinematic viscosity, ε_x, ε_z, and ε_θ are the $\tilde{x}$ and $\tilde{z}$ eddy viscosities and thermal conductivity, respectively, and K_1 and K_2 are geodesic curvature parameters which are defined in Appendix G.

Boundary conditions for equations (H.10), (H.11), and (H.12) are given by

$$\left.\begin{aligned} \eta = 0: \quad & f = 0, \quad g = 0, \quad f' = 0, \quad g' = 0 \\ & \theta = \theta_w \quad \text{or} \quad \theta' = \theta'_w \end{aligned}\right\} \tag{H.36}$$

$$\left.\begin{aligned} \eta = \eta_\delta: \quad & f' = 1, \quad g' = 1, \quad \theta = 1 \end{aligned}\right\} \tag{H.37}$$

The boundary conditions for f and g in equation (H.36) follow from the transformed equation for $\overline{\rho\tilde{v}}$ which is given by

$$\overline{\rho\tilde{v}} = -(\rho_e \mu_e \tilde{u}_e / \tilde{x})^{\frac{1}{2}} (P_2 f + P_3 g)$$

$$- (\rho_e \mu_e \tilde{u}_e \tilde{x})^{\frac{1}{2}} \left(\frac{1}{h_1} \frac{\partial f}{\partial \tilde{x}} + \frac{1}{h_2} \frac{\tilde{w}_e}{\tilde{u}_e} \frac{\partial g}{\partial \tilde{z}} \right) + (\rho \tilde{v})_w \tag{H.38}$$

It should be noted that the above equations assume that H_e is effectively constant.

3. TRANSFORMED ATTACHMENT LINE EQUATIONS

As for the three-dimensional boundary layer equations, the attachment line equations can be transformed by defining a two-component vector potential given by

$$\rho h_2 \tilde{u} = \frac{\partial \psi}{\partial \tilde{y}} \tag{H.39}$$

$$\rho h_1 \tilde{w}_z = \frac{\partial \phi}{\partial \tilde{y}} \tag{H.40}$$

$$h_1 h_2 \overline{\rho\tilde{v}} = -\left[\frac{\partial\psi}{\partial\tilde{x}} + \phi\right] + h_1 h_2 (\rho\tilde{v})_w \tag{H.41}$$

The transformation relations given by equations (H.4) to (H.7) are also employed for the attachment line flow. Moreover, the vector potential given by equation (H.8) is again used. The vector potential ϕ, however, is now defined by

$$\phi = \left(\rho_e \mu_e \tilde{u}_e \tilde{x}\right)^{\frac{1}{2}} h_1 \frac{\tilde{w}_{ze}}{\tilde{u}_e} g(\tilde{x}, n, \tilde{z}) \tag{H.42}$$

Substituting equations (H.39), (H.40), and (H.41) into the continuity equation given by equation (G.20) identically satisfies that equation. Substituting the above equations into equations (G.21), (G.22), and (G.23) yields the following system of equations:

$$\left[C(1+\varepsilon_x^+)f''\right]' + P_2 ff'' + \frac{P_1}{h_2} gf'' + \frac{M}{h_1}\left[\frac{\rho_e}{\rho} - (f')^2\right] - Tf''$$

$$= \frac{\tilde{x}}{h_1}\left[f' \frac{\partial f'}{\partial\tilde{x}} - f'' \frac{\partial f}{\partial\tilde{x}}\right] \tag{H.43}$$

$$\left[C(1+\varepsilon_z^+)g''\right]' + P_2 fg'' + \frac{P_1}{h_2} gg'' + P_8\left[f'g' - \frac{\rho_e}{\rho}\right]$$

$$+ \frac{P_1}{h_2}\left[\frac{\rho_e}{\rho} - (g')^2\right] + P_9\left[\frac{\rho_e}{\rho} - (f')^2\right] - Tg''$$

$$= \frac{\tilde{x}}{h_1}\left[f' \frac{\partial g'}{\partial\tilde{x}} - g'' \frac{\partial f}{\partial\tilde{x}}\right] \tag{H.44}$$

$$\left\{C\left[\left(1 + \varepsilon^{+}\frac{Pr}{Pr_t}\right)\frac{\theta'}{Pr} + \frac{\tilde{u}_e^2}{H_e}\left(1 - \frac{1}{Pr}\right)ff''\right]\right\}'$$

$$+ P_2 f\theta' + \frac{P_1}{h_2} g\theta' - T\theta' = \frac{\tilde{x}}{h_1}\left(f'\frac{\partial\theta}{\partial\tilde{x}} - \theta'\frac{\partial f}{\partial\tilde{x}}\right) \qquad \text{(H.45)}$$

Equations (H.43), (H.44), and (H.45) represent the streamwise momentum, cross flow momentum, and energy equations, respectively. The following new parameter definitions are employed in equations (H.43), (H.44), and (H.45).

$$f' = \tilde{u}/\tilde{u}_e \qquad \text{(H.46)}$$

$$g' = \tilde{w}_z/\tilde{w}_{ze} \qquad \text{(H.47)}$$

$$\theta = H/H_e \qquad \text{(H.48)}$$

$$P_1 = \frac{\tilde{x}}{\tilde{u}_e}\frac{\partial\tilde{w}_e}{\partial\tilde{z}} \qquad \text{(H.49)}$$

$$P_8 = \left(K_1 h_1 \tilde{x} - \frac{\tilde{x}}{\tilde{w}_{ze}}\frac{\partial\tilde{w}_{ze}}{\partial\tilde{x}}\right)\frac{1}{h_1} \qquad \text{(H.50)}$$

$$P_9 = \frac{\tilde{x}\tilde{u}_e}{\tilde{w}_{ze}}\frac{\partial K_2}{\partial\tilde{z}} \qquad \text{(H.51)}$$

Boundary conditions for equations (H.43), (H.44), and (H.45) are given by

$$\left.\begin{aligned} \eta = 0: \quad & f = 0, \quad g = 0, \quad f' = 0, \quad g' = 0 \\ & \theta = \theta_w, \quad \text{or} \quad \theta' = \theta'_w \end{aligned}\right\} \qquad \text{(H.52)}$$

$$\left.\eta = \eta_\delta: \quad f' = 1, \quad g' = 1, \quad \theta = 1 \right\} \qquad \text{(H.53)}$$

The boundary conditions for f and g in equation (H.52) follow from the transformed equation for $\overline{\rho\tilde{v}}$, which is given by

$$\overline{\rho\tilde{v}} = -(\rho_e\mu_e)^{\frac{1}{2}} \left[\left[\frac{\tilde{u}_e}{\tilde{x}}\right]^{\frac{1}{2}} P_2 f + (\tilde{u}_e\tilde{x})^{\frac{1}{2}} \left[\frac{1}{h_1}\frac{\partial f}{\partial \tilde{x}} + \frac{1}{h_2}\left(\frac{\tilde{w}_{ze}}{\tilde{u}_e}\right) g\right]\right] + (\rho\tilde{v})_w \qquad \text{(H.54)}$$

The above equations assume that H_e is effectively constant.

APPENDIX I

SOLUTION OF THE BOUNDARY LAYER EQUATIONS

1. INTRODUCTION

The transformed boundary layer equations presented in Appendix H form a parabolic system of partial differential equations. Those equations are solved in the present investigation using a second-order implicit finite difference algorithm in which marching is performed in the streamwise direction. The numerical algorithm that is employed is based on the Keller box scheme (12). Cebeci and Keller have successfully applied this method to the computation of two-dimensional boundary layer flows (13). Recently, Cebeci, Khattab, and Stewartson (14) have suggested an extension of this scheme for three-dimensional flows. The analysis given in Reference (14) accounts for the wave-like properties of the three-dimensional boundary layer flow in planes parallel to the body surface, and as such is capable of computing both positive and negative cross flows.

The numerical solution technique used for the boundary layer computation is presented in this appendix. Three differencing schemes are employed in the boundary layer computation; the choice of which scheme depending upon whether the cross-flow velocity is positive, negative, or identically zero (attachment line flow). Each differencing scheme is discussed fully below. See Appendix H for the nomenclature employed in this appendix.

2. FINITE DIFFERENCE ALGORITHM FOR THE ATTACHMENT LINE FLOW

The numerical solution algorithm that is employed for the boundary layer computation is based upon solving a system of first-order partial differential equations. The transformed streamwise momentum, cross-flow momentum, and energy equations for the attachment line flow, given by equations (H.43), (H.44), and (H.45), respectively, can be written as a first-order system of equations by defining the following variables:

$$f' = u \tag{I.1}$$

$$u' = v = f'' \tag{I.2}$$

$$g' = w \tag{I.3}$$

$$w' = t = g'' \tag{I.4}$$

$$\theta' = \Delta \tag{I.5}$$

where the primes denote differentiation with respect to the stretched normal coordinate η (see Appendix H for definition of the flow variables). Introducing equations (I.1) to (I.5) into equations (H.43), (H.44), and (H.45) yields the following system of first-order equations:

$$bv' + (b' + P_2 f + P_1 g/h_2 - T)v + \frac{M}{h_1}(\lambda - u^2)$$

$$= \frac{\tilde{x}}{h_1}\left(u\frac{\partial u}{\partial \tilde{x}} - v\frac{\partial f}{\partial \tilde{x}}\right) \tag{I.6}$$

$$ct' + (c' + P_2 f + P_1 g/h_2)t + P_8(uw - \lambda) + \frac{P_1}{h_2}(\lambda - w^2)$$

$$+ P_9(\lambda - u^2) - Tt = \frac{\tilde{x}}{h_1}\left(u\frac{\partial w}{\partial \tilde{x}} - t\frac{\partial f}{\partial \tilde{x}}\right) \qquad (I.7)$$

$$d\Delta' + (d' + P_2 f + P_1 g/h_2 - T)\Delta + e'fv + e(f'v + fv')$$

$$= \frac{\tilde{x}}{h_1}\left(u\frac{\partial \theta}{\partial \tilde{x}} - \Delta\frac{\partial f}{\partial \tilde{x}}\right) \qquad (I.8)$$

In equations (I.6), (I.7), and (I.8), the following parameter definitions are used:

$$b = C(1 + \varepsilon_x^+) \qquad (I.9)$$

$$c = C(1 + \varepsilon_z^+) \qquad (I.10)$$

$$d = C\left(1 + \varepsilon^+ \frac{Pr}{Pr_t}\right)\Big/Pr \qquad (I.11)$$

$$e = C\frac{\tilde{u}_e^2}{H_e}(1 - 1/Pr) \qquad (I.12)$$

$$\lambda = \rho_e/\rho \qquad (I.13)$$

The computational network used in solving equations (I.1) to (I.8) is illustrated in Figure I.1. In this figure, the computational cell step sizes are given by

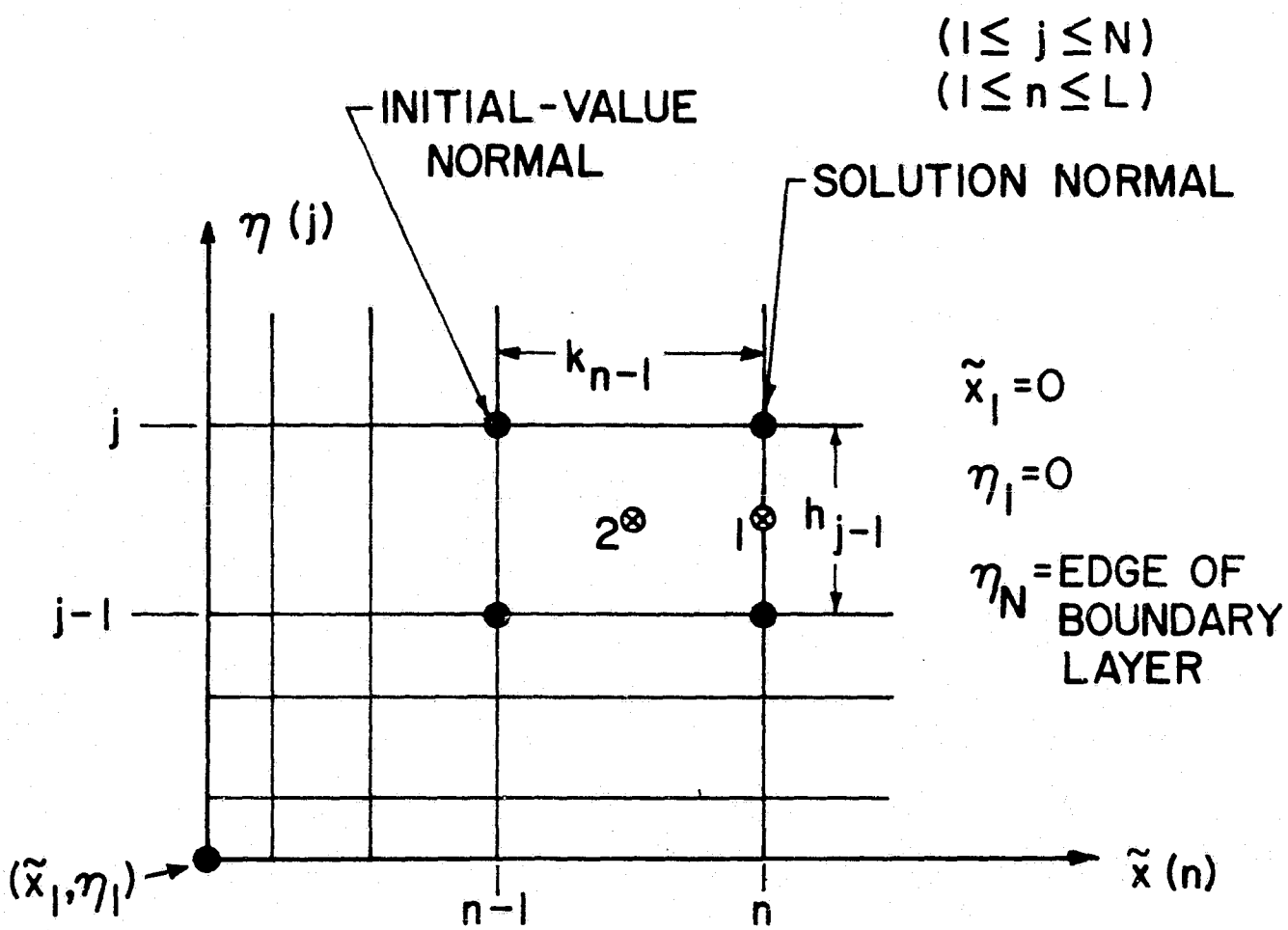

FIGURE I.1. ATTACHMENT LINE FLOW COMPUTATIONAL NETWORK.

$$\eta_j = \eta_{j-1} + h_{j-1} \tag{I.14}$$

$$\tilde{x}_n = \tilde{x}_{n-1} + k_{n-1} \tag{I.15}$$

where h_{j-1} and k_{n-1} denote the mesh lengths in the η- and $\tilde{x}$-coordinate directions, respectively. Both h_j and k_n are varied in the computation as deemed necessary. In particular, the η mesh is determined by

$$h_j = K\, h_{j-1} \tag{I.16}$$

$$\eta_j = \sum_{i=1}^{j-1} h_i = \sum_{i=1}^{j-1} K^{i-1}\, h_1 \tag{I.17}$$

where K is the ratio of consecutive cell mesh lengths (assumed constant), and h_1 is the η mesh length of the first cell.

The finite difference expressions used to approximate equations (I.1) to (I.8) are now written using the computational network illustrated in Figure I.1. Equations (I.1) to (I.5) are approximated by using second-order accurate centered difference and averaging expressions taken about point (1) in Figure (I.1). Point (1) is the midpoint of the cell segment connecting points $(\tilde{x}_n, \eta_j)$ and $(\tilde{x}_n, \eta_{j-1})$. Performing the differencing yields the following system of equations:

$$f_j^n - f_{j-1}^n - \frac{h_{j-1}}{2}\,(u_j^n + u_{j-1}^n) = 0 \tag{I.18}$$

$$u_j^n - u_{j-1}^n - \frac{h_{j-1}}{2}\,(v_j^n + v_{j-1}^n) = 0 \tag{I.19}$$

$$g_j^n - g_{j-1}^n - \frac{h_{j-1}}{2}(w_j^n + w_{j-1}^n) = 0 \tag{I.20}$$

$$w_j^n - w_{j-1}^n - \frac{h_{j-1}}{2}(t_j^n + t_{j-1}^n) = 0 \tag{I.21}$$

$$\theta_j^n - \theta_{j-1}^n - \frac{h_{j-1}}{2}(\Delta_j^n + \Delta_{j-1}^n) = 0 \tag{I.22}$$

The finite difference approximations to equations (I.6), (I.7), and (I.8) are obtained using second-order accurate centered difference and averaging expressions taken about point (2) in Figure I.1. Point (2) is the midpoint of the computational cell. Performing the differencing yields the following system of equations:

$$\begin{aligned}
&\overline{b}_{j*}\left(\frac{\overline{v}_j - \overline{v}_{j-1}}{h_{j-1}}\right) + \left[\frac{\overline{b}_j - \overline{b}_{j-1}}{h_{j-1}} + (\overline{P_2})\overline{f}_{j*} + \left(\frac{\overline{P_1}}{h_2}\right)\overline{g}_{j*} - (\overline{T})\right]\overline{v}_{j*} \\
&\qquad + \left(\frac{\overline{M}}{h_1}\right)\left[\overline{\lambda}_{j*} - (\overline{u_{j*}})^2\right] \\
&\quad = \left(\frac{\overline{\tilde{x}}}{h_1}\right)\left[\overline{u}_{j*}\left(\frac{\overline{u}_n - \overline{u}_{n-1}}{k_{n-1}}\right) - \overline{v}_{j*}\left(\frac{\overline{f}_n - \overline{f}_{n-1}}{k_{n-1}}\right)\right]
\end{aligned} \tag{I.23}$$

$$\begin{aligned}
&\overline{c}_{j*}\left(\frac{\overline{t}_j - \overline{t}_{j-1}}{h_{j-1}}\right) + \left[\frac{\overline{c}_j - \overline{c}_{j-1}}{h_{j-1}} + (\overline{P_2})\overline{f}_{j*} + \left(\frac{\overline{P_1}}{h_2}\right)\overline{g}_{j*}\right]\overline{t}_{j*} \\
&\qquad + (\overline{P_8})(\overline{u}_{j*}\overline{w}_{j*} - \overline{\lambda}_{j*}) + \left(\frac{\overline{P_1}}{h_2}\right)\left[\overline{\lambda}_{j*} - (\overline{w_{j*}})^2\right] \\
&\qquad + (\overline{P_9})\left[\overline{\lambda}_{j*} - (\overline{u}_{j*})^2\right] - (\overline{T})\overline{t}_{j*} \\
&\quad = \left(\frac{\overline{\tilde{x}}}{h_1}\right)\left[\overline{u}_{j*}\left(\frac{\overline{w}_n - \overline{w}_{n-1}}{k_{n-1}}\right) - \overline{t}_{j*}\left(\frac{\overline{f}_n - \overline{f}_{n-1}}{k_{n-1}}\right)\right]
\end{aligned} \tag{I.24}$$

$$\bar{d}_{j*}\left[\frac{\bar{\Delta}_j - \bar{\Delta}_{j-1}}{h_{j-1}}\right] + \left[\frac{\bar{d}_j - \bar{d}_{j-1}}{h_{j-1}} + (\bar{P}_2)\bar{f}_{j*} + \left(\frac{\bar{P}_1}{h_2}\right)\bar{g}_{j*} - (\bar{T})\right]\bar{\Delta}_{j*}$$

$$+ \left[\frac{\bar{e}_j - \bar{e}_{j-1}}{h_{j-1}}\right]\bar{f}_{j*}\bar{v}_{j*} + \bar{e}_{j*}\left[\bar{v}_{j*}\left[\frac{\bar{f}_j - \bar{f}_{j-1}}{h_{j-1}}\right] + \bar{f}_{j*}\left[\frac{\bar{v}_j - \bar{v}_{j-1}}{h_{j-1}}\right]\right]$$

$$= \left(\frac{\tilde{x}}{h_1}\right)\left[\bar{u}_{j*}\left[\frac{\bar{\theta}_n - \bar{\theta}_{n-1}}{k_{n-1}}\right] - \bar{\Delta}_{j*}\left[\frac{\bar{f}_n - \bar{f}_{n-1}}{k_{n-1}}\right]\right] \qquad \text{(I.25)}$$

In equations (I.23), (I.24), and (I.25), the following averaging notations are employed:

$$(\bar{\alpha}) = \frac{1}{2}\left(\alpha^n + \alpha^{n-1}\right) \qquad \text{(I.26)}$$

$$\bar{\alpha}_j = \frac{1}{2}\left(\alpha_j^n + \alpha_j^{n-1}\right) \qquad \text{(I.27)}$$

$$\bar{\alpha}_n = \frac{1}{2}\left(\alpha_j^n + \alpha_{j-1}^n\right) \qquad \text{(I.28)}$$

$$\bar{\alpha}_{j*} = \frac{1}{4}\left(\alpha_j^n + \alpha_{j-1}^n + \alpha_j^{n-1} + \alpha_{j-1}^{n-1}\right) \qquad \text{(I.29)}$$

where α denotes a general function. Equation (I.26) is used solely for variables which are dependent upon $\tilde{x}$ and $\tilde{z}$ only.

Equations (I.18) to (I.25) form a system of 8(N - 1) equations when written for N points along the solution normal. An additional eight relations can be obtained from the boundary conditions given below:

$$\left.\begin{aligned} \eta = \eta_1 = 0: \quad & f = 0, \quad g = 0, \quad u = 0, \quad w = 0 \\ & \theta = \theta_w \quad \text{or} \quad \Delta = \Delta_w \end{aligned}\right\} \tag{I.30}$$

$$\left.\eta = \eta_N: \quad u = 1, \quad w = 1, \quad \theta = 1 \quad \right\} \tag{I.31}$$

This yields a total of 8N relations for the 8N unknowns along the attachment line solution normal provided that the flow properties at the streamwise station $\tilde{x}_{n-1}$ are known.

In order to accelerate convergence, the system of difference equations is solved using Newton's method. Newton's method expresses any dependent variable at the (k + 1)th iteration as the sum of that variable at the (k)th iteration and a perturbation. Thus,

$$\left[f_j^n\right]^{(k+1)} = \left[f_j^n\right]^{(k)} + \left[\delta f_j^n\right]^{(k)} \tag{I.32}$$

where f_j^n denotes any dependent variable at point $(\tilde{x}_n, \eta_j)$, the superscript in parentheses ( ) denotes the iteration number, and δf_j^n denotes the perturbation or difference in f_j^n between successive iterations.

The final forms of the finite difference equations are obtained by substituting expressions like equation (I.32) for each of the eight dependent variables into equations (I.18) to (I.25), expanding all products of the dependent variables in terms of the perturbation quantities, and then neglecting all quadratic or higher-order terms. Performing this operation for equations (I.18) to (I.22) yields the

following results (note that the iteration superscript is omitted):

$$\delta f_j^n - \delta f_{j-1}^n - \frac{h_{j-1}}{2}(\delta u_j^n + \delta u_{j-1}^n) = R_1 \tag{I.33}$$

$$\delta u_j^n - \delta u_{j-1}^n - \frac{h_{j-1}}{2}(\delta v_j^n + \delta v_{j-1}^n) = R_2 \tag{I.34}$$

$$\delta g_j^n - \delta g_{j-1}^n - \frac{h_{j-1}}{2}(\delta w_j^n + \delta w_{j-1}^n) = R_3 \tag{I.35}$$

$$\delta w_j^n - \delta w_{j-1}^n - \frac{h_{j-1}}{2}(\delta t_j^n + \delta t_{j-1}^n) = R_4 \tag{I.36}$$

$$\delta \theta_j^n - \delta \theta_{j-1}^n - \frac{h_{j-1}}{2}(\delta \Delta_j^n + \delta \Delta_{j-1}^n) = R_5 \tag{I.37}$$

where

$$R_1 = f_{j-1}^n - f_j^n + \frac{h_{j-1}}{2}(u_j^n + u_{j-1}^n) \tag{I.38}$$

$$R_2 = u_{j-1}^n - u_j^n + \frac{h_{j-1}}{2}(v_j^n + v_{j-1}^n) \tag{I.39}$$

$$R_3 = g_{j-1}^n - g_j^n + \frac{h_{j-1}}{2}(w_j^n + w_{j-1}^n) \tag{I.40}$$

$$R_4 = w_{j-1}^n - w_j^n + \frac{h_{j-1}}{2}(t_j^n + t_{j-1}^n) \tag{I.41}$$

$$R_5 = \theta_{j-1}^n - \theta_j^n + \frac{h_{j-1}}{2}(\Delta_j^n + \Delta_{j-1}^n) \tag{I.42}$$

Incorporating Newton's method into equation (I.23) yields

$$S_1\delta f_j^n + S_2\delta f_{j-1}^n + S_3\delta u_j^n + S_4\delta u_{j-1}^n + S_5\delta v_j^n + S_6\delta v_{j-1}^n$$

$$+ S_7\delta g_j^n + S_8\delta g_{j-1}^n + S_9\delta w_j^n + S_{10}\delta w_{j-1}^n = Y_1 \qquad \text{(I.43)}$$

where

$$S_1 = \frac{(\overline{P_2})X_4}{4} + \left(\frac{\tilde{x}}{h_1}\right)\frac{k_{n-1}^{-1}X_4}{2} \qquad \text{(I.44)}$$

$$S_2 = \frac{(\overline{P_2})X_4}{4} + \left(\frac{\tilde{x}}{h_1}\right)\frac{k_{n-1}^{-1}X_4}{2} \qquad \text{(I.45)}$$

$$S_3 = -\left(\frac{\overline{M}}{h_1}\right)\frac{X_6}{2} - \left(\frac{\tilde{x}}{h_1}\right)k_{n-1}^{-1}\left[\frac{(X_7 - \overline{u}_{n-1})}{4} + \frac{X_6}{2}\right] \qquad \text{(I.46)}$$

$$S_4 = -\left(\frac{\overline{M}}{h_1}\right)\frac{X_6}{2} - \left(\frac{\tilde{x}}{h_1}\right)k_{n-1}^{-1}\left[\frac{(X_7 - \overline{u}_{n-1})}{4} + \frac{X_6}{2}\right] \qquad \text{(I.47)}$$

$$S_5 = \frac{\overline{b}_{j*}\,h_{j-1}^{-1}}{2} + \frac{X_5}{4} + \left(\frac{\tilde{x}}{h_1}\right)\frac{k_{n-1}^{-1}}{4}(X_8 - \overline{f}_{n-1}) \qquad \text{(I.48)}$$

$$S_6 = -\frac{\overline{b}_{j*}\,h_{j-1}^{-1}}{2} + \frac{X_5}{4} + \left(\frac{\tilde{x}}{h_1}\right)\frac{k_{n-1}^{-1}}{4}(X_8 - \overline{f}_{n-1}) \qquad \text{(I.49)}$$

$$S_7 = \left(\frac{\overline{P_1}}{h_2}\right)\frac{X_4}{4} \qquad \text{(I.50)}$$

$$S_8 = \left(\frac{\overline{P_1}}{h_2}\right)\frac{X_4}{4} \qquad \text{(I.51)}$$

$$S_9 = 0 \qquad \text{(I.52)}$$

$$S_{10} = 0 \qquad \text{(I.53)}$$

$$Y_1 = -X_1 - X_4X_5 + \left(\frac{\overline{M}}{h_1}\right)(X_6^2 - \overline{\lambda}_{j*}) + \left(\frac{\overline{\tilde{x}}}{h_1}\right) k_{n-1}^{-1}\left[X_6(X_7 - \overline{u}_{n-1}) - X_4(X_8 - \overline{f}_{n-1})\right] \quad (I.54)$$

Incorporating Newton's method into equation (I.24) yields

$$T_1\delta f_j^n + T_2\delta f_{j-1}^n + T_3\delta u_j^n + T_4\delta u_{j-1}^n + T_5\delta g_j^n + T_6\delta g_{j-1}^n + T_7\delta w_j^n + T_8\delta w_{j-1}^n + T_9\delta t_j^n + T_{10}\delta t_{j-1}^n + T_{11}\delta v_j^n + T_{12}\delta v_{j-1}^n = Y_2 \quad (I.55)$$

where

$$T_1 = \frac{(\overline{P_2})\ X_{10}}{4} + \left(\frac{\overline{\tilde{x}}}{h_1}\right)\frac{k_{n-1}^{-1}\ X_{10}}{2} \quad (I.56)$$

$$T_2 = \frac{(\overline{P_2})\ X_{10}}{4} + \left(\frac{\overline{\tilde{x}}}{h_1}\right)\frac{k_{n-1}^{-1}\ X_{10}}{2} \quad (I.57)$$

$$T_3 = \frac{(\overline{P_8})\ X_{12}}{4} - \frac{(\overline{P_9})\ X_6}{2} - \left(\frac{\overline{\tilde{x}}}{h_1}\right)\frac{k_{n-1}^{-1}}{4}(X_{13} - \overline{w}_{n-1}) \quad (I.58)$$

$$T_4 = \frac{(\overline{P_8})\ X_{12}}{4} - \frac{(\overline{P_9})\ X_6}{2} - \left(\frac{\overline{\tilde{x}}}{h_1}\right)\frac{k_{n-1}^{-1}}{4}(X_{13} - \overline{w}_{n-1}) \quad (I.59)$$

$$T_5 = \left(\frac{\overline{P_1}}{h_2}\right)\frac{X_{10}}{4} \quad (I.60)$$

C-4

$$T_6 = \left(\frac{\overline{P_1}}{h_2}\right) \frac{X_{10}}{4} \tag{I.61}$$

$$T_7 = \frac{(\overline{P_8})\ X_6}{4} - \left(\frac{\overline{P_1}}{h_2}\right) \frac{X_{12}}{2} - \left(\frac{\overline{\tilde{x}}}{h_1}\right) \frac{k_{n-1}^{-1}\ X_6}{2} \tag{I.62}$$

$$T_8 = \frac{(\overline{P_8})\ X_6}{4} - \left(\frac{\overline{P_1}}{h_2}\right) \frac{X_{12}}{2} - \left(\frac{\overline{\tilde{x}}}{h_1}\right) \frac{k_{n-1}^{-1}\ X_6}{2} \tag{I.63}$$

$$T_9 = \frac{\overline{c_{j*}}\ h_{j-1}^{-1}}{2} + \frac{X_{11}}{4} + \left(\frac{\overline{\tilde{x}}}{h_1}\right) \frac{k_{n-1}^{-1}}{4} (X_8 - \overline{f}_{n-1}) \tag{I.64}$$

$$T_{10} = \frac{-\overline{c_{j*}}\ h_{j-1}^{-1}}{2} + \frac{X_{11}}{4} + \left(\frac{\overline{\tilde{x}}}{h_1}\right) \frac{k_{n-1}^{-1}}{4} (X_8 - \overline{f}_{n-1}) \tag{I.65}$$

$$T_{11} = 0.0 \tag{I.66}$$

$$T_{12} = 0.0 \tag{I.67}$$

$$\begin{aligned} Y_2 = &- X_9 - X_{10}X_{11} - (\overline{\rho_8})\ (X_6X_{12} - \overline{\lambda}_{j*}) \\ &+ \left(\frac{\overline{P_1}}{h_2}\right) (X_{12}^2 - \overline{\lambda}_{j*}) + (\overline{P_9})(X_6^2 - \overline{\lambda}_{j*}) \\ &+ \left(\frac{\overline{\tilde{x}}}{h_1}\right) k_{n-1}^{-1} \left[X_6\ (X_{13} - \overline{w}_{n-1}) - X_{10}\ (X_8 - \overline{f}_{n-1})\right] \end{aligned} \tag{I.68}$$

Incorporating Newton's method into equation (I.25) yields

$$U_1\delta f_j^n + U_2\delta f_{j-1}^n + U_3\delta u_j^n + U_4\delta u_{j-1}^n + U_5\delta g_j^n + U_6\delta g_{j-1}^n$$

$$+ U_7\delta w_j^n + U_8\delta w_{j-1}^n + U_9\delta t_j^n + U_{10}\delta t_{j-1}^n + U_{11}\delta v_j^n$$

$$+ U_{12}\delta v_{j-1}^n + U_{13}\delta\Delta_j^n + U_{14}\delta\Delta_{j-1}^n + U_{15}\delta\theta_j^n$$

$$+ U_{16}\delta\theta_{j-1}^n = Y_3 \tag{I.69}$$

where

$$U_1 = \frac{(\overline{P_2})\ X_{15}}{4} + \frac{\beta X_4}{4} + \overline{e_{j*}}\left[\frac{h_{j-1}^{-1}\ X_4}{2} + \frac{X_{18}}{4}\right] + \left(\frac{\overline{\tilde{x}}}{h_1}\right)\frac{k_{n-1}^{-1}\ X_{15}}{2} \tag{I.70}$$

$$U_2 = \frac{(\overline{P_2})\ X_{15}}{4} + \frac{\beta X_4}{4} + \overline{e_{j*}}\left[\frac{-h_{j-1}^{-1}\ X_4}{2} + \frac{X_{18}}{4}\right] + \left(\frac{\overline{\tilde{x}}}{h_1}\right)\frac{k_{n-1}^{-1}\ X_{15}}{2} \tag{I.71}$$

$$U_3 = -\left(\frac{\overline{\tilde{x}}}{h_1}\right)\frac{k_{n-1}^{-1}}{4}\left(X_{19} - \overline{\theta}_{n-1}\right) \tag{I.72}$$

$$U_4 = -\left(\frac{\overline{\tilde{x}}}{h_1}\right)\frac{k_{n-1}^{-1}}{4}\left(X_{19} - \overline{\theta}_{n-1}\right) \tag{I.73}$$

$$U_5 = \left(\frac{\overline{P_1}}{h_2}\right)\frac{X_{15}}{4} \tag{I.74}$$

$$U_6 = \left(\frac{\overline{P_1}}{h_2}\right)\frac{X_{15}}{4} \tag{I.75}$$

$$U_7 = 0 \tag{I.76}$$

$$U_8 = 0 \tag{I.77}$$

$$U_9 = 0 \tag{I.78}$$

$$U_{10} = 0 \tag{I.79}$$

$$U_{11} = \frac{\beta X_2}{4} + \frac{\overline{e_{j*}}\, X_{17}}{4} + \frac{\overline{e_{j*}}\, X_2\, h_{j-1}^{-1}}{2} \tag{I.80}$$

$$U_{12} = \frac{\beta X_2}{4} + \frac{\overline{e_{j*}}\, X_{17}}{4} - \frac{\overline{e_{j*}}\, X_2\, h_{j-1}^{-1}}{2} \tag{I.81}$$

$$U_{13} = \frac{\overline{d}_{j*}\, h_{j-1}^{-1}}{2} + \frac{X_{16}}{4} + \left(\frac{\overline{\tilde{x}}}{h_1}\right) \frac{k_{n-1}^{-1}}{4} (X_8 - \overline{f}_{n-1}) \tag{I.82}$$

$$U_{14} = \frac{-\overline{d}_{j*}\, h_{j-1}^{-1}}{2} + \frac{X_{16}}{4} + \left(\frac{\overline{\tilde{x}}}{h_1}\right) \frac{k_{n-1}^{-1}}{4} (X_8 - \overline{f}_{n-1}) \tag{I.83}$$

$$U_{15} = -\left(\frac{\overline{\tilde{x}}}{h_1}\right) \frac{k_{n-1}^{-1}\, X_6}{2} \tag{I.84}$$

$$U_{16} = -\left(\frac{\overline{\tilde{x}}}{h_1}\right) \frac{k_{n-1}^{-1}\, X_6}{2} \tag{I.85}$$

$$Y_3 = -X_{14} - X_{15}X_{16} - \beta X_2 X_4 - \overline{e_{j*}}(X_4 X_{17} + X_2 X_{18})$$

$$+ \left(\frac{\overline{\tilde{x}}}{h_1}\right) k_{n-1}^{-1}\left[X_6(X_{19} - \overline{\theta}_{n-1}) - X_{15}(X_8 - \overline{f}_{n-1})\right] \tag{I.86}$$

In equations (I.43) to (I.86), the following parameter definitions have been employed:

$$X_1 = \frac{\bar{b}_{j*}\, h_{j-1}^{-1}}{2} \left(v_j^n + v_j^{n-1} - v_{j-1}^n - v_{j-1}^{n-1}\right) \tag{I.87}$$

$$X_2 = \frac{1}{4} \left(f_j^n + f_{j-1}^n\right) + f_{j*}^* \tag{I.88}$$

$$X_3 = \frac{1}{4} \left(g_j^n + g_{j-1}^n\right) + g_{j*}^* \tag{I.89}$$

$$X_4 = \frac{1}{4} \left(v_j^n + v_{j-1}^n\right) + v_{j*}^* \tag{I.90}$$

$$X_5 = h_{j-1}^{-1} \left(\bar{b}_j - \bar{b}_{j-1}\right) + \left(\overline{P_2}\right) X_2 + \left(\frac{\overline{P_1}}{h_2}\right) X_3 - \left(\bar{T}\right) \tag{I.91}$$

$$X_6 = \frac{1}{4} \left(u_j^n + u_{j-1}^n\right) + u_{j*}^* \tag{I.92}$$

$$X_7 = \frac{1}{2} \left(u_j^n + u_{j-1}^n\right) \tag{I.93}$$

$$X_8 = \frac{1}{2} \left(f_j^n + f_{j-1}^n\right) \tag{I.94}$$

$$X_9 = \frac{\bar{c}_{j*}\, h_{j-1}^{-1}}{2} \left(t_j^n + t_j^{n-1} - t_{j-1}^n - t_{j-1}^{n-1}\right) \tag{I.95}$$

$$X_{10} = \frac{1}{4} \left(t_j^n + t_{j-1}^n\right) + t_{j*}^* \tag{I.96}$$

$$X_{11} = h_{j-1}^{-1} \left(\bar{c}_j - \bar{c}_{j-1}\right) + \left(\overline{P_2}\right) X_2 + \left(\frac{\overline{P_1}}{h_2}\right) X_3 - \left(\bar{T}\right) \tag{I.97}$$

$$X_{12} = \frac{1}{4}\left(w_j^n + w_{j-1}^n\right) + w_{j*}^* \tag{I.98}$$

$$X_{13} = \frac{1}{2}\left(w_j^n + w_{j-1}^n\right) \tag{I.99}$$

$$X_{14} = \frac{\overline{d_{j*}}\, h_{j-1}^{-1}}{2}\left(\Delta_j^n + \Delta_j^{n-1} - \Delta_{j-1}^n - \Delta_{j-1}^{n-1}\right) \tag{I.100}$$

$$X_{15} = \frac{1}{4}\left(\Delta_j^n + \Delta_{j-1}^n\right) + \Delta_{j*}^* \tag{I.101}$$

$$X_{16} = h_{j-1}^{-1}\left(\overline{d}_j - \overline{d}_{j-1}\right) + \left(\overline{P_2}\right) X_2 + \left(\frac{\overline{P_1}}{h_2}\right) X_3 - \left(\overline{T}\right) \tag{I.102}$$

$$X_{17} = \frac{h_{j-1}^{-1}}{2}\left(f_j^n + f_j^{n-1} - f_{j-1}^n - f_{j-1}^{n-1}\right) \tag{I.103}$$

$$X_{18} = \frac{h_{j-1}^{-1}}{2}\left(v_j^n + v_j^{n-1} - v_{j-1}^n - v_{j-1}^{n-1}\right) \tag{I.104}$$

$$X_{19} = \frac{1}{2}\left(\theta_j^n + \theta_{j-1}^n\right) \tag{I.105}$$

$$\beta = h_{j-1}^{-1}\left(\overline{e}_j - \overline{e}_{j-1}\right) \tag{I.106}$$

$$T = \frac{(\rho v)_w}{\rho_e \tilde{u}_e} R_x^{\frac{1}{2}} \tag{I.107}$$

In equations (I.33) to (I.107), the following averaging notations are used:

$$(\bar{\alpha}) = \frac{1}{2}(\alpha^{n} + \alpha^{n-1}) \tag{I.108}$$

$$\overline{\alpha_{j*}} = \frac{1}{4}(\alpha_{j}^{n} + \alpha_{j-1}^{n} + \alpha_{j}^{n-1} + \alpha_{j-1}^{n-1}) \tag{I.109}$$

$$\alpha_{j*}^{*} = \frac{1}{4}(\alpha_{j}^{n-1} + \alpha_{j-1}^{n-1}) \tag{I.110}$$

$$\overline{\alpha_{j}} = \frac{1}{2}(\alpha_{j}^{n} + \alpha_{j}^{n-1}) \tag{I.111}$$

$$\overline{\alpha_{n}} = \frac{1}{2}(\alpha_{j}^{n} + \alpha_{j-1}^{n}) \tag{I.112}$$

where α denotes a general function. Equation (I.108) is used solely for variables which are dependent upon $\tilde{x}$ and $\tilde{z}$, only.

The above finite difference equations for the perturbation quantities are solved using an efficient block tridiagonal matrix factorization procedure presented later in this appendix.

3. FINITE DIFFERENCE ALGORITHM FOR POSITIVE CROSS FLOW

The transformed streamwise momentum, cross-flow momentum, and energy equations for three-dimensional boundary layer flow, given by equations (H.10), (H.11), and (H.12), respectively, can be written as a system of first-order equations by employing equations (I.1) to (I.5). Introducing those parameter definitions into equations (H.10), (H.11), and (H.12), yields the following first-order system of equations:

$$bv' + (b' + P_2 f + P_3 g - T)v + \frac{M}{h_1}(\lambda - u^2) + P_4(\lambda - w^2)$$

$$+ P_5(uw - \lambda)$$

$$= \frac{\tilde{x}}{h_1}\left(u\frac{\partial u}{\partial \tilde{x}} - v\frac{\partial f}{\partial \tilde{x}}\right) + \left(\frac{\tilde{w}_e \tilde{x}}{\tilde{u}_e h_2}\right)\left(w\frac{\partial u}{\partial \tilde{z}} - v\frac{\partial g}{\partial \tilde{z}}\right) \qquad \text{(I.113)}$$

$$ct' + (c' + P_2 f + P_3 g - T)t + P_6(\lambda - u^2) + \left(\frac{\tilde{w}_e}{\tilde{u}_e}\frac{P}{h_2}\right)(\lambda - w^2)$$

$$+ P_7(uw - \lambda)$$

$$= \frac{\tilde{x}}{h_1}\left(u\frac{\partial w}{\partial \tilde{x}} - t\frac{\partial f}{\partial \tilde{x}}\right) + \left(\frac{\tilde{w}_e \tilde{x}}{\tilde{u}_e h_2}\right)\left(w\frac{\partial w}{\partial \tilde{z}} - t\frac{\partial g}{\partial \tilde{z}}\right) \qquad \text{(I.114)}$$

$$d\Delta' + (d' + P_2 f + P_3 g - T)\Delta + e'\left[uv + \left(\frac{\tilde{w}_e}{\tilde{u}_e}\right)^2 wt\right]$$

$$+ e(uv' + u'v) + e\left(\frac{\tilde{w}_e}{\tilde{u}_e}\right)^2 (wt' + w't)$$

$$= \frac{\tilde{x}}{h_1}\left(u\frac{\partial \theta}{\partial \tilde{x}} - \Delta\frac{\partial f}{\partial \tilde{x}}\right) + \left(\frac{\tilde{w}_e \tilde{x}}{\tilde{u}_e h_2}\right)\left(w\frac{\partial \theta}{\partial \tilde{z}} - \Delta\frac{\partial g}{\partial \tilde{z}}\right) \qquad \text{(I.115)}$$

In equations (I.113), (I.114), and (I.115), the parameters b, c, d, e, and λ are again defined by equations (I.9) to (I.13).

Equations (I.1) to (I.5) and equations (I.113) to (I.115) are solved for positive cross-flow velocities ($\tilde{w} > 0$) using the computational network illustrated in Figure I.2. The cell step sizes are

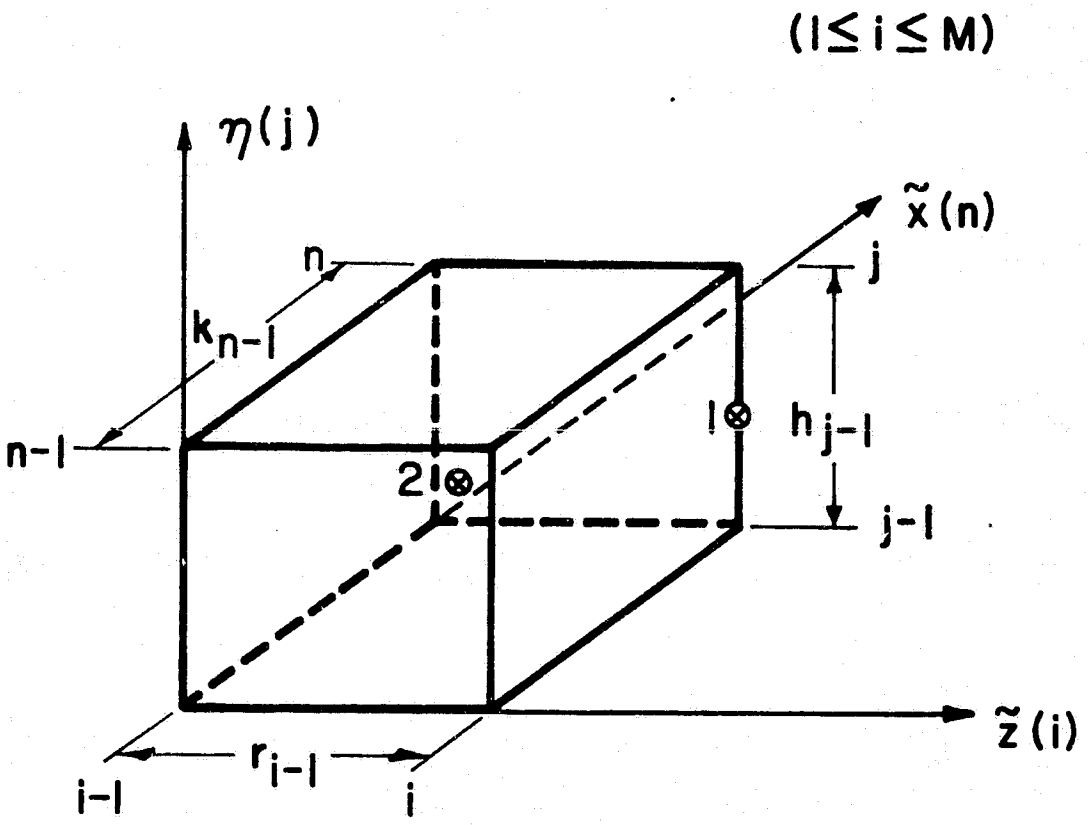

FIGURE I.2. THREE-DIMENSIONAL POSITIVE CROSS FLOW COMPUTATIONAL NETWORK.

again given by equations (I.14) and (I.15), and by

$$\tilde{z}_i = \tilde{z}_{i-1} + r_{i-1} \tag{I.116}$$

where r_{i-1} is the cell mesh length in the $\tilde{z}$-coordinate direction.

The finite difference equations used to approximate equations (I.1) to (I.5) are obtained by using second-order accurate centered difference and averaging expressions taken about point (1) in Figure I.2. Point (1) is the midpoint of the cell segment connecting points $(\tilde{x}_n, \eta_j, \tilde{z}_i)$ and $(\tilde{x}_n, \eta_{j-1}, \tilde{z}_i)$. The differencing procedure yields the following system of equations:

$$f_j^{n,i} - f_{j-1}^{n,i} - \frac{h_{j-1}}{2}(u_j^{n,i} + u_{j-1}^{n,i}) = 0 \tag{I.117}$$

$$u_j^{n,i} - u_{j-1}^{n,i} - \frac{h_{j-1}}{2}(v_j^{n,i} + v_{j-1}^{n,i}) = 0 \tag{I.118}$$

$$g_j^{n,i} - g_{j-1}^{n,i} - \frac{h_{j-1}}{2}(w_j^{n,i} + w_{j-1}^{n,i}) = 0 \tag{I.119}$$

$$w_j^{n,i} - w_{j-1}^{n,i} - \frac{h_{j-1}}{2}(t_j^{n,i} + t_{j-1}^{n,i}) = 0 \tag{I.120}$$

$$\theta_j^{n,i} - \theta_{j-1}^{n,i} - \frac{h_{j-1}}{2}(\Delta_j^{n,i} + \Delta_{j-1}^{n,i}) = 0 \tag{I.121}$$

The finite difference approximations to equations (I.113), (I.114), and (I.115) are obtained using second-order accurate centered difference and averaging expressions taken about point (2) in Figure I.2. Point (2) is the midpoint of the computational cell. Performing the differencing yields the following system of equations:

$$\bar{b}_{j*}\left[\frac{\bar{v}_j - \bar{v}_{j-1}}{h_{j-1}}\right] + \left[\frac{\bar{b}_j - \bar{b}_{j-1}}{h_{j-1}} + (\overline{P_2})\bar{f}_{j*} + (\overline{P_3})\bar{g}_{j*} - (\overline{T})\right]\bar{v}_{j*}$$

$$+ \left(\frac{\overline{M}}{h_1}\right)\left[\bar{\lambda}_{j*} - (\overline{u_{j*}})^2\right] + (\overline{P_4})\left[\bar{\lambda}_{j*} - (\overline{w_{j*}})^2\right]$$

$$+ (\overline{P_5})(\overline{u_{j*}\, w_{j*}} - \bar{\lambda}_{j*})$$

$$= \left(\frac{\tilde{x}}{h_1}\right)\left[\bar{u}_{j*}\left(\frac{\bar{u}_n - \bar{u}_{n-1}}{k_{n-1}}\right) - \bar{v}_{j*}\left(\frac{\bar{f}_n - \bar{f}_{n-1}}{k_{n-1}}\right)\right]$$

$$+ \left(\frac{\tilde{w}_e \tilde{x}}{\tilde{u}_e h_2}\right)\left[\bar{w}_{j*}\left(\frac{\bar{u}_i - \bar{u}_{i-1}}{r_{i-1}}\right) - \bar{v}_{j*}\left(\frac{\bar{g}_i - \bar{g}_{i-1}}{r_{i-1}}\right)\right] \qquad \text{(I.122)}$$

$$\bar{c}_{j*}\left[\frac{\bar{t}_j - \bar{t}_{j-1}}{h_{j-1}}\right] + \left[\frac{\bar{c}_j - \bar{c}_{j-1}}{h_{j-1}} + (\overline{P_2})\bar{f}_{j*} + (\overline{P_3})\bar{g}_{j*} - (\overline{T})\right]\bar{t}_{j*}$$

$$+ (\overline{P_6})\left[\bar{\lambda}_{j*} - (\bar{u}_{j*})^2\right] + \left(\frac{\overline{\tilde{w}_e P}}{\tilde{u}_e h_2}\right)\left[\bar{\lambda}_{j*} - (\bar{w}_{j*})^2\right]$$

$$+ (\overline{P_7})(\bar{u}_{j*}\, \bar{w}_{j*} - \bar{\lambda}_{j*})$$

$$= \left(\frac{\tilde{x}}{h_1}\right)\left[\bar{u}_{j*}\left(\frac{\bar{w}_n - \bar{w}_{n-1}}{k_{n-1}}\right) - \bar{t}_{j*}\left(\frac{\bar{f}_n - \bar{f}_{n-1}}{k_{n-1}}\right)\right]$$

$$+ \left(\frac{\overline{\tilde{w}_e \tilde{x}}}{\tilde{u}_e h_2}\right)\left[\bar{w}_{j*}\left(\frac{\bar{w}_i - \bar{w}_{i-1}}{r_{i-1}}\right) - \bar{t}_{j*}\left(\frac{\bar{g}_i - \bar{g}_{i-1}}{r_{i-1}}\right)\right] \qquad \text{(I.123)}$$

$$\bar{d}_{j*}\left[\frac{\bar{\Delta}_j - \bar{\Delta}_{j-1}}{h_{j-1}}\right] + \left[\frac{\bar{d}_j - \bar{d}_{j-1}}{h_{j-1}} + (\overline{P_2})\bar{f}_{j*} + (\overline{P_3})\bar{g}_{j*} - (\bar{T})\right]\bar{\Delta}_{j*}$$

$$+ \frac{\bar{e}_j - \bar{e}_{j-1}}{h_{j-1}}\left[\bar{u}_{j*}\,\bar{v}_{j*} + \left(\frac{\tilde{w}_e}{\tilde{u}_e}\right)^2 \bar{w}_{j*}\,\bar{t}_{j*}\right]$$

$$+ \bar{e}_{j*}\left[\bar{u}_{j*}\left(\frac{\bar{v}_j - \bar{v}_{j-1}}{h_{j-1}}\right) + \bar{v}_{j*}\left(\frac{\bar{u}_j - \bar{u}_{j-1}}{h_{j-1}}\right)\right]$$

$$+ \bar{e}_{j*}\left(\frac{\tilde{w}_e}{\tilde{u}_e}\right)^2\left[\bar{w}_{j*}\left(\frac{\bar{t}_j - \bar{t}_{j-1}}{h_{j-1}}\right) + \bar{t}_{j*}\left(\frac{\bar{w}_j - \bar{w}_{j-1}}{h_{j-1}}\right)\right]$$

$$= \left(\frac{\tilde{x}}{h_1}\right)\left[\bar{u}_{j*}\left(\frac{\bar{\theta}_n - \bar{\theta}_{n-1}}{k_{n-1}}\right) - \bar{\Delta}_{j*}\left(\frac{\bar{f}_n - \bar{f}_{n-1}}{k_{n-1}}\right)\right]$$

$$+ \left(\frac{\tilde{w}_e\tilde{x}}{\tilde{u}_e h_2}\right)\left[\bar{w}_{j*}\left(\frac{\bar{\theta}_i - \bar{\theta}_{i-1}}{r_{i-1}}\right) - \bar{\Delta}_{j*}\left(\frac{\bar{g}_i - \bar{g}_{i-1}}{r_{i-1}}\right)\right] \qquad \text{(I.124)}$$

In equations (I.122), (I.123), and (I.124), the following averaging notations are used:

$$(\bar{\alpha}) = \frac{1}{4}\left(\alpha^{n,i} + \alpha^{n,i-1} + \alpha^{n-1,i} + \alpha^{n-1,i-1}\right) \qquad \text{(I.125)}$$

$$\bar{\alpha}_j = \frac{1}{4}\left(\alpha_j^{n,i} + \alpha_j^{n,i-1} + \alpha_j^{n-1,i} + \alpha_j^{n-1,i-1}\right) \qquad \text{(I.126)}$$

$$\bar{\alpha}_n = \frac{1}{4}\left(\alpha_j^{n,i} + \alpha_j^{n,i-1} + \alpha_{j-1}^{n,i} + \alpha_{j-1}^{n,i-1}\right) \qquad \text{(I.127)}$$

$$\bar{\alpha}_i = \frac{1}{4}\left(\alpha_j^{n,i} + \alpha_j^{n-1,i} + \alpha_{j-1}^{n,i} + \alpha_{j-1}^{n-1,i}\right) \qquad \text{(I.128)}$$

$$\bar{\alpha}_{j*} = \frac{1}{8}\left(\alpha_j^{n,i} + \alpha_{j-1}^{n,i} + \alpha_j^{n-1,i} + \alpha_{j-1}^{n-1,i} + \alpha_j^{n,i-1}\right.$$

$$\left. + \alpha_{j-1}^{n,i-1} + \alpha_j^{n-1,i-1} + \alpha_{j-1}^{n-1,i-1}\right) \qquad . \text{(I.129)}$$

where α denotes a general function. Equation (I.125) is used solely for variables which are dependent upon $\tilde{x}$ and $\tilde{z}$, only.

Boundary conditions for the above equations are given by equations (I.30) and (I.31). Taken with the boundary conditions, equations (I.117) to (I.129) form a system of 8N equations for the 8N unknowns along the boundary layer normal located at $\tilde{x} = \tilde{x}_n$ and $\tilde{z} = \tilde{z}_i$. The solution may be determined if the flow properties at stations $(\tilde{x}_n, \tilde{z}_{i-1})$, $(\tilde{x}_{n-1}, \tilde{z}_i)$, and $(\tilde{x}_{n-1}, \tilde{z}_{i-1})$ are known.

Newton's method is again employed for obtaining the solution to the difference equations. Relations of the form given by equation (I.32) are again substituted for each dependent variable into the appropriate difference equations. A linear system of equations is obtained by neglecting quadratic and higher-order terms in the perturbation quantities. Incorporating Newton's method into equations (I.18) to (I.22) yields

$$\delta f_j^{n,i} - \delta f_{j-1}^{n,i} - \frac{h_{j-1}}{2}\left(\delta u_j^{n,i} + \delta u_{j-1}^{n,i}\right) = R_1 \qquad \text{(I.130)}$$

$$\delta u_j^{n,i} - \delta u_{j-1}^{n,i} - \frac{h_{j-1}}{2}\left(\delta v_j^{n,i} + \delta v_{j-1}^{n,i}\right) = R_2 \qquad \text{(I.131)}$$

$$\delta g_j^{n,i} - \delta g_{j-1}^{n,i} - \frac{h_{j-1}}{2}\left(\delta w_j^{n,i} + \delta w_{j-1}^{n,i}\right) = R_3 \qquad \text{(I.132)}$$

$$\delta w_j^{n,i} - \delta w_{j-1}^{n,i} - \frac{h_{j-1}}{2}(\delta t_j^{n,i} + \delta t_{j-1}^{n-1}) = R_4 \qquad \text{(I.133)}$$

$$\delta\theta_j^{n,i} - \delta\theta_{j-1}^{n,i} - \frac{h_{j-1}}{2}(\delta\Delta_j^{n,i} + \delta\Delta_{j-1}^{n,i}) = R_5 \qquad \text{(I.134)}$$

where

$$R_1 = f_{j-1}^{n,i} - f_j^{n,i} + \frac{h_{j-1}}{2}(u_j^{n,i} + u_{j-1}^{n,i}) \qquad \text{(I.135)}$$

$$R_2 = u_{j-1}^{n,i} - u_j^{n,i} + \frac{h_{j-1}}{2}(v_j^{n,i} + v_{j-1}^{n,i}) \qquad \text{(I.136)}$$

$$R_3 = g_{j-1}^{n,i} - g_j^{n,i} + \frac{h_{j-1}}{2}(w_j^{n,i} + w_{j-1}^{n,i}) \qquad \text{(I.137)}$$

$$R_4 = w_{j-1}^{n,i} - w_j^{n,i} + \frac{h_{j-1}}{2}(t_j^{n,i} + t_{j-1}^{n,i}) \qquad \text{(I.138)}$$

$$R_5 = \theta_{j-1}^{n,i} - \theta_j^{n,i} + \frac{h_{j-1}}{2}(\Delta_j^{n,i} + \Delta_{j-1}^{n,i}) \qquad \text{(I.139)}$$

Incorporating Newton's method into equation (I.122) yields

$$S_1\,\delta f_j^{n,i} + S_2\,\delta f_{j-1}^{n,i} + S_3\,\delta u_j^{n,i} + S_4\,\delta u_{j-1}^{n,i} + S_5\,\delta v_j^{n,i} + S_6\,\delta v_{j-1}^{n,i} + S_7\,\delta g_j^{n,i} + S_8\,\delta g_{j-1}^{n,i} + S_9\,\delta w_j^{n,i} + S_{10}\,\delta w_{j-1}^{n,i} = Y_1 \qquad \text{(I.140)}$$

where

$$S_1 = \frac{(\overline{P_2})X_4}{8} + \left(\frac{\tilde{x}}{h_1}\right) \frac{k_{n-1}^{-1} X_4}{4} \tag{I.141}$$

$$S_2 = \frac{(\overline{P_2})X_4}{8} + \left(\frac{\tilde{x}}{h_1}\right) \frac{k_{n-1}^{-1} X_4}{4} \tag{I.142}$$

$$S_3 = -\left(\frac{\overline{M}}{h_1}\right) \frac{X_6}{4} + X_8\left[\frac{(\overline{P_5})}{8} - \frac{\alpha r_{i-1}^{-1}}{4}\right]$$

$$- \left(\frac{\tilde{x}}{h_1}\right) k_{n-1}^{-1} \left[\frac{1}{8}(X_{10} - \overline{u}_{n-1}) + \frac{X_6}{4}\right] \tag{I.143}$$

$$S_4 = -\left(\frac{\overline{M}}{h_1}\right) \frac{X_6}{4} + X_8\left[\frac{(\overline{P_5})}{8} - \frac{\alpha r_{i-1}^{-1}}{4}\right]$$

$$- \left(\frac{\tilde{x}}{h_1}\right) k_{n-1}^{-1} \left[\frac{1}{8}(X_{10} - \overline{u}_{n-1}) + \frac{X_6}{4}\right] \tag{I.144}$$

$$S_5 = \frac{1}{4}\overline{b}_{j*} h_{j-1}^{-1} + \frac{X_5}{8} + \left(\frac{\tilde{x}}{h_1}\right) \frac{k_{n-1}^{-1}}{8}(X_{11} - \overline{f}_{n-1})$$

$$+ \frac{\alpha r_{i-1}^{-1}}{8}(X_{13} - \overline{g}_{i-1}) \tag{I.145}$$

$$S_6 = -\frac{1}{4}\overline{b}_{j*} h_{j-1}^{-1} + \frac{X_5}{8} + \left(\frac{\tilde{x}}{h_1}\right) \frac{k_{n-1}^{-1}}{8}(X_{11} - \overline{f}_{n-1})$$

$$+ \frac{\alpha r_{i-1}^{-1}}{8}(X_{13} - \overline{g}_{i-1}) \tag{I.146}$$

$$S_7 = \frac{(\overline{P_3})X_4}{8} + \frac{\alpha r_{i-1}^{-1} X_4}{4} \tag{I.147}$$

$$S_8 = \frac{(\overline{P_3})X_4}{8} + \frac{\alpha r_{i-1}^{-1} X_4}{4} \tag{I.148}$$

$$S_9 = -\frac{(\overline{P_4})X_8}{4} + \frac{(\overline{P_5})X_6}{8} - \frac{\alpha r_{i-1}^{-1}}{8}(X_{12} - \overline{u}_{i-1}) \tag{I.149}$$

$$S_{10} = -\frac{(\overline{P_4})X_8}{4} + \frac{(\overline{P_5})X_6}{8} - \frac{\alpha r_{i-1}^{-1}}{8}(X_{12} - \overline{u}_{i-1}) \tag{I.150}$$

$$\begin{aligned} Y_1 = {} & -X_1 - X_4X_5 - X_7 - X_9 + (\overline{P_5})(\overline{\lambda}_{j*} - X_6X_8) \\ & + \left(\frac{\tilde{\tilde{x}}}{h_1}\right) k_{n-1}^{-1} \left[X_6(X_{10} - \overline{u}_{n-1}) - X_4(X_{11} - \overline{f}_{n-1})\right] \\ & + \alpha r_{i-1}^{-1} \left[X_8(X_{12} - \overline{u}_{i-1}) - X_4(X_{13} - \overline{g}_{i-1})\right] \end{aligned} \tag{I.151}$$

Incorporating Newton's method into equation (I.123) yields

$$\begin{aligned} & T_1\delta f_j^{n,i} + T_2\delta f_{j-1}^{n,i} + T_3\delta u_j^{n,i} + T_4\delta u_{j-1}^{n,i} + T_5\delta g_j^{n,i} \\ & + T_6\delta g_{j-1}^{n,i} + T_7\delta w_j^{n,i} + T_8\delta w_{j-1}^{n,i} + T_9\delta t_j^{n,i} \\ & + T_{10}\delta t_{j-1}^{n,i} = Y_2 \end{aligned} \tag{I.152}$$

where

$$T_1 = \frac{(\overline{P_2})X_{15}}{8} + \left(\frac{\tilde{x}}{h_1}\right)\frac{k_{n-1}^{-1}\,X_{15}}{4} \tag{I.153}$$

$$T_2 = \frac{(\overline{P_2})X_{15}}{8} + \left(\frac{\tilde{x}}{h_1}\right)\frac{k_{n-1}^{-1}\,X_{15}}{4} \tag{I.154}$$

$$T_3 = -\frac{(\overline{P_6})X_6}{4} + \frac{(\overline{P_7})X_8}{8} - \left(\frac{\tilde{x}}{h_1}\right)\frac{k_{n-1}^{-1}}{8}(X_{19} - \overline{w}_{n-1}) \tag{I.155}$$

$$T_4 = -\frac{(\overline{P_6})X_6}{4} + \frac{(\overline{P_7})X_8}{8} - \left(\frac{\tilde{x}}{h_1}\right)\frac{k_{n-1}^{-1}}{8}(X_{19} - \overline{w}_{n-1}) \tag{I.156}$$

$$T_5 = \frac{(\overline{P_3})X_{15}}{8} + \frac{\alpha r_{i-1}^{-1}\,X_{15}}{4} \tag{I.157}$$

$$T_6 = \frac{(\overline{P_3})X_{15}}{8} + \frac{\alpha r_{i-1}^{-1}\,X_{15}}{4} \tag{I.158}$$

$$T_7 = -\left(\frac{\overline{\tilde{w}_e P}}{\tilde{u}_e h_2}\right)\frac{X_8}{4} + X_6\left[\frac{(\overline{P_7})}{8} - \left(\frac{\overline{\tilde{x}}}{h_1}\right)\frac{k_{n-1}^{-1}}{4}\right]$$

$$- \frac{\alpha r_{i-1}^{-1}}{8}(X_{20} - \overline{w}_{i-1}) - \frac{\alpha r_{i-1}^{-1}\,X_8}{4} \tag{I.159}$$

$$T_8 = -\left(\frac{\overline{\tilde{w}_e P}}{\tilde{u}_e h_2}\right)\frac{X_8}{4} + X_6\left[\frac{(\overline{P_7})}{8} - \left(\frac{\overline{\tilde{x}}}{h_1}\right)\frac{k_{n-1}^{-1}}{4}\right]$$

$$- \frac{\alpha r_{i-1}^{-1}}{8}(X_{20} - \overline{w}_{i-1}) - \frac{\alpha r_{i-1}^{-1}\,X_8}{4} \tag{I.160}$$

$$T_9 = \frac{\bar{c}_{j*}\, h_{j-1}^{-1}}{4} + \frac{X_{16}}{8} + \left[\frac{\tilde{x}}{h_1}\right] \frac{k_{n-1}^{-1}}{8} (X_{11} - \bar{f}_{n-1})$$

$$+ \frac{\alpha r_{i-1}^{-1}}{8} (X_{13} - \bar{g}_{i-1}) \qquad \text{(I.161)}$$

$$T_{10} = -\frac{\bar{c}_{j*}\, h_{j-1}^{-1}}{4} + \frac{X_{16}}{8} + \left[\frac{\tilde{x}}{h_1}\right] \frac{k_{n-1}^{-1}}{8} (X_{11} - \bar{f}_{n-1})$$

$$+ \frac{\alpha r_{i-1}^{-1}}{8} (X_{13} - \bar{g}_{i-1}) \qquad \text{(I.162)}$$

$$Y_2 = -X_{14} - X_{15}X_{16} - X_{17} - X_{18} + (\overline{P_7})(\bar{\lambda}_{j*} - X_6X_8)$$

$$+ \left[\frac{\tilde{x}}{h_1}\right] k_{n-1}^{-1} \left[\overline{X}_6(X_{19} - \bar{w}_{n-1}) - X_{15}(X_{11} - \bar{f}_{n-1})\right]$$

$$+ \alpha r_{i-1}^{-1} \left[\overline{X}_8(X_{20} - \bar{w}_{i-1}) - X_{15}(X_{13} - \bar{g}_{i-1})\right] \qquad \text{(I.163)}$$

Incorporating Newton's method into equation (I.124) yields

$$U_1\delta f_j^{n,i} + U_2\delta f_{j-1}^{n,i} + U_3\delta u_j^{n,i} + U_4\delta u_{j-1}^{n,i} + U_5\delta g_j^{n,i}$$

$$+ U_6\delta g_{j-1}^{n,i} + U_7\delta w_j^{n,i} + U_8\delta w_{j-1}^{n,i} + U_9\delta t_j^{n,i}$$

$$+ U_{10}\delta t_{j-1}^{n,i} + U_{11}\delta v_j^{n,i} + U_{12}\delta v_{j-1}^{n,i} + U_{13}\delta\Delta_j^{n,i}$$

$$+ U_{14}\delta\Delta_{j-1}^{n,i} + U_{15}\delta\theta_j^{n,i} + U_{16}\delta\theta_{j-1}^{n,i} = Y_3 \qquad \text{(I.164)}$$

where

$$U_1 = \frac{(\overline{P_2})X_{22}}{8} + \left(\frac{\tilde{x}}{h_1}\right) \frac{k_{n-1}^{-1} X_{22}}{4} \tag{I.165}$$

$$U_2 = \frac{(\overline{P_2})X_{22}}{8} + \left(\frac{\tilde{x}}{h_1}\right) \frac{k_{n-1}^{-1} X_{22}}{4} \tag{I.166}$$

$$U_3 = \frac{\beta X_4}{8} + \overline{e}_{j*} h_{j-1}^{-1} \left(\frac{X_{24}}{8} + \frac{X_4}{4}\right)$$

$$- \left(\frac{\tilde{x}}{h_1}\right) \frac{k_{n-1}^{-1}}{8} (X_{28} - \overline{\theta}_{n-1}) \tag{I.167}$$

$$U_4 = \frac{\beta X_4}{8} + \overline{e}_{j*} h_{j-1}^{-1} \left(\frac{X_{24}}{8} - \frac{X_4}{4}\right)$$

$$- \left(\frac{\tilde{x}}{h_1}\right) \frac{k_{n-1}^{-1}}{8} (X_{28} - \overline{\theta}_{n-1}) \tag{I.168}$$

$$U_5 = \frac{(\overline{P_3})X_{22}}{8} + \frac{\alpha r_{i-1}^{-1} X_{22}}{4} \tag{I.169}$$

$$U_6 = \frac{(\overline{P_3})X_{22}}{8} + \frac{\alpha r_{i-1}^{-1} X_{22}}{4} \tag{I.170}$$

$$U_7 = \left(\frac{\overline{\tilde{w}_e}}{\tilde{u}_e}\right)^2 \frac{\beta X_{15}}{8} + \gamma h_{j-1}^{-1} \left(\frac{X_{26}}{8} + \frac{X_{15}}{4}\right)$$

$$- \frac{\alpha r_{i-1}^{-1}}{8} (X_{29} - \overline{\theta}_{i-1}) \tag{I.171}$$

$$U_8 = \left(\frac{\overline{\tilde{w}_e}}{\tilde{u}_e}\right)^2 \frac{\beta X_{15}}{8} + \gamma h_{j-1}^{-1} \left(\frac{X_{26}}{8} - \frac{X_{15}}{4}\right)$$

$$- \frac{\alpha r_{i-1}^{-1}}{8} (X_{29} - \overline{\theta}_{i-1}) \qquad \text{(I.172)}$$

$$U_9 = \left(\frac{\overline{\tilde{w}_e}}{\tilde{u}_e}\right)^2 \frac{\beta X_8}{8} + \gamma h_{j-1}^{-1} \left(\frac{X_8}{4} + \frac{X_{27}}{8}\right) \qquad \text{(I.173)}$$

$$U_{10} = \left(\frac{\overline{\tilde{w}_e}}{\tilde{u}_e}\right)^2 \frac{\beta X_8}{8} + \gamma h_{j-1}^{-1} \left(- \frac{X_8}{4} + \frac{X_{27}}{8}\right) \qquad \text{(I.174)}$$

$$U_{11} = \frac{\beta X_6}{8} + \overline{e}_{j*} \, h_{j-1}^{-1} \left(\frac{X_6}{4} + \frac{X_{25}}{8}\right) \qquad \text{(I.175)}$$

$$U_{12} = \frac{\beta X_6}{8} + \overline{e}_{j*} \, h_{j-1}^{-1} \left(- \frac{X_6}{4} + \frac{X_{25}}{8}\right) \qquad \text{(I.176)}$$

$$U_{13} = \frac{\overline{d}_{j*} \, h_{j-1}^{-1}}{4} + \frac{X_{23}}{8} + \left(\frac{\tilde{x}}{h_1}\right) \frac{k_{n-1}^{-1}}{8} (X_{11} - \overline{f}_{n-1})$$

$$+ \frac{\alpha r_{i-1}^{-1}}{8} (X_{13} - \overline{g}_{i-1}) \qquad \text{(I.177)}$$

$$U_{14} = - \frac{\overline{d}_{j*} \, h_{j-1}^{-1}}{4} + \frac{X_{23}}{8} + \left(\frac{\tilde{x}}{h_1}\right) \frac{k_{n-1}^{-1}}{8} (X_{11} - \overline{f}_{n-1})$$

$$+ \frac{\alpha r_{i-1}^{-1}}{8} (X_{13} - \overline{g}_{i-1}) \qquad \text{(I.178)}$$

$$U_{15} = - \left(\frac{\tilde{x}}{h_1}\right) \frac{k_{n-1}^{-1} \, X_6}{4} - \frac{\alpha r_{i-1}^{-1} \, X_8}{4} \qquad \text{(I.179)}$$

$$U_{16} = - \left(\frac{\tilde{x}}{h_1}\right) \frac{k_{n-1}^{-1} X_6}{4} - \frac{\alpha r_{i-1}^{-1} X_8}{4} \tag{I.180}$$

$$Y_3 = - \bar{d}_{j*} h_{j-1}^{-1} X_{21} - X_{22}X_{23} - \beta X_4 X_6 - \left(\frac{\bar{\tilde{w}}_e}{\tilde{u}_e}\right)^2 \beta X_8 X_{15}$$

$$- \bar{e}_{j*} h_{j-1}^{-1} (X_6 X_{24} + X_4 X_{25}) - \gamma h_{j-1}^{-1} (X_8 X_{26} + X_{15} X_{27})$$

$$+ \left(\frac{\tilde{x}}{h_1}\right) k_{n-1}^{-1} \left[X_6 (X_{28} - \bar{\theta}_{n-1}) - X_{22}(X_{11} - \bar{f}_{n-1})\right]$$

$$+ \alpha r_{i-1}^{-1} \left[X_8 (X_{29} - \bar{\theta}_{i-1}) - X_{22}(X_{13} - \bar{g}_{i-1})\right] \tag{I.181}$$

In equations (I.140) to (I.181), the following parameter definitions have been employed:

$$X_1 = \bar{b}_{j*} h_{j-1}^{-1} \left[\frac{1}{4}(v_j^{n,i} - v_{j-1}^{n,i}) + v_j^* - v_{j-1}^*\right] \tag{I.182}$$

$$X_2 = (\overline{P_2}) \left[\frac{1}{8}(f_j^{n,i} + f_{j-1}^{n,i}) + f_{j*}^*\right] \tag{I.183}$$

$$X_3 = (\overline{P_3}) \left[\frac{1}{8}(g_j^{n,i} + g_{j-1}^{n,i}) + g_{j*}^*\right] \tag{I.184}$$

$$X_4 = \frac{1}{8} (v_j^{n,i} + v_{j-1}^{n,i}) + v_{j*}^* \tag{I.185}$$

$$X_5 = h_{j-1}^{-1} (\bar{b}_j - \bar{b}_{j-1}) + X_2 + X_3 - (\bar{T}) \tag{I.186}$$

$$X_6 = \frac{1}{8} (u_j^{n,i} + u_{j-1}^{n,i}) + u_{j*}^* \tag{I.187}$$

$$X_7 = \left[\frac{M}{h_1}\right] (\bar{\lambda}_{j*} - X_6^2) \tag{I.188}$$

$$X_8 = \frac{1}{8} (w_j^{n,i} + w_{j-1}^{n,i}) + w_{j*}^{*} \tag{I.189}$$

$$X_9 = (\overline{P_4}) (\bar{\lambda}_{j*} - X_8^2) \tag{I.190}$$

$$X_{10} = \frac{1}{4} (u_j^{n,i} + u_{j-1}^{n,i}) + u_n^{**} \tag{I.191}$$

$$X_{11} = \frac{1}{4} (f_j^{n,i} + f_{j-1}^{n,i}) + f_n^{**} \tag{I.192}$$

$$X_{12} = \frac{1}{4} (u_j^{n,i} + u_{j-1}^{n,i}) + u_i^{***} \tag{I.193}$$

$$X_{13} = \frac{1}{4} (g_j^{n,i} + g_{j-1}^{n,i}) + g_i^{***} \tag{I.194}$$

$$X_{14} = \bar{c}_{j*} h_{j-1}^{-1} \left[\frac{1}{4} (t_j^{n,i} - t_{j-1}^{n,i}) + t_j^{*} - t_{j-1}^{*}\right] \tag{I.195}$$

$$X_{15} = \frac{1}{8} (t_j^{n,i} + t_{j-1}^{n,i}) + t_{j*}^{*} \tag{I.196}$$

$$X_{16} = h_{j-1}^{-1} (\bar{c}_j - \bar{c}_{j-1}) + X_2 + X_3 - (\bar{T}) \tag{I.197}$$

$$X_{17} = (\overline{P_6})(\bar{\lambda}_{j*} - X_6^2) \tag{I.198}$$

$$X_{18} = \left[\frac{\overline{\tilde{w}_e P}}{\tilde{u}_e h_2}\right] (\bar{\lambda}_{j*} - X_8^2) \tag{I.199}$$

$$X_{19} = \frac{1}{4}\left(w_j^{n,i} + w_{j-1}^{n,i}\right) + w_n^{**} \tag{I.200}$$

$$X_{20} = \frac{1}{4}\left(w_j^{n,i} + w_{j-1}^{n,i}\right) + w_i^{***} \tag{I.201}$$

$$X_{21} = \frac{1}{4}\left(\Delta_j^{n,i} - \Delta_{j-1}^{n,i}\right) + \Delta_j^{*} - \Delta_{j-1}^{*} \tag{I.202}$$

$$X_{22} = \frac{1}{8}\left(\Delta_j^{n,i} + \Delta_{j-1}^{n,i}\right) + \Delta_{j*}^{*} \tag{I.203}$$

$$X_{23} = h_{j-1}^{-1}\left(\overline{d}_j - \overline{d}_{j-1}\right) + X_2 + X_3 - \left(\overline{T}\right) \tag{I.204}$$

$$X_{24} = \frac{1}{4}\left(v_j^{n,i} - v_{j-1}^{n,i}\right) + v_j^{*} - v_{j-1}^{*} \tag{I.205}$$

$$X_{25} = \frac{1}{4}\left(u_j^{n,i} - u_{j-1}^{n,i}\right) + u_j^{*} - u_{j-1}^{*} \tag{I.206}$$

$$X_{26} = \frac{1}{4}\left(t_j^{n,i} - t_{j-1}^{n,i}\right) + t_j^{*} - t_{j-1}^{*} \tag{I.207}$$

$$X_{27} = \frac{1}{4}\left(w_j^{n,i} - w_{j-1}^{n,i}\right) + w_j^{*} - w_{j-1}^{*} \tag{I.208}$$

$$X_{28} = \frac{1}{4}\left(\theta_j^{n,i} + \theta_{j-1}^{n,i}\right) + \theta_n^{**} \tag{I.209}$$

$$X_{29} = \frac{1}{4}\left(\theta_j^{n,i} + \theta_{j-1}^{n,i}\right) + \theta_i^{***} \tag{I.210}$$

$$\alpha = \left(\frac{\overline{\tilde{w}_e \tilde{x}}}{\tilde{u}_e h_2}\right) \tag{I.211}$$

$$\beta = h_{j-1}^{-1}\left(\overline{e}_j - \overline{e}_{j-1}\right) \tag{I.212}$$

$$\gamma = \overline{e}_{j*} \left(\frac{\overline{\tilde{w}_e}}{\tilde{u}_e}\right)^2 \tag{I.213}$$

$$T = \frac{(\rho v)_w}{\rho_e \tilde{u}_e} R_x^{\frac{1}{2}} \tag{I.214}$$

In equations (I.130) to (I.214), the following averaging notations are employed:

$$(\overline{\alpha}) = \frac{1}{4} (\alpha^{n,i} + \alpha^{n,i-1} + \alpha^{n-1,i} + \alpha^{n-1,i-1}) \tag{I.215}$$

$$\overline{\alpha}_{j*} = \frac{1}{8} (\alpha_j^{n,i} + \alpha_{j-1}^{n,i} + \alpha_j^{n-1,i} + \alpha_{j-1}^{n-1,i} + \alpha_j^{n,i-1} + \alpha_{j-1}^{n,i-1} + \alpha_j^{n-1,i-1} + \alpha_{j-1}^{n-1,i-1}) \tag{I.216}$$

$$\alpha_{j*}^* = \frac{1}{2} (\alpha_j^* + \alpha_{j-1}^*) \tag{I.217}$$

$$\alpha_j^* = \frac{1}{4} (\alpha_j^{n,i-1} + \alpha_j^{n-1,i} + \alpha_j^{n-1,i-1}) \tag{I.218}$$

$$\overline{\alpha}_j = \frac{1}{4} (\alpha_j^{n,i} + \alpha_j^{n-1,i} + \alpha_j^{n,i-1} + \alpha_j^{n-1,i-1}) \tag{I.219}$$

$$\overline{\alpha}_n = \frac{1}{4} (\alpha_j^{n,i} + \alpha_{j-1}^{n,i} + \alpha_j^{n,i-1} + \alpha_{j-1}^{n,i-1}) \tag{I.220}$$

$$\alpha_n^{**} = \frac{1}{4} (\alpha_j^{n,i-1} + \alpha_{j-1}^{n,i-1}) \tag{I.221}$$

$$\overline{\alpha}_i = \frac{1}{4} (\alpha_j^{n,i} + \alpha_{j-1}^{n,i} + \alpha_j^{n-1,i} + \alpha_{j-1}^{n-1,i}) \tag{I.222}$$

$$\alpha_i^{***} = \frac{1}{4}\left(\alpha_j^{n-1,i} + \alpha_{j-1}^{n-1,i}\right) \qquad \text{(I.223)}$$

where α denotes a general function. Equation (I.215) is used solely for variables which are dependent upon $\tilde{x}$ and $\tilde{z}$, only.

The above finite difference equations for the perturbation quantities are solved using an efficient block tridiagonal matrix factorization procedure presented later in this appendix.

4. FINITE DIFFERENCE ALGORITHM FOR NEGATIVE CROSS FLOW

The previous section presented the finite difference algorithm used for the computation of three-dimensional boundary layer flow when the cross-flow velocity is positive. Due to numerical stability considerations, alterations to the above scheme must be made when attempting to compute boundary layer flows with a negative cross-flow velocity component. The physical reasoning behind this and the resulting algorithm are presented in this section.

Although the three-dimensional boundary layer equations are formally parabolic, they do exhibit a hyperbolic or wave-like character in planes parallel to the local body surface. This behavior was first noted by Raetz (21) who enumerated the general principles to which any successful three-dimensional boundary layer numerical solution procedure must conform. Because of the wave-like character of the governing equations, it is possible to identify wedge-type zones of influence and dependence of any point in the three-dimensional boundary layer flow. In two-dimensional boundary layer flow, these

zones collapse into the plane of computation, and, consequently, further consideration of this aspect need not be given.

Figure I.3 illustrates two possible streamline orientations for three-dimensional boundary-layer flow. Both Figures I.3.(a) and I.3.(b) represent streamline projections in a plane that is parallel to the local body surface, and in both cases the streamline passes through the body normal located at the station $\tilde{x} = \tilde{x}_n$ and $\tilde{z} = \tilde{z}_i$. Figure I.3.(a) illustrates the case when the cross-flow velocity is positive ($\tilde{w} > 0$), whereas Figure I.3.(b) illustrates the case when the cross-flow velocity is negative ($\tilde{w} < 0$). In order to achieve numerical stability, it is mandatory that the finite difference algorithm employ field points at the initial-data station $\tilde{x} = \tilde{x}_{n-1}$ which engulf the zone of dependence of the solution point. The zone of dependence of the solution point is delineated by the streamline passing through the point. Consequently, for the situation occurring in Figure I.3.(a), points from stations at $\tilde{z}_{i-1}$ and $\tilde{z}_i$ should be used, whereas for the situation occurring in Figure I.3.(b), points from the stations at $\tilde{z}_i$ and $\tilde{z}_{i+1}$ should be used. Examination of the finite difference algorithm presented in Section 3 of this appendix indicates that it is applicable for the positive cross-flow velocity case provided that the streamwise marching step is not so great as to have a streamline intersection at station $\tilde{x} = \tilde{x}_{n-1}$ such that $\tilde{z}^* < \tilde{z}_{i-1}$. The finite difference algorithm that is employed for the negative cross-flow velocity case is now presented.

The pertinent governing equations for reversed cross-flow cases are again given by equations (I.1) to (I.5) and equations (I.113) to

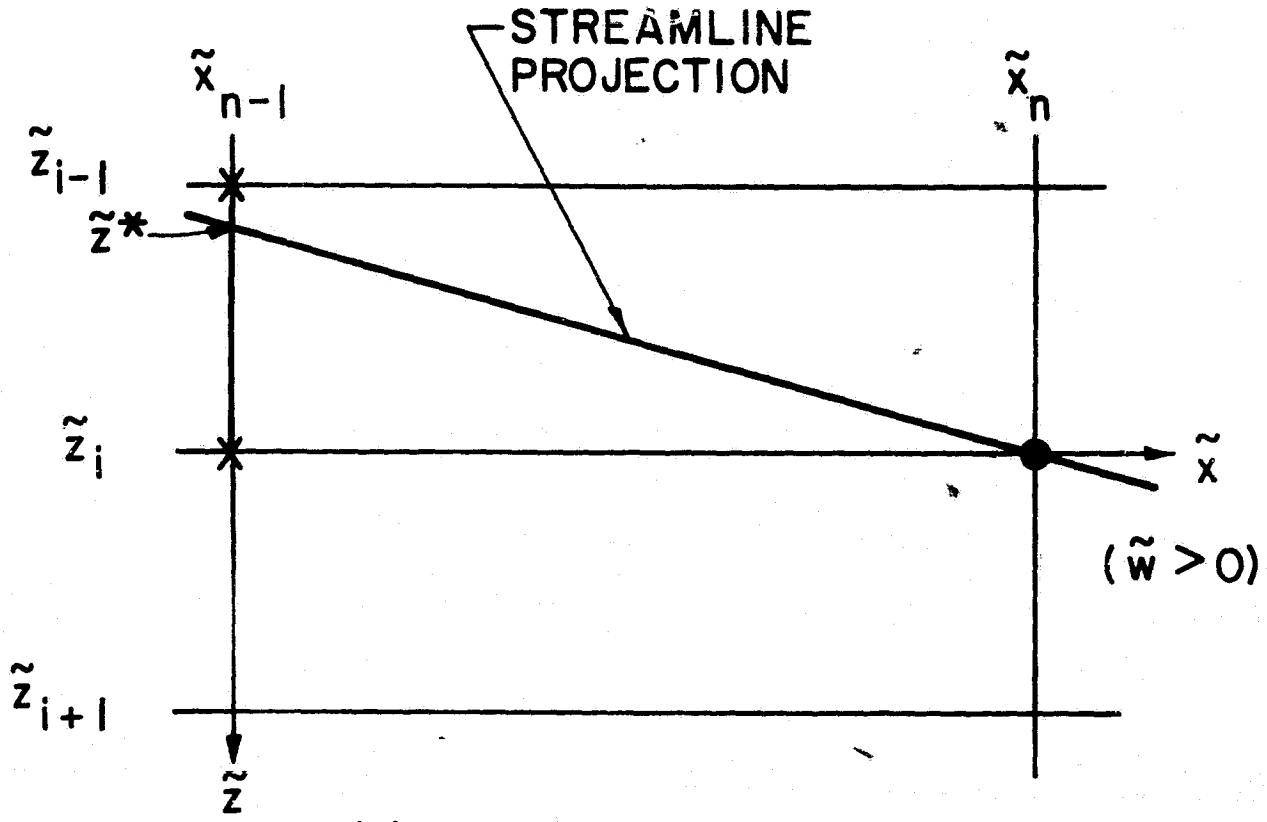

(a) POSITIVE CROSS FLOW.

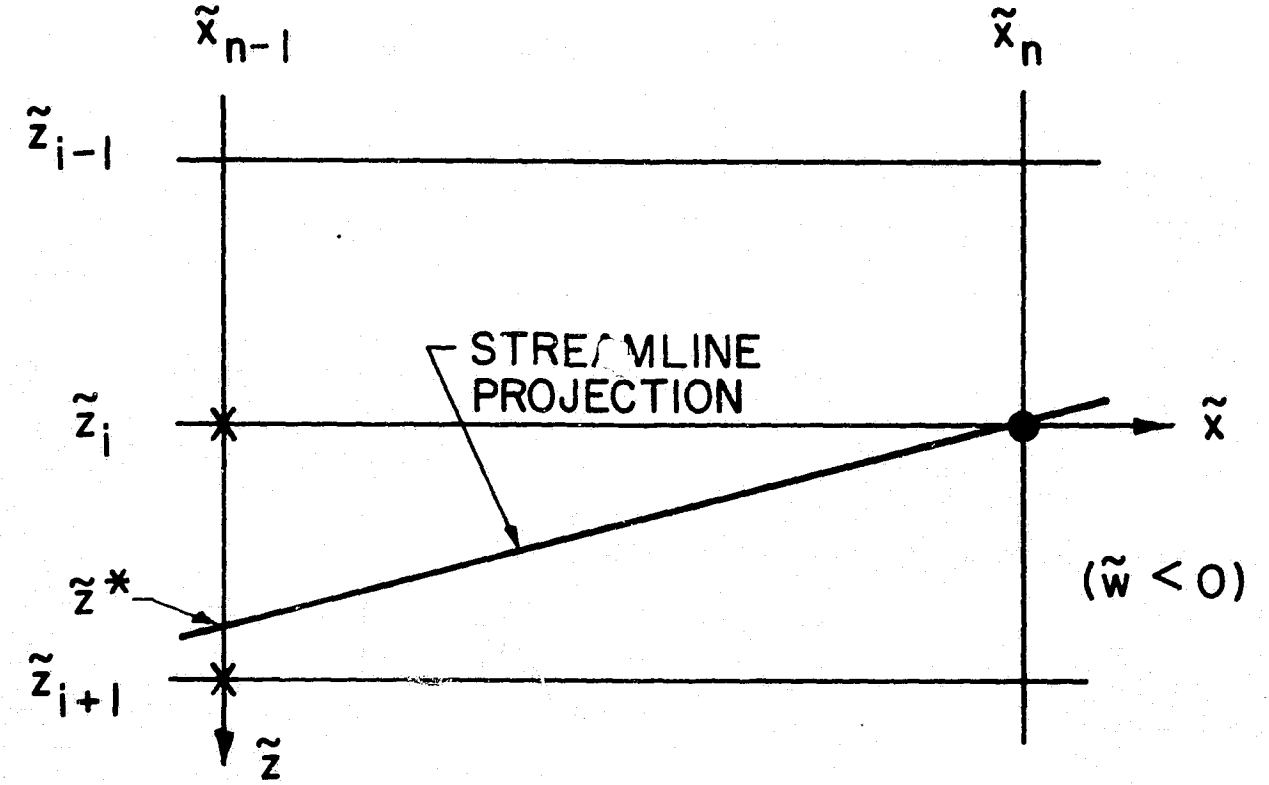

(b) NEGATIVE CROSS FLOW.

FIGURE I.3. STREAMLINE PATTERNS FOR POSITIVE AND NEGATIVE CROSS FLOW.

(I.115). Those equations are solved for negative cross-flow cases using the computational network illustrated in Figure I.4. The computational cell step sizes in the η-and $\tilde{x}$-coordinate directions are again given by equations (I.14) and (I.15), respectively. The computational cell now is staggered in the $\tilde{z}$-coordinate direction with the respective step sizes being given by

$$\tilde{z}_i = \tilde{z}_{i-1} + r_{i-1} \tag{I.224}$$

$$\tilde{z}_{i+1} = \tilde{z}_i + r_i \tag{I.225}$$

The finite difference equations used to approximate equations (I.1) to (I.5) are obtained by using second-order accurate centered difference and averaging expressions taken about point (1) in Figure I.4. Point (1) is the point midway between points $(\tilde{x}_n, n_j, \tilde{z}_i)$ and $(\tilde{x}_n, n_{j-1}, \tilde{z}_i)$. Performing the differencing again yields equations (I.117) to (I.121). The finite difference approximations to equations (I.113), (I.114), and (I.115) are obtained by using second-order accurate centered difference and averaging expressions taken about points (2), (3), and (4) in Figure I.4. Points (2), (3), and (4) are the midpoints of the three faces of the computational cell. Performing the differencing yields the following system of equations:

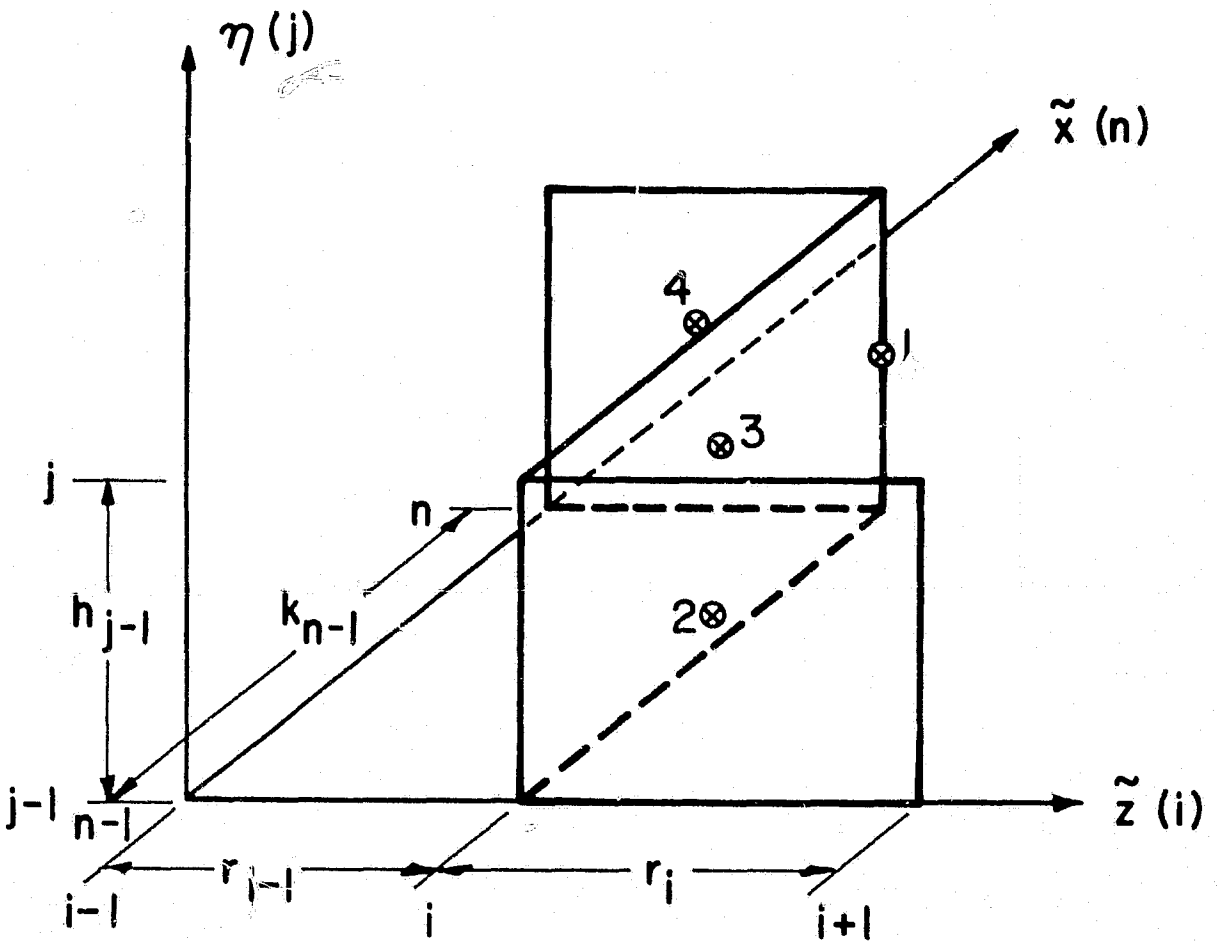

FIGURE I.4. THREE-DIMENSIONAL NEGATIVE CROSS FLOW COMPUTATIONAL NETWORK.

$$\overline{b}_{j*}\left(\frac{\overline{v}_j - \overline{v}_{j-1}}{h_{j-1}}\right) + \left[\frac{\overline{b}_j - \overline{b}_{j-1}}{h_{j-1}} + (\overline{P_2})\,\overline{f}_{j*} + (\overline{P_3})\,\overline{g}_{j*} - (\overline{T})\right]\overline{v}_{j*}$$

$$+ \left(\frac{M}{h_1}\right)\left[\overline{\lambda}_{j*} - (\overline{u_{j*}})^2\right] + (\overline{P_4})\left[\overline{\lambda}_{j*} - (\overline{w_{j*}})^2\right]$$

$$+ (\overline{P_5})\,(\overline{u}_{j*}\overline{w}_{j*} - \overline{\lambda}_{j*})$$

$$= \left(\frac{\overline{\tilde{x}}}{h_1}\right)\left[\overline{u}_{j*}\left(\frac{\overline{u}_n - \overline{u}_{n-1}}{k_{n-1}}\right) - \overline{v}_{j*}\left(\frac{\overline{f}_n - \overline{f}_{n-1}}{k_{n-1}}\right)\right]$$

$$+ \left(\frac{\overline{\tilde{w}_e\tilde{x}}}{\tilde{u}_e h_2}\right)\left[\xi\left(w\frac{\partial u}{\partial\tilde{z}} - v\frac{\partial q}{\partial\tilde{z}}\right)\Bigg|_2 + (1-\xi)\left(w\frac{\partial u}{\partial\tilde{z}} - v\frac{\partial q}{\partial\tilde{z}}\right)\Bigg|_4\right] \qquad \text{(I.226)}$$

$$\overline{c}_{j*}\left(\frac{\overline{t}_j - \overline{t}_{j-1}}{h_{j-1}}\right) + \left[\frac{\overline{c}_j - \overline{c}_{j-1}}{h_{j-1}} + (\overline{P_2})\,\overline{f}_{j*} + (\overline{P_3})\,\overline{g}_{j*} - (\overline{T})\right]\overline{t}_{j*}$$

$$+ (\overline{P_6})\left[\overline{\lambda}_{j*} - (\overline{u}_{j*})^2\right] + \left(\frac{\overline{\tilde{w}_e P}}{\tilde{u}_e h_2}\right)\left[\overline{\lambda}_{j*} - (\overline{w}_{j*})^2\right]$$

$$+ (\overline{P_7})(\overline{u}_{j*}\overline{w}_{j*} - \overline{\lambda}_{j*}) = \left(\frac{\overline{\tilde{x}}}{h_1}\right)\left[\overline{u}_{j*}\left(\frac{\overline{w}_n - \overline{w}_{n-1}}{k_{n-1}}\right)\right.$$

$$\left. - \overline{t}_{j*}\left(\frac{\overline{f}_n - \overline{f}_{n-1}}{k_{n-1}}\right)\right]$$

$$+ \left(\frac{\overline{\tilde{w}_e\tilde{x}}}{\tilde{u}_e h_2}\right)\left[\xi\left(w\frac{\partial w}{\partial\tilde{z}} - t\frac{\partial q}{\partial\tilde{z}}\right)\Bigg|_2 + (1-\xi)\left(w\frac{\partial w}{\partial\tilde{z}} - t\frac{\partial q}{\partial\tilde{z}}\right)\Bigg|_4\right] \qquad \text{(I.227)}$$

$$\overline{d}_{j*}\left[\frac{\overline{\Delta}_j - \overline{\Delta}_{j-1}}{h_{j-1}}\right] + \left[\frac{\overline{d}_j - \overline{d}_{j-1}}{h_{j-1}} + (\overline{P_2})\,\overline{f}_{j*} + (\overline{P_3})\,\overline{g}_{j*} - (\overline{T})\right]\overline{\Delta}_{j*}$$

$$+ \left(\frac{\overline{e}_j - \overline{e}_{j-1}}{h_{j-1}}\right)\left[\overline{u}_{j*}\overline{v}_{j*} + \left(\frac{\overline{\tilde{w}_e}}{\tilde{u}_e}\right)^2 \overline{w}_{j*}\overline{t}_{j*}\right]$$

$$+ \overline{e}_{j*}\left[\overline{u}_{j*}\left(\frac{\overline{v}_j - \overline{v}_{j-1}}{h_{j-1}}\right) + \overline{v}_{j*}\left(\frac{\overline{u}_j - \overline{u}_{j-1}}{h_{j-1}}\right)\right]$$

$$+ \overline{e}_{j*}\left(\frac{\overline{\tilde{w}_e}}{\tilde{u}_e}\right)^2\left[\overline{w}_{j*}\left(\frac{\overline{t}_j - \overline{t}_{j-1}}{h_{j-1}}\right) + \overline{t}_{j*}\left(\frac{\overline{w}_j - \overline{w}_{j-1}}{h_{j-1}}\right)\right]$$

$$= \left(\frac{\overline{\tilde{x}}}{h_1}\right)\left[\overline{u}_{j*}\left(\frac{\overline{\theta}_n - \overline{\theta}_{n-1}}{k_{n-1}}\right) - \overline{\Delta}_{j*}\left(\frac{\overline{f}_n - \overline{f}_{n-1}}{k_{n-1}}\right)\right]$$

$$+ \left(\frac{\overline{\tilde{w}_e\tilde{x}}}{\tilde{u}_e h_2}\right)\left[\xi\left(w\frac{\partial\theta}{\partial\tilde{z}} - \Delta\frac{\partial g}{\partial\tilde{z}}\right)\Bigg|_2 + (1-\xi)\left(w\frac{\partial\theta}{\partial\tilde{z}} - \Delta\frac{\partial g}{\partial\tilde{z}}\right)\Bigg|_4\right] \qquad \text{(I.228)}$$

In equations (I.226), (I.227), and (I.228), the following averaging notations are employed:

$$(\overline{\alpha}) = \frac{1}{2}\left(\alpha^{n,i} + \alpha^{n-1,i}\right) \qquad \text{(I.229)}$$

$$\overline{\alpha}_j = \frac{1}{2}\left(\alpha_j^{n,i} + \alpha_j^{n-1,i}\right) \qquad \text{(I.230)}$$

$$\bar{\alpha}_n = \frac{1}{2}\left(\alpha_j^{n,i} + \alpha_{j-1}^{n,i}\right) \tag{I.231}$$

$$\bar{\alpha}_{j*} = \frac{1}{4}\left(\alpha_j^{n,i} + \alpha_{j-1}^{n,i} + \alpha_j^{n-1,i} + \alpha_{j-1}^{n-1,i}\right) \tag{I.232}$$

where α denotes a general function. Equation (I.229) is used solely for variables which are dependent on $\tilde{x}$ and $\tilde{z}$, only. The final terms in equations (I.226), (I.227), and (I.228) are centered at points (2), (3), and (4). The mesh parameter ξ is given by

$$\xi = \frac{\tilde{z}_{i+1} - \tilde{z}_i}{\tilde{z}_{i+1} - \tilde{z}_{i-1}} \tag{I.233}$$

The above equations are again linearized using Newton's method. This again results in the finite difference relations given by equations (I.130) to (I.139), which employ the parameter definition equations given by equations (I.117) to (I.121). Incorporating Newton's method into equation (I.226) yields

$$S_1\,\delta f_j^{n,i} + S_2\,\delta f_{j-1}^{n,i} + S_3\,\delta u_j^{n,i} + S_4\,\delta u_{j-1}^{n,i} + S_5\,\delta v_j^{n,i}$$

$$+ S_6\,\delta v_{j-1}^{n,i} + S_7\,\delta g_j^{n,i} + S_8\,\delta g_{j-1}^{n,i} + S_9\,\delta w_j^{n,i}$$

$$+ S_{10}\,\delta w_{j-1}^{n,i} = Y_1 \tag{I.234}$$

where

$$S_1 = \frac{(\overline{P_2})X_4}{4} + \frac{\alpha_1 k_{n-1}^{-1} X_4}{2} \tag{I.235}$$

$$S_2 = \frac{(\overline{P_2})X_4}{4} + \frac{\alpha_1 k_{n-1}^{-1} X_4}{2} \tag{I.236}$$

$$S_3 = -\left(\frac{\overline{M}}{h_1}\right)\frac{X_6}{2} + \frac{(\overline{P_5})X_7}{4} - \alpha_1 k_{n-1}^{-1}\left(\frac{X_8}{4} + \frac{X_6}{2}\right) - \alpha_2\alpha_3(1 - \xi)X_{14} \tag{I.237}$$

$$S_4 = -\left(\frac{\overline{M}}{h_1}\right)\frac{X_6}{2} + \frac{(\overline{P_5})X_7}{4} - \alpha_1 k_{n-1}^{-1}\left(\frac{X_8}{4} + \frac{X_6}{2}\right) - \alpha_2\alpha_3(1 - \xi)X_{14} \tag{I.238}$$

$$S_5 = \frac{\overline{b}_{j*} h_{j-1}^{-1}}{2} + \frac{X_5}{4} + \frac{\alpha_1 k_{n-1}^{-1} X_9}{4} + \alpha_2\alpha_3(1 - \xi)\frac{X_{17}}{4} \tag{I.239}$$

$$S_6 = -\frac{\overline{b}_{j*} h_{j-1}^{-1}}{2} + \frac{X_5}{4} + \frac{\alpha_1 k_{n-1}^{-1} X_9}{4} + \alpha_2\alpha_3(1 - \xi)\frac{X_{17}}{4} \tag{I.240}$$

$$S_7 = \frac{(\overline{P_3})X_4}{4} + \alpha_2\alpha_3(1 - \xi)X_{15} \tag{I.241}$$

$$S_8 = \frac{(\overline{P_3})X_4}{4} + \alpha_2\alpha_3(1 - \xi)X_{15} \tag{I.242}$$

$$S_9 = -\frac{(\overline{P_4})X_7}{2} + \frac{(\overline{P_5})X_6}{4} - \alpha_2\alpha_3(1 - \xi)\frac{X_{16}}{4} \tag{I.243}$$

$$S_{10} = -\frac{(\overline{P_4})X_7}{2} + \frac{(\overline{P_5})X_6}{4} - \alpha_2\alpha_3(1 - \xi)\frac{X_{16}}{4} \tag{I.244}$$

$$Y_1 = -\overline{b}_{j*}h_{j-1}^{-1}X_1 - X_4X_5 + \left(\frac{\overline{M}}{h_1}\right)(X_6^2 - \overline{\lambda}_{j*}) + (\overline{P_4})(X_7^2 - \overline{\lambda}_{j*})$$

$$+ (\overline{P_5})(\overline{\lambda}_{j*} - X_6X_7) + \alpha_1k_{n-1}^{-1}(X_6X_8 - X_4X_9)$$

$$+ \alpha_2\xi(X_{10}X_{12} - X_{11}X_{13})$$

$$+ \alpha_2\alpha_3(1 - \xi)(X_{14}X_{16} - X_{15}X_{17}) \tag{I.245}$$

Introducing Newton's method into equation (I.227) yields

$$T_1\,\delta f_j^{n,i} + T_2\,\delta f_{j-1}^{n,i} + T_3\,\delta u_j^{n,i} + T_4\,\delta u_{j-1}^{n,i} + T_5\,\delta g_j^{n,i}$$

$$+ T_6\,\delta g_{j-1}^{n,i} + T_7\,\delta w_j^{n,i} + T_8\,\delta w_{j-1}^{n,i} + T_9\,\delta t_j^{n,i}$$

$$+ T_{10}\,\delta t_{j-1}^{n,i} = Y_2 \tag{I.246}$$

where

$$T_1 = \frac{(\overline{P_2})X_{19}}{4} + \alpha_1k_{n-1}^{-1}\frac{X_{19}}{2} \tag{I.247}$$

$$T_2 = \frac{(\overline{P_2})X_{19}}{4} + \alpha_1k_{n-1}^{-1}\frac{X_{19}}{2} \tag{I.248}$$

$$T_3 = -\frac{(\overline{P_6})X_6}{2} + \frac{(\overline{P_7})X_7}{4} - \alpha_1 \frac{k_{n-1}^{-1}X_{21}}{4} \tag{I.249}$$

$$T_4 = -\frac{(\overline{P_6})X_6}{2} + \frac{(\overline{P_7})X_7}{4} - \alpha_1 \frac{k_{n-1}^{-1}X_{21}}{4} \tag{I.250}$$

$$T_5 = \frac{(\overline{P_3})X_{19}}{4} + \alpha_2\alpha_3(1 - \xi)X_{24} \tag{I.251}$$

$$T_6 = \frac{(\overline{P_3})X_{19}}{4} + \alpha_2\alpha_3(1 - \xi)X_{24} \tag{I.252}$$

$$T_7 = -\alpha_4 \frac{X_7}{2} + X_6\left[\frac{(\overline{P_7})}{4} - \frac{\alpha_1 k_{n-1}^{-1}}{2}\right] - \alpha_2\alpha_3(1 - \xi)\left[\frac{X_{25}}{4} + X_{14}\right] \tag{I.253}$$

$$T_8 = -\alpha_4 \frac{X_7}{2} + X_6\left[\frac{(\overline{P_7})}{4} - \frac{\alpha_1 k_{n-1}^{-1}}{2}\right] - \alpha_2\alpha_3(1 - \xi)\left[\frac{X_{25}}{4} + X_{14}\right] \tag{I.254}$$

$$T_9 = \frac{\overline{c}_{j*}h_{j-1}^{-1}}{2} + \frac{X_{20}}{4} + \alpha_1 k_{n-1}^{-1}\frac{X_9}{4} + \alpha_2\alpha_3(1 - \xi)\frac{X_{17}}{4} \tag{I.255}$$

$$T_{10} = -\frac{\overline{c}_{j*}h_{j-1}^{-1}}{2} + \frac{X_{20}}{4} + \alpha_1 k_{n-1}^{-1}\frac{X_9}{4} + \alpha_2\alpha_3(1 - \xi)\frac{X_{17}}{4} \tag{I.256}$$

$$Y_2 = -\bar{c}_{j*}h_{j-1}^{-1} X_{18} - X_{19}X_{20} + (\overline{P_6})(X_6^2 - \bar{\lambda}_{j*})$$

$$+ \alpha_4(X_7^2 - \bar{\lambda}_{j*}) + (\overline{P_7})(\bar{\lambda}_{j*} - X_6X_7)$$

$$+ \alpha_1 k_{n-1}^{-1} (X_6X_{21} - X_9X_{19}) + \alpha_2\xi(X_{10}X_{23} - X_{22}X_{13})$$

$$+ \alpha_2\alpha_3(1 - \xi)(X_{14}X_{25} - X_{17}X_{24}) \qquad (I.257)$$

Incorporating Newton's method into equation (I.228) yields

$$U_1\delta f_j^{n,i} + U_2\delta f_{j-1}^{n,i} + U_3\delta u_j^{n,i} + U_4\delta u_{j-1}^{n,i} + U_5\delta g_j^{n,i}$$

$$+ U_6\delta g_{j-1}^{n,i} + U_7\delta w_j^{n,i} + U_8\delta w_{j-1}^{n,i} + U_9\delta t_j^{n,i} + U_{10}\delta t_{j-1}^{n,i}$$

$$+ U_{11}\delta v_j^{n,i} + U_{12}\delta v_{j-1}^{n,i} + U_{13}\delta\Delta_j^{n,i} + U_{14}\delta\Delta_{j-1}^{n,i}$$

$$+ U_{15}\delta\theta_j^{n,i} + U_{16}\delta\theta_{j-1}^{n,i} = Y_3 \qquad (I.258)$$

where

$$U_1 = \frac{(\overline{P_2})X_{27}}{4} + \alpha_1 k_{n-1}^{-1} \frac{X_{27}}{2} \qquad (I.259)$$

$$U_2 = \frac{(\overline{P_2})X_{27}}{4} + \alpha_1 k_{n-1}^{-1} \frac{X_{27}}{2} \qquad (I.260)$$

$$U_3 = \alpha_5 \frac{X_4}{4} + \bar{e}_{j*} h_{j-1}^{-1} \left[\frac{X_1}{4} + \frac{X_4}{2}\right] - \alpha_1 k_{n-1}^{-1} \frac{X_{31}}{4} \tag{I.261}$$

$$U_4 = \alpha_5 \frac{X_4}{4} + \bar{e}_{j*} h_{j-1}^{-1} \left[\frac{X_1}{4} - \frac{X_4}{2}\right] - \alpha_1 k_{n-1}^{-1} \frac{X_{31}}{4} \tag{I.262}$$

$$U_5 = \frac{(\overline{P_3})X_{27}}{4} + \alpha_2\alpha_3(1 - \xi)X_{34} \tag{I.263}$$

$$U_6 = \frac{(\overline{P_3})X_{27}}{4} + \alpha_2\alpha_3(1 - \xi)X_{34} \tag{I.264}$$

$$U_7 = \alpha_5 \left(\frac{\overline{\tilde{w}_e}}{\tilde{u}_e}\right)^2 \frac{X_{19}}{4} + \alpha_6 h_{j-1}^{-1} \left[\frac{X_{18}}{4} + \frac{X_{19}}{2}\right] - \alpha_2\alpha_3(1 - \xi) \frac{X_{35}}{4} \tag{I.265}$$

$$U_8 = \alpha_5 \left(\frac{\overline{\tilde{w}_e}}{\tilde{u}_e}\right)^2 \frac{X_{19}}{4} + \alpha_6 h_{j-1}^{-1} \left[\frac{X_{18}}{4} - \frac{X_{19}}{2}\right] - \alpha_2\alpha_3(1 - \xi) \frac{X_{35}}{4} \tag{I.266}$$

$$U_9 = X_7 \left[\frac{\alpha_5}{4} \left(\frac{\overline{\tilde{w}_e}}{\tilde{u}_e}\right)^2 + \frac{\alpha_6 h_{j-1}^{-1}}{2}\right] + \alpha_6 h_{j-1}^{-1} \frac{X_{30}}{4} \tag{I.267}$$

$$U_{10} = X_7 \left[\frac{\alpha_5}{4} \left(\frac{\overline{\tilde{w}_e}}{\tilde{u}_e}\right)^2 - \frac{\alpha_6 h_{j-1}^{-1}}{2}\right] + \alpha_6 h_{j-1}^{-1} \frac{X_{30}}{4} \tag{I.268}$$

$$U_{11} = \frac{\alpha_5 X_6}{4} + \bar{e}_{j*} h_{j-1}^{-1} \left[\frac{X_6}{2} + \frac{X_{29}}{4}\right] \tag{I.269}$$

$$U_{12} = \frac{\alpha_5 X_6}{4} + \bar{e}_{j*} h_{j-1}^{-1} \left[-\frac{X_6}{2} + \frac{X_{29}}{4}\right] \tag{I.270}$$

$$U_{13} = \frac{\bar{d}_{j*} h_{j-1}^{-1}}{2} + \frac{X_{28}}{4} + \alpha_1 k_{n-1}^{-1} \frac{X_9}{4} + \alpha_2\alpha_3(1 - \xi) \frac{X_{17}}{4} \tag{I.271}$$

$$U_{14} = \frac{-\bar{d}_{j*}h_{j-1}^{-1}}{2} + \frac{X_{28}}{4} + \alpha_1 k_{n-1}^{-1}\frac{X_9}{4} + \alpha_2\alpha_3(1-\xi)\frac{X_{17}}{4} \qquad (I.272)$$

$$U_{15} = -\alpha_1 k_{n-1}^{-1}\frac{X_6}{2} - \alpha_2\alpha_3(1-\xi)X_{14} \qquad (I.273)$$

$$U_{16} = -\alpha_1 k_{n-1}^{-1}\frac{X_6}{2} - \alpha_2\alpha_3(1-\xi)X_{14} \qquad (I.274)$$

$$\begin{aligned} Y_3 = {} & -\bar{d}_{j*}h_{j-1}^{-1}X_{26} - X_{27}X_{28} - \alpha_5\left[X_4X_6 + \left(\frac{\tilde{w}_e}{\tilde{u}_e}\right)^2 X_7X_{19}\right] \\ & - \bar{e}_{j*}h_{j-1}^{-1}(X_1X_6 + X_4X_{29}) - \alpha_6 h_{j-1}^{-1}(X_7X_{18} + X_{19}X_{30}) \\ & + \alpha_1 k_{n-1}^{-1}(X_6X_{31} - X_9X_{27}) + \alpha_2\xi(X_{10}X_{33} - X_{32}X_{13}) \\ & + \alpha_2\alpha_3(1-\xi)(X_{14}X_{35} - X_{17}X_{34}) \end{aligned} \qquad (I.275)$$

In equations (I.234) to (I.275), the following parameter definitions are employed:

$$X_1 = \frac{1}{2}\left(v_j^{n,i} + v_j^{n-1,i} - v_{j-1}^{n,i} - v_{j-1}^{n-1,i}\right) \qquad (I.276)$$

$$X_2 = \frac{1}{4}\left(f_j^{n,i} + f_{j-1}^{n,i} + f_j^{n-1,i} + f_{j-1}^{n-1,i}\right) \qquad (I.277)$$

$$X_3 = \frac{1}{4}(g_j^{n,i} + g_{j-1}^{n,i} + g_j^{n-1,i} + g_{j-1}^{n-1,i}) \tag{I.278}$$

$$X_4 = \frac{1}{4}(v_j^{n,i} + v_{j-1}^{n,i} + v_j^{n-1,i} + v_{j-1}^{n-1,i}) \tag{I.279}$$

$$X_5 = h_{j-1}^{-1}(\bar{b}_j - \bar{b}_{j-1}) + (\overline{P_2})X_2 + (\overline{P_3})X_3 - (\bar{T}) \tag{I.280}$$

$$X_6 = \frac{1}{4}(u_j^{n,i} + u_{j-1}^{n,i} + u_j^{n-1,i} + u_{j-1}^{n-1,i}) \tag{I.281}$$

$$X_7 = \frac{1}{4}(w_j^{n,i} + w_{j-1}^{n,i} + w_j^{n-1,i} + w_{j-1}^{n-1,i}) \tag{I.282}$$

$$X_8 = \frac{1}{2}(u_j^{n,i} + u_{j-1}^{n,i}) - \bar{u}_{n-1} \tag{I.283}$$

$$X_9 = \frac{1}{2}(f_j^{n,i} + f_{j-1}^{n,i}) - \bar{f}_{n-1} \tag{I.284}$$

$$X_{10} = \frac{1}{4}(w_j^{n-1,i+1} + w_{j-1}^{n-1,i+1} + w_j^{n-1,i} + w_{j-1}^{n-1,i}) \tag{I.285}$$

$$X_{11} = \frac{1}{4}(v_j^{n-1,i+1} + v_{j-1}^{n-1,i+1} + v_j^{n-1,i} + v_{j-1}^{n-1,i}) \tag{I.286}$$

$$X_{12} = \alpha_7(u_j^{n-1,i+1} + u_{j-1}^{n-1,i+1} - u_j^{n-1,i} - u_{j-1}^{n-1,i}) \tag{I.287}$$

$$X_{13} = \alpha_7(g_j^{n-1,i+1} + g_{j-1}^{n-1,i+1} - g_j^{n-1,i} - g_{j-1}^{n-1,i}) \tag{I.288}$$

$$X_{14} = \frac{1}{4}(w_j^{n,i} + w_{j-1}^{n,i} + w_j^{n,i-1} + w_{j-1}^{n,i-1}) \tag{I.289}$$

$$X_{15} = \frac{1}{4}(v_j^{n,i} + v_{j-1}^{n,i} + v_j^{n,i-1} + v_{j-1}^{n,i-1}) \tag{I.290}$$

$$X_{16} = u_j^{n,i} + u_{j-1}^{n,i} - u_j^{n,i-1} - u_{j-1}^{n,i-1} \tag{I.291}$$

$$X_{17} = g_j^{n,i} + g_{j-1}^{n,i} - g_j^{n,i-1} - g_{j-1}^{n,i-1} \tag{I.292}$$

$$X_{18} = \frac{1}{2}(t_j^{n,i} + t_j^{n-1,i} - t_{j-1}^{n,i} - t_{j-1}^{n-1,i}) \tag{I.293}$$

$$X_{19} = \frac{1}{4}(t_j^{n,i} + t_{j-1}^{n,i} + t_j^{n-1,i} + t_{j-1}^{n-1,i}) \tag{I.294}$$

$$X_{20} = h_{j-1}^{-1}(\overline{c}_j - \overline{c}_{j-1}) + (\overline{P_2})X_2 + (\overline{P_3})X_3 - (\overline{T}) \tag{I.295}$$

$$X_{21} = \frac{1}{2}(w_j^{n,i} + w_{j-1}^{n,i}) - \overline{w}_{n-1} \tag{I.296}$$

$$X_{22} = \frac{1}{4}(t_j^{n-1,i+1} + t_{j-1}^{n-1,i+1} + t_j^{n-1,i} + t_{j-1}^{n-1,i}) \tag{I.297}$$

$$X_{23} = \alpha_7(w_j^{n-1,i+1} + w_{j-1}^{n-1,i+1} - w_j^{n-1,i} - w_{j-1}^{n-1,i}) \tag{I.298}$$

$$X_{24} = \frac{1}{4}(t_j^{n,i} + t_{j-1}^{n,i} + t_j^{n,i-1} + t_{j-1}^{n,i-1}) \tag{I.299}$$

$$X_{25} = w_j^{n,i} + w_{j-1}^{n,i} - w_j^{n,i-1} - w_{j-1}^{n,i-1} \tag{I.300}$$

$$X_{26} = \frac{1}{2}(\Delta_j^{n,i} + \Delta_j^{n-1,i} - \Delta_{j-1}^{n,i} - \Delta_{j-1}^{n-1,i}) \tag{I.301}$$

$$X_{27} = \frac{1}{4}(\Delta_j^{n,i} + \Delta_{j-1}^{n,i} + \Delta_j^{n-1,i} + \Delta_{j-1}^{n-1,i}) \tag{I.302}$$

$$X_{28} = h_{j-1}^{-1}(\overline{d}_j - \overline{d}_{j-1}) + (\overline{P_2})X_2 + (\overline{P_3})X_3 - (\overline{T}) \tag{I.303}$$

$$X_{29} = \frac{1}{2}(u_j^{n,i} + u_j^{n-1,i} - u_{j-1}^{n,i} - u_{j-1}^{n-1,i}) \tag{I.304}$$

$$X_{30} = \frac{1}{2}(w_j^{n,i} + w_j^{n-1,i} - w_{j-1}^{n,i} - w_{j-1}^{n-1,i}) \tag{I.305}$$

$$X_{31} = \frac{1}{2}(\theta_j^{n,i} + \theta_{j-1}^{n,i}) - \overline{\theta}_{n-1} \tag{I.306}$$

$$X_{32} = \frac{1}{4}(\Delta_j^{n-1,i+1} + \Delta_{j-1}^{n-1,i+1} + \Delta_j^{n-1,i} + \Delta_{j-1}^{n-1,i}) \tag{I.307}$$

$$X_{33} = \alpha_7(\theta_j^{n-1,i+1} + \theta_{j-1}^{n-1,i+1} - \theta_j^{n-1,i} - \theta_{j-1}^{n-1,i}) \tag{I.308}$$

$$X_{34} = \frac{1}{4}(\Delta_j^{n,i} + \Delta_{j-1}^{n,i} + \Delta_j^{n,i-1} + \Delta_{j-1}^{n,i-1}) \tag{I.309}$$

$$X_{35} = \theta_j^{n,i} + \theta_{j-1}^{n,i} - \theta_j^{n,i-1} - \theta_{j-1}^{n,i-1} \tag{I.310}$$

$$\alpha_1 = \left(\overline{\frac{\tilde{x}}{h_1}}\right) \tag{I.311}$$

$$\alpha_2 = \left(\overline{\frac{\tilde{w}_e\tilde{x}}{\tilde{u}_e h_2}}\right) \tag{I.312}$$

$$\alpha_3 = (\tilde{z}_i - \tilde{z}_{i-1})^{-1}/2 \tag{I.313}$$

$$\alpha_4 = \left(\overline{\frac{\tilde{w}_e P}{\tilde{u}_e h_2}}\right) \tag{I.314}$$

$$\alpha_5 = h_{j-1}^{-1}(\bar{e}_j - \bar{e}_{j-1}) \tag{I.315}$$

$$\alpha_6 = \bar{e}_{j*}\left(\frac{\overline{\tilde{w}_e}}{\overline{\tilde{u}_e}}\right)^2 \tag{I.316}$$

$$\alpha_7 = (\tilde{z}_{i+1} - \tilde{z}_i)^{-1}/2 \tag{I.317}$$

In equations (I.234) to (I.317), the following averaging notations are employed:

$$(\bar{\alpha}) = \frac{1}{2}(\alpha^{n,i} + \alpha^{n-1,i}) \tag{I.318}$$

$$\bar{\alpha}_{j*} = \frac{1}{4}(\alpha_j^{n,i} + \alpha_{j-1}^{n,i} + \alpha_j^{n-1,i} + \alpha_{j-1}^{n-1,i}) \tag{I.319}$$

$$\bar{\alpha}_j = \frac{1}{2}(\alpha_j^{n,i} + \alpha_j^{n-1,i}) \tag{I.320}$$

$$\bar{\alpha}_n = \frac{1}{2}(\alpha_j^{n,i} + \alpha_{j-1}^{n,i}) \tag{I.321}$$

where α denotes a general function. Equation (I.318) is used solely for functions which are dependent upon $\tilde{x}$ and $\tilde{z}$, only.

The solution for points at which the cross-flow velocity is negative is obtained by substituting the above equations into the algorithm presented in Section 3 for those cells at which the average cross-flow velocity is negative.

5. SOLUTION OF THE DIFFERENCE EQUATIONS

The difference equations for the Newton iterates are solved using an efficient direct matrix factorization procedure. The difference equations can be ordered into a linear system of simultaneous equations which has a coefficient matrix that is block tridiagonal in form. Except for minor alterations, the matrix solution algorithms for both the three-dimensional flow and the attachment line flow are identical. The solution algorithm for three-dimensional flow is outlined below.

The boundary conditions for three-dimensional flow, given by equations (I.30) and (I.31), are repeated below:

$$\left.\begin{aligned} \eta = 0: \quad & f = 0, \quad g = 0, \quad u = 0, \quad w = 0 \\ & \theta = \theta_w \quad \text{or} \quad \Delta = \Delta_w \end{aligned}\right\} \qquad \text{(I.322)}$$

$$\left.\begin{aligned} \eta = \eta_N: \quad & u = 1, \quad w = 1, \quad \theta = 1 \end{aligned}\right\} \qquad \text{(I.323)}$$

Using Newton's method, any function f at the (k+1)th iteration is given by

$$[f]^{(k+1)} = [f]^{(k)} + [\delta f]^{(k)} \qquad \text{(I.324)}$$

where $[f]^{(k)}$ is the functional value at the (k)th iteration, and $[\delta f]^{(k)}$ is the Newton iterate at the (k)th iteration. Noting the wall conditions by the subscript 1 and the edge conditions by the subscript N, the boundary conditions given by equations (I.322) and (I.323) can be written as

$$\left.\begin{aligned} f_1^{(k)} &= g_1^{(k)} = u_1^{(k)} = w_1^{(k)} = 0 \\ \theta_1^{(k)} &= \theta_w \qquad \Delta_1^{(k)} = \Delta_w \end{aligned}\right\} \tag{I.325}$$

$$\left.u_N^{(k)} = w_N^{(k)} = \theta_N^{(k)} = 1\right\} \tag{I.326}$$

This mandates that the Newton iterates have the following values for any iteration:

$$\left.\begin{aligned} &\delta f_1^{(k)} = 0, \quad \delta g_1^{(k)} = 0, \quad \delta u_1^{(k)} = 0, \quad \delta w_1^{(k)} = 0 \\ &\delta\theta_1^{(k)} = 0 \quad \text{or} \quad \delta\Delta_1^{(k)} = 0 \end{aligned}\right\} \tag{I.327}$$

$$\left.\delta u_N^{(k)} = 0, \quad \delta w_N^{(k)} = 0, \quad \delta\theta_N^{(k)} = 0\right\} \tag{I.328}$$

The pertinent finite difference equations for the Newton iterates for three-dimensional flow are given by equations (I.130) to (I.134) and by equations (I.140), (I.152), and (I.164). Those equations, plus the boundary conditions given by equations (I.327) and (I.328), can be written for N points across the boundary layer in the following matrix form:

$$\Gamma\overline{\Delta} = \overline{Q} \tag{I.329}$$

In equation (I.329), the solution vector $\overline{\Delta}$ is defined by the column vector

$$\overline{\Delta} = \begin{bmatrix} \overline{\delta}_1 \\ \overline{\delta}_2 \\ \overline{\delta}_3 \\ \vdots \\ \overline{\delta}_{N-1} \\ \overline{\delta}_N \end{bmatrix} \tag{I.330}$$

where $\overline{\delta}_j$ $(1 \leq j \leq N)$ denotes the jth vector subset which is defined by the eight element column vector

$$\overline{\delta}_j = \begin{bmatrix} \delta f_j \\ \delta u_j \\ \delta g_j \\ \delta w_j \\ \delta \theta_j \\ \delta v_j \\ \delta t_j \\ \delta \Delta_j \end{bmatrix} \tag{I.331}$$

In the above and subsequent equations, the iteration superscript will not be noted. The right-hand side vector $\overline{Q}$ in equation (I.329) is given by

$$\bar{Q} = \begin{bmatrix} \bar{q}_1 \\ \bar{q}_2 \\ \bar{q}_3 \\ \vdots \\ \bar{q}_{N-1} \\ \bar{q}_N \end{bmatrix} \qquad \text{(I.332)}$$

where $\bar{q}_j$ $(1 \leq j \leq N)$ denotes the jth right-hand side vector subset which is a column vector of dimension eight. The coefficient matrix Γ in equation (I.329) is defined by the block-tridiagonal matrix

$$\Gamma = \begin{bmatrix} A_1 & C_1 & 0 & 0 & 0 & \cdots & & & & & \\ B_2 & A_2 & C_2 & 0 & 0 & \cdots & & & & & \\ 0 & B_3 & A_3 & C_3 & 0 & \cdots & & & & & \\ \vdots & \vdots & \vdots & \vdots & & & & & & & \vdots \\ & & & & & & & B_{N-1} & A_{N-1} & C_{N-1} & \\ \cdots & \cdots & \cdots & \cdots & \cdots & \cdots & \cdots & 0 & B_N & A_N & \end{bmatrix} \qquad \text{(I.333)}$$

where A_j, B_j, and C_j $(1 \leq j \leq N)$ are square submatrices of dimension eight by eight. The forms of A_j, B_j, C_j, and $\overline{q}_j$ $(1 \leq j \leq N)$ are given below.

For $j = 1$:

$$A_1 = \begin{bmatrix} 1 & 0 & 0 & 0 & 0 & 0 & 0 & 0 \\ 0 & 1 & 0 & 0 & 0 & 0 & 0 & 0 \\ 0 & 0 & 1 & 0 & 0 & 0 & 0 & 0 \\ 0 & 0 & 0 & 1 & 0 & 0 & 0 & 0 \\ 0 & 0 & 0 & 0 & 1 & 0 & 0 & 0 \\ S_2 & S_4 & S_8 & S_{10} & 0 & S_6 & 0 & 0 \\ T_2 & T_4 & T_6 & T_8 & 0 & 0 & T_{10} & 0 \\ U_2 & U_4 & U_6 & U_8 & U_{16} & U_{12} & U_{10} & U_{14} \end{bmatrix} \tag{I.334}$$

For $(2 \leq j \leq N-1)$:

$$A_j = \begin{bmatrix} 1 & -h/2 & 0 & 0 & 0 & 0 & 0 & 0 \\ 0 & 1 & 0 & 0 & 0 & -h/2 & 0 & 0 \\ 0 & 0 & 1 & -h/2 & 0 & 0 & 0 & 0 \\ 0 & 0 & 0 & 1 & 0 & 0 & -h/2 & 0 \\ 0 & 0 & 0 & 0 & 1 & 0 & 0 & -h/2 \\ S_2 & S_4 & S_8 & S_{10} & 0 & S_6 & 0 & 0 \\ T_2 & T_4 & T_6 & T_8 & 0 & 0 & T_{10} & 0 \\ U_2 & U_4 & U_6 & U_8 & U_{16} & U_{12} & U_{10} & U_{14} \end{bmatrix} \tag{I.335}$$

For j = N:

$$A_N = \begin{bmatrix} 1 & -h/2 & 0 & 0 & 0 & 0 & 0 & 0 \\ 0 & 1 & 0 & 0 & 0 & -h/2 & 0 & 0 \\ 0 & 0 & 1 & -h/2 & 0 & 0 & 0 & 0 \\ 0 & 0 & 0 & 1 & 0 & 0 & -h/2 & 0 \\ 0 & 0 & 0 & 0 & 1 & 0 & 0 & -h/2 \\ 0 & 1 & 0 & 0 & 0 & 0 & 0 & 0 \\ 0 & 0 & 0 & 1 & 0 & 0 & 0 & 0 \\ 0 & 0 & 0 & 0 & 1 & 1 & 0 & 0 \end{bmatrix} \qquad \text{(I.336)}$$

For all j:

$$B_j = \begin{bmatrix} -1 & -h/2 & 0 & 0 & 0 & 0 & 0 & 0 \\ 0 & -1 & 0 & 0 & 0 & -h/2 & 0 & 0 \\ 0 & 0 & -1 & -h/2 & 0 & 0 & 0 & 0 \\ 0 & 0 & 0 & -1 & 0 & 0 & -h/2 & 0 \\ 0 & 0 & 0 & 0 & -1 & 0 & 0 & -h/2 \\ 0 & 0 & 0 & 0 & 0 & 0 & 0 & 0 \\ 0 & 0 & 0 & 0 & 0 & 0 & 0 & 0 \\ 0 & 0 & 0 & 0 & 0 & 0 & 0 & 0 \end{bmatrix} \qquad \text{(I.337)}$$

For all j:

$$C_j = \begin{bmatrix} 0 & 0 & 0 & 0 & 0 & 0 & 0 & 0 \\ 0 & 0 & 0 & 0 & 0 & 0 & 0 & 0 \\ 0 & 0 & 0 & 0 & 0 & 0 & 0 & 0 \\ 0 & 0 & 0 & 0 & 0 & 0 & 0 & 0 \\ 0 & 0 & 0 & 0 & 0 & 0 & 0 & 0 \\ S_1 & S_3 & S_7 & S_9 & 0 & S_5 & 0 & 0 \\ T_1 & T_3 & T_5 & T_7 & 0 & 0 & T_9 & 0 \\ U_1 & U_3 & U_5 & U_7 & U_{15} & U_{11} & U_9 & U_{13} \end{bmatrix} \qquad \text{(I.338)}$$

For j = 1:

$$\overline{q}_1 = \begin{bmatrix} 0 \\ 0 \\ 0 \\ 0 \\ 0 \\ Y_1 \\ Y_2 \\ Y_3 \end{bmatrix} \qquad \text{(I.339)}$$

For $(2 \leq j \leq N-1)$:

$$\overline{q}_j = \begin{bmatrix} R_1 \\ R_2 \\ R_3 \\ R_4 \\ R_5 \\ Y_1 \\ Y_2 \\ Y_3 \end{bmatrix} \qquad \text{(I.340)}$$

For $j = N$:

$$\overline{q}_N = \begin{bmatrix} R_1 \\ R_2 \\ R_3 \\ R_4 \\ R_5 \\ 0 \\ 0 \\ 0 \end{bmatrix} \qquad \text{(I.341)}$$

The parameters Y_k, R_k, S_k, T_k, U_k, and h in equations (I.334) to (I.341) are applied between successive normal (n) stations (i.e., j-1, j, j+1). The above equations are for the case when the wall temperature is specified. If, instead, the normal temperature derivative at the wall is specified, then the submatrix A_1 takes the following form:

$$A_1 = \begin{bmatrix} 1 & 0 & 0 & 0 & 0 & 0 & 0 & 0 \\ 0 & 1 & 0 & 0 & 0 & 0 & 0 & 0 \\ 0 & 0 & 1 & 0 & 0 & 0 & 0 & 0 \\ 0 & 0 & 0 & 1 & 0 & 0 & 0 & 0 \\ 0 & 0 & 0 & 0 & 0 & 0 & 0 & 1 \\ S_2 & S_4 & S_8 & S_{10} & 0 & S_6 & 0 & 0 \\ T_2 & T_4 & T_6 & T_8 & 0 & 0 & T_{10} & 0 \\ U_2 & U_4 & U_6 & U_8 & U_{16} & U_{12} & U_{10} & U_{14} \end{bmatrix} \qquad \text{(I.342)}$$

A similar set of matrix definitions exists for the attachment line flow. Only minor modifications must be made to the previously defined submatrices A_j and C_j $(1 \leq j \leq N)$.

The system of linear equations given by the matrix equation (I.329) is solved using a direct matrix factorization procedure (22). This procedure assumes that the coefficient matrix Γ can be factored into two matrices; one of which is upper triangular, the other of which is lower triangular. Denoting the upper and lower triangular matrices by U and L, respectively, then

$$\Gamma = LU \qquad \text{(I.343)}$$

where

$$L = \begin{bmatrix} \lambda_1 & 0 & 0 & \cdot & \cdot & \cdot & \cdot & \cdot & \cdot \\ B_2 & \lambda_2 & 0 & \cdot & \cdot & \cdot & \cdot & \cdot & \cdot \\ 0 & B_3 & \lambda_3 & & & & & & \cdot \\ \cdot & & & \cdot & & & & & \cdot \\ \cdot & & & & \cdot & & & & \cdot \\ \cdot & & & & & \cdot & & & \cdot \\ \cdot & & & & & & \cdot & & \cdot \\ \cdot & & & & & & & \cdot & \cdot \\ \cdot & \cdot & \cdot & \cdot & \cdot & \cdot & \cdot & B_N & \lambda_N \end{bmatrix} \qquad \text{(I.344)}$$

and

$$U = \begin{bmatrix} I_1 & \gamma_1 & 0 & 0 & \cdot & \cdot & \cdot & \cdot & \cdot \\ 0 & I_2 & \gamma_2 & 0 & & & & & \\ 0 & 0 & I_3 & \gamma_3 & & & & & \\ \cdot & & & \cdot & & & & & \\ \cdot & & & & \cdot & & & & \\ \cdot & & & & & \cdot & & & \\ \cdot & & & & & & \cdot & & \\ \cdot & \cdot & \cdot & \cdot & \cdot & \cdot & \cdot & \cdot & I_N \end{bmatrix} \qquad \text{(I.345)}$$

In equations (I.344) and (I.345), λ_j and γ_j $(1 \leq j \leq N)$ denote square submatrices of order eight which are to be determined in the analysis, and I_j denotes the identity matrix of order eight. Performing the matrix multiplication of L and U and equating like elements to those in Γ yields the following recursion relations for determining λ_j and γ_j:

$$\lambda_1 = A_1 \qquad \text{(I.346)}$$

$$\lambda_j = A_j - B_j \gamma_{j-1} \qquad \text{(I.347)}$$

$$\gamma_j = \lambda_j^{-1} C_j \tag{I.348}$$

With the elements of U and L determined, an intermediate solution vector $\overline{\beta}$ is obtained from

$$\overline{\beta} = L^{-1} \overline{Q} \tag{I.349}$$

where

$$\overline{\beta} = \begin{bmatrix} \overline{\sigma}_1 \\ \overline{\sigma}_2 \\ \overline{\sigma}_3 \\ \vdots \\ \overline{\sigma}_{N-1} \\ \overline{\sigma}_N \end{bmatrix} \tag{I.350}$$

The elements of $\overline{\beta}$ are obtained from the recursion relations

$$\overline{\sigma}_1 = A_1^{-1} \overline{q}_1 \tag{I.351}$$

$$\overline{\sigma}_j = \lambda_j^{-1} (\overline{q}_j - B_j \ \overline{\sigma}_{j-1}) \tag{I.352}$$

With the elements of $\overline{\beta}$ determined, the solution vector $\overline{\Delta}$ is found from the backward recursion relations

$$\overline{\delta}_N = \overline{\sigma}_N \tag{I.353}$$

$$\overline{\delta}_j = \overline{\sigma}_j - \gamma_j \overline{\delta}_{j+1} \tag{I.354}$$

It should be noted that it is inefficient to compute matrix inverses for use in the respective recursive formulae. Better efficiency can be realized if the linear systems are solved using direct methods.

APPENDIX J

SHOCK WAVE-BOUNDARY LAYER INTERACTION ANALYSIS

1. INTRODUCTION

The second-order inplicit finite difference algorithm, presented in Appendix I, is used to compute all of the boundary layer flow except for that in the shock wave-boundary layer interaction regions. The interaction region flow exhibits an elliptical character in that downstream disturbances can propagate through the subsonic portion of the boundary layer to affect the upstream flow. This phenomenon is evidenced by a thickening of the boundary layer ahead of the shock wave reflection. Because of this, it is not possible to adequately model the interaction region flow by solving a parabolic system of governing partial differential equations which by their very character do not allow for downstream influence. An accurate simulation of the interaction region flow requires using a three-dimensional compressible Navier-Stokes analysis with appropriate modeling of the outflow boundary conditions. Although such an analysis is possible, the large attendant increase in computer execution time makes this method undesirable.

Realizing this, an efficient three-dimensional integral analysis was chosen for use in the present investigation. The analysis presented herein solves integral forms of the continuity, streamwise momentum, and cross-flow momentum equations. The energy equation is approximated by assuming that flow in the interaction region is isoenergetic.

The integral analysis is based on the following assumptions (most of which are supported by experimental evidence):

1. The flow is quasi-two-dimensional in a plane normal to the shock wave

and the wall, and the flow properties are approximately constant parallel to the shock wave.

2. The static pressure is constant in the wall normal direction downstream of the interaction region.

3. The interaction region is sufficiently short so that mass entrainment and viscous shear stress effects may be neglected.

4. Mass bleed occurs normal to the wall.

5. The flow in the interaction region is isoenergetic.

6. The boundary layer velocity profiles may be represented by power laws.

7. The boundary layer thickness is small compared to the local body radius, and thereby a local planar analysis is applicable.

The shock wave-boundary layer interaction region analysis is presented in this appendix. This analysis presented herein represents an extension of the methods reported in References (23) to (27).

2. INTEGRAL ANALYSIS FOR THE SHOCK WAVE-BOUNDARY LAYER INTERACTION REGION

The three-dimensional integral conservation equations are applied to a series of control volumes where each control volume comprises a circumferential segment of the three-dimensional shock wave-boundary layer interaction region, as illustrated in Figure J.1. A given control volume is bounded by the current boundary layer initial-value and solution surfaces in the streamwise direction, and by the wall and the boundary layer edge surfaces in the normal direction.

Following the suggestion of Paynter (25), Peake(26) and Green (27), the conservation equations are applied in a plane which is orthogonal to both the wall and to the space curve defined by the intersection of the shock wave with the wall. This plane is shown in Figure J.2. passing through the point (P), and can be defined by the orthonormal triad of vectors $\hat{t}$, $\hat{n}_b$, and $\hat{o}$. The unit vector $\hat{t}$ is tangent to the space curve at

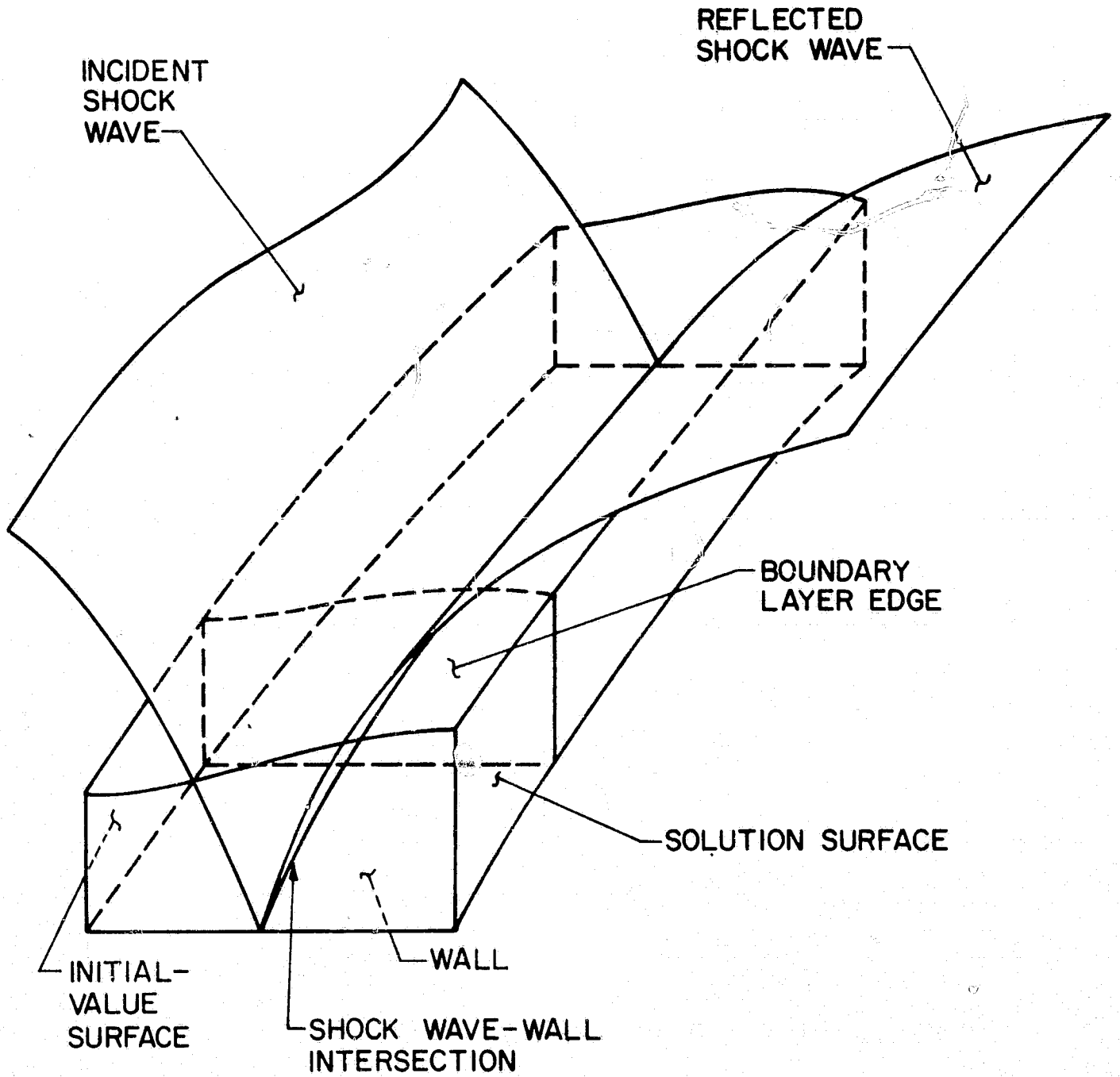

FIGURE J.I. SHOCK WAVE-BOUNDARY LAYER INTERACTION REGION

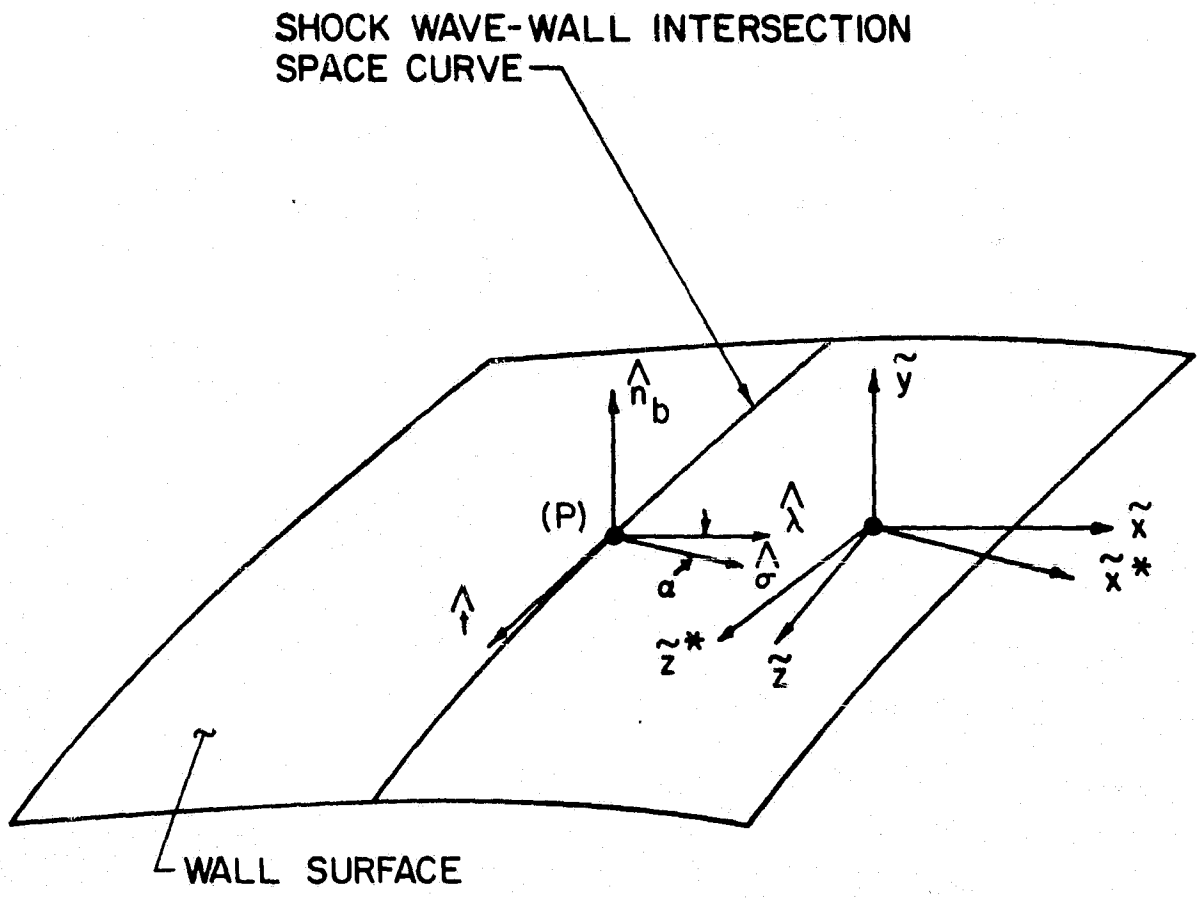

FIGURE J.2. UNIT VECTOR SPECIFICATION FOR SHOCK WAVE-BOUNDARY LAYER INTERACTION ANALYSIS

point (P), the unit vector $\hat{n}_b$ is orthogonal to the solid boundary at point (P), and the unit vector $\hat{\sigma}$ is orthogonal to both $\hat{t}$ and $\hat{n}_b$ at point (P) and is given by

$$\hat{\sigma} = \hat{n}_b \times \hat{t} \tag{J.1}$$

The tangential unit vector $\hat{t}$ can be determined from

$$\hat{t} = (\frac{dx}{ds})\hat{i} + (\frac{dy}{ds})\hat{j} + (\frac{dz}{ds})\hat{k} \tag{J.2}$$

where ds is the differential arc length along the space curve and can be expressed as

$$(ds)^2 = (dx)^2 + (dy)^2 + (dz)^2 \tag{J.3}$$

where x, y, and z form the base coordinate system of Figure 1, and $\hat{i}$, $\hat{j}$, and $\hat{k}$ are the unit vectors in the x-, y-, and z-directions, respectively.

After determining the unit vector $\hat{\sigma}$, the angle α subtended by the unit vectors $\hat{\sigma}$ and $\hat{\lambda}$ may by determined, where $\hat{\lambda}$ is tangent to the body and lies in the meridional plane of point (P). A coordinate rotation may then be employed to obtain the upstream boundary layer velocity components in the plane containing $\hat{n}_b$ and $\hat{\sigma}$. The coordinate rotation formulae are given by

$$\tilde{u}^* = \tilde{u}\cos\alpha + \tilde{w}\sin\alpha \tag{J.4}$$

$$\tilde{w}^* = \tilde{w}\cos\alpha - \tilde{u}\sin\alpha \tag{J.5}$$

$$\tilde{u} = \tilde{u}^*\cos\alpha - \tilde{w}^*\sin\alpha \tag{J.6}$$

$$\tilde{w} = \tilde{u}^*\sin\alpha + \tilde{w}^*\cos\alpha \tag{J.7}$$

$$\tilde{v} = \tilde{v}^* \tag{J.8}$$

where $\tilde{u}$, $\tilde{v}$, and $\tilde{w}$ represent the velocity components in the curvilinear coordinate directions $\tilde{x}$, $\tilde{y}$, and $\tilde{z}$, respectively, and $\tilde{u}^*$, $\tilde{v}^*$, and $\tilde{w}^*$ represent the velocity components in the curvilinear coordinate directions $\tilde{x}^*$, $\tilde{y}$, and $\tilde{z}^*$, respectively (see Figure J.2). The body tangent curvilinear coordinates contained in and orthogonal to the plane of $\hat{n}_b$ and $\hat{\sigma}$ are

denoted by $\tilde{x}^*$ and $\tilde{z}^*$, respectively (see Figure J.2).

After the velocity components at the initial-value surface have been transformed into the $(\tilde{x}^*, \tilde{y}, \tilde{z}^*)$-coordinate system, the integral conservation equations are applied to determine the boundary layer property profiles on the downstream side of the interaction region. A cross-section of the control surface used in the integral analysis is depicted in Figure J.3, where the initial-value surface corresponds to station 1 and the solution surface corresponds to station 2. The respective boundary layer thicknesses are denoted by δ_1 and δ_2.

The conservation equations consist of integral forms of the continuity equation, the streamwise $(\tilde{x}^*)$ momentum equation, and the cross-flow $(\tilde{z}^*)$ momentum equation. The energy equation is approximated by the assumption that the total enthalpy at station 2 is constant in the $\tilde{y}$-direction, and is equal to the average total enthalpy at station 1. The integral conservation equations take the form

$$\int_0^{\delta_1} \rho\tilde{u}^* d\tilde{y} = \int_0^{\delta_2} \rho\tilde{u}^* d\tilde{y} + \dot{m}_{bleed} \tag{J.9}$$

$$P_1\delta_1 - P_2\delta_2 + \overline{P}(\delta_2 - \delta_1) = \int_0^{\delta_2} \rho(\tilde{u}^*)^2 d\tilde{y} - \int_0^{\delta_1} \rho(\tilde{u}^*)^2 d\tilde{y} \tag{J.10}$$

$$\int_0^{\delta_1} \rho\tilde{u}^*\tilde{w}^* d\tilde{y} = \int_0^{\delta_2} \rho\tilde{u}^*\tilde{w}^* d\tilde{y} \tag{J.11}$$

$$\overline{H}_1 = H_2 \tag{J.12}$$

where equations(J.9) to (J.12) represent the continuity, streamwise momentum,

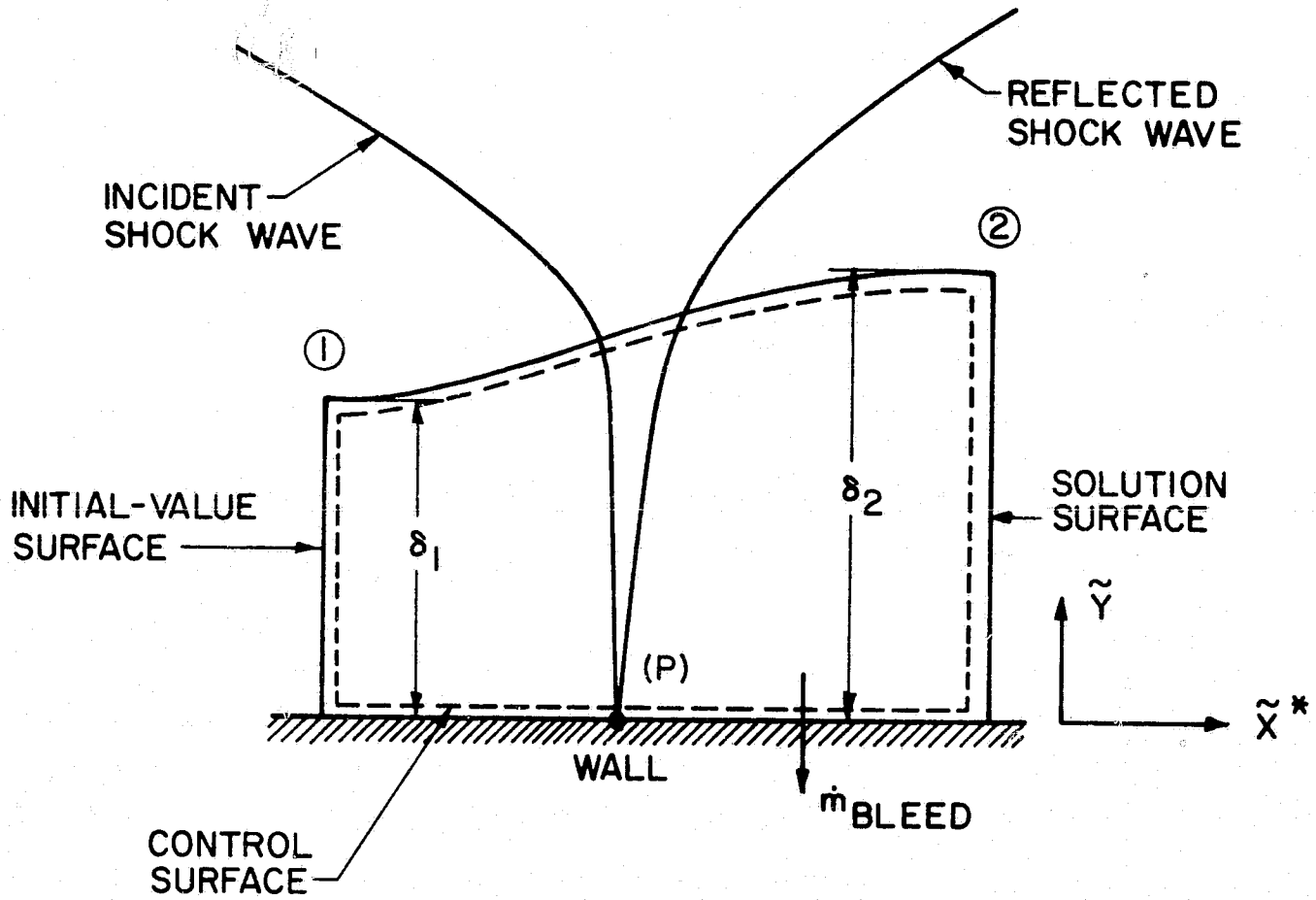

FIGURE J.3. INTERACTION REGION CONTROL SURFACE

cross-flow momentum, and energy equations, respectively. In the above equations, P_1 and P_2 represent the static pressure at stations 1 and 2, respectively, and are assumed to be constant in the $\tilde{y}$-direction, and $\overline{P}$ is an appropriately weighted average pressure acting on the upper surface of the control volume and is determined from the supersonic core flow solution. The mean density and total enthalpy are denoted by ρ and H, respectively. It was assumed in writing the above expressions, that negligible mass is entrained into the boundary layer between stations 1 and 2, that mass bleed occurs normal to the wall and is denoted by $\dot{m}_{bleed}$, and that viscous shear stress effects are of secondary importance.

Since the upstream flow properties have been determined by application of the finite difference algorithm, the integrals appearing in equations (J.9) to (J.11) that are evaluated at station 1 may be determined directly by numerical quadrature. To evaluate the integrals at station 2 requires that representations for the downstream velocity profiles be chosen. In the present investigation, the following turbulent power law profiles have been selected

$$\tilde{u}^* = \tilde{u}_e^* \eta^{\beta_1} \tag{J.13}$$

$$\tilde{w}^* = \tilde{w}_e^* \eta^{\beta_2} \tag{J.14}$$

where

$$\eta = \tilde{y}/\delta \tag{J.15}$$

The exponents β_1 and β_2 appearing in equations (J.13) and (J.14) are bounded in the range

$$0 < \beta_1 < 1 \tag{J.16}$$

$$0 < \beta_2 < 1 \tag{J.17}$$

The mean total enthalpy H may be expressed in terms of the mean static

enthalpy h as

$$H = h + \frac{1}{2}\left[(\tilde{u}_e^*)^2\,\eta^{2\beta_1} + (\tilde{w}_e^*)^2\,\eta^{2\beta_2}\right] \tag{J.18}$$

Since both β_1 and β_2 are bounded and, in general, $(\tilde{w}_e^*)^2 << (\tilde{u}_e^*)^2$, equation (J.18) may be approximated as

$$h \cong H - \frac{1}{2}(\tilde{u}_e^*)^2\,\eta^{2\beta_1} \tag{J.19}$$

which serves to uncouple equation (J.11) from equations (J.9) and (J.10). For a simple system in thermodynamic equilibrium, the following expression can be written

$$\rho = \rho(h,P) \tag{J.20}$$

where for a thermally and calorically perfect gas

$$\rho = K/h \tag{J.21}$$

with

$$K = \frac{\gamma}{\gamma - 1}P \tag{J.22}$$

where γ is the specific heat ratio.

Using the above relations allows the downstream integrals in equations (J.9), (J.10), and (J.11) to be written for a thermally and calorically perfect gas as

$$\int_o^{\delta_2} \rho\tilde{u}^*\,d\tilde{y} = K_2\delta_2\tilde{u}_{e_2}^* \int_o^1 \frac{\eta^{\beta_1}d\eta}{[H_2 - \frac{1}{2}(\tilde{u}_{e_2}^*)^2\eta^{2\beta_1}]} \tag{J.23}$$

$$\int_o^{\delta_2} \rho(\tilde{u}^*)^2\,d\tilde{y} = K_2\delta_2(\tilde{u}_{e_2}^*)^2 \int_o^1 \frac{\eta^{2\beta_1}d\eta}{[H_2 - \frac{1}{2}(\tilde{u}_{e_2}^*)^2\eta^{2\beta_1}]} \tag{J.24}$$

$$\int_o^{\delta_2} \rho\tilde{u}^*\tilde{w}^*\,d\tilde{y} = K_2\delta_2\tilde{u}_{e_2}^*\tilde{w}_{e_2}^* \int_o^1 \frac{\eta^{\beta_1}\eta^{\beta_2}d\eta}{[H_2 - \frac{1}{2}(\tilde{u}_{e_2}^*)^2\eta^{2\beta_1}]} \tag{J.25}$$

To obtain the downstream property profiles, initial estimates are made for the exponents β_1 and β_2. Then equations (J.9), (J.10), and (J.12) are solved simultaneously while incorporating equations (J.23) and (J.24) for the downstream integrals. This produces a system of two equations for the downstream unknown quantities δ_2 and β_1. These equations are solved using a Newton-Raphson iteration scheme with β_1 serving as the perturbation quantity. After convergence has been obtained for δ_2 and β_1, equation (J.25) is incorporated into equation (J.11), with the resulting expression being solved using a Newton-Raphson iteration scheme employing β_2 as the perturbation quantity.

Determining the downstream boundary layer thickness δ_2 and the power law exponents β_1 and β_2 completely defines the downstream property field since H_2 was determined from equation (J.12). After the downstream velocity components $\tilde{u}_2^*$ and $\tilde{w}_2^*$ have been calculated, the velocity components $\tilde{u}_2$ and $\tilde{w}_2$ can be determined by a coordinate rotation using equations (J.6) and (J.7).

By applying the above analysis to a series of control volumes, the flow properties downstream of the shock wave-boundary layer interaction region may be determined for the entire computed sector. This solution is then used as initial data for restarting the finite difference boundary layer computation.

APPENDIX K

OVERALL NUMERICAL ALGORITHM

1. INTRODUCTION

In this appendix, the control logic used in the numerical algorithm is discussed. Regulation of the marching step size, generation of the initial data, and considerations of flow symmetry are also discussed. All of the characteristic unit processes referred to in this appendix are discussed in Appendix E. The boundary layer subalgorithms referred to this in this appendix are discussed in Appendices I and J.

2. GENERAL COMMENTS CONCERNING COMPUTATION OF THE SUPERSONIC CORE FLOW

The overall numerical algorithm for the supersonic flow consists of the repetitive application of the various characteristic unit processes to generate the global solution for given boundary conditions and a specified set of initial data.

The goemetric boundary conditions are represented by the formulations presented in Appendix D. The initial data are specified on a space-like plane of constant x (see Figure K.1). The x-coordinate axis is the longitudinal axis of the forebody/centerbody and the cowl. Moreover, the mean supersonic flow direction is assumed to be in the x-coordinate direction.

An inverse marching scheme is employed in the supersonic flow overall numerical algorithm. The supersonic flow solution is obtained on space-like planes of constant x. The solution points on each plane represent the intersection points of continuous streamlines which are propagated from the data points specified on the initial-value plane. In addition to the streamline solution points, are the solution points representing

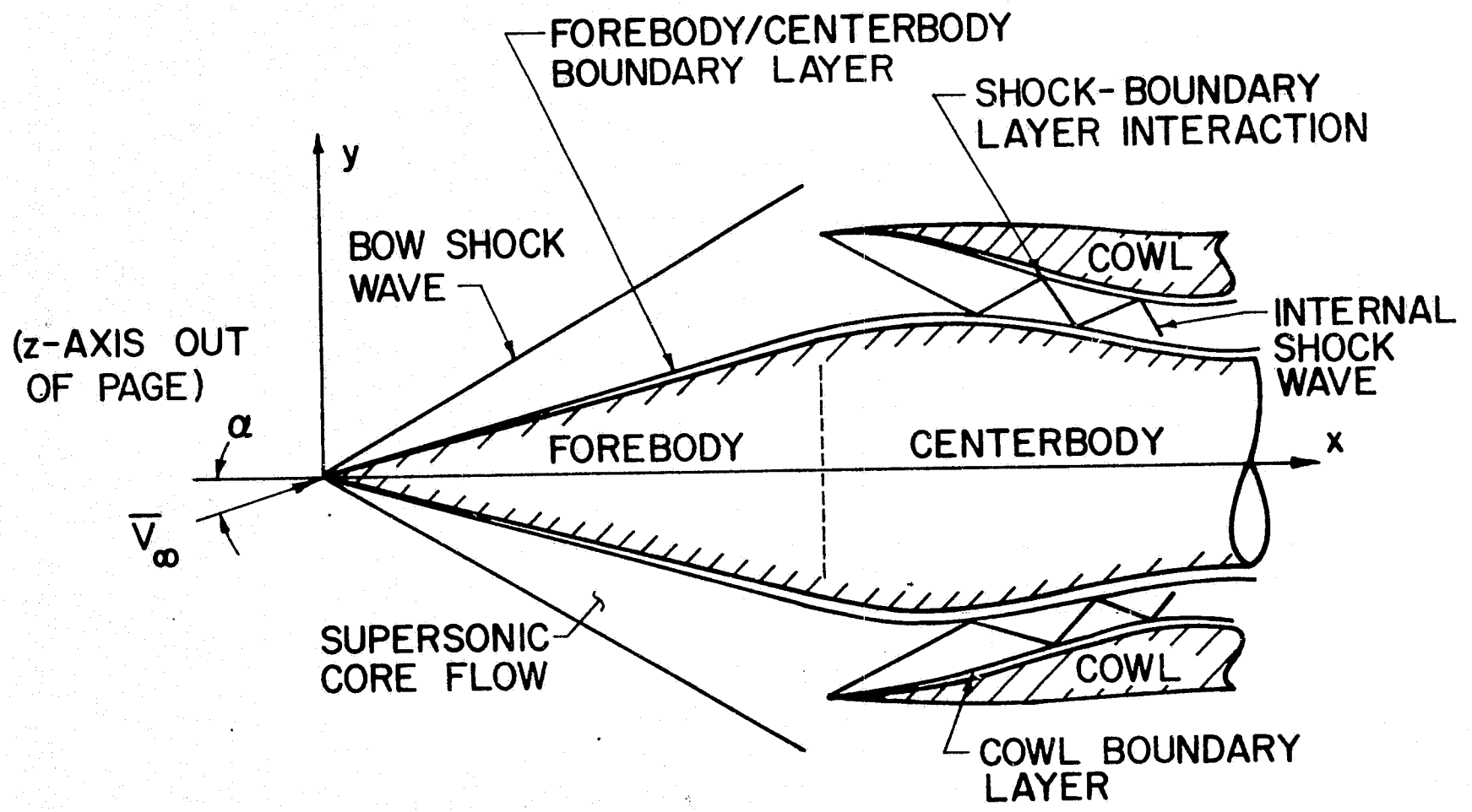

FIGURE K.I. MIXED-COMPRESSION AIRCRAFT INLET

the intersection of either the external or the internal shock wave with the solution plane. For the internal flow, the solution is also obtained on the space curves which represent the intersection of the internal shock wave with the solid boundaries. These space curves are defined by the locus of shock wave solution points.

Except in the vicinity of a shock wave reflection with a solid boundary, the axial (x) distance between successive solution planes is determined by the application of the Courant-Friedrichs-Lewy (CFL) stability criterion. In the vicinity of a shock wave intersection with a solid boundary, the axial step is controlled by special constraints which ensure that the entire shock wave-solid boundary intersection falls between two adjacent solution planes.

After each solution plane is computed, the mass flow rate across that plane is calculated using trapezoidal rule integration. Constancy of the overall mass flow rate in the internal flow field computation gives an indication of the overall accuracy of the numerical integration if the inlet walls are impermeable. The stagnation pressure and stagnation temperature are calculated at each solution point. For the adiabatic flow of a calorically perfect gas, the stagnation temperature should remain constant.

In the numerical analysis, the flow field is divided into two regimes: the internal flow regime and the external flow regime, as illustrated in Figure K.1. The supersonic flow field integration in each of these two regimes is controlled by separate logic modules in the computer program. The forebody supersonic flow field integration is performed first. Then, the internal supersonic flow field is computed. The computer program developed in the present investigation has the capability to perform the

internal supersonic flow field integration with or without the discrete fitting of the internal shock wave system. The option in which shock waves are not discretely fitted might be employed if the internal shock waves are of relatively weak strength, and thereby an acceptable solution could be obtained by smearing the internal discontinuities.

From a computation point of view, the internal supersonic flow field in which shock waves are not discretely fitted is the easiest solution to compute. For flow fields in which shock waves are discretely fitted, the external supersonic flow about the forebody is less difficult to obtain than the internal flow, since in the external flow the shock wave represents a bound to the computational regime. Discrete fitting of the shock wave throughout the computational regime, as is done in the internal supersonic flow field integration, greatly complicates the numerical algorithm.

3. COURANT-FRIEDRICHS-LEWY (CFL) STABILITY CRITERION

Except in the vicinity of an internal shock wave-solid boundary intersection, the axial marching step between successive solution planes in the supersonic flow solution is determined by the application of the Courant-Friedrichs-Lewy (CFL) stability criterion (8). The CFL stability criterion will be satisfied at each solution point if the convex hull of the finite difference network contains the differential zone of dependence of the solution point. The convex hull of the finite difference network, illustrated in Figure K.2, is defined by the outer periphery of initial-value plane field points used in determining the fit point stencil for the quadratic bivariate interpolation polynomial. The differential zone of dependence, also illustrated in Figure K.2, is the region defined by the intersection of the Mach cone (whose apex is at the solution point)

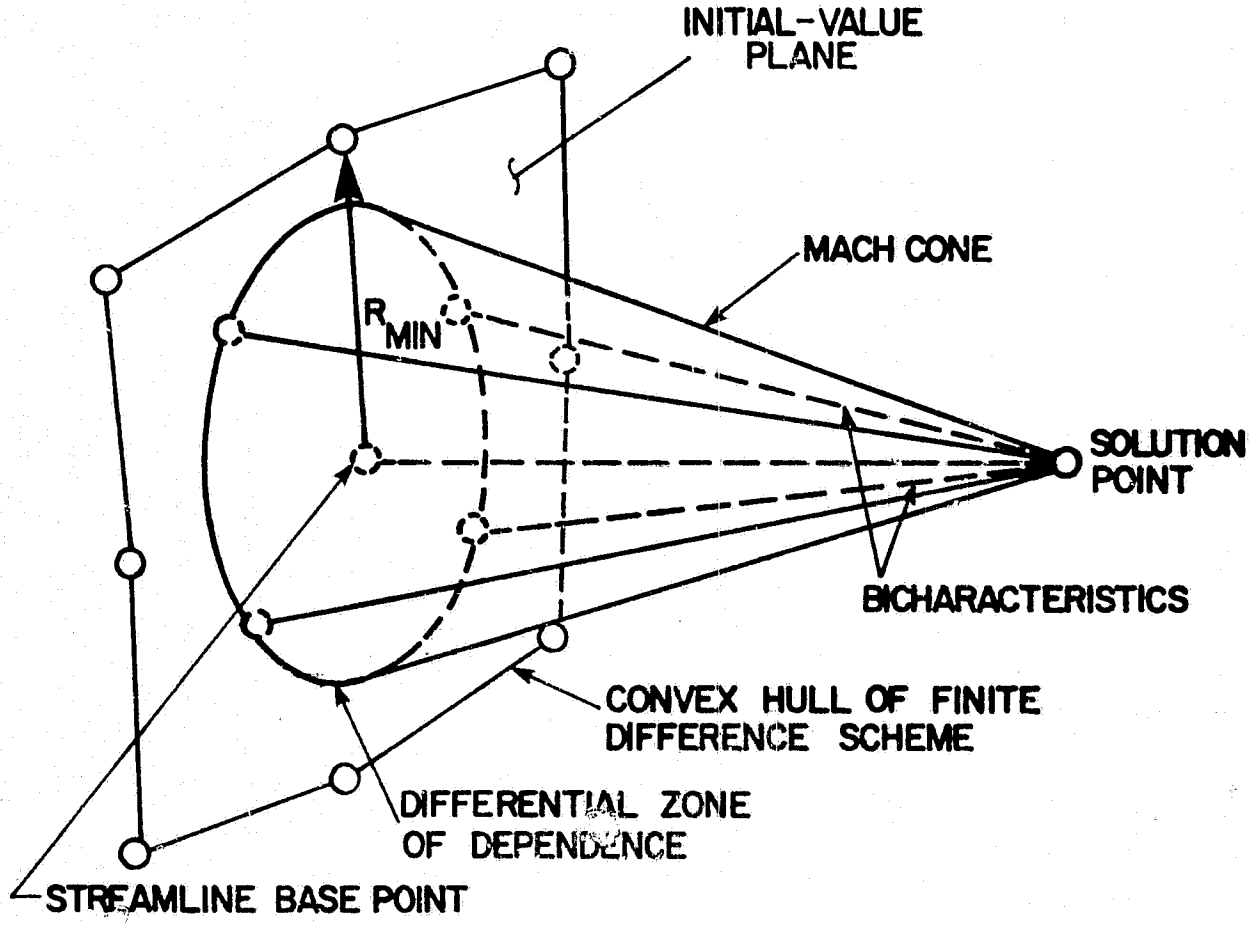

FIGURE K.2. CFL STABILITY CRITERION

with the initial-value plane.

The maximum allowable marching step for each streamline is the x-step for which the Mach cone just touches the convex hull. That step size is given by

$$\Delta x = [u^2/(cq)][1 - (c/q)(q^2/u^2 - 1)^{1/2}]R_{min} \qquad (K.1)$$

where Δx is the maximum allowable axial step, u is the x-component of the velocity, q is the velocity magnitude, and c is given by

$$c^2 = a^2q^2/(q^2 - a^2) \qquad (K.2)$$

where a is the local sonic speed. In equation (K.1), R_{min} is the distance from the streamline base point in the initial-value plane to the nearest field point on the convex hull of the finite difference network (see Figure K.2).

Equation (K.1) is applied at every streamline solution point, the actual marching step being selected as the Δx value at the most restrictive point. It should be noted that this expression is applied only to streamline points, the shock wave points being excluded. Furthermore, in the internal flow field integration, the shock wave points are ignored in defining the convex hull of the finite difference network when application of the stability criterion is made to a streamline point.

4. SUPERSONIC FLOW INITIAL-VALUE PLANE

The supersonic flow initial data are specified on a plane of constant x. The flow must be supersonic at every point on this plane. For uniqueness and existence of a genuine solution, the values of the dependent variables prescribed on this surface must have at least continuous first partial derivatives.

If the forebody flow field is to be determined, the initial-value plane must be specified at an axial (x) station that is upstream of the forebody computational flow regime (see Figure K.1). The solution is then found along the streamlines that pass through the data points specified on the initial-value plane, although some streamline addition and deletion are performed on the ensuing solution planes as described in Section 6 of this appendix.

If only the internal flow field is to be determined, the supersonic flow initial-value plane must be specified at the axial station which corresponds to the x-position of the cowl lip (see Figure K.1). The cowl lip is assumed to be contained in a plane of constant x. For the integration of the internal flow field, a point redistribution is performed on the initial-value plane. This point redistribution is required in order to have streamlines which lie in the stream surface formed by the cowl boundary. The solution is then found along the streamlines that pass through the redistributed points on the plane at the cowl lip axial station.

The supersonic flow initial-value plane may be specified by the user, or if the forebody is conical up to the axial station where the initial-value plane is located, the flow property field on the initial-value plane can be generated internally in the computer program by one of two methods.

One method of internally generating the supersonic flow initial-value plane is by using an approximate technique which employs the Taylor-Maccoll solution for the flow about a circular cone at zero incidence. A superposition procedure is used to obtain an approximation to the flow about a circular cone at nonzero angle of attack by neglecting the cross

flow effects. This superposition procedure effectively amounts to computing the flow turning angle in the meridional plane of the given solution point, and then obtaining the flow properties at that point by applying the Taylor-Maccoll solution for a cone half-angle equal to the flow turning angle. The shock wave angle is then measured from the original streamline direction in the appropriate meridional plane. It must be emphasized that this is only an approximate technique, giving the well accepted Taylor-Maccoll solution at zero incidence, but becoming increasingly less accurate as the angle of attack is increased.

An alternate method of generating the supersonic flow initial data is to employ the solution obtained by Jones (28) for the flow about a circular cone at incidence. The Jones algorithm has been incorporated into the computer program developed in the present investigation. Many of the computed results presented in Section X were obtained using the results of the Jones algorithm as initial data. For situations in which the forebody is conical up to the axial station where the supersonic flow initial-value plane is located, the Jones algorithm is the recommended source for the initial data.

If the forebody is not conical ahead of the axial station of the initial-value plane, another source of initial data must be used. If available, experimental data may be employed.

5. SUPERSONIC FLOW SOLUTION PLANE POINT NETWORK AND FLOW SYMMETRY

The supersonic flow computational point network is based on a series of circumferential and radial stations. The point networks for the various flow symmetry options are illustrated in Figure K.3. In this figure, the index i corresponds to the i th circumferential station and the index j corresponds to the j th radial station. In all cases, the streamlines on

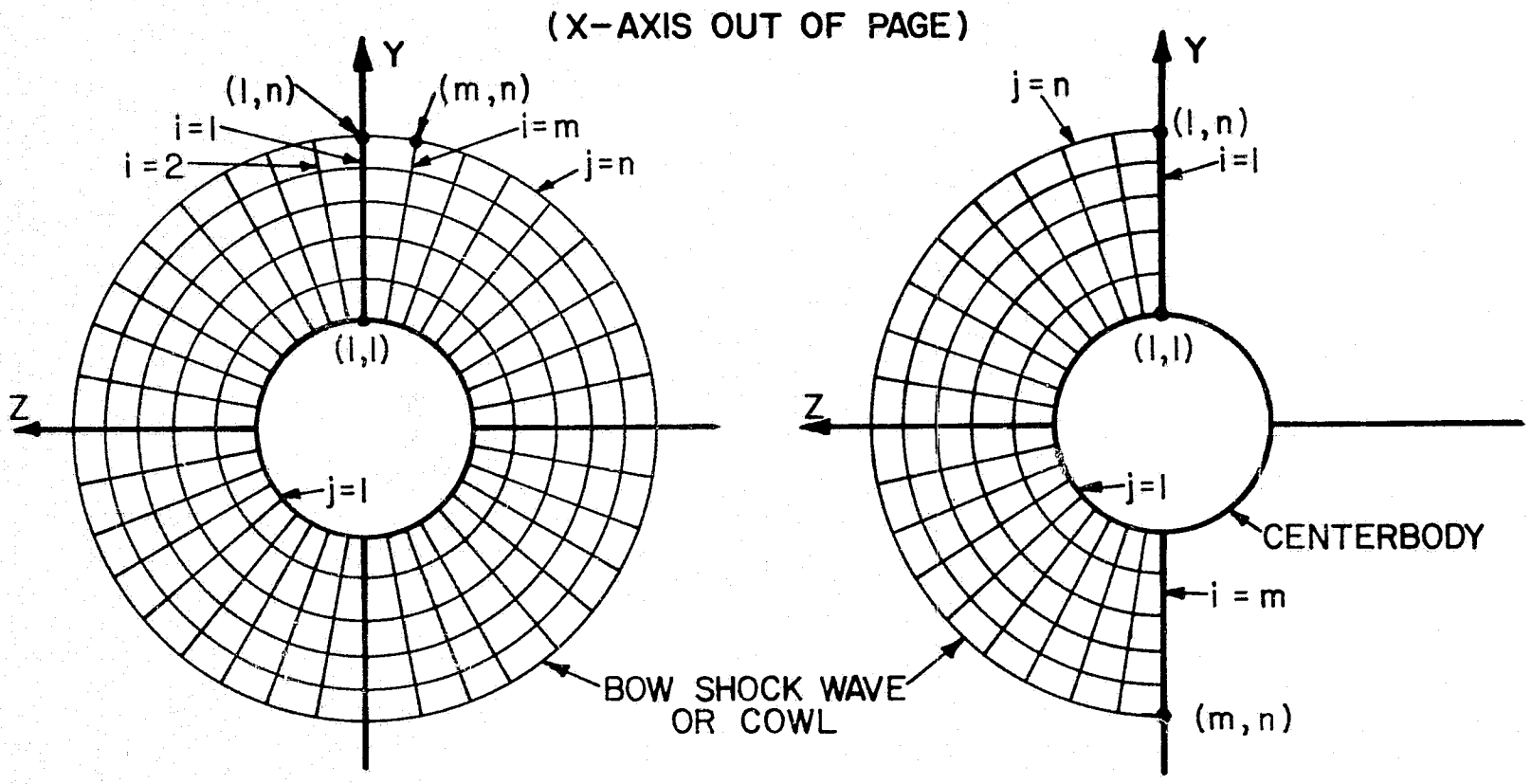

(a) NO PLANES OF SYMMETRY (b) ONE PLANE OF SYMMETRY

FIGURE K.3. SUPERSONIC FLOW COMPUTATIONAL POINT NETWORKS

(c) TWO PLANES OF SYMMETRY (d) AXISYMMETRIC FLOW

FIGURE K.3. (CONTINUED)

the surface of the centerbody are denoted by j = 1. For the forebody flow field, the bow shock wave solution points are denoted by j = n. For the internal flow field, the streamlines on the surface of the cowl are denoted by j = n. The computed sector, in general, is bounded by the circumferential stations corresponding to i = 1 and i = m. This point arrangement produces a rectangular logic array in the computer program.

The points at any circumferential station in axisymmetric flow, or on a plane of flow symmetry in three-dimensional flow, lie on a straight line. Moreover, for axisymmetric flow, the radial stations correspond to circular rings. In general, however, the solution points ar a given circumferential station do not lie on a ray, nor do the radial stations correspond to circular rings.

For the internal flow option in which shock waves are discretely fitted, the shock wave solution points are also represented in this point arrangement. Special logic is used in the computer program such that the shock wave solution points float in the storage arrays as the shock wave travels between the centerbody and cowl on successive solution planes. On a given solution plane, the shock wave solution points at adjacent circumferential stations do not, in general, have to lie at the same radial station.

The computer program takes advantage of flow symmetry when it exists in the flow field. In these instances, the entire solution plane does not have to be computed, but rather only an appropriate section of it. The remaining sections of the solution plane may be obtained by reflection of the points in the computed sector. This procedure yields a significant reduction in computer execution time.

The four flow symmetry options that have been incorporated into the

analysis are depicted in Figure K.3. Figure K.3(a) illustrates the most general case when no flow symmetry is present. Figure K.3(b) illustrates the case when one plane of flow symmetry is present. In this case the computed sector is the half-plane bounded by the y-axis and containing the +z-axis. The integration region in this case is bounded by the i = 1 circumferential station on the +y-axis and by the i = m circumferential station on the -y-axis. This case of flow symmetry is the one most likely to arise in the class of problems being considered in this investigation. Figure K.3(c) illustrates the case when two planes of flow symmetry are present. This option would be used to compute the flow field about asymmetric bodies at zero angle of attack. In this instance, the computed sector is the quadrant bounded by the +y-axis and the +z-axis. The circumferential station corresponding to i = 1 lies on the +y-axis and the circumferential station corresponding to i = m lies on the +z-axis. Finally, Figure K.3(d) illustrates the axisymmetric flow option where the computed sector is limited to the single circumferential station (ray) lying on the +y-axis. This option would be used to compute the flow field about axisymmetric bodies at zero angle of attack.

The numerical algorithm does not apply special characteristic unit processes when a solution point lies on a plane of symmetry. Rather, a point reflection about the plane of symmetry is performed in the initial-value plane, and the appropriate unit process is then applied in standard form. This procedure yields satisfactory results and eliminates the need for devising special unit processes.

6. SUPERSONIC EXTERNAL FLOW ABOUT THE FOREBODY

With the forebody geometry specified and the flow property field on the initial-value plane determined, the supersonic external flow about

the forebody can be calculated. In the computation of this flow field, the distance between successive solution planes is determined by the application of the CFL stability criterion. Ths last solution plane in the forebody flow field computation is made to coincide with the x-position of the cowl lip.

After the axial step between the current initial-value plane and the current solution plane has been determined, the solid boundary point unit process (see Appendix E) and the interior point unit process (see Appendix E) are applied. These unit processes achieve second-order accuracy without the need for global iteration. Hence, these unit processes are applied at the appropriate points until convergence is obtained without using information from neighboring points in the solution plane.

Once the solution at each solid boundary point and interior point has been determined, the bow shock wave point unit process (see Appendix E) is applied at each shock wave solution point in the computed sector. Global correction is then applied for these points, if desired. The position of each shock wave solution point is made to lie in the meridional plane defined by the outer-most interior field point which is on the same circumferential station as the shock wave point. As a consequence, in axisymmetric flow, the streamline and shock wave solution points on a given circumferential station lie in the same meridional plane on all succeeding solution planes. In three-dimensional flow, however, except on a plane of flow symmetry, the solution points corresponding to a given circumferential station do not lie in the same meridional plane on successive solution planes.

In the forebody flow field integration, periodic streamline addition and deletion are performed. The streamline addition is required to retain

a well-dispersed computational mesh, since at successive solution planes more and more mass is captured. Moreover, convergence of the streamlines towards the forebody occurs as the flow progresses downstream. Periodic point deletion is required since the continued addition of streamlines would produce an excessively large number of computational mesh points, thereby unduly increasing computer execution time and machine storage requirements. The streamline addition and deletion procedures are outlined in the following. A depiction of a typical forebody flow streamline pattern is given in Figure K.4.

For the purposes of point addition, after the points on the solution plane have been computed, the mass flow rate across that plane is calculated. If this mass flow rate is significantly larger than the mass flow rate across the last solution plane where point redistribution was performed, a new ring of solution points is added between the ring of shock wave solution points ($j = n$) and the ring of outermost interior field solution points ($j = n - 1$). The coordinates of each of these inserted solution points is obtained by forming the arithmetic average of the coordinates of the shock wave solution point and the outermost interior field point corresponding to the circumferential station of the new point. The flow properties at each of the inserted solution points are obtained by interpolation using the quadratic bivariate polynomial

$$f(y,z) = a_1 + a_2 y + a_3 z + a_4 yz + a_5 y^2 + a_6 z^2 \qquad (K.3)$$

where $f(y,z)$ denotes a general function of the coordinates y and z. The coefficients a_i (i=1 to 6) in equation (K.3) are obtained by a least squares fit of nine data points in the solution plane, as described in Appendix C.

Point deletion occurs when the number of radial stations has reached

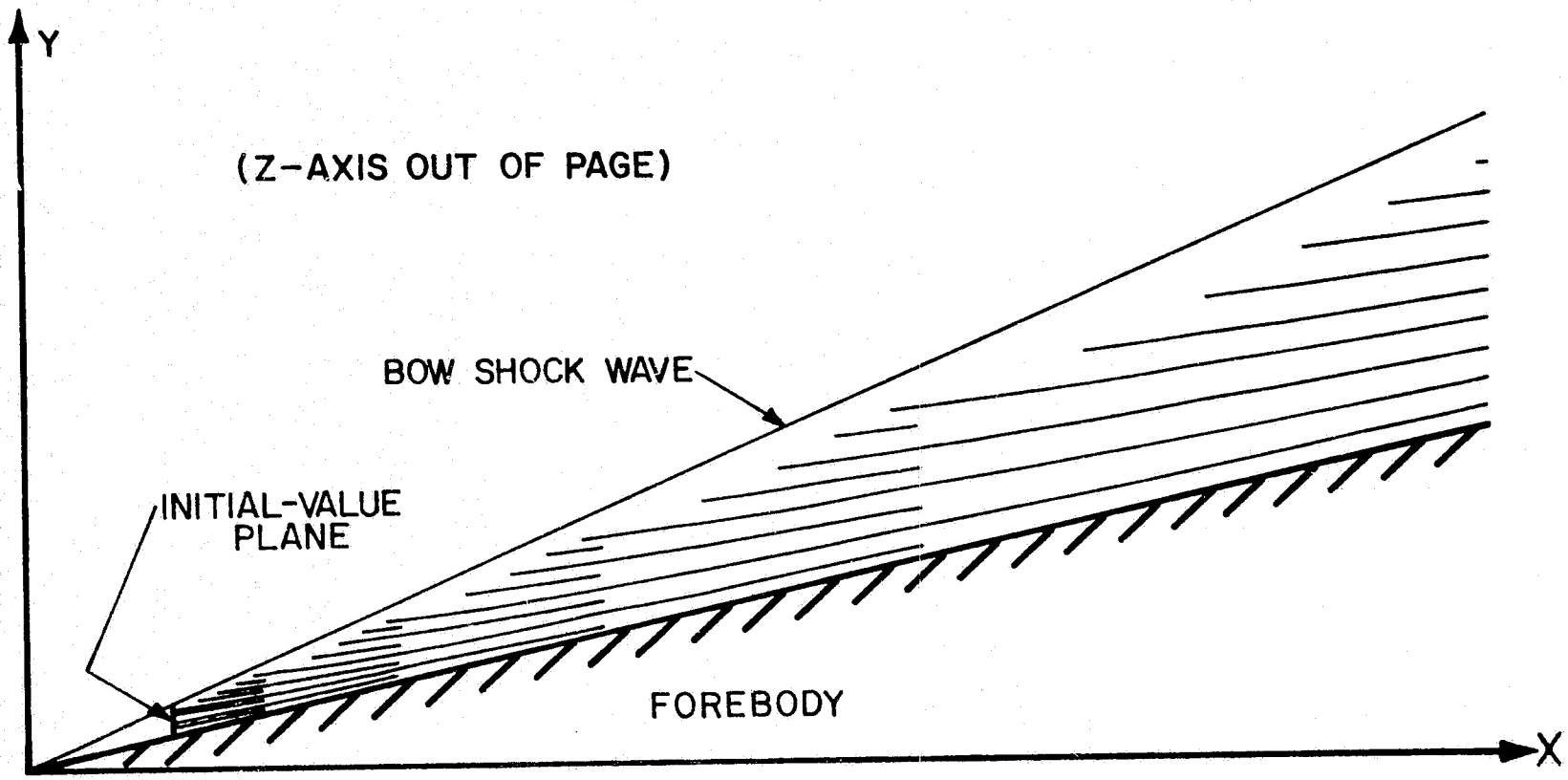

FIGURE K.4. TYPICAL FOREBODY FLOW STREAMLINE PATTERN

a specified limit. In point deletion, the body streamline points are retained in storage, while selected interior streamline points are deleted from storage. Refinement of this technique is provided by having two limits to the number of allowable radial stations. The first limit is employed when the mass flow rate at the given solution plane is less than a specified fraction of the estimated flow rate at the cowl lip. The second and larger limit is employed when that fraction has been exceeded.

7. SUPERSONIC INTERNAL FLOW IN WHICH SHOCK WAVES ARE NOT DISCRETELY FITTED

The program option in which the supersonic internal flow field is computed without the discrete fitting of the internal shock wave system might be employed in the cases where the internal shock waves are weak in strength, and thereby an acceptable solution could be obtained by smearing all internal discontinuities. This option requires that only two unit processes be employed: the interior point unit process and the solid boundary point unit process. The influence of molecular transport can be included in the computation of this flow field.

The initial-value plane of the internal flow computation is constituted by the last solution plane of the forebody flow field integration. Alternatively, the initial-value plane may be specified at the cowl lip axial station without employing the forebody flow field integration option. This technique is recommended if the forebody is conical up to the cowl lip axial station.

The computer program developed in the present investigation assumes that the bow shock wave falls outside of the cowl lip, or, in the limit, intersects the cowl lip exactly. The program does not have the capability to compute the internal flow field when the bow shock wave has been ingested into the annulus.

With the initial-value plane specified, a point redistribution on this plane is performed to obtain a uniform point distribution and to obtain streamlines which lie in the stream surface formed by the cowl boundary. The redistributed points are arranged symmetrically in the computed sector. These points lie on rays which have equal angular increments from one another, with the points on each ray being spaced at equal radial increments. The radial station j = 1 corresponds to the centerbody streamline points, and j = n corresponds to the cowl streamline points. The properties at these points are obtained by interpolation.

With the point redistribution performed, the internal flow field integration proceeds in a manner similar to the external flow field integration, except that only two unit processes are used: the interior point unit process and the solid boundary point unit process. No point addition or deletion is performed. The internal flow field integration is terminated either when a specified axial station is reached or when the flow becomes subsonic.

8. SUPERSONIC INTERNAL FLOW IN WHICH SHOCK WAVES ARE DISCRETELY FITTED

A point redistribution is first performed on the initial-value plane at the axial station of the cowl lip as described in the previous section. After the upstream flow properties have been determined at each of the cowl lip solution points in the computed sector, the downstream flow properties are obtained at each of these points by application of the solid body-shock wave point unit process.

In the integration of the internal flow field in which shock waves are discretely fitted, the axial step is obtained by the application of the CFL stability criterion, except in the vicinity of a shock wave reflection, where special constraints are employed. After the axial

station of the solution plane has been determined, the internal shock wave is projected from the current initial-value plane to the current solution plane in the meridional plane passing through the x-axis and the previous shock wave point on the initial-value plane as illustrated in Figure K.5. The location of the shock wave solution point is obtained by applying the following equation.

$$dr_s/dx = \tan\beta_I \qquad (K.4)$$

In equation (K.4), dr_s is the increment in radius between the projected shock wave point and the previous shock wave point on the initial-value plane, dx is the corresponding increment in axial distance, and β_I is the angle subtended by the shock wave and the x-axis at the initial-value plane shock wave point and in the meridional plane defined by the initial-value plane shock wave point. Equation (K.4) is applied for each shock wave point in the computed sector, thereby yielding the locus of projected shock wave points in the solution plane. Interpolated values of the shock wave radius in the solution plane are obtained by employing the following equation.

$$r_s(\theta) = a_1 + a_2\theta + a_3\theta^2 \qquad (K.5)$$

In equation (K.5), $r_s(\theta)$ is the shock wave radius at the polar angle $\theta = \tan^{-1}(z/y)$, and the coefficients a_i (i=1,2,3) are obtained by fitting this expression to three projected shock wave points, as described in Appendix C. Equation (K.5) is applied at every circumferential station in the computed sector. Hence, the shock wave location in the solution plane is represented by a series of overlaping one-dimensional curve fits.

After the tentative position of the shock wave in the solution plane

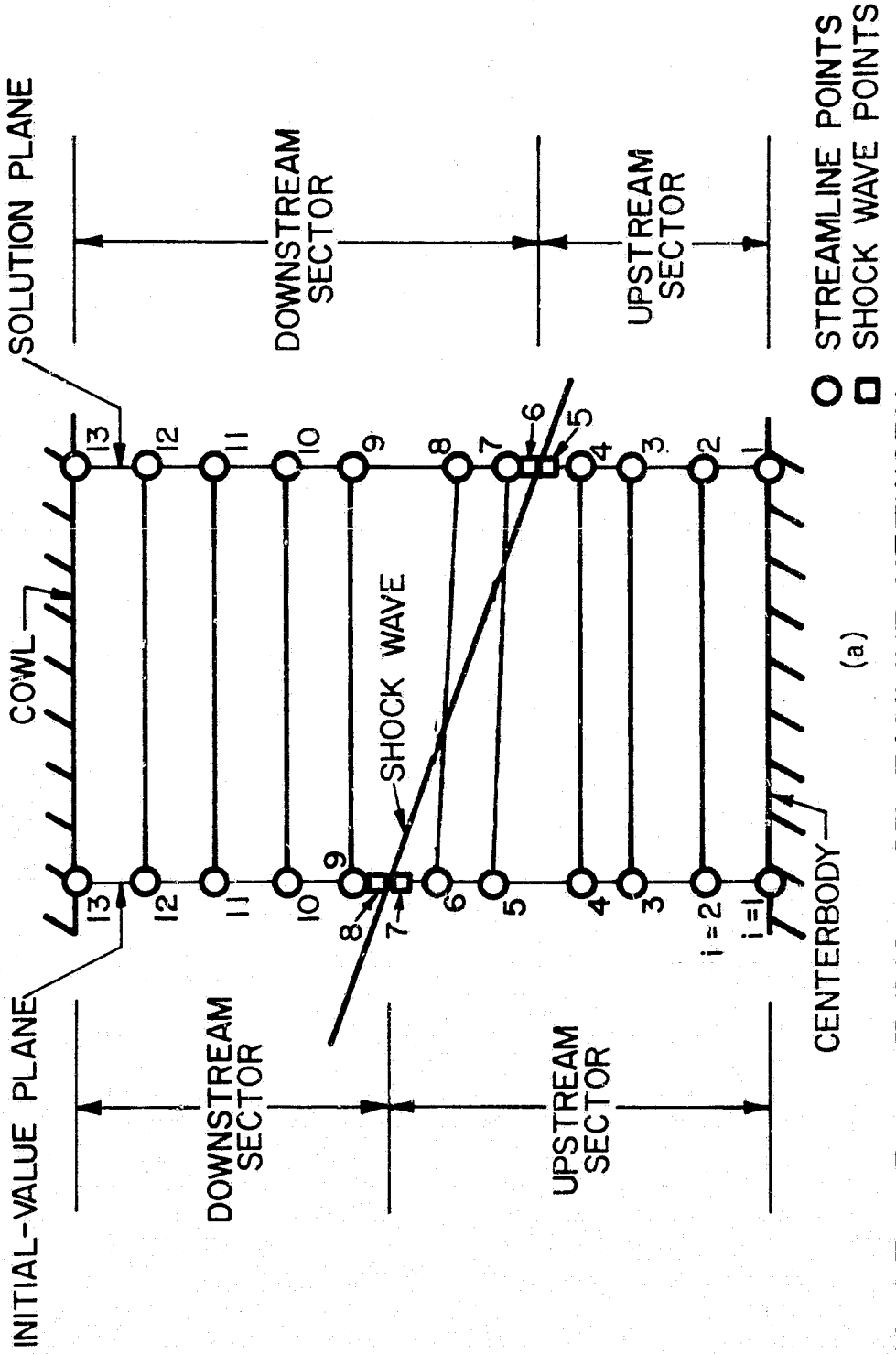

FIGURE K.5. TYPICAL STREAMLINE NETWORK FOR INTERNAL FLOW

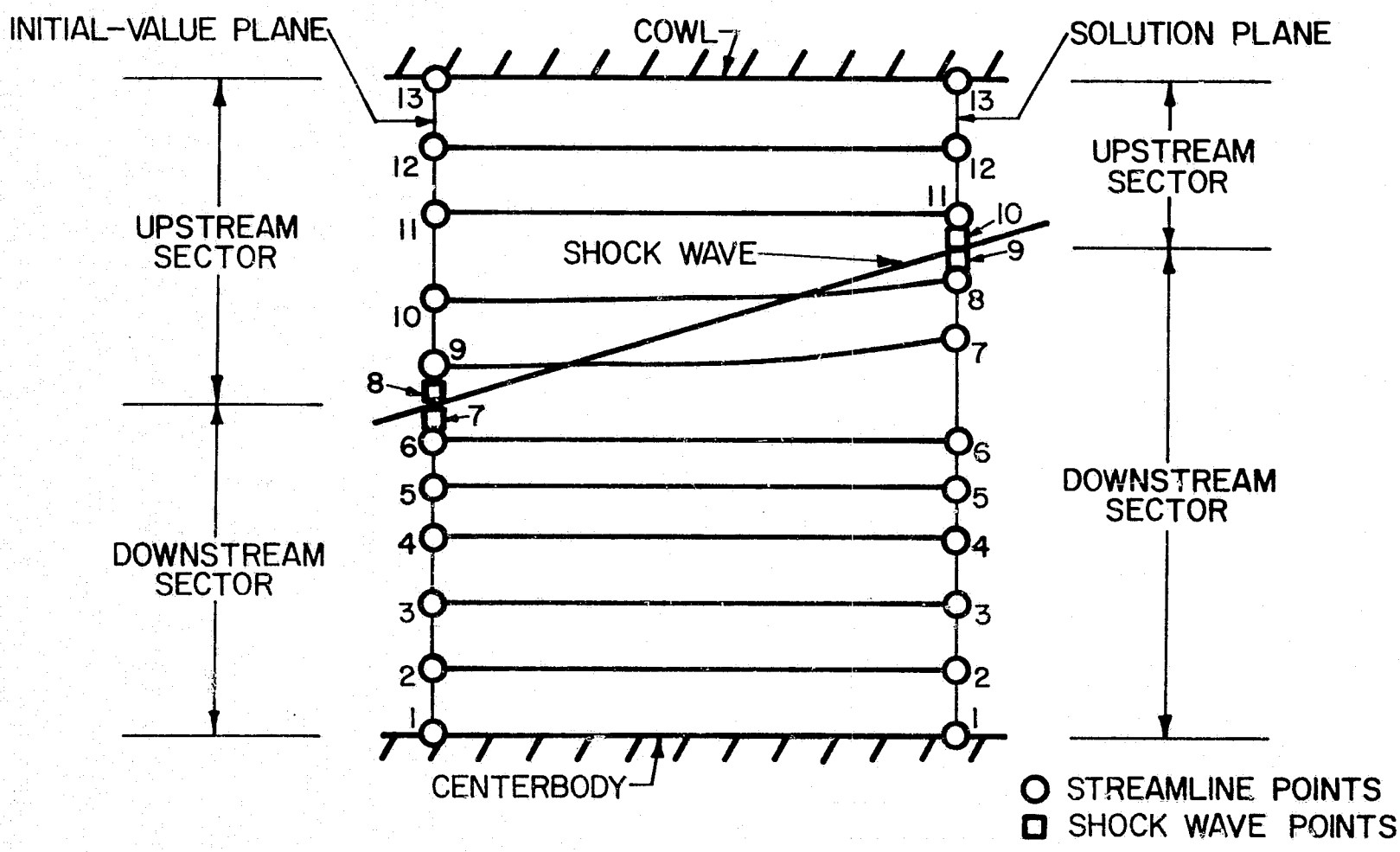

(b)

FIGURE K.5. (CONTINUED)

has been determined, the streamlines that are in the flow field sector that is upstream of the shock wave in the initial-value plane are projected from the initial-value plane to the solution plane, as illustrated by streamlines 1 to 6 in Figure K.5(a) and by streamlines 9 to 13 in Figure K.5(b). This is accomplished by applying the equation of a streamline

$$dx_i = u_i dt \qquad (i=1,2,3) \tag{K.6}$$

where x_i (i=1,2,3) denotes the three cartesian coordinates x, y, and z, respectively, u_i (i=1,2,3) denotes the corresponding velocity components u, v, and w, respectively, and t is the time of travel of a fluid particle along the streamline. Equation (K.6) is first applied in the x direction. Since the axial step dx is known from the application of the CFL stability criterion, the time parameter dt may be determined. Then, application of equation (K.6) for the y and z directions allows the y and z coordinates of the projected streamline point to be computed. The radius $r=(y^2+z^2)^{1/2}$ and polar angle $\theta = \tan^{-1}(z/y)$ of each of the projected streamline points are then computed.

The radius of the projected streamline point is then compared to the radius of the shock wave, given by equation (K.5), in the meridional plane defined by the projected streamline point. If the projected streamline point is in the upstream flow field sector on the solution plane (i.e., the streamline does not intersect the shock wave), then a standard interior point or solid boundary point unit process is applied to obtain the solution at this point. If the streamline appears to intersect the shock wave, as illustrated by streamlines 5 and 6 in Figure K.5(a) and streamlines 9 and 10 in Figure K.5(b), then the application of the unit process

to determine the solution is deferred.

At this stage, the upstream and downstream shock wave solution points are determined at each circumferential station in the solution plane computed sector using the internal shock wave point unit process. This procedure defines the property field on both the upstream and downstream sides of the internal shock wave.

Next, the body streamline solution points are computed at every circumferential station in the downstream flow field sector on the solution plane. In some instances, computing the solution at these points may entail using flow property information from the downstream side of the internal shock wave if the Mach cone, with apex at the solution point, intersects the shock wave surface. Determining the solution at each of these points thereby defines the flow property field on the boundary stream surface in the downstream flow field sector.

At this stage, the solution on each of the streamlines which have not yet been computed is determined. The streamlines that are in the downstream flow field sector on the initial-value plane will remain in the downstream flow field sector on the solution plane (see Figure K.5). The solution at these points is determined by the application of the standard interior point unit process, unless a portion of the Mach cone, with apex at the solution point, intersects the internal shock wave or the solid boundary, in which case the modified interior point unit process is applied. For streamlines which penetrate the internal shock wave [streamlines 5 and 6 in Figure K.5(a) and streamlines 9 and 10 in Figure K.5(b)], the appropriate modified interior point unit process is applied. For the streamlines whose solution was deferred due to a possible shock wave penetration, but which ultimately did not intersect the shock wave, the standard interior

point scheme is applied. The solution points are ordered in the storage arrays in the order of increasing radius on a given circumferential station. So a post computation interchange of the streamline solution points with the shock wave solution points is performed for the streamlines which initially appeared to intersect the shock wave but ultimately did not.

The process just outlined is applied repetitively until the internal shock wave intersects a solid boundary. Special logic is used in the computer program for the computation of a shock wave reflection. The overall scheme used in this case is now presented.

The initial step in the computation of the shock wave-solid boundary reflection is to obtain an estimate of the axial location, at a discrete number of points, where the incident shock wave intersects the solid boundary. Except for the case of axisymmetric flow, the intersection of the incident shock wave with the solid boundary defines a three-dimensional space curve, as illustrated in Figure K.6. In axisymmetric flow, this curve lies in a plane of constant x. Points along the space curve are determined by obtaining the intersection of the shock wave and the solid boundary, where both of these surfaces are represented as straight line segments in the meridional planes passing through the shock wave points in the initial-value plane. For a given meridional plane, the shock wave is represented by equation (K.4), where dr_s is the increment in radius between the shock wave-body intersection point and the shock wave point in the initial-value plane, dx is the corresponding increment in axial distance, and β_I is the angle subtended by the shock wave and the x-axis in the meridional plane defined by the appropriate shock wave solution point in the initial-value plane. The local body surface is approximated in the meridional plane by the equation

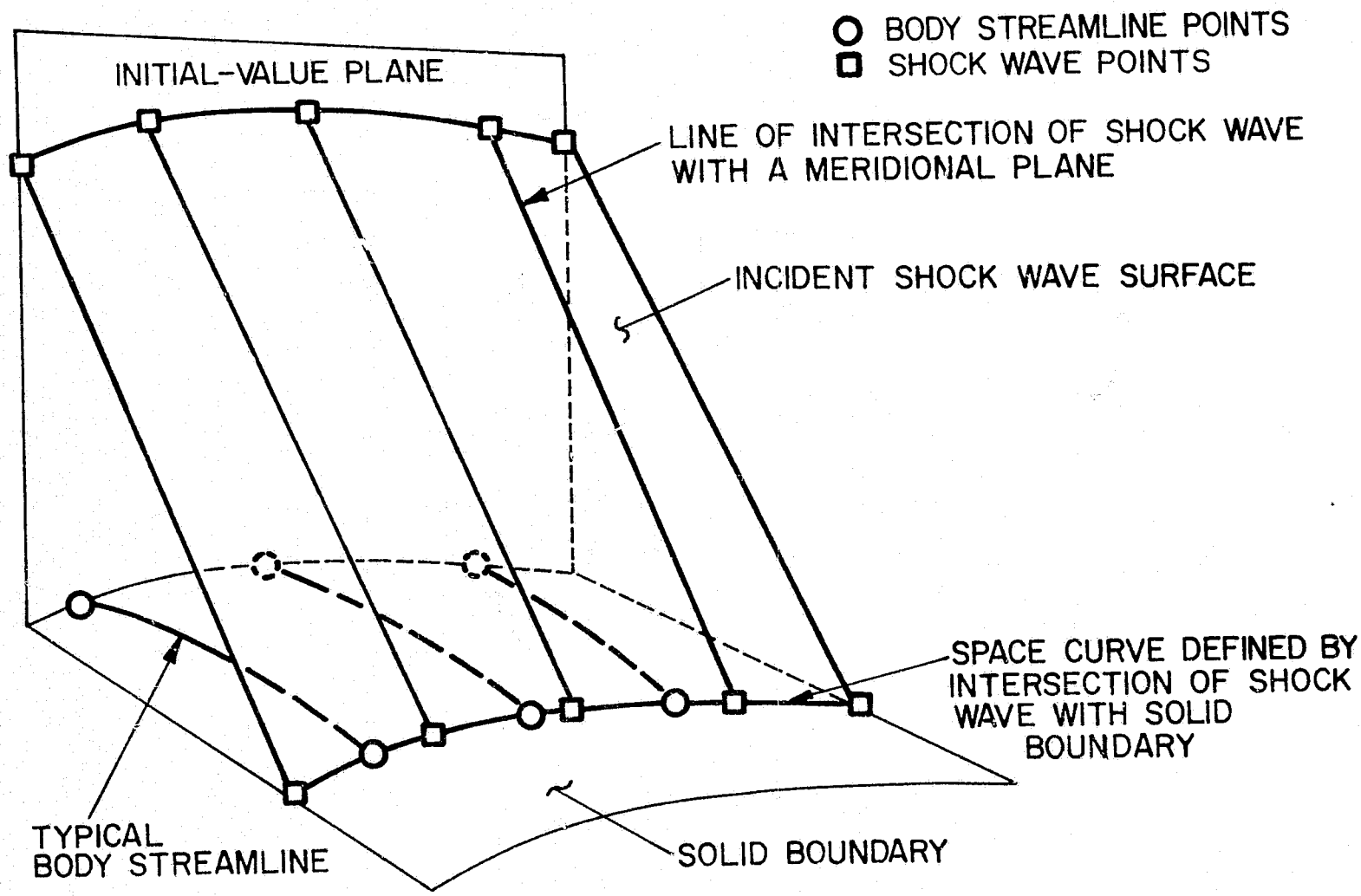

FIGURE K.6. INCIDENT SHOCK WAVE-BODY INTERSECTION

$$dr_b/dx = m \tag{K.7}$$

where dr_b is the change in the radius of the body between the shock wave-body intersection point and the body point in the initial-value plane, dx is the corresponding increment in axial distance, and m is the local slope of the body in the given meridional plane. Equations (K.4) and (K.7) are solved simultaneously to obtain the intersection point in the given meridional plane. The intersection point for every meridional plane defined by the shock wave points on the initial-value plane is so determined. The locus of these intersection points determines the space curve illustrated in Figure K.6.

At this stage, the points on the space curve which are nearest to and farthest away from the initial-value plane are determined. If the axial distance between the nearest point and the initial-value plane is greater than a specified fraction of the marching step allowed by the CFL stability criterion, then another solution plane is computed, the location of this plane being just slightly upstream of the shock wave-body intersection. The entire procedure outlined above is then repeated. Alternatively, if the distance between the nearest shock wave-body intersection point and the initial-value plane is less than this fraction of the allowable marching step, then the axial position of the next solution plane is selected such that the space curve representing the incident shock wave-body intersection is entirely contained between the initial-value plane and the solution plane. At high angles of attack, this procedure may require that the axial step between the initial-value plane and the solution plane be greater than that allowed by the CFL stability criterion. This implies that the Courant number, which is the ratio of the axial step

taken to the axial step allowed by the CFL stability criterion, is greater than unity. To maintain an effective Courant number less than unity, the fit point stencils used in the univariate, bivariate, and trivariate interpolation polynomials are adjusted in accord with the Courant number of the actual step taken. That is, if the Courant number is approximately two, then every other point is used in the interpolation fit point stencils instead of the immediate neighbors (which correspond to a unity Courant number), etc. This ensures that the convex hull of the finite difference network engulfs the differential domain of dependence, thereby satisfying the CFL stability criterion.

After the axial position of the solution plane has been determined and the Courant number computed, the internal shock wave point unit process is applied at every circumferential station in the computed sector at the intersection of the incident shock wave with the solid boundary. This procedure defines the property field on both the upstream and downstream sides of the incident shock wave.

At this stage, the initial-value plane upstream sector body streamlines are extended from the initial-value plane to the space curve defined by the intersection of the incident shock wave with the solid boundary, as illustrated in Figure K.6. The solution for both the upstream and downstream shock wave properties has been obtained on the space curve by the application of the internal shock wave point unit process. Hence, both the upstream and downstream properties at the points where the body streamlines intersect the space curve may be found by interpolation. For this purpose the following quadratic univariate polynomial is employed

$$f(\theta) = a_1 + a_2\theta + a_3\theta^2 \qquad \text{(K.8)}$$

where $f(\theta)$ denotes a general function of the polar angle θ. The coefficients a_i (i=1,2,3) in equation (K.8) are obtained by fitting this expression to three data points on the space curve as described in Appendix C. To determine the intersection point of the body streamline with the space curve, an iterative technique is used. Moreover, after each iteration, the projected streamline point is adjusted along the direction of the body normal projection in the (y,z)-plane such that the streamline point lies on the boundary surface. Equation (K.8) is applied for both the upstream and downstream shock wave properties. Hence, the incident shock wave downstream properties are known at the body streamline points.

At this stage, the solid body-shock wave point unit process is applied at each of the body streamline points in the computed sector that are on the space curve. This defines the reflected shock wave downstream properties at the body streamline points on the space curve.

Using a procedure similar to that used previously, the shock wave is then projected from the space curve to the current solution plane. This projection is performed in the meridional planes containing the body streamline points on the space curve. This procedure yields the tentative shock wave shape in the solution plane.

At this stage, the body streamline points in the solution plane that are in the downstream flow field sector in the initial-value plane are computed by use of the solid boundary point unit process (see Figure K.7). This unit process is applied at every such point in the computed sector. As a consequence, the flow property field on the stream surface formed by the solid boundary is defined.

Next, the remaining streamlines that are in the initial-value plane downstream flow field sector are projected from the initial-value plane

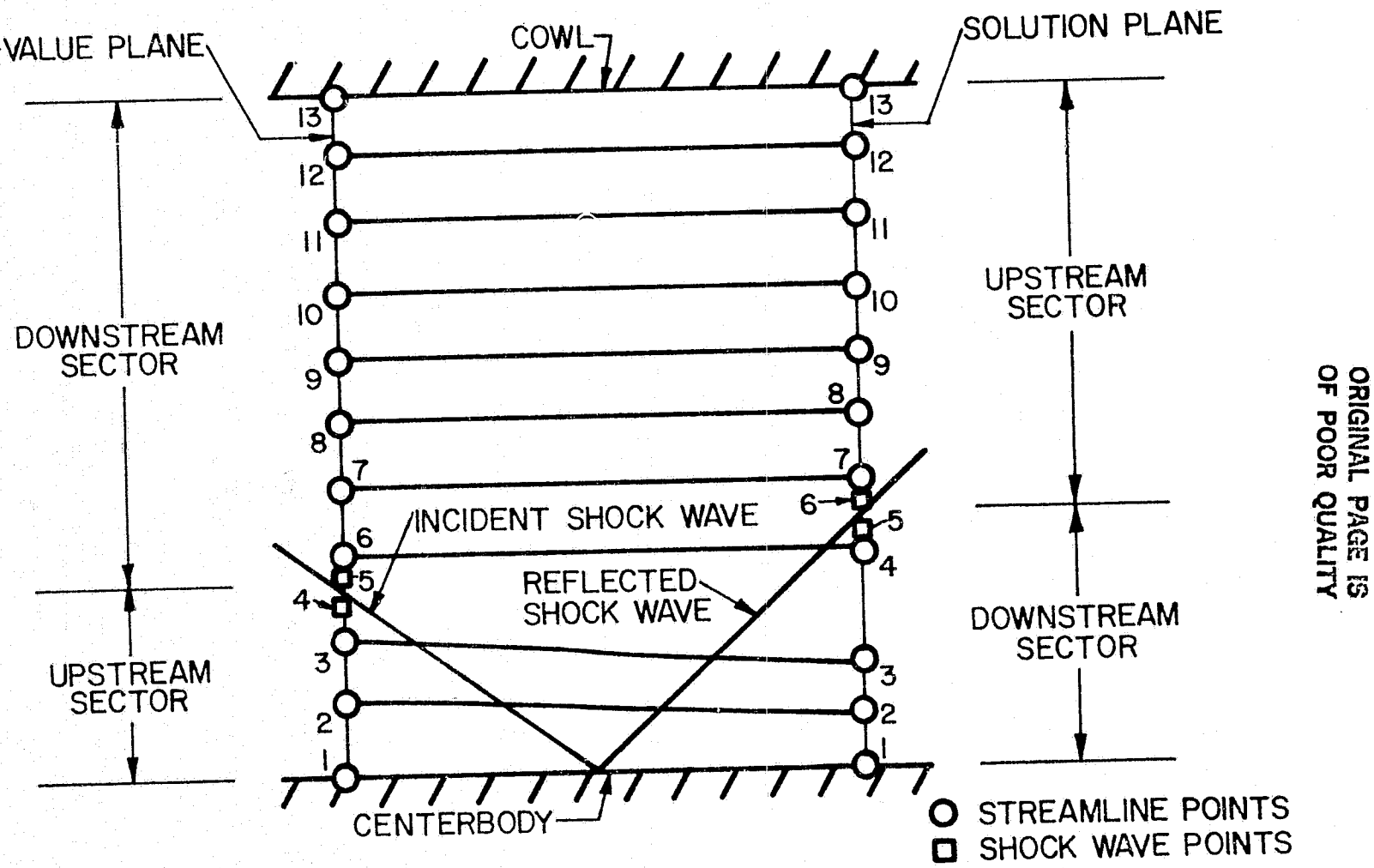

FIGURE K.7. TYPICAL STREAMLINE NETWORK AT AN INTERNAL SHOCK WAVE REFLECTION

onto the solution plane. A test is then made to determine whether or not each of these streamlines intersects the reflected shock wave (see Figure K.7). Those streamlines which do not intersect the reflected shock wave will lie in the upstream flow field sector on the solution plane (points 7 to 13 in Figure K.7). The solution at these points is determined using the standard interior point scheme, or if the Mach cone, with apex at the solution point, intersects the incident shock wave or solid boundary, the appropriate modified interior point unit process is applied. Those streamlines which appear to intersect the reflected shock wave have their computation deferred.

At this stage, the upstream and downstream shock wave points are determined at every circumferential station in the solution plane computed sector. This procedure defines the property field on both the upstream and downstream sides of the reflected internal shock wave.

Next, the solution is obtained at each body streamline point in the downstream flow field sector on the solution plane (see Figure K.7). The modified solid boundary point unit process is applied in this situation, which requires using flow property information on the downstream side of the reflected shock wave. After the application of the body point unit process at each point in the computed sector, the property field on the solid boundary is defined.

At this stage, the streamlines that are in the downstream flow field sector in the initial-value plane and that intersect the reflected shock wave are computed. These points require using the modified interior point unit process and use flow property information on both the upstream and downstream sides of the reflected internal shock wave (see Figure K.7).

Finally, the streamlines that are in the upstream flow field sector

in the initial-value plane are extended to the surface of the incident shock wave and their respective intersection points with this surface are determined (see Figures K.7 and K.8). These streamlines are then extended from the downstream side of the shock wave to the current solution plane. If the projected streamline does not intersect the reflected shock wave, a modified interior point unit process is applied using flow property information on the downstream side of the incident shock wave. If the projected streamline intersects the reflected shock wave, the intersection point is found with this surface. A modified interior point unit process is then applied on the downstream side of the reflected shock wave.

After all of the points have been determined on the solution plane that is immdiately downstream of the shock wave-solid body reflection, control is returned to the driving algorithm until another shock wave-solid body reflection is encountered.

Figures K.6 to K.8 illustrate the intersection of the shock wave with the centerbody. Similar results hold when the shock wave intersects the cowl.

The internal flow field integration is terminated when either a specified axial station is reached or when the flow becomes subsonic.

9. COMPUTATION OF THE BOUNDARY LAYER FLOW

The overall numerical algorithm for the boundary layer flow computation consists of the repetitive application of the attachment line flow, three-dimensional flow, and shock wave-boundary layer interaction region flow subalgorithms to generate the global solution for given boundary conditions and a specified set of initial-data.

The boundary layer flow initial-data are specified on body normal rays of constant $\tilde{x}$. The $\tilde{x}$-coordinate axis is the streamwise curvilinear

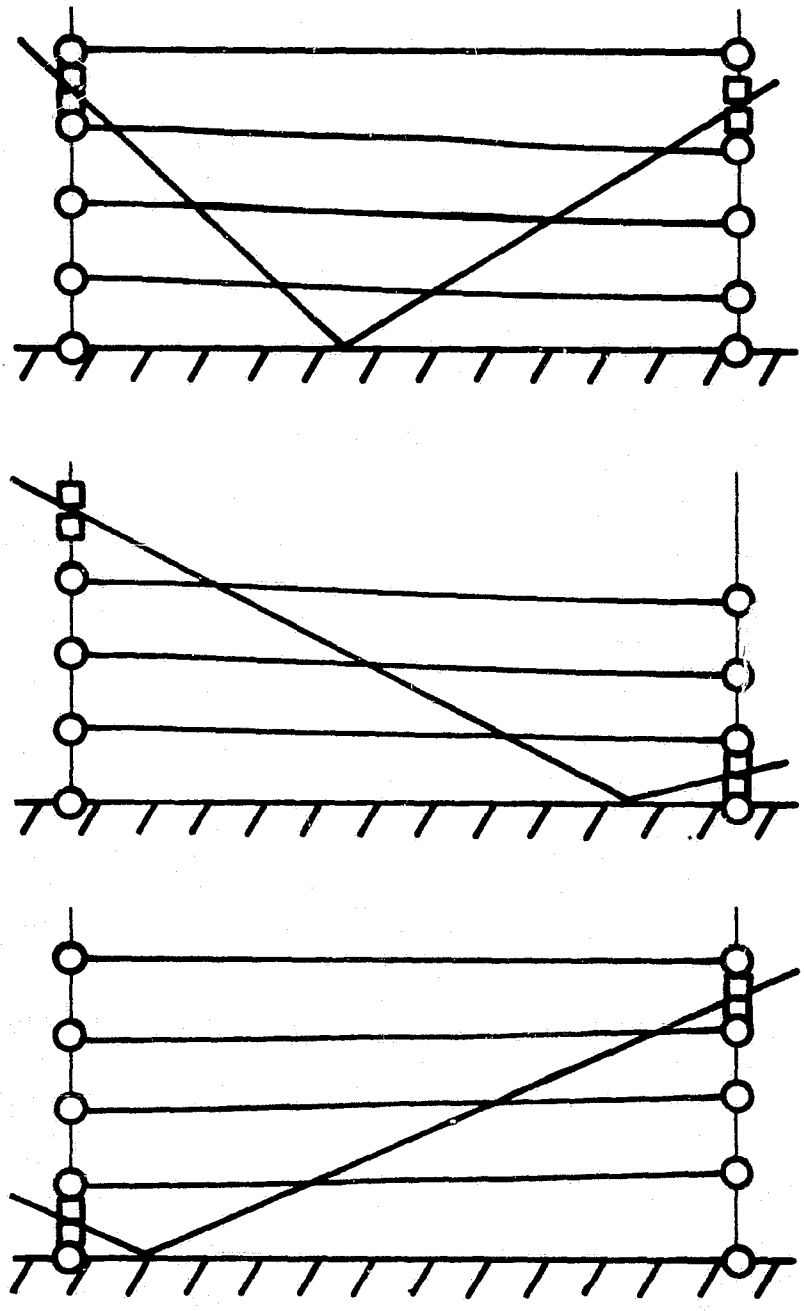

FIGURE K.8. POSSIBLE STREAMLINE PATTERNS AT A REFLECTION

coordinate coincident with the body and contained in a given meridional plane (see Figure 9). The mean boundary flow direction is assumed to be in the $\tilde{x}$-coordinate direction. Separate sets of initial data are required to initiate the forebody/centerbody and cowl boundary layer computations.

The implicit finite difference algorithm is applied to compute all of the boundary layer flow except for that in the shock wave-boundary layer interaction regions where the integral analysis is employed. The finite difference algorithm first applies the attachment line flow subalgorithm to calculate the boundary layer flow on the windward and leeward planes of symmetry. The three-dimensional flow subalgorithm is then applied to compute the boundary layer flow between the planes of flow symmetry starting at the windward meridian and marching to the leeward meridian for a given solution surface. The boundary layer solution is obtained on an orthogonal curvilinear mesh conforming to the local surface curvature. As opposed to the bicharacteristic supersonic flow solution, individual streamlines are not followed in the boundary layer computation. The boundary layer external flow properties are determined by interpolation of the supersonic flow solution.

When a shock wave-boundary layer interaction region has been encountered, the three-dimensional integral analysis is applied to compute the property profiles on the downstream side of the interaction region. The boundary layer properties on the upstream side of the interaction region are supplied by application of the implicit finite difference algorithm. The external flow properties are obtained from the supersonic core flow solution.

The streamwise step size used in the boundary layer computation is selected to correspond to the axial marching step determined from the

Courant-Friedrichs-Lewy stability criterion used in the supersonic flow computation. As a consequence, the supersonic flow and boundary layer flow solutions are determined at the same axial stations.

10. BOUNDARY LAYER FLOW INITIAL DATA

The boundary layer flow initial data are specified at stations of constant $\tilde{x}$ (see Figure 9). Separate sets of initial data must be specified to initiate the forebody/centerbody and cowl boundary layer computations. For uniqueness and existence of a genuine solution, the prescribed initial data must have at least continuous first partial derivatives.

The forebody/centerbody boundary layer flow initial data must be specified at the same axial station at which the supersonic flow initial data are specified. If the forebody is conical ahead of the axial station where the computation is to be started, then the initial data may be generated using the implicit finite difference algorithm developed by Adams (29), which is applicable to determining the boundary layer flow for a circular cone at incidence. The Adams algorithm has been incorporated into the computer program developed in the present investigation. Use of the Adams algorithm mandates specification of the wall temperature.

If the forebody is not conical ahead of the axial station where the computation is to begin, then the initial data must be specified by the user. Experimental data may be employed, if available.

The cowl boundary layer initial data must be specified at the axial location of the first supersonic flow solution plane inside the annulus since the boundary layer thickness at the cowl lip is identically zero. The cowl boundary layer initial data may be internally generated in the computer program using an approximate technique. Alternatively, arbitrary initial data may be specified by the user.

The internally generated cowl boundary layer initial data are obtained by an approximate analysis. The boundary layer thickness at each circumferential station is approximated by formulae appropriate for two-dimensional flow (4). For laminar flow, the boundary layer thickness δ is calculated from

$$\delta(\tilde{x}) = 5.0\left(\frac{\nu_e \tilde{x}}{\tilde{u}_e}\right)^{1/2} \tag{K.9}$$

whereas for turbulent flow, the boundary layer thickness is given by

$$\delta(\tilde{x}) = 0.37\ \tilde{x}\left(\frac{\tilde{u}_e \tilde{x}}{\nu_e}\right)^{-1/5} \tag{K.10}$$

In equations (K.9) and (K.10), $\tilde{x}$ denotes the streamwise body-coincident curvilinear coordinate contained in a given meridional plane and measured from the cowl lip (see Figure K.9), $\tilde{u}_e$ is the $\tilde{x}$-velocity component measured at the boundary layer edge, and ν_e is the kinematic viscosity at the boundary layer edge. Although $\tilde{x}$ is constant at each circumferential station used in the initial data specification, the boundary layer edge properties do vary, and thereby so does the boundary layer thickness.

With the local boundary layer thickness determined, the velocity profiles at each circumferential station are obtained by assuming profile functional forms. For laminar flow, the following functional forms are assumed

$$\tilde{u}/\tilde{u}_e = a_1 + a_2\eta + a_3\eta^2 \tag{K.11}$$

$$\tilde{w}/\tilde{w}_e = b_1 + b_2\eta + b_3\eta^2 \tag{K.12}$$

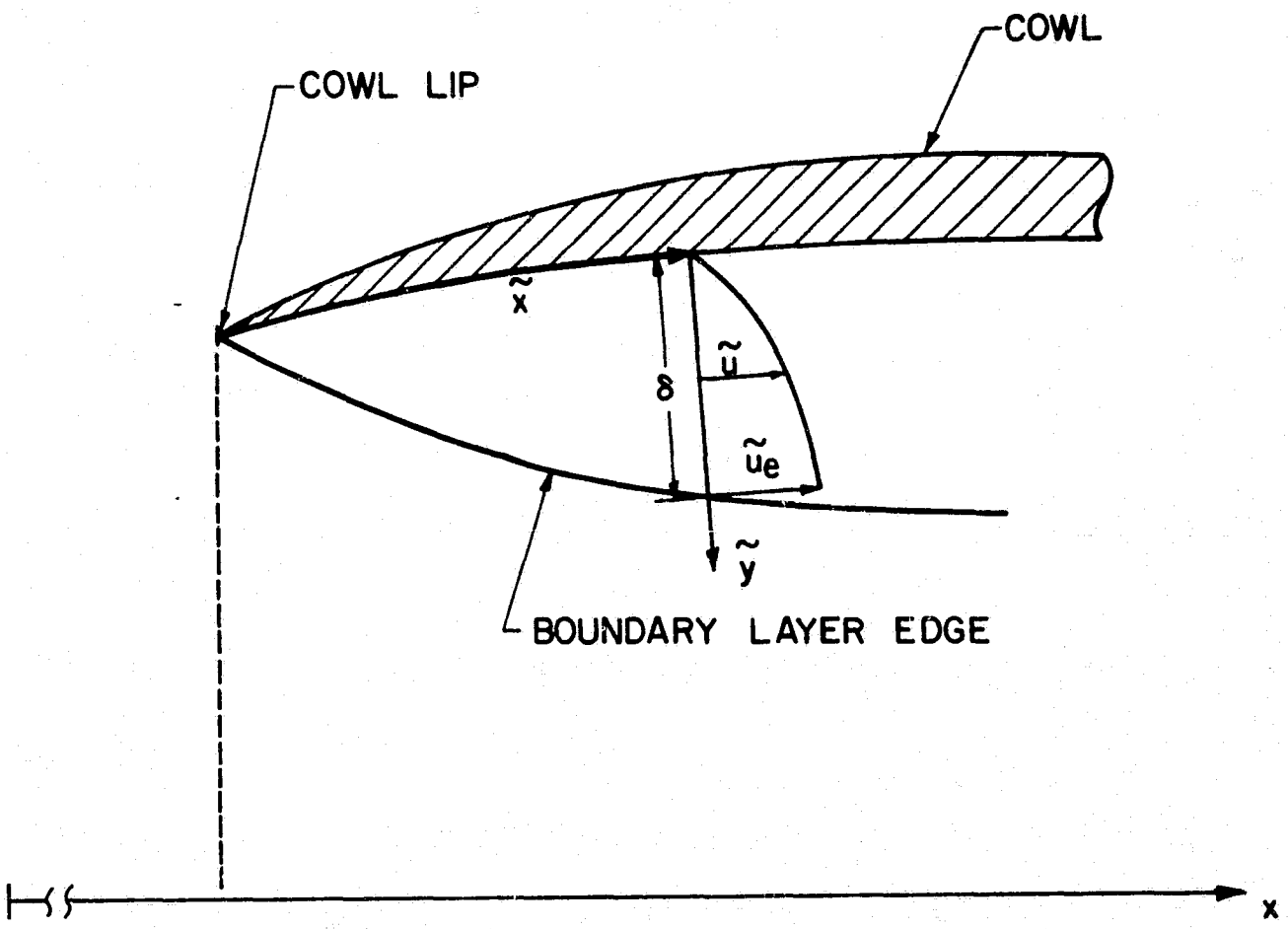

FIGURE K.9. COWL BOUNDARY LAYER INITIAL DATA SPECIFICATION

with

$$\eta = \tilde{y}/\delta \tag{K.13}$$

In equations (K.11), (K.12), and (K.13), $\tilde{u}$ and $\tilde{w}$ denote the boundary layer velocity components in the streamwise ($\tilde{x}$) and cross flow ($\tilde{z}$) directions, respectively, $\tilde{u}_e$ and $\tilde{w}_e$ are the respective velocity components at the boundary layer edge, $\tilde{y}$ is the distance measured normal to the wall (see Figure K.9), and a_i and b_i (i=1,2,3) are coefficients in the polynomial expansions which are ascertained by applying the following boundary conditions:

$$y = 0 \ (\eta = 0): \quad \tilde{u} = 0, \ \tilde{w} = 0 \tag{K.14}$$

$$y = \delta \ (\eta = 1): \quad \tilde{u} = \tilde{u}_e, \ \tilde{w} = \tilde{w}_e \tag{K.15}$$

$$y = \delta \ (\eta = 1): \quad \frac{\partial \tilde{u}}{\partial \tilde{y}} \cong 0, \ \frac{\partial \tilde{w}}{\partial \tilde{y}} \cong 0 \tag{K.16}$$

Applying equations (K.14), (K.15), and (K.16) yields the following final forms for equations (K.11) and (K.12)

$$\tilde{u}/\tilde{u}_e = 2\eta - \eta^2 \tag{K.17}$$

$$\tilde{w}/\tilde{w}_e = 2\eta - \eta^2 \tag{K.18}$$

The velocity profiles for turbulent flow are assumed to be given by

$$\tilde{u}/\tilde{u}_e = \eta^{\alpha} \tag{K.19}$$

$$\tilde{w}/\tilde{w}_e = \eta^{\beta} \tag{K.20}$$

where the power law exponents α and β are user specified. In obtaining

equation (K.10), the following exponent values were assumed

$$\alpha = \beta = 1/7 \tag{K.21}$$

However, α and β generally can fall in the Reynolds number dependent range

$$\frac{1}{10} \leq \alpha \leq \frac{1}{5} \tag{K.22}$$

$$\frac{1}{10} \leq \beta \leq \frac{1}{5} \tag{K.23}$$

The mean total enthalpy H distribution across the boundary layer is assumed to be given by

$$H = c_1 + c_2\eta + c_3\eta^2 \tag{K.24}$$

where the polynomial coefficients c_i (i=1,2,3) are obtained by application of the appropriate boundary conditions. For the case of a specified wall temperature, or equivalently a specified total enthalpy at the wall H_w, the following conditions apply

$$\tilde{y} = 0 \ (\eta = 0): \quad H = H_w \tag{K.25}$$

$$\tilde{y} = \delta \ (\eta = 1): \quad H = H_e \tag{K.26}$$

$$\tilde{y} = \delta \ (\eta = 1): \quad \frac{\partial H}{\partial \tilde{y}} \cong 0 \tag{K.27}$$

where H_e is the total enthalpy at the boundary layer edge. Applying equations (K.25), (K.26), and (K.27) yields the following final form of equation (K.24)

$$H = H_w + 2(H_e - H_w)\eta + (H_w - H_e)\eta^2 \tag{K.28}$$

For the case of a specified normal temperature gradient at the wall, or equivalently a specified total enthalpy gradient at the wall H_w', the following conditions apply

$$\tilde{y} = 0 \ (\eta = 0): \quad \frac{\partial H}{\partial \tilde{y}} = H_w' \tag{K.29}$$

$$\tilde{y} = \delta \ (\eta = 1): \quad H = H_e \tag{K.30}$$

$$\tilde{y} = \delta \ (\eta = 1): \quad \frac{\partial H}{\partial \tilde{y}} \cong 0 \tag{K.31}$$

Applying equations (K.29), (K.30), and (K.31) yields the following final form of equation (K.24)

$$H = (H_e - \frac{1}{2} H_w' \delta) + H_w' \delta\eta - \frac{1}{2} H_w' \delta\eta^2 \tag{K.32}$$

With the total enthalpy and velocity profiles determined for a given circumferential station, the mean static enthalpy h profile is obtained from

$$h \cong H - \frac{1}{2} (\tilde{u}^2 + \tilde{w}^2) \tag{K.33}$$

Assuming a constant pressure along a given normal then allows the temperature and density to be computed by using the caloric and thermal equations of state, respectively.

11. BOUNDARY LAYER FLOW SOLUTION MESH AND FLOW SYMMETRY

The boundary layer flow is determined on a body-fitted computational mesh. The solution points are located on body normal rays, the circumfer-

ential distribution of the rays being the same on each solution surface. Each solution surface corresponds to stations of constant $\tilde{x}$ where $\tilde{x}$ is the curvilinear streamwise coordinate coincident with the body and contained in a given meridional plane.

The point network on a given boundary layer solution surface is illustrated in Figure K.10. In this figure, the index i corresponds to the i th circumferential station and the index j corresponds to the j th radial (or normal) station. In all cases, the points on the body are denoted by $j = 1$ and the points at the boundary layer edge are denoted by $j = n_a$ or $j = n_b$ for the forebody/centerbody and cowl boundary layers, respectively. The computed sector, in general, is bounded by the circumferential stations $i = 1$ and $i = m$ for the forebody/centerbody and cowl boundary layers. The spacing in the normal direction is specified by the use of the formulations given in Appendix I.

One flow symmetry option has been incorporated into the boundary layer algorithm. This option is for the case of one plane of flow symmetry as illustrated in Figure K.10. In this case the computed sector is bounded by the $i = 1$ circumferential station on the -y-axis and by the $i = m$ circumferential station on the +y-axis.

12. TEMPERATURE AND MASS TRANSFER BOUNDARY CONDITIONS

The boundary layer computation requires specification of the temperature or of the normal temperature derivative at the wall. Constant temperature or temperature derivative boundary conditions may be specified. Alternatively, an arbitrary wall temperature or temperature derivative distribution may be specified by tabular input. Quadratic interpolation is

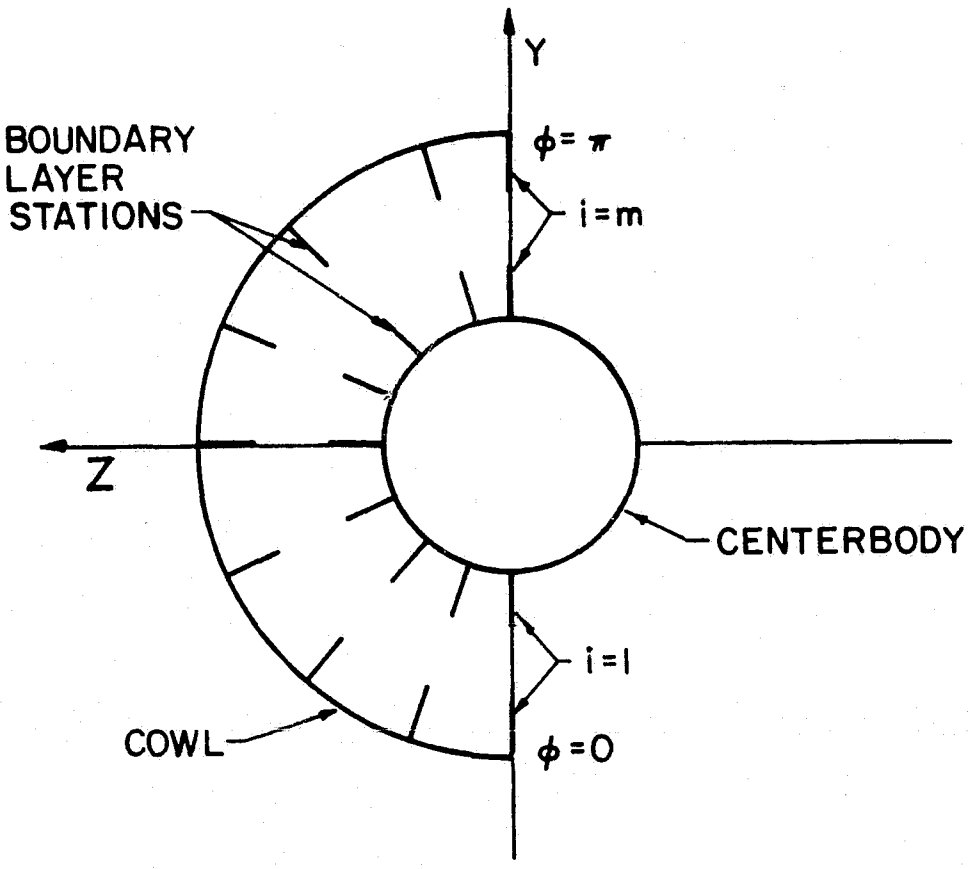

(a) CIRCUMFERENTIAL NETWORK

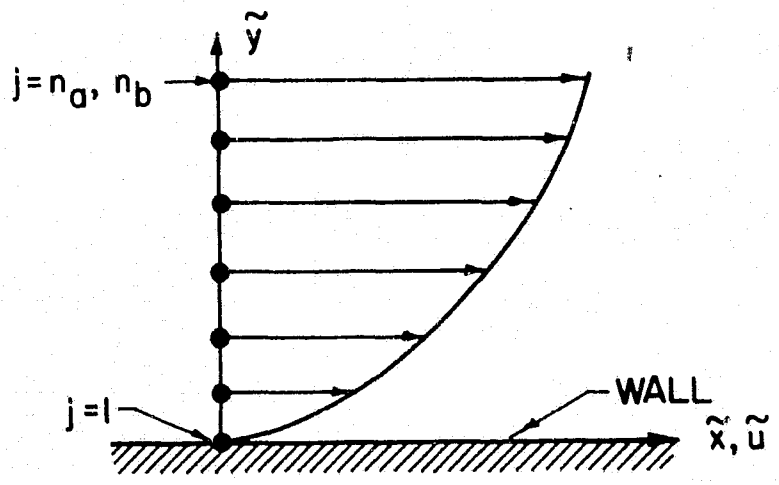

(b) RADIAL NETWORK

FIGURE K.10. BOUNDARY LAYER FLOW COMPUTATIONAL POINT NETWORKS

employed to obtain the temperature boundary condition at the required axial stations when the tabular input option is employed.

Mass transfer boundary conditions are specified by entering the axial locations of the boundary layer bleed zones and the mass flux within each zone.

APPENDIX L

NOMENCLATURE FOR SELECTED VARIABLES

ENGLISH SYMBOLS

a	sonic speed
a_i, b_i, c_i, d_i	general curve fit coefficients
A^+	van Driest damping factor
B_i	body force vector in index notation
c	velocity of divergence of Mach conoid surface
e	internal energy per unit mass
f	general interpolation polynomial function
F_x, F_y, F_z, F_e	forcing functions in the x, y, and z component momentum equations and energy equation, respectively
h	mean static enthalpy per unit mass
H	mean total enthalpy per unit mass
h_1, h_2	metric coefficients
$\hat{i}, \hat{j}, \hat{k}$	unit vectors in the x, y, and z directions, respectively
$\hat{i}', \hat{j}', \hat{k}'$	unit vectors in the x', y', and z' directions, respectively
K_1, K_2	geodesic curvature terms
$\hat{\ell} = (\ell_{x'}, \ell_{y'}, \ell_{z'})$	unit vector along the space curve defined by the intersection of the shock wave with either the initial-value plane or a solid boundary
L	mixing length

$\dot{m}_{bleed}$	bleed mass flow rate
M	Mach number
$\hat{n} = (n_x, n_y, n_z)$	unit vector normal to a wave surface
n_i	above unit vector in index notation
$\hat{n}_b = (n_{bx}, n_{by}, n_{bz})$	unit vector normal to a solid boundary
n_{bi}	above unit vector in index notation
$\hat{n}_s=(n_{sx'}, n_{sy'}, n_{sz'})$	unit vector normal to the shock wave surface [expressed in the (x',y',z')-system]
$\overline{N} = (N_x, N_y, N_z)$	vector normal to either a wave surface or a stream surface
P	pressure
Pr	laminar Prandtl number
Pr_t	turbulent Prandtl number
q	velocity magnitude
r	radial position of a point
R	gas constant
R_c	cowl lip radius
R_{min}	distance from streamline base point to nearest point on convex hull
s	either entropy per unit mass, or arc length
S	temperature base in Sutherland's formula
$\overline{S} = (S_x, S_y, S_z)$	vector in the wave surface and normal to the bicharacteristic direction
t	time or time-like parameter
$\hat{t}$	unit vector along the space curve defined by the intersection of the shock wave with a meridional plane

T	absolute temperature, or mass transpiration term
u,v,w	velocity components in the x, y, and z directions, respectively
$\tilde{u},\tilde{v},\tilde{w}$	mean velocity components in the $\tilde{x}$, $\tilde{y}$, and $\tilde{z}$ directions, respectively
u_i	velocity in index notation
$\overline{V}$	velocity vector
x,y,z	cartesian coordinates of base coordinate system
$\tilde{x},\tilde{y},\tilde{z}$	orthogonal curvilinear coordinates for the boundary layer computation
x_i	base system coordinates in index notation
x',y',z'	cartesian coordinates of local coordinate system

GREEK SYMBOLS

α	either the angle of attack, the angle subtended by the unit vector $\hat{\ell}$ and the z'-axis, or turbulence model constant
α_i,β_i	unit vectors used in the parameterization of the characteristic equations
γ	specific heat ratio
δ	boundary layer thickness
δ_{ij}	Kronecker delta
δ_{TR}	intermittency factor
ε	turbulent eddy viscosity
ε_θ	turbulent eddy thermal conductivity

η	second coefficient of viscosity, or transformed normal coordinate
θ	either the angle used in the parameterization of the characteristic equations, or the angle subtended by a meridian and the (x,y)-plane
κ	thermal conductivity, or von Karman parameter
λ	term in the wave surface compatibility relation
μ	dynamic viscosity
ν	kinematic viscosity
ξ	thermodynamic parameter
ρ	density
σ	term in the noncharacteristic relation
ϕ	angle subtended by the unit vector $\hat{t}$ and the x'-axis, or vector potential function
Φ	either the viscous dissipation function, or a term in the wave surface compatibility relation
ψ	vector potential function

SUBSCRIPTS

e	boundary layer edge conditions
i,j,k	rectangular cartesian coordinate indices ranging from 1 to 3
w	wall conditions
x,y,z	denotes either partial differentiation with respect to x, y, and z, or the x, y, and z components of a vector
∞	free-stream conditions

OPERATORS

$D( )/Dt$	material derivative
$\bar{(\ )}$	vector
$\hat{(\ )}$	unit vector
$( )'$	time fluctuation component, or partial derivative with respect to η
$\frac{\partial( )}{\partial x_i}$	partial derivative with resepct to x_i

LIST OF REFERENCES

1. Vadyak, J., and Hoffman, J. D., "Calculation of the Flow Field in Supersonic Mixed-Compression Inlets at Angle of Attack Using the Three-Dimensional Method of Characteristics with Discrete Shock Wave Fitting," NASA CR-135425, 1978.

2. Vadyak, J., Hoffman, J. D., and Bishop, A. R., "A Computer Program for the Calculation of the Flow Field in Supersonic Mixed-Compression Inlets at Angle of Attack Using the Three-Dimensional Method of Characteristics with Discrete Shock Wave Fitting," NASA TM-78947, 1978.

3. Hughes, W. F., and Gaylord, E. W., Basic Equations of Engineering Science, Schaum Publishing Co., New York, 1964.

4. Schlichting, H., Boundary-Layer Theory, 6th Edition, McGraw-Hill Book Company, New York, 1968.

5. Van Wylen, G. J., and Sonntag, R. E., Fundamentals of Classical Thermodynamics, Wiley, New York, 1965, Chapters 3 and 7.

6. Rusanov, V. V., "The Characteristics of General Equations of Gas Dynamics," Zhurnal Vychistlitel 'noi matematiki: matematicheskoi fiziki, Vol. 3, No. 3, 1963, pp. 508-527. Translated by Trirogoff, K. N., Report No. LRG-65-T-38, Literature Research Group, Aerospace Library Services, Aerospace Corp., San Bernadino, California

7. Butler, D. S., "The Numerical Solution of Hyperbolic Systems of Partial Differential Equations in Three Independent Variables," Proceedings of the Royal Society of London, A255, 1960, pp. 232-252.

8. Courant, R., Friedrichs, K. O., and Lewy, H. "Uber die Partiellen Differenzialgleichungen der Mathematischen Physik," Mathematische Annalen, Vol. 100, 1928, pp. 32-74.

9. Ransom, V. H., Hoffman, J. D., and Thompson, H. D., "A Second-Order Numerical Method of Characteristics for Three-Dimensional Supersonic Flow, Volume I, Theoretical Development and Results," Report No. AFAPL-TR-69-98, Air Force Aero Propulsion Laboratory, Wright-Patterson Air Force Base, Ohio, 1969.

10. Vaglio-Laurin, R., "Turbulent Heat Transfer on Blunt-Nosed Bodies in Two-Dimensional and General Three-Dimensional Hypersonic Flow," Journal of the Aerospace Sciences, Vol. 27, No. 1, Jan. 1960, pp. 27-36.

11. Moore, F. K., Theory of Laminar Flows, Vol. IV, Princeton University Press, Princeton, N.J., 1964.

12. Keller, H. B., "A New Difference Scheme for Parabolic Problems," in Numerical Solution of Partial Differential Equations, Vol. II, Academic Press, New York, 1970.

13. Keller, H. B., and Cebeci, T., "Simple Accurate Numerical Methods for Boundary Layers; Two-Dimensional Turbulent Flows," AIAA Journal, Vol. 10, No. 9, Sept. 1972.

14. Cebeci, T., Khattab, A. A., and Stewartson, K., "Studies on Three-Dimensional Boundary Layers on Bodies of Revolution; Three-Dimensional Laminar Boundary Layers and the Ok of Accessibility," Report No. MDC J8716, Douglas Aircraft Company, 1980.

15. Courant, R. and Hilbert, D., Methods of Mathematical Physics, Volume II, Partial Differential Equations, Interscience Publishers, New York, 1966.

16. Zucrow, M. J., and Hoffman, J. D., Gas Dynamics, Volumes I and II, Wiley, New York, 1977.

17. Cline, M. C., and Hoffman, J. D., "The Analysis of Nonequilibrium, Chemically Reacting, Supersonic Flow in Three Dimensions, Volume I, Theoretical Development and Results," Report No. AFAPL-TR-71-73, Air Force Aero Propulsion Laboratory, Wright Patterson Air Force Base, Ohio, 1971.

18. Hamming, R. W., Numerical Methods for Scientists and Engineers, 2nd Edition, McGraw-Hill, New York, 1973.

19. Butler, D. S., Private Communication with V. H. Ransom, October 1968.

20. Cebeci, T., Kaups, K., Mosinskis, G. J., and Rehn, J. A., "Some Problems of the Calculation of Three-Dimensional Boundary Layer Flows on General Configurations," NASA CR-2285, 1973.

21. Raetz, G. S., "A Method of Calculating Three-Dimensional Laminar Boundary Layers of Steady Compressible Flows," Report No. NAI 58-73, Northrop Corp., 1957.

22. Isaacson, E., and Keller, H. B., Analysis of Numerical Methods, Wiley, New York, 1966.

23. Reyhner, T. A., and Hickcox, T. E., "A Procedure for Combined Viscous-Inviscid Analysis of Supersonic Inlet Flow Fields," Journal of Aircraft, Vol. 9, No. 8, August 1972, pp. 589-595.

24. Syberg, J., and Koncsek, J. L., "Bleed System Design Technology for Supersonic Inlets," Journal of Aircraft, Vol. 10, No. 7, July 1973, pp. 407-413.

25. Paynter, G. C., "Analysis of Weak Glancing Shock/Boundary Layer Interactions," AIAA Paper No. 79-0144, 1979.

26. Peake, D. J., "Three-Dimensional Swept Shock/Turbulent Boundary-Layer Separations with Control by Air Injection," National Research Council of Canada, Report LR-592, 1976.

27. Green, J. E., "Interactions Between Shock Waves and Turbulent Boundary Layers," Progress in Aerospace Sciences, Vol. 11, Pergamon Press, Oxford, 1970, pp. 235-340.

28. Jones, D. J., "Numerical Solutions of the Flow Field for Conical Bodies in a Supersonic Stream," National Research Council of Canada, Report LR-507, 1968.

29. Adams, J. C., "Finite Difference Analysis of the Three-Dimensional Turbulent Boundary Layer on a Sharp Cone at Angle of Attack in a Supersonic Flow," AIAA Paper No. 72-186, 1972.

30. Syberg, J., and Hickcox, T. E., "Design of a Bleed System for a Mach 3.5 Inlet," NASA CR-2187, 1973.

31. Anderson, B. H., Tassa, Y., and Reshotko, E., "Characteristic Procedure for Supersonic Flows Including Consideration of Viscous Contributions to Flow Rotationality," Paper No. 76-426, 1976.

32. Presley, Leroy L., Private Communication, November 1977.

33. Presley, Leroy, L., "Internal Flow Calculations for Axisymmetric Supersonic Inlets at Angle of Attack," AIAA Paper 75-1214, 1975.

34. Kutler, P., Lomax, H., and Warming, R. F., "Computation of Space Shuttle Flow Fields Using Noncentered Finite-Difference Schemes," AIAA Journal, 1973, p. 196.